Imperial College London

Doctoral Thesis

Multi-scale modelling of thermo-hydro-mechanical-chemical processes in fractured rocks

Author:
Philipp Stefan Lang

Supervisors:
Dr. Adriana Paluszny
Prof. Robert W. Zimmerman

A thesis submitted in fulfilment of the requirements for the degree of Doctor of Philosophy

in

Rock Mechanics

Department of Earth Science and Engineering
Faculty of Engineering

July 2016

Abstract

Multi-scale modelling of thermo-hydro-mechanical-chemical processes in fractured rocks

A first-principle modelling framework for thermo-hydro-mechanical-chemical processes in fractured rock is developed. The key characteristics of such rocks are incorporated by direct representation: the power law nature of fracture size distribution, the fractal nature of rock surfaces, the scale dependence of discrete contact between these, and the mechanically induced fluid-flow anisotropy. It is shown that hydro-mechanical modelling in fractured rock can be reduced to a single free parameter, the friction coefficient. Properties of fractured rock, such as transmissivity, stiffness and permeability, emerge as direct results of physical processes, and need not be complemented by empirical relationships or distribution functions. Results reproduce the field observation that critically-oriented fractures are likely hydraulic conduits; while the established reasoning of shear activation and associated fracture dilation for this fact is confirmed, it is also shown, for the first time, that chemically-mediated processes have the potential to contribute to this effect. Compaction mechanisms of pressure solution and precipitation act preferably on fractures with stress ratios far from Coulomb failure, which increases the relative contribution of near-critical fractures. New insights also emerge as to the likely orientation of the maximum permeability of a fractured rock mass. Due to shear-induced anisotropy of fracture transmissivity, the preferential flow direction tends to be aligned with the orientation of the intermediate stress. The capability to accurately determine the upscaled permeability tensor is facilitated by a novel algorithm that is independent of geometry and reference system, and accounts for locally anisotropic matrix permeability and fracture transmissivity. The developed framework presents a path forward in fractured rock modelling. It accounts for state of the art knowledge of the internal processes of fractured rock across multiple scales, and perhaps aids to overcome the necessity for using isotropic effective properties that is prevalent in many applications.

Copyright Declaration

The copyright of this thesis rests with the author and is made available under a Creative Commons Attribution Non-Commercial No Derivatives licence. Researchers are free to copy, distribute or transmit the thesis on the condition that they attribute it, that they do not use it for commercial purposes, and that they do not alter, transform or build upon it. For any reuse or redistribution, researchers must make clear to others the licence terms of this work.

Declaration of Originality

I, Philipp Stefan Lang, declare that this thesis titled, 'Multi-scale modelling of thermo-hydro-mechanical-chemical processes in fractured rocks' and the work presented in it are my own. I confirm that:

- This work was done wholly or mainly while in candidature for a research degree at this University.
- Where any part of this thesis has previously been submitted for a degree or any other qualification at this University or any other institution, this has been clearly stated.
- Where I have consulted the published work of others, this is always clearly attributed.
- Where I have quoted from the work of others, the source is always given. With the exception of such quotations, this thesis is entirely my own work.
- I have acknowledged all main sources of help.
- Where the thesis is based on work done by myself jointly with others, I have made clear exactly what was done by others and what I have contributed myself.

Acknowledgements

Firstly, I would like to express my sincere gratitude to Dr. Adriana Paluszny. Her approach to supervision is sure to set the bar for wherever I will find myself in the future. Rising to the top of your profession is a hard thing to accomplish. Being able to truly help others in the pursuit of the same is even more elusive. I will truly miss our collaboration.

My sincere thanks goes to Prof. Zimmerman, who provided me an opportunity to join the rock mechanics group at Imperial. Embarking a PhD here in London proved to be one of the best decisions in my life, and opportunities of this sort are rare.

The contribution of raw surface data by Prof. Hideaki Yasuhara and Dr. Takuya Ishibashi of raw surface measurement data is greatly appreciated.

This work was conducted within the international DECOVALEX Project, with funding from Radioactive Waste Management Limited (RWM), a wholly-owned subsidiary of the Nuclear Decommissioning Authority. Discussions with members of the C1 task group have been very fruitful and contributed greatly to my critical thinking with regards to the subject. Dr. Alex Bond provided thoughtful management as the task leader, which allowed the team to focus on their research as much as possible. Throughout the duration of the project, Dr. Simon Norris always emphasized quality of research over quantity of results, which allowed me to pursue a range of approaches and allowed for freedom I very much appreciate.

Last but not the least, I would like to thank my family. My sister, for showing me what kind of person I want to be. My parents, for helping me to become who I am, and supporting me in my life so far. And my love, for supporting me for the rest of it, and helping me to become much better.

Contents

Declaration of Originality **3**

Acknowledgements **4**

Contents **5**

List of Figures **8**

List of Tables **10**

Abbreviations **11**

Physical Constants **12**

Symbols **13**

1 Introduction **17**
1.1 Focus of this work 18
1.2 Three scales, three power-laws 19
1.2.1 Fracture network 20
1.2.2 Fracture surfaces 22
1.2.3 Surface contact 24
1.3 Experiments 26
1.4 Transmissivity altering processes in rock fractures 29
1.5 Anisotropy of fractured rock permeability 35
1.6 Previous work 37
1.7 Outline 42

2 Methods **44**
2.1 Single fracture 45
2.1.1 No shear displacement - isotropic aperture fields 45
2.1.2 Shear displacement - anisotropic aperture fields 53
2.1.3 Contact 54
2.1.4 Pressure solution 60
2.1.5 Precipitation 65
2.1.6 Flow 68
2.1.7 Coupled dissolution and reactive transport 69

2.2 Fracture network . . . 73
2.2.1 Contact . . . 75
2.2.2 Hypothesised opening-closure process . . . 77
2.2.3 Flow . . . 79
2.2.4 Permeability . . . 80
2.2.5 Two-scale coupling . . . 90
2.3 Implementation . . . 92
2.4 Computational effort . . . 93

3 Hydro-mechanical characteristics of a single fracture 95
3.1 Tensorial transmissivity and scalar stiffness . . . 96
3.2 Stiffness as a function of size and shear displacement . . . 102
3.3 Representative elementary volumes and non-uniqueness . . . 104
3.4 Evolution of contact area with load . . . 105

4 Chemically-mediated compaction of a single fracture 108
4.1 Evolution of pore-space due to dissolution and precipitation . . . 109
4.2 Pressure solution formulations . . . 113
4.3 Effects of roughness cut-off . . . 114
4.4 Changes in transmissivity . . . 116
4.5 Compaction mechanisms over time . . . 120
4.6 Core flood experiments . . . 121
4.6.1 Novaculite results . . . 121
4.6.2 Granite results . . . 126
4.6.3 The relationship between aperture and contact ratio . . . 129
4.6.4 Discussion . . . 132
4.7 Changes in stiffness . . . 133
4.7.1 Fracture closure and stiffness-compliance relationships . . . 136
4.8 Fractures with shear displacement . . . 138
4.9 Summary . . . 140

5 Hydro-mechanical characteristics of fractured rock masses 145
5.1 Single and conjugate fractures embedded in a rock matrix . . . 146
5.1.1 Embedded single fracture . . . 148
5.1.2 Embedded pair of conjugate fractures . . . 150
5.2 Fracture networks . . . 153

6 Chemically mediated compaction of fractured rock masses 159
6.1 Single and conjugate fractures embedded in a rock matrix . . . 160
6.2 Fracture networks . . . 162

7 Discussion and Conclusions 166

References 195

A Application IO **196**
A.1 THMC module 196

B Permissions **200**

List of Figures

1.1 Scaling of fractures in a natural network 21
1.2 Roughness of fracture surfaces 23
1.3 Contact between randomly rough surfaces 26
1.4 Fractured core flood experiments I 29
1.5 Fractured core flood experiments II 30
1.6 THMC processes: time-scales and relative magnitudes 36
1.7 Pre- and post-experiment CT image of a fracture 36

2.1 Isotropic surfaces 48
2.2 Hurst exponent 50
2.3 Composite surface concept 52
2.4 Anisotropic void space due to shear 55
2.5 Single fracture contact 57
2.6 Rigid and mechanical aperture 58
2.7 Hydro-mechanical model at the fracture scale 59
2.8 Frictionless elastic contact verification 60
2.9 Dissolution of a single grain 66
2.10 Flow chart THMC 67
2.11 Mineral composition and dissolution rate models 70
2.12 Flow chart single fracture reactive transport 74
2.13 Fracture network contact 78
2.14 Boundary effects 86
2.15 Sampling region 87
2.16 Effective permeability benchmark 90
2.17 Two-scale flow chart 92

3.1 Experimental-numerical comparison single fracture - transmissivity 98
3.2 Single fracture transmissivity anisotropy 99
3.3 Experimental-numerical comparison single fracture - stiffness 101
3.4 Stiffness as a function of size and shear displacement 103
3.5 Mechanical REV and non-uniqueness of transmissivity-stiffness . . . 105
3.6 Contact area with load and shear displacement 106

4.1 Evolution of fracture surfaces with dissolution and precipitation . . 109
4.2 Early time effects of pressure solution 111

4.3 Qualitative evolution of hydro-mechanical state for 'closed' and 'open' fractures . . . 112
4.4 Qualitative and quantitative illustration of precipitation-dissolution 113
4.5 Comparison Lehner-Leroy and Bernabé-Evans formulation . . . 114
4.6 Effects of roughness cut-off on dissolution results . . . 115
4.7 Long-time effects of pressure solution . . . 117
4.8 Changes in transmissivity over time due to dissolution . . . 119
4.9 Relative dominance of compaction mechanisms over time . . . 120
4.10 Core flood modelling calibration factors . . . 123
4.11 Aperture and concentration comparison Novaculite experiment . . . 123
4.12 Tracemap illustrating opening-closing history of the Novaculite . . . 125
4.13 Comparison of numerical and experimental post-mortem contact . . . 125
4.14 Aperture and concentration comparison Granite experiment (AC) . 128
4.15 Aperture and concentration comparison Granite experiment (DC) . 130
4.16 Relationship between aperture and contact ratio . . . 131
4.17 Dependence of hydraulic aperture on contact ratio . . . 132
4.18 Qualitative evolution of closure-stiffness for 'closed' and 'open' fractures . . . 134
4.19 Curve fit to changing closure behaviour during dissolution . . . 138
4.20 Changes in transmissivity over time due to dissolution in fractures with offset . . . 139
4.21 Closure and stiffness evolution due to dissolution in fractures with offset . . . 141

5.1 Single and conjugate fracture DFMs . . . 146
5.2 Single fracture DFM results . . . 151
5.3 Conjugate fracture pair DFM results . . . 152
5.4 Qualitative network DFM results . . . 154
5.5 Quantitative network DFM results . . . 156
5.6 Distributions of maximum permeability and hydraulic aperture . . . 158

6.1 Single fracture DFM results, before and after compaction . . . 161
6.2 Conjugate fracture pair DFM results, before and after compaction . 162
6.3 Quantitative network DFM results, before and after compaction . . 163
6.4 Distributions of maximum permeability and hydraulic aperture, before and after compaction . . . 164

List of Tables

2.1 Representative runtimes 94

3.1 Single fracture mechanical properties 96

4.1 Water-Quartz system chemical properties 109
4.2 Input conditions for numerical core flood experiments 122

Abbreviations

CT	X-ray **C**omputed **T**omography
DFM	**D**iscrete **F**racture **M**odel
FE	**F**inite **E**lement
FFT	**F**ast **F**ourier **T**ransform
PSD	**P**ower **S**pectral **D**ensity
REV	**R**epresentative **E**lementary **V**olume
THMC	**T**hermo-**H**ydro-**M**echanical-**C**hemical

Physical Constants

Avogadro constant	N_a	$6.022\ 140\ 857 \times 10^{23}$	mol^{-1}
Molar gas constant	R	8.314 4598	$\mathrm{J\ mol}^{-1}\ \mathrm{K}^{-1}$
Boltzmann constant R/N_a	k_b	$1.380\ 648\ 52 \times 10^{-23}$	$\mathrm{J\ K}^{-1}$

Symbols

a	rigid aperture	m
a_h	hydraulic aperture	m
a'_h	length-normalised hydraulic aperture	-
a_m	mechanical aperture due to elastic compression	m
A_0	nominal fracture area	m^2
c	concentration	- or $\mathrm{kg\ m}^{-3}$
c_eq	free temperature-dependent equilibrium concentration	-
$c_\mathrm{eq,s}$	stressed temperature-dependent equilibrium concentration	-
C	roughness power	m^4 (3D), m^3 (2D)
C_0	roughness spectrum normalization factor	m^4 (3D), m^3 (2D)
D	temperature-dependent diffusion constant	$\mathrm{m}^2\ \mathrm{s}^{-1}$
D^*	diffusion constant in the grain-to-grain boundary	$\mathrm{m}^2\ \mathrm{s}^{-1}$
E	elastic modulus	Pa
E^*	composite elastic modulus	Pa
F	normal force	N
f	grain-to-grain contact diffusivity multiplier	-
$\hat{\boldsymbol{g}}_\mathrm{T}$	shear displacement before contact	m
$\boldsymbol{g}_\mathrm{T}$	shear displacement in contact	m
h	surface height	m
h^-, h^+	lower and upper surface height	m
h_rms	root-mean-square roughness	m
H	Hurst exponent	-
J	pressure dissolution mass flux	$\mathrm{kg\ m}^{-2}\ \mathrm{s}^{-1}$

k_d	temperature-dependent dissolution rate constant	$\mathrm{m\ s^{-1}}$
$\boldsymbol{K}$	transmissivity	$\mathrm{m^3}$
$\boldsymbol{k}$	permeability	$\mathrm{m^2}$
$k_\mathrm{max,med,min}$	permeability eigenvalues	$\mathrm{m^2}$
$\boldsymbol{k}'$	matrix-normalised permeability	-
$\tilde{\boldsymbol{k}}$	equivalent permeability	$\mathrm{m^2}$
ℓ	lattice size, cell length	m
$\mathcal{L}$	cell count along one axis in regular, square mesh	-
L	fracture length	m
M	mass	kg
m	element mass	$\mathrm{kg\ mol^{-1}}$
n	power law exponent	-
$\mathcal{N}$	anisotropy	-
p	normal component of nominal contact traction	Pa
p_f	fluid pressure	Pa
$\boldsymbol{q}$	roughness wave vector	$\mathrm{m^{-1}}$
q	wave number, or spatial frequency or roughness	$\mathrm{m^{-1}}$
q_L	lower frequency limit due to sample size	$\mathrm{m^{-1}}$
q_ℓ	upper frequency limit due to lattice size	$\mathrm{m^{-1}}$
q_0	roll-off frequency	$\mathrm{m^{-1}}$
q_1	cut-off frequency	$\mathrm{m^{-1}}$
q_m	mismatch frequency	$\mathrm{m^{-1}}$
Q	volumetric inflow rate	$\mathrm{m^3\ s^{-1}}$
r	grain radius	m
r_c	contact radius	m
r_d	diffusion radius	m
R_c	contact ratio	-
t	time	s
Δt	discrete time increment	s
$\mathcal{S}$	volume-normalised concentration source	$\mathrm{kg\ m^{-3}\ s^{-1}}$
$\boldsymbol{S}$	far-field stress tensor	Pa

T	temperature	K
$\boldsymbol{u} = (u_x, u_y)$	flow velocity	m/s
v	stoichiometric coefficient	-
V_m	molar volume	$\mathrm{m^3\ mol^{-1}}$
V	volume	$\mathrm{m^3}$
w	grain-to-grain contact interface thickness	m
W	inlet width of a non-square fracture	m
$\boldsymbol{x} = (x, y)$	fracture in-plane coordinate vector	m
$\boldsymbol{x} = (x, y, z)$	coordinate vector	m
α	power law pre-factor	-
δ	body approach	m
$\boldsymbol{\delta}_\mathrm{T}$	total shear displacement between fracture surfaces	m
$\boldsymbol{\delta}'_\mathrm{T}$	length-normalised shear displacement	-
η	dissolution rate pre-factor	-
κ	normal stiffness	$\mathrm{Pam^{-1}}$
λ	roughness wavelength	m
λ_L	upper wavelength limit due to sample size	m
λ_ℓ	lower wavelength limit due to lattice size	m
λ_0	roll-off wavelength	m
λ_1	cut-off wavelength	m
λ_m	mismatch wavelength	m
μ_f	dynamic fluid viscosity	Pa s
μ	friction coefficient	-
ν	Poisson's ratio	-
Ω_s	molecular volume	$\mathrm{m^3}$
Ω	upscaling domain	-
ψ_d	temperature-dependent dissolution rate constant	$\mathrm{mol\ s^{-1}\ m^{-2}}$
ρ_s	solid density	$\mathrm{kg\ m^{-3}}$
ρ_f	fluid density	$\mathrm{kg\ m^{-3}}$
σ	discrete contact normal stress	Pa

χ	volume fraction	-
ζ	magnification factor	-

Chapter 1

Introduction

Engineering endeavours concerned with natural rock masses cannot expect to encounter a continuous medium. Instead, it is likely that fractures dominate the overall behaviour of the system. Being discontinuities with imperfect interfaces, fractures represent weaknesses both in a mechanical and hydraulic sense. In the former, they limit the strength of a rock mass, mostly due to a lack of cohesion. In the latter, they represent preferred conduits for fluid flow, due to flow channels that form between the rough surfaces in contact. Isolating the behaviour of just the fractures in a rock formation often represents a bounding scenario for safety cases. In geological carbon dioxide storage, for example, a project is commonly considered unsafe when injection induced overpressure may cause slip along fractures. In geological nuclear waste disposal, the limiting case is often considered as one in which fluid flow occurs only within the connected system of fractures, and whether the ensuing radionuclide transport within this network exceeds some threshold. It follows that fractures are a logical point to start investigations on the impact that human interference has on an embedded geological setting in terms of its mechanical and hydraulic properties.

For geologic disposal of spent nuclear fuel, models are required to predict fluid flow and transport properties in the vicinity of a site over large periods of time. To model fluid flow in rock, it is imperative to account for the contribution of individual fractures, and the combined effect that arises from the connected network

they so often form. The transmissivity of a single fracture is highly sensitive to the acting confining pressure, which reflects the relatively large amount of volume change that occurs within a fracture void as it is being compressed. As a consequence, heat and mass transport, fluid flow, and the velocity and attenuation of seismic waves are all subject to stress dependence in fractured rock. Additionally, fracture properties depend upon the structural formation history, such as shear offset and abrasion related damage. Apart from this mechanical and structural aspect, the transmissivity of fractures rarely remains constant. Rather, chemical processes that are functions of stress, temperature, and flow conditions can lead to rapid changes in transmissivity, and thus have a large impact on network scale flow.

What makes modelling of physical processes in fractured rock particularly challenging is the fractal nature of the geometries that fractures tend to form. On the network scale, the rock surface scale and the scale of 'discrete' contacts between surfaces, this fractality makes it difficult for the modeller to define scales at which to derive the governing equations. This difficulty is directly related to the choice of which geometric features to represent explicitly in a distributed model, and which features to represent by means of parameters in constitutive relationships that describe a continuum.

1.1 Focus of this work

This work has two objectives. First, to devise a modelling framework that addresses scaling issues in fractured rock. The approach should be capable of translating effects at the micron range to scales relevant to engineering problems, i.e., the decametre-scale to kilometre-scale. Secondly, to implement and apply this approach for qualitative and quantitative predictions of the effects that thermo-hydro-mechanical-chemical (THMC) processes may have on the permeability of fractured rock masses. Emphasis will be made throughout to account for anisotropy, which is an intrinsic feature of fractured rock.

To arrive at a more tractable scope for the developed model, the types of rock under consideration are restricted to granitic and siliciclastic. This limits the number of mineral constituents, and thereby the chemical complexity of the reactions involved. Findings for these rock types should be useful in the context of geological disposal of nuclear waste, and have been the focus of the C1 task of the international DECOVALEX 2015 project, of which this study has been a part. In addition to these restrictions on the host rock, pore fluids will be assumed groundwater-like. These assumptions also reduce the number of applicable experiments to a more manageable number.

1.2 Three scales, three power-laws

Theories of reversible poroelastic compressibility [Zimmerman, 1990] or irreversible diagenetic compaction [Lehner and Leroy, 2004] of sandstones provide a useful illustration for the concept of scale. At the millimetre-scale, a few solid grains and void spaces between will present themselves. The behaviour of these grains and voids can be approximated by idealised descriptions of spheres and ellipsoids, for example. By the very definition of the grain size range that constitutes sandstone [Boggs, 2006], an intact piece of this type of rock at the metre-scale can be expected to contain a large number of these small forming parts. More importantly, the definition of sandstone guarantees that, for a metre-scale sample, none of the forming grains are close to the sample size. Thus, the scale at which the behaviour of the constituting parts are described, and the scale at which these parts act together as a continuum, can be clearly separated. It follows that the behaviour of such rock at the meter-scale will not be controlled by a single grain, but a representative number thereof. This separation of scales facilitates the derivation of governing equations that treat the ensemble of voids and solids as a continuum [Bear, 1972].

1.2.1 Fracture network

Many accepted classifications akin to that of sandstone exist for sedimentary rock, based on ranges of observed grain size [Boggs, 2006]. No such classification exists for fractured rock in terms of fracture length or intact rock block size. This is due to the power law-nature of fracture size distributions which extend from the kilometre- to the metre-scale [Barton, 1995, Bonnet et al., 2001] and even down to the millimetre-scale [Katz, 2004]. Detailed trace mapping of the Swedish Forsmark site for geological disposal of nuclear waste illustrates this pervasive nature of faults and fractures; see Figure 1.1. Single faults of kilometre-length span the extent of the entire site (Figure 1.1a). Fractures of decametre-length also span the scale of tunnel excavations and the distance between them (Figure 1.1b). The size distribution across these scales can be approximated by a power law distribution (Figure 1.1c) of the form $f(L) = \alpha L^n$, where α is a pre-factor and n is the exponent.

The exponent n is often referred to as the fractal dimension of the network, despite the fact that fractures in a network can obey a power law size distribution without forming a fractal geometry [see also Munier, 2004]. In a modelling context, the power law size distribution suggests that at any scale of investigation a single fracture should be expected to control the domain. This is in sharp contrast to the classic representative elementary volume (REV) concept [Bear, 1972] applied to sandstones, as discussed above. The lack of separation of scales between fractures and the domain of interest has led to the development of distributed models that represent fractures explicitly [Cundall, 1980, Long et al., 1982]. This approach has been termed discrete fracture modelling (DFM), which indicates that fractures and intact rock are both explicitly represented, and governed by separate sets of equations [*e.g.* Ahmed et al., 2015, Geiger et al., 2004, Matthäi et al., 2007, Nick and Matthäi, 2011, Paluszny et al., 2007, Sandve et al., 2012, Zhang et al., 2016].

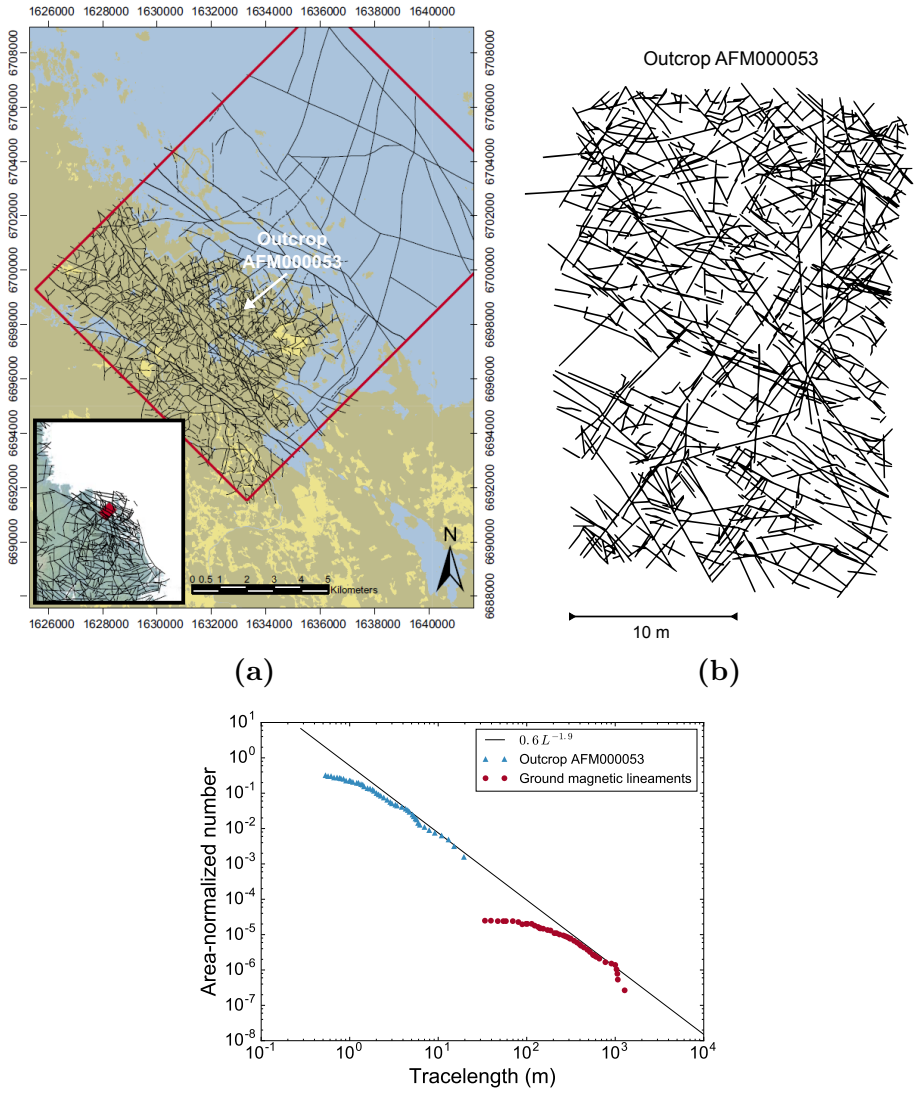


Figure 1.1: Scaling of fractures in a natural network: (a) A kilometre-scale lineament map of the area around the Swedish Forsmark site for geological disposal of nuclear waste [as in Munier, 2004]. (b) A metre-scale fracture tracemap of the outcrop AFM000053 [modified after Hermanson et al., 2003]. (c) Tracelength distributions from the kilometre-scale fault traces to centimetre-scale fractures in above maps [modified after Fox et al., 2007].

1.2.2 Fracture surfaces

Rock surfaces formed by the fracturing process can be approximated by a Gaussian height distribution and self-affine organization [Brown and Scholz, 1985a, Poon et al., 1992, Schmittbuhl et al., 1995]. A self-affine surface forms a fractal geometry with statistical invariance under a scale transformation of anisotropic aspect ratio: $\Delta \boldsymbol{x} \rightarrow \zeta \Delta \boldsymbol{x}$ and $\Delta h \rightarrow \zeta^H \Delta h$, where $\boldsymbol{x} = (x, y)$ is the fracture in-plane coordinate vector, h is the surface height, H is the Hurst exponent, and ζ is a constant quantifying the transformation magnitude. A nearly universal scaling exponent of $H \approx 0.8$ has been found to apply for surfaces of tensile fractures across a range of different rock types and grain size distributions [e.g. Poon et al., 1992]. The concept of statistical invariance can be illustrated by magnifying portions of a surface profile; see Figures 1.2a and 1.2b.

Surfaces of this kind can be interpreted as a series of superimposed sine curves of decreasing wavelength and amplitude, or power (Figure 1.2c). By means of Fourier Transform based analysis, roughness features can be identified by their wavelength, λ, or spatial frequency/wavenumber, $q = 2\pi/\lambda$, and associated with a measure of their roughness power, C. The slope of the resulting roughness power spectrum $C(q)$ on a log-log plot (Figure 1.2d) is equal to the Hurst exponent H. The root-mean-square roughness of the surface controls the amplitude of the power spectrum, $h_{\mathrm{rms}} = \langle h^2 \rangle^{1/2} = \left(2\pi \int qC(q)\mathrm{d}q\right)^{1/2}$; its length-scaling is less clear [Fardin et al., 2004, 2001, Schmittbuhl et al., 1995, Tatone and Grasselli, 2013], mostly due to the unavailability of large, undamaged tensile fracture surfaces. Surfaces formed by fracture propagation are in general expected to be fractal-like across all length scales [e.g. Persson et al., 2005]. In fact, no evidence of a roll-off wavelength has been found for measurements over multiple length scales [Candela et al., 2012, Power et al., 1987].

The existence of roughness across all relevant length-scales in rock fracture modelling and contradicts an obvious characteristic or homogenization length scale. To elaborate, is not clear *a priori* if the pore structure formed between two such surfaces forms an REV, and above which scale this would apply. This is even

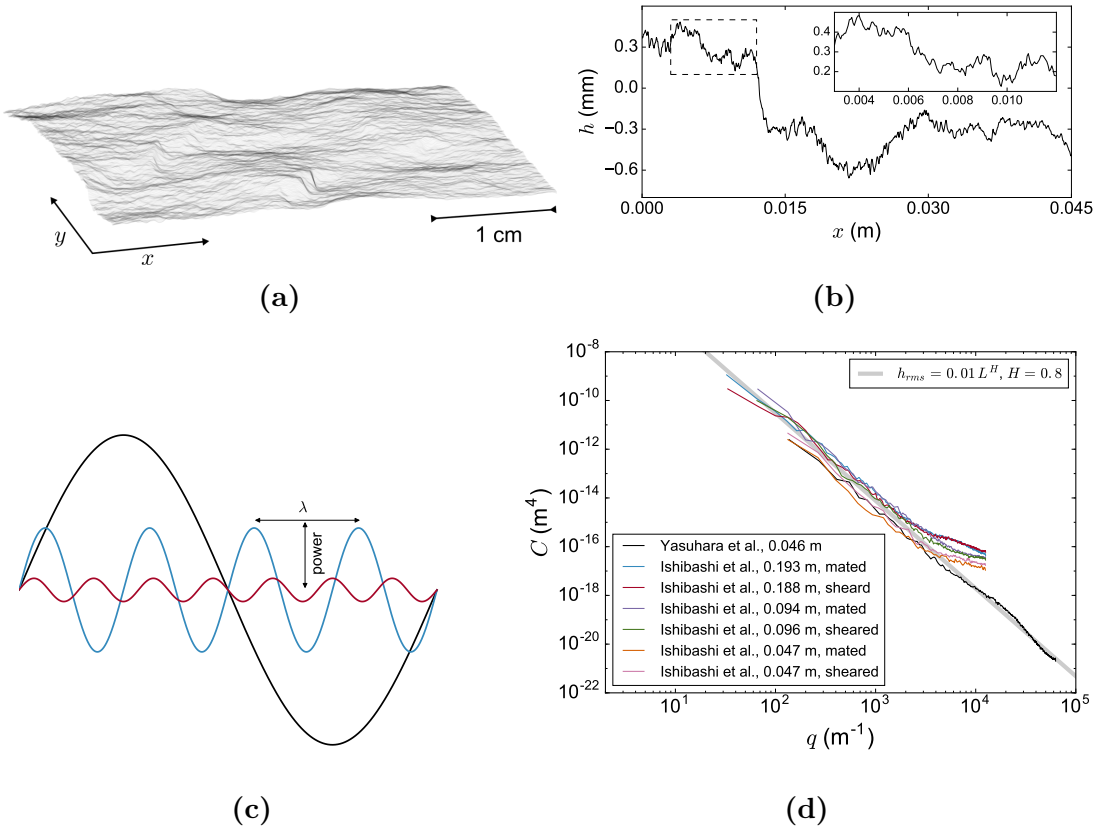


Figure 1.2: Roughness of fracture surfaces: (a) Laser scan visualisation of a sandstone surface and (b) a single trace of this surface [raw data from Hideaki Yasuhara], with a zoomed inset illustrating the self-affine fractal nature of rock surfaces. (c) A conceptual model of a self-affine surface as a superposition of sine-curves of decreasing wavelength, λ, and amplitude. (d) Radially averaged surface roughness power spectra for sandstone and granite surfaces [with additional raw data from Takuya Ishibashi].

less clear considering the infinite number of shear displacements that can occur between two surfaces. The power law scaling of the h_{rms} roughness of rock surfaces follows roughly the relationship $0.01L^{0.8}$ (Figure 1.2d), up to the kilometre-scale of large-displacement faults [Candela et al., 2012]. A further peculiar characteristic of fractal surfaces is that the surface area, in an Euclidean sense, increases as smaller and smaller roughness wavelengths are included. It follows that without a lower cut-off, fractal surface has an infinite area. This is a particularly challenging aspect when the extent of chemical reactions over such surfaces is to be quantified. As a consequence, the concept of a geometrically determined area is usually replaced by an effective area specific to the kind of process involved and the scale of investigation [e.g. Farin and Avnir, 1987].

1.2.3 Surface contact

It has long been recognised that the contact between rough surfaces is never complete, but rather occurs over a small fraction of the nominal area [e.g. Archard, 1957]. The discrete contact of two nominally flat bodies under confining pressure takes place over a two-dimensional plane, when viewed at a sufficiently small scale [e.g. Greenwood and Williamson, 1966]; see also Figure 1.3a. For a range of different materials, the size distribution of discrete contacts (Figure 1.3b) has been shown to follow a power law [Dieterich and Kilgore, 1996]. These experiments have also confirmed the theoretically predicted [Greenwood and Williamson, 1966] linear increase in total contact area with increasing load up to 30 MPa. This linear relationship is sometimes referred to as the physical origin of Coulomb's law of friction [e.g. Persson, 2006], in which the friction force depends linearly on the normal load.

The qualitative relationships of power law-sized contacts and linear dependence of contact area on load have been reproduced numerically for small deformations and negligible adhesion [Borri-Brunetto et al., 2001, Hyun et al., 2004, Putignano et al., 2012, Yang et al., 2006, Yastrebov et al., 2015]. In contrast to these relative relationships, the absolute value of contact area in a continuum mechanics sense has no clearly defined value. Similarly to the area of fractal surfaces, contact area depends on a chosen scale of investigation; see Figure 1.3c. This scaling problem is best illustrated by considering numerical models, which use a discrete representation of self-affine surfaces. In these models, the smallest representable roughness wavelength, λ_ℓ, is limited by some minimum lattice size, ℓ, which represents the smallest possible area of discrete contact. Below this scale, the surface is either in contact or not, *i.e.*, the surface is considered flat without further structure. As this cut-off scale decreases, so does the obtained area of contact. In fact, the contact area approaches zero with decreasing lower cut-off wavelength [Borri-Brunetto et al., 2001], down to the atomic scale where true contact in a continuum mechanics sense does not occur, but is a matter of interpretation of repulsive forces and atomic separations [Yang et al., 2006].

This dependence of the area of contact on spatial resolution is not only evident in numerical investigations, but also when quantified experimentally. For example, in direct visual interpretations of contacts, image resolution dictates that below 3.5 μm^2 only contact or no-contact can be detected, and no further small-scale structure [Dieterich and Kilgore, 1996]. The penetration of Wood's metal injection into fractures [Pyrak-Nolte et al., 1987, Yasuhara et al., 2006], as another example, is limited by capillary effects and is expected to yield a resolution in the 0.5 µm range [Cook, 1992]. Manual, optical and digital post-processing of the cast, however, should be expected to significantly lower the overall resolution. The self-affine nature of the contact area is a direct consequence of the fractal nature of the surfaces in contact, which has been shown to apply down to the molecular scale [Luan and Robbins, 2005].

The absolute value of contact area, which follows from the scale of investigation, thus should be related to the process under consideration. A good example for this concept is the simulation of fluid flow in fractures. Under assumption of laminar flow and the cubic law [Witherspoon et al., 1980], the local transmissivity scales with the cube of the local separation between the opposing fracture surfaces. It follows that small apertures, for all intents and purposes, effectively render that part of the fracture impermeable. For accurate quantification of the fluid flow in the fracture, it suffices to treat all regions below a certain aperture as contacting, without further regards for their internal structure. This cut-off, which is related to the physical problem of fluid flow and a desired accuracy of modelling, determines the lower scale of investigation and, as a consequence, the absolute value for contact area. For this reason, the absolute value of contact ratio should not be a primary focus, and rarely is. Rather, the qualitative characteristics of contact ratio related functions are important, *e.g.*, how contact area increases with increasing load [Yastrebov et al., 2015].

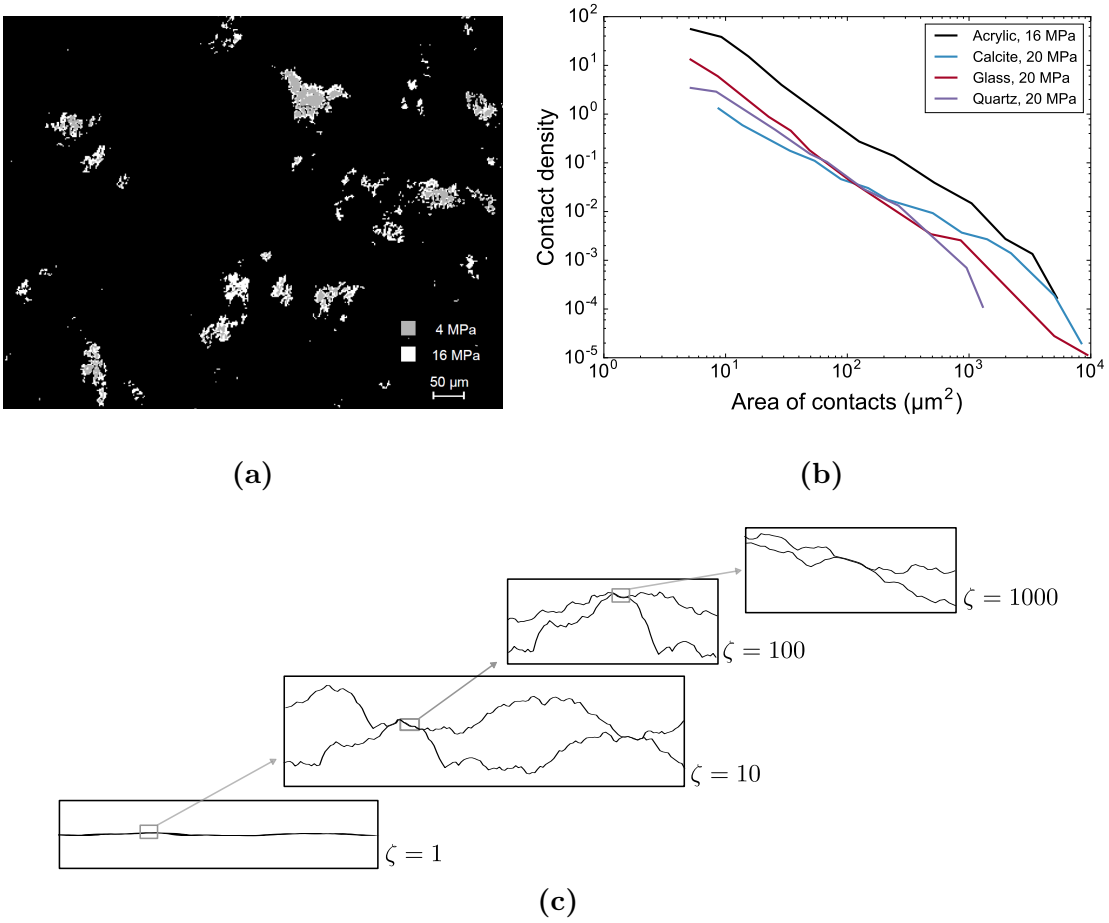


Figure 1.3: Contact between randomly rough surfaces: Contact patch image (a) between two #60 acrylic surfaces under 4 and 16 MPa confining pressure [Dieterich and Kilgore, 1996, with permission from Elsevier], (b) the contact patch size distribution for four #60 surfaces of different materials [modified after Dieterich and Kilgore, 1996], and (c) a conceptualisation of scale dependent contact area, where ζ is a factor of magnification [modified after Persson et al., 2005].

1.3 Experiments

Experiments on THMC induced changes in fracture transmissivity have been conducted in the field, on partially excavated blocks of rock that contain natural fractures [Voegele et al., 1981, Zimmerman, 1984], and in the laboratory, on fractured core samples [Beeler and Hickman, 2004, Blaisonneau et al., 2016, Caulk et al., 2016, Deng et al., 2013, 2015, Detwiler, 2008, Elkhoury et al., 2013, Faoro et al., 2015, Farough et al., 2016, McGuire et al., 2013, Moore et al., 1994, Morrow et al., 2001, Polak et al., 2003, Yasuhara et al., 2011, 2015, 2006]. Apart from the

restrictions on rock type and permeant, only experiments on freshly induced rock fractures are considered here. This is due to the uncertainties regarding the *in situ* history of natural fractures, which translate to a high degree of uncertainty in the initial conditions for subsequent flow experiments. As an example, recent experiments by Blaisonneau et al. [2016] were conducted on a cored natural fracture in granite. This natural fracture showed a significant degree of calcite coating over the surface, and the authors noted that reactions involving this coating had the most pronounced effect on observed transmissivity changes.

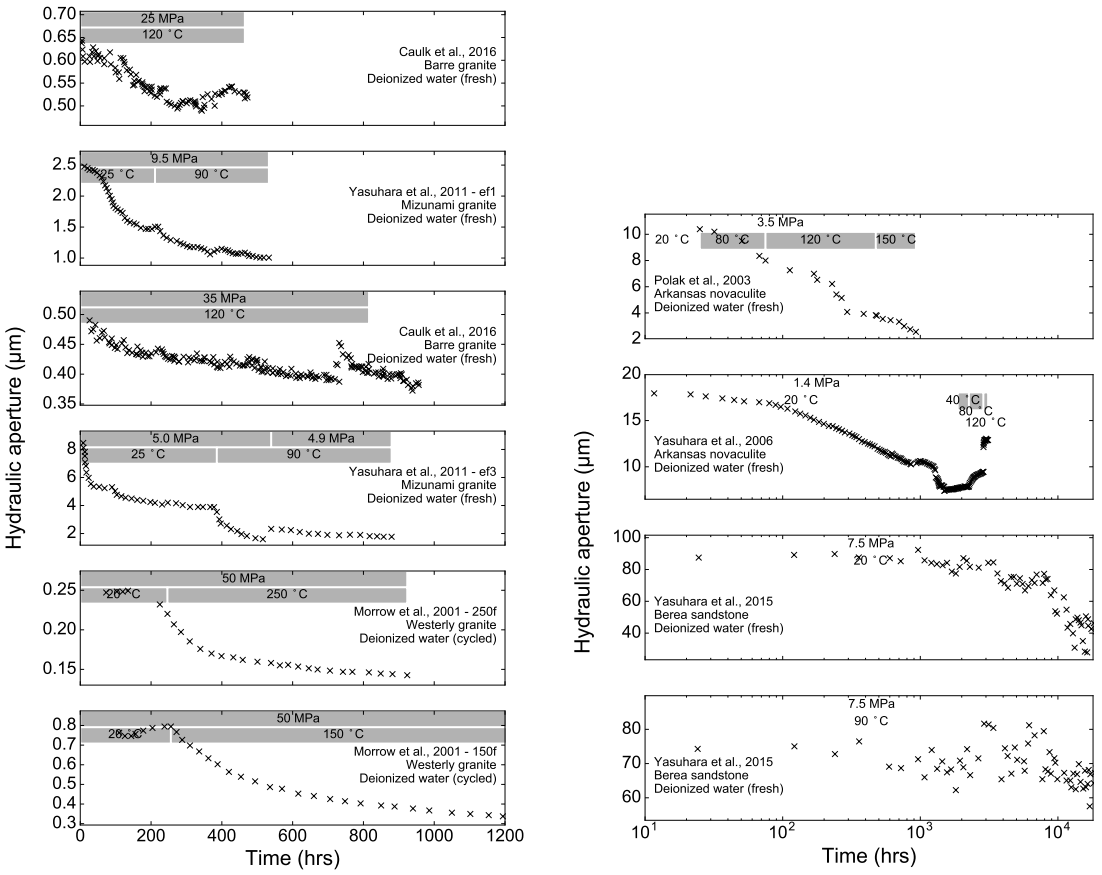
A common set-up for fractured core flood experiments [*e.g.* Polak et al., 2004] involves at least an injection pump, which usually operates at a constant rate, and a core-holder, which is held under a constant confining pressure. This holder contains a cylindrical rock sample of below 10 cm in length and diameter, which has been fractured and reassembled with minimum mismatch between the surfaces. The fracture is introduced either by a form of Brazilian test or by a wedge, which produces tensile fractures. In some experiments [Yasuhara et al., 2015], the fracture has been saw-cut, which leads to surfaces that are self-affine only below a certain wavelength, *i.e.*, surfaces with an upper wavelength roll-off. The core-holder is then placed inside a heating chamber. All experiments use deionized water as a permeant, with two options for the fluid-injection mechanism. The most common option is continuous injection of fresh permeant. The other option is to collect the effluent fluid and re-inject it [Moore et al., 1994, Morrow et al., 2001], which mimics continuous flow in a larger natural fracture system. These two ways of injection will herein be referred to as 'fresh' and 'cyclic', respectively. The effluent fluid is usually monitored for ion concentrations, and the equivalent hydraulic aperture of the fracture is computed by monitoring the build-up pressure at the core's inlet in response to the set injection rate. Depending on the experiment, injection rate, temperature and confining pressure are held constant or vary over time.

Many experiments on reactive flow in rock fractures report an increase in transmissivity over time [Deng et al., 2015, Detwiler, 2008, Elkhoury et al., 2013, Polak et al., 2004]. Common to these experiments are the relatively high reaction rates

between the fluid, which is often acidic, and the rock, which is usually some form of carbonate. The same type of experiments conducted on siliciclastic or granitic rock, however, dominantly show a steady decline of hydraulic aperture; see Figure 1.4. Specifically, in experiments with constant or increasing confining pressure and temperature (Figures 1.4a and 1.4b), only one experiment shows an eventual increase in aperture [Yasuhara et al., 2006]. The confining pressure in this experiment is the lowest of all, and the observed increase is not continuous, but rather step-wise, and coincides with an increase in temperature.

All experiments on induced tensile fractures show a typical dependence of initial aperture on the confining pressure. The initial aperture of the saw-cut samples is much higher [Yasuhara et al., 2015], which reflects that the two opposing surfaces created by the saw are not well correlated and thus don't create as tight a fit as in the case for tensile fractures. The evolution of aperture is not notably sensitive to changes in flow rate when it is not constant [Polak et al., 2003, Yasuhara et al., 2006], but is controlled, to first order, by temperature and pressure. Recent experiments on granite [Faoro et al., 2015] indicate that a part of the observed transmissivity loss is reversible, at least under low temperature and pressure conditions, and over relatively short periods of time; see Figure 1.5.

One of five rock types was used for all studies. (1) Arkansas novaculite with porosity below 1%, quartz content of above 99.5%, and very uniform grain size in the micron range [Polak et al., 2003, Yasuhara et al., 2006]. (2) Berea sandstone with dominantly quartz but significant fractions of feldspar, kaolinite and dolimite, and porosity of about 17% [Yasuhara et al., 2015]. (3) Westerly granite with porosity below 1% and plagioclase, feldspar, quartz and biotite as main components [Faoro et al., 2015, Morrow et al., 2001]. (4) Mizunami granite with a similar porosity and quartz, orthoclase, albite, anorthite and biotite as main components [Yasuhara et al., 2011]. (5) Barre granite, also of low porosity, and the main minerals quartz, oligoclase, biotite and muscovite [Caulk et al., 2016].



(a) **(b)**

Figure 1.4: Fractured core flood experiments with constant or increasing confining pressure and ambient temperature on (a) granite and (b) sandstone [Caulk et al., 2016, Morrow et al., 2001, Polak et al., 2003, Yasuhara et al., 2011, 2015, 2006].

1.4 Transmissivity altering processes in rock fractures

The process which causes an increase in hydraulic aperture [Deng et al., 2015, Detwiler, 2008, Elkhoury et al., 2013, Polak et al., 2004] is well understood: Non-contacting, free fractions of the fracture surfaces dissolve upon reaction with the fluid to form new flow channels and extended existing ones. This process is often referred to as free-face dissolution [e.g. Yasuhara et al., 2015], and has been modelled successfully for discretised models of mapped apertures [Deng et al., 2015, Detwiler, 2008, Elkhoury et al., 2013]. Whether the result of dissolution in the

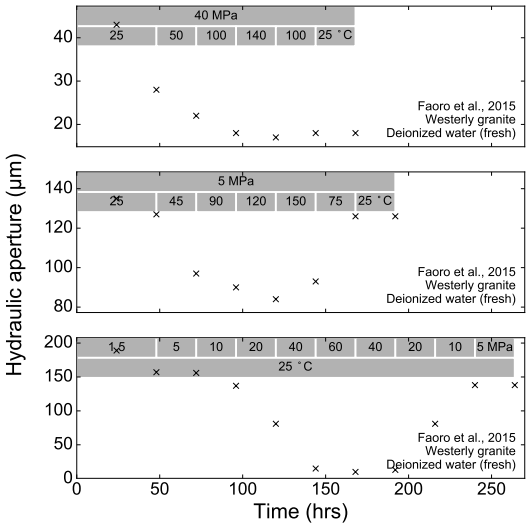


Figure 1.5: Partially reversible transmissivity loss observed in granite fractured core flood experiments with cyclic temperature or pressure [Faoro et al., 2015].

pore space produces such percolating channels has also been quantified by means of the dimensionless Damköhler and Péclet numbers [Elkhoury et al., 2013]. Both the numerical model of free-face dissolution and the model of dimensionless numbers fail to predict the observed aperture decline (Figure 1.4) for systems with low fluid-rock reaction rates. For example, the reaction rate constant for a limestone-carbonic acid system at 60 °C has been estimated to be $\approx 10^{-1}$ cm/s [Elkhoury et al., 2013]. At the same temperature, on the other hand, quartz-water dissolution occurs at $\approx 10^{-15}$ cm/s [Rimstidt and Barnes, 1980]. The fact that in both systems absolute aperture changes of similar magnitudes are observed, but of opposite sign, illustrates that the evolution of transmissiviy is controlled by very different mechanisms. The multitude of processes that occur in such systems demands an identification of which of these processes constitute first-order controls, to arrive at a tractable model. It follows that systems relevant to carbon sequestration and disposal of nuclear waste, for example, have to be treated separately when predicting changes due to THMC processes.

The mechanisms that control aperture decline are vast and much less understood. As opposed to transmissivity increasing processes, which act over the free fractions of the fracture that support fluid flow, compaction processes are assumed to act

at the discrete contacts. This means that the two phenomena act over different length scales. In a conducting fracture, flow channels percolate, and significant increase in transmissivity is achieved when channels are formed or extended over the entire length of investigation, *i.e.*, between inflow and outflow boundaries. Surface contacts in a conducting fracture, on the other hand, form isolated, small patches. Another significant difference is that compaction processes should be expected to be a function of the confining pressure to some extent. The definitions of Damköhler and Péclet numbers [e.g. Elkhoury et al., 2013], however, do not account for confining pressure. For models based on theses numbers, therefore, an experiment with constant displacement and one with constant stress boundary conditions cannot be distinguished. To derive a predictive model for the observed compaction during flow experiments (Figure 1.4), an account of possibly responsible processes is required, along with a classification based on their characteristic time-scale and compaction potential; see Figure 1.6. Then, possible first-order mechanisms can be identified and incorporated into a model.

Precipitation If the concentration of dissolved ions in the pore fluid is near equilibrium, mineral precipitation can take place to reduce the available pore space. For pure quartz-water systems, precipitation can occur rather uniformly [Lehner and Leroy, 2004], but for polymineralic rock, such as granite, precipitation has been observed to happen locally [Morrow et al., 2001, Yasuhara et al., 2011], in the form of growing crystals. Precipitation has been directly observed, by means of post-mortem microscopy, for multiple granite experiments [Morrow et al., 2001, Yasuhara et al., 2011]. For experiments on sandstone, however, effluent concentrations remained under-saturated throughout all experiments [Polak et al., 2003, Yasuhara et al., 2015, 2006], which probably excludes precipitation within the fracture.

Plastic damage The fact that contact between rough surfaces is only partial requires the pressure at discrete contacts to exceed the nominal pressure. The amplification factor depends, to first order, on the ratio of discrete contact to

nominal area. This ratio, as discussed above, depends itself on the scale of investigation. As this scale becomes smaller, so does the area of discrete contact, in a continuum mechanics sense [Borri-Brunetto et al., 1999]. It follows that at some scale, local contact pressure will exceed the material yield strength and deform plastically. From the self-affine scaling, it follows that there will always be plastic deformation below some roughness wavelength, albeit too small to be measurable and relevant to most problems. Plastic deformation leads to a convergence of the opposing surfaces, thus acting to reduce the fracture aperture.

Hydrodynamic particle release A permeability deterioration mechanism that is well-known from petroleum engineering, near-well bore observations, is the hydrodynamic release of fines. These smaller particles, often of clay-type nature, are released from the larger sand grains they're attached to by hydrodynamic forces [Ochi and Vernoux, 1998]. Downstream, they plug pore-throats and thus act as a permeability deteriorating mechanism. This process has been observed in sandstones having noticeable clay content. Characteristic to this process is a strong sensitivity to flow rate, and an increase thereof usually is accompanied by a sudden decline in permeability due to the release-plugging effect within short times [Ochi and Vernoux, 1998].

Viscoelastic creep It has been shown that time-dependent deformation in response only to continued confining pressure can lead to significant fracture closure [Matsuki et al., 2001]. The observed relative magnitude of creep-related compaction is comparable to that observed during typical THMC experiments. Closure due to this process, however, usually reaches a residual after about 20 hours for confining pressures of up to 20 MPa [Matsuki et al., 2001].

Stress corrosion A corrosive environment can lead to crack propagation even when the mechanical stress alone does not suffice to cause crack growth by itself. Such propagation is often referred to as sub-critical growth, and driven by the

combined effect of dissolution and tensile stress at the tip of micro-cracks [Atkinson, 1980, Dove, 1995, Yasuhara and Elsworth, 2008], where tensile stresses result at the perimeter of contact zone [Johnson, 1985]. This can eventually lead to fragmentation and collapse of contacts, and, as a consequence of confining pressure, to the convergence of opposing surfaces and ensuing compaction of the fracture.

Pressure solution Solubility increases with pressure in a similar manner as with temperature. The mechanical stress within contacts exceeds the hydraulic pressure acting on the free surface. A reaction-diffusion process results, in which mass dissolves between the contacts and is being transported to the free pore-space following a gradient in concentration [Lehner, 1995, Revil, 2001, Robin, 1978, Rutter, 1976, Spiers et al., 1990, Weyl, 1959]. The resulting dissolution of contacts, over time, leads to convergence of opposing surfaces and, thus acts to compact the fracture.

Undercutting Free-face dissolution at the perimeter of contacts acts, over time, as a form of local erosion. This can lead to a reduction in local contact area and eventual collapse, when the increasing contact stress exceeds the yield strength [Bernabé and Evans, 2007, Detwiler, 2008, Karcz et al., 2008]. The ensuing compaction results from the approach between the opposing surfaces.

Contact overgrowth Under diffusion-dominated transport conditions in the free pore-fluid, mass dissolves from free-surface fraction and precipitates at the the contact perimeter due to a capillary driven process [Beeler and Hickman, 2015]. The capillary force is a result of the small, high curvature pore system that is formed between the rough contacts. A loss in fracture transmissivity due to this process is not a result of convergence between the surfaces, but rather a plugging of flow junctions where the preferential precipitation may take place.

Thermal over-closure Several thermo-mechanical effects contribute to a phenomenon referred to as thermal over-closure [e.g. Barton, 2007]. It is assumed

that fracture surfaces fit best at the temperature under which they were formed, and subsequent temperature changes lead to a increasing misfit due to thermal expansion/contraction. For polymineralic rock in particular, differences in thermal expansion coefficients of the constituent minerals lead to inhomogeneous expansion/contraction during temperature changes, causing misfit between the surfaces and thus alter the void space, which in turn affects permeability.

It is difficult to attribute the observed closure directly to any subset of these processes. This difficulty is mostly due to the indirect nature of the available observations, such as hydraulic aperture and effluent concentration. A reduction in hydraulic aperture, for example, can be caused by precipitation without an actual approach of the two fracture surfaces in contact. Also, dissolved ions in the effluent concentration can have multiple sources. To date, no direct, high resolution visual observations of the pore-space during the experiments are available, as is the case in reactive-flow experiments in porous media [e.g. Menke et al., 2016]. Evidence that suggests precipitation is not the main driver for the observed transmissivity decline is given by the under-saturated effluent concentrations measured in the Polak et al. [2003] and Yasuhara et al. [2006] experiments. Moreover, post-experiment CT scans of a granite fracture [Caulk et al., 2016] show significant convergence of the two opposing surfaces; see Figure 1.7.

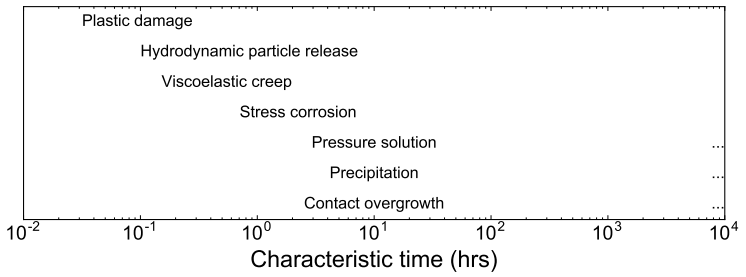
Physical approach between the fracture surfaces as the driving factor of transmissivity loss is further supported by excluding particle release and contact overgrowth as first-order mechanisms. Hydrodynamic particle release in the Arkansas Novaculite is unlikely, because this rock has been chosen specifically for its high purity and negligible clay content [Polak et al., 2003]. Also, the observed aperture decline was sustained over long periods, and appeared rather insensitive to changes in flow-rate. Contact overgrowth, another convergence neutral compaction process, relies on diffusion-dominated transport conditions. The commonly high injection rates, however, result in Péclet numbers indicative of clearly advection-dominated systems [Yasuhara and Elsworth, 2006].

Following the observation of a physical approach between the surfaces during the experiments, a significant contribution of plastic damage at surface contacts to the observed closure can be ruled out, because of the relatively high indentation hardness of the investigated rock types. A combined analysis of surface roughness spectra and analytic solution for the contact pressure distribution [Lang et al., 2015] showed that plastic deformation of the Yasuhara et al. [2006] experiment is below the μm-range, and thus is not responsible for the observed aperture decline. This finding has been corroborated by an independent approach [Li et al., 2015]. Moreover, the time scale for plastic deformation is instantaneous compared to the time it takes for a residual aperture to be reached for all experiments.

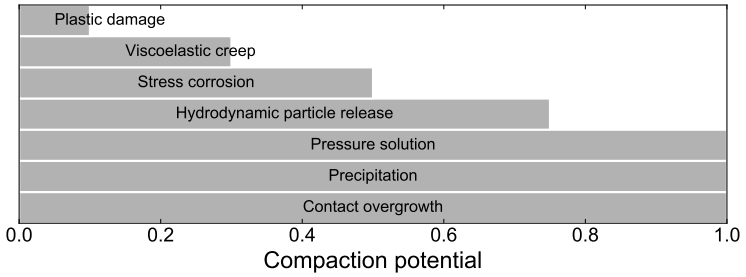
Viscous creep should be expected to be at least partially responsible for the observed compaction during the initial period of the experiments. However, in dry granite experiments, compaction due to viscous creep lasted for less than 20 hours [Matsuki et al., 2001]. Moreover, viscous creep does not explain dissolved minerals measured in the effluent over the entire duration of the experiments, or their temperature dependence. Two processes remain that, in theory, are capable of explaining the continued convergence of surfaces and the pressure dependence of the observed dissolved minerals in the permeant. These are the processes of pressure solution and stress corrosion. Thereof, pressure solution should be expected to act until complete compaction of the pore space, and has directly been observed on quartz grains [Lehner and Leroy, 2004, Spiers et al., 1990]. It has been chosen that accurate, first-principle modelling of pressure solution and ensuing precipitation will be the focus of this work's chemical component.

1.5 Anisotropy of fractured rock permeability

Anisotropy is intrinsic to fractured rock permeability for various reasons. The state of stress at any point in the Earth's crust is hardly ever isotropic, but has a significant deviatoric component [Zoback et al., 1989]. Fracture networks that form under these conditions cannot be expected to be isotropic, but to show highly



(a)



(b)

Figure 1.6: Tentative proposal of (a) characteristic time-scales and (b) relative compaction potential of transmissivity deteriorating processes in rock fractures, assuming constant conditions.

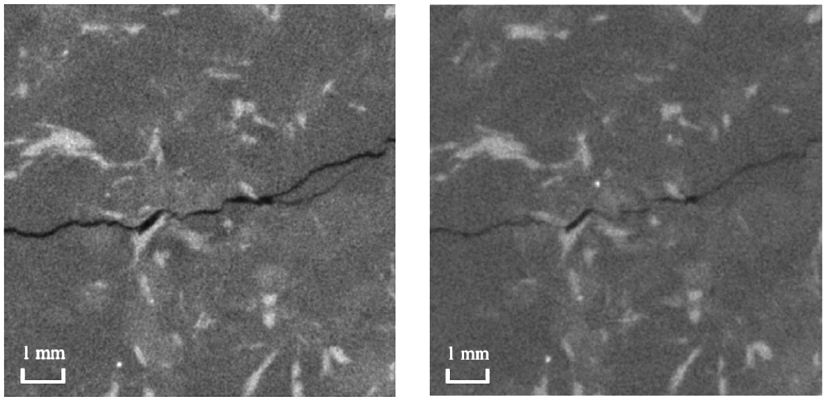


Figure 1.7: Pre- and post-experiment CT image of a fracture granite core cross-section, illustrating contact profile before (left) and after (right) the core flood [Caulk et al., 2016, with permission from Elsevier]. The reduction of hydraulic aperture of the fracture was $\sim$1 μm.

directional patterns [Pollard and Aydin, 1988]. Depending on their individual orientation, they will experience different magnitudes of compression and shear-displacement, both of which have a strong influence on fracture transmissivity. Moreover, fractures with significant shear displacement have locally anisotropic transmissivity. Specifically, they tend to be more permeable in the direction perpendicular to the shear direction than parallel to it [Auradou et al., 2005, Gentier and Hopkins, 1997, Matsuki et al., 2006, Nemoto et al., 2009, Yeo et al., 1998]. It is the aim of the developed approach to account for the anisotropic contribution of all these effects on the macroscopic permeability of a fractured rock mass.

1.6 Previous work

Investigation of geologically plausible, non-trivial fracture geometries with respect to rock permeability has its origin in analytic models. Initially limited to impermeable rock matrix, anisotropic permeability tensors were estimated from geometric fracture pattern analysis Snow [1969]. Accounting for a permeable rock matrix, analytic methods have been extended to compute permeability tensors in which the resulting eigenvectors can bet taken to be oriented coaxial to the block principal axes [Oda, 1985]. Effective media approximations models that represent individual fractures as conductors Zimmerman and Bodvarsson [1996a], have been extended to capture geometric parameters, size distributions and correlated permeability [Leung and Zimmerman, 2012]. Analytic methods usually have generic limitations: they either consider the matrix to be impermeable or uniform, and often assume hydraulic conductivity to obey some form of distribution or length dependence. More often than not, they are limited to two dimensions.

Mesh-based methods are able to capture property distributions, such as those derived from geomechanical fracture aperture models [Paluszny and Matthai, 2010], outcrop analysis [Bisdom et al., 2016, Hardebol et al., 2015, Lei and Wang, 2016], or statistical rock facies descriptions. Finite-element analysis of two-dimensional stochastic fracture models was first developed to evaluate inflow as a result of

applied hydraulic head [Long et al., 1982], for which the ensemble permeability is subsequently computed using Darcy's law. Numerous researchers have followed this approach, differing mostly in their treatment of the geometry of the fracture networks, aperture models, and consideration of geomechanical effects [e.g. Baghbanan and Jing, 2008, Davy et al., 2006, De Dreuzy et al., 2001, Figueiredo et al., 2015, Liu et al., 2016, Min et al., 2004a, Rutqvist et al., 2013, Zhang et al., 1996]. The limitations thereof lie in the two-dimensional nature of the analyses and the assumption of an impermeable rock matrix, which reduces the fracture network to a subset of hydraulically connected pathways. However, this approach cannot model the behaviour of permeable rock in which isolated fractures significantly affect permeability [Taylor et al., 1999], and also introduce a much unknown error for most fracture geometries through the reduction from three to two dimensions [Lang et al., 2014].

A complete three-dimensional numerical analysis of the steady-state fluid flow in fractured porous media overcame these limitations [Bogdanov et al., 2003], introducing the use of discrete fracture and matrix (DFM) models to the investigation of effective permeability of fractured rock. The methods allow for a computation of the full permeability tensor only if the underlying fracture network is periodic [Malinouskaya et al., 2014], which requires a dedicated generation process [Huseby et al., 1997]. For arbitrary networks, a diagonal tensor is assumed [Bogdanov et al., 2007, 2003, Hamzehpour et al., 2009, Mourzenko et al., 2005, 2011], or an orthorhombic fracture alignment is chosen [Sævik et al., 2013, 2014], in which the eigenvectors are aligned with the bounding box coordinate axes. Investigating geologically motivated fracture patterns and employing a control-volume finite-element discretisation of the governing equations, Matthäi and Belayneh [2004] computed the permeability along the axes of cuboid DFM models, aligned with the dominant fracture orientation; wherein the authors stressed the uncertainty in the directionality of the effective permeability given the assumption that the block axes are aligned with the directions of principal permeability.

Most studies that found a REV, or homogenisation scale above which fractured rock permeability reaches a constant, use fracture transmissivities that either obey

some form of distribution, are a sole function of fracture length, or are considered to be uniform [Bogdanov et al., 2003, Davy et al., 2006, De Dreuzy et al., 2001, Ebigbo et al., 2016, Min et al., 2004a, Mourzenko et al., 2011, Sævik et al., 2013, 2014]. Furthermore, fracture length is commonly limited to under $L/4$, where L is the domain length [Ebigbo et al., 2016, Mourzenko et al., 2011]. For geometries where an REV has been found to exist for log-normal aperture distributions, no REV-scale was found to exist when the aperture distribution changed to a power-law [Davy et al., 2006]. *De facto*, network permeability in all these approaches is a pure function of network geometry, since fracture transmissivity is either a constant, correlates with fracture length, or follows a direction independent distribution. Even when statistically realistic fracture geometries were constructed, models reverted to a uniform fracture permeability [Malinouskaya et al., 2014]. Justification for using a mean transmissivity for all fractures in a model is sometimes based on DFM studies where single fractures have locally varying transmissivity fields. [De Dreuzy et al., 2012, Hamzehpour et al., 2009]. Results show little [Hamzehpour et al., 2009] to a factor of six [De Dreuzy et al., 2012] difference in the obtained network permeability, and, to no surprise, no effect on the orientation of the principle permeabilities. These investigations, however, are missing a main point: heterogeneous fracture transmissivity in nature is not based on some random, isotropic distribution or correlation structure. Rather, it results from physical processes or states, such as shear deformation, orientation dependent compression, and non-uniform preferential chemical alterations. At their core, all these approaches have in common that fracture transmissivity, and as a consequence network permeability, are not a result of a physical process, but purely a function of the underlying network geometry.

This field observation defying abstraction has not been lost on the rock mechanics community, which, in parallel but almost independent, followed their own line of investigations into fractured rock permeability. One of the main characteristics of field observations are that fractured rock permeability shows a pronounced

anisotropy [*e.g.* Barton and Quadros, 2015], not only a result of network geometry but also of the state of stress. These observations lead to empirical relationships that relate fracture hydraulic apertures to the physical process of shear displacement, and the state of compression, *i.e* the acting normal stress [Barton et al., 1985]. Hydro-mechanical numerical models using such empirical relationships found that fractured rock masses cannot be treated as equivalent porous media [Lei et al., 2015a, Min et al., 2004b, Zhang and Sanderson, 2002, Zhang et al., 1996]. Modelling efforts of similar nature also found that no REV can be identified even when the geometry itself should permit the existence of such, once stress dependent mechanisms are incorporated [Baghbanan and Jing, 2008]. This is due to preferential mechanical activation of single fractures with a certain orientation to the far-field stress. These few fractures form high-conductivity pathways that can span the entire domain, rendering the definition of a REV meaningless. Further two-dimensional studies found that the direction of maximum permeability of a fractured rock mass is aligned with the orientation of the maximum principal stress [Baghbanan and Jing, 2008, Jing et al., 2013]. As stated by the authors, a major shortcoming of their two-dimensional representation lies the *de facto* isotropic transmissivity of individual fractures, and the inability to incorporate effects due to the intermediate principal stress. The incorporation of mechanical deformation into numerical simulations on the rock mechanics side had a two-dimensional representation as a main drawback [Baghbanan and Jing, 2008, Bisdom et al., 2016, Jing et al., 2013, Min et al., 2004b, Rutqvist et al., 2013, Ucar et al., 2015, Zhang and Sanderson, 2002, Zhang et al., 1996], compared to the three dimensional representation in pure fluid flow studies [Bogdanov et al., 2007, 2003, Ebigbo et al., 2016, Lang et al., 2014, Mourzenko et al., 2011, Sævik et al., 2014]. Recently developed approaches have been extended to three dimensions [Garipov and Tchelepi, 2016, Lei et al., 2015b], but ignore shear induced dilation [Garipov and Tchelepi, 2016], or implement constitutive models that account for shear induced dilation in an isotropic manner [Lei et al., 2015b].

On the single fracture scale, numerical modelling efforts have been made to relate the mechanical and hydraulic characteristics of stiffness and transmissivity,

respectively [Hopkins et al., 1990, Petrovitch et al., 2014, Pyrak-Nolte and Morris, 2000, Pyrak-Nolte and Nolte, 2016, Zimmerman et al., 1990]. As a common characteristic, numerical studies on hydro-mechanical coupling in rock fractures so far used isotropic aperture fields [Petrovitch et al., 2014, Pyrak-Nolte and Morris, 2000, Pyrak-Nolte and Nolte, 2016, Zimmerman et al., 1990]. The difference between simulation cases are correlation lengths and cut-off values, as well as the unstressed pore volume of the fracture [Pyrak-Nolte and Morris, 2000]. No direct relationship between the physical processes that have acted on a fracture and its used morphology have been incorporated. Anisotropy of fracture transmissivity due to shear [Auradou et al., 2005, Gentier and Hopkins, 1997, Matsuki et al., 2006, Nemoto et al., 2009, Yeo et al., 1998] and the resulting anisotropic pore space and its effect on deformation have received no attention in these studies; one exception is the mechanical work of Borri-Brunetto et al. [1999]. Similar to the reduction of fracture network scale flow to a purely geometric problem, single fracture geometries have been decoupled from the physical processes that form them, and have been reduced to a set of mathematical parameters that are used to generate their numerical representation.

Pressure solution in rock fractures has so far been modelled by means of macroscopic average formulations [Neretnieks, 2014, Taron and Elsworth, 2010, Yasuhara and Elsworth, 2004, Zhao et al., 2014]. These approaches have their origin in the modelling of granular aggregates [Lehner and Leroy, 2004], and the ensuing approximations translate to their application in fractures: (1) the use of an average, uniform value for contact stress; (2) the idealisation of fracture contact as a circular or square shape; (3) uniform dissolution over the contact zone; (4) evaluation of the hydraulic aperture as a mean of local apertures; and (5) the assumption of no elastic deformation of the pore space. The only direct simulation approach for pressure solution has been developed for two dimensions and axisymmetric asperities [Bernabé and Evans, 2007]. Since the absolute volume of the pore space in these models is assumed directly proportional to the hydraulic aperture, no non-trivial relationships between transmissivity and dissolution induced changes to the fracture morphology emerge.

The resulting objectives for the work to be developed herein follow from the above discussion. The properties of fractures and fractured rock should result from a set of physical processes under consideration, and an underlying geometry of the fracture network. These properties include fracture transmissivity and stiffness, and, as a consequence, the permeability of the fractured rock mass. This is accomplished by combining efforts of the hydrology and mechanics fraction of the fractured rock community, and by integrating efforts developed for different scales. Where needed, existing approaches are extended. A novel method is developed to accurately compute the full permeability tensor of an arbitrarily fractured rock mass, which accounts for locally anisotropic fracture transmissivity. A direct solution to the pressure dissolution problem [Bernabé and Evans, 2007] is extended to the elastic contact between randomly rough surfaces, which operates on a direct representation of the fracture morphology. An algorithm for the generation of opposing rock surfaces that incorporates fracturing induced damage [Matsuki et al., 2006] is coupled with an elastic contact solution for such surfaces. This facilitates the computation of contact between surfaces as they experience shear induced shifts [Borri-Brunetto et al., 1999]. This approach further allows transmissivity that results from offset and elastic contact, and dissolution induced changes to the fracture morphology to be computed. Bringing the hydro-mechanical approach from 2D to 3D allows, for the first time, the effects of large scale deformation on transmissivity anisotropy on single fractures, and, in turn, their effects on fluid flow on the large scale to be studied. The developed framework is independent of empirical relationships, and relies on first principles as much as possible. Free parameters are reduced to the friction coefficient, which represents the link between the scale where fractures are considered as planar discontinuities and the scale where they are represented as rough surfaces.

1.7 Outline

The Methods section starts with the characterisation and generation of rock surfaces, the computation of elastic contact between them, and the ensuing fluid

flow within the resulting pore space. It is at this single fracture scale, where surfaces are rough and dissolution-precipitation induced changes directly affect the fracture morphology. The section goes on to show how the single fracture scale approach is integrated into a method of contact at the fracture network scale. This mechanical part is then extended by a hydraulic section that covers the integration of anisotropic transmissivity at the fracture scale and resulting anisotropic permeability of the larger fracture network.

Similar to the Methods section, the Results section works its way up from the single fracture to the fracture network scale. First, basic hydro-mechanical results are presented. For a single fracture, transmissivity and stiffness are related to shear displacement between the surfaces. Then, consequences due to dissolution-precipitation induced changes to the fracture morphology are studied. The fracture network scale section proceeds in a similar manner. First, the hydro-mechanical behaviour in response to the far-field stress is illustrated. Then, compaction induced changes are investigated on the same fractured rock mass models.

This thesis concludes with a short section on fundamental aspects of fractured rock modelling. The major contributions developed herein are highlighted, along with assumptions made and their implications. A final summary of all findings with respect to permeability of fractured rock, and its evolution due to the studied chemical processes, concludes this work.

Chapter 2

Methods

At the single fracture scale, surfaces are rough, and the void space and partial contact between them is discretely represented. Based on shear displacement between the surfaces and the elastic compression to which they are subjected, the fracture pore-space can be directly represented, and the ensuing transmissivity can be computed. Changes in this transmissivity over time, due to diagenetic processes, are captured directly by capturing changes in the fracture morphology at this single fracture scale. For experimental comparison, the single fracture model is coupled with a reactive-transport module to facilitate simulation of fractured core-flood experiments. At the rock mass scale, fractures are represented as plane surfaces. The small-scale results are now represented as parameters in the governing equations. Through the solution of flow equations and a novel averaging method, the full permeability tensor of the rock mass can be computed. The shear displacement and normal pressure on each fracture result from a deformation-contact algorithm at the network scale, in response to triaxial far-field stress. Thus, an approach free of empirical relationships is devised to assess fractured rock permeability magnitude and direction, solely dependent on material properties, state of stress, and network geometry. Finally, given *in situ*-temperature conditions, changes in network permeability that would occur due to pressure-solution and precipitation can be assessed through updated fracture transmissivities.

2.1 Single fracture

Single fractures have historically been categorised as mated and unmated [e.g. Brown and Scholz, 1985b], or matched and mismatched [e.g. Bandis et al., 1983], among other terms along the same lines. Classifications of this nature arise from visual inspection of exhumed natural fractures at the laboratory scale, which can be misleading. The existence of roughness across all length scales suggests that the opposing surfaces of a fracture will always be correlated above some wavelength [Brown, 1987]; the only way for this not to happen is a relative offset larger than half the fracture length or significant rotation, both of which are physically unlikely scenarios. In other words, just because the exhumed part of a fracture, often in the cm- to m-scale, appears uncorrelated, does not mean that this will be the case for the *in situ* fracture as a whole. Rather, it should be expected that, above some scale proportional to the amount of shear displacement, fractures will always be correlated to some extent. This contributes to the fact that contact between parts of opposing surfaces is not representative of the contact between the surfaces as a whole [Wei and Hudson, 1988]. Rather than using terms related to the correlation between surfaces, a notion which is very much scale dependent, the two cases distinguished here will simply be fractures with negligible, or significant shear, displacement.

2.1.1 No shear displacement - isotropic aperture fields

A fracturing process produces two surfaces of isotropic, self-affine nature of near Gaussian height distribution [Brown and Scholz, 1985b, Poon et al., 1992, Schmittbuhl et al., 1995]. The roughness power spectrum $C(q)$ sufficiently characterises both the root-mean-squared roughness, and the height correlation of such surfaces as [Nayak, 1971]

$$C(q) = \frac{1}{(2\pi)^2} \int \langle h(\boldsymbol{x}) h(\boldsymbol{o}) \rangle \mathrm{e}^{-\mathrm{i}\boldsymbol{q}\cdot\boldsymbol{x}} \mathrm{d}^2 x \tag{2.1}$$

where $\boldsymbol{q}$ is the roughness wave vector, and $q = |\boldsymbol{q}|$ its magnitude, the wavenumber, or spatial frequency. For measured data of $h(\boldsymbol{x})$, which are shifted to obtain

$\langle h \rangle = 0$, Equation 2.1 can be evaluated using a *Discrete Fourier Transform* and radial averaging; a numerical algorithm based on a mathematical recipe in Persson et al. [2005], pp.76-79, has been implemented for this purpose.

Loosely speaking, the power spectrum relates wave-amplitudes to wavelengths. In terms of naturally induced surface roughness, it relates the elevation of roughness features to their length, when conceptualised as sinus-like structures (Figure 1.2c). An ideal spectrum $C(q)$ for surfaces of this kind is given by [e.g. Pastewka et al., 2013]

$$C(q) = C_0 \begin{cases} 1 & q_L < q < q_0 \\ (q/q_0)^{-2(H+1)} & q_0 \leq q \leq q_1 \\ 0 & q_1 < q \end{cases} \tag{2.2}$$

where $q_L = 2\pi/L$ is the smallest roughness frequency that can possibly occur in the surface, limited by the length L, and C_0 is a normalisation factor as described below. This wavenumber q_L corresponds to the largest possible roughness wavelength $\lambda_L = L/2\pi$ occurring in the surface. The largest possible roughness frequency, $q_\ell = 2\pi/2\ell = \pi/\ell$, or smallest roughness wavelength, is limited by the lattice size ℓ. Note that q_L, or λ_L, is a consequence of the physical size of the surface of interest, and q_ℓ, or λ_ℓ, is a consequence of discretisation. The discretisation limit may result from a numerical lattice or grid size, or may result from limitations in measurement resolution. For example, a surface of length L has a cell size of $\ell = L/\mathcal{L}$, where $\mathcal{L}$ is the number of equally sized square cells. Surfaces in nature have no notion of a discretisation-induced limit λ_ℓ, but are rough down to the molecular scale [Luan and Robbins, 2005, Yang et al., 2006]. A surface with roughness wavelengths bound by its size and discretisation limit is shown in Figure 2.1a, and the associated power spectrum in Figure 2.1b. Surfaces of this kind are good models of naturally induced tensile fracture surfaces [Persson, 2014], apart from that they have a lower limit q_ℓ, which is a necessary numerical artefact. In between the limits (q_L, q_ℓ), two more characteristic wavelengths may exist.

If the smallest roughness wavelength present on a surface is larger than the discretisation limit λ_ℓ, a so-called cut-off wavelength $\lambda_1 > \lambda_\ell$ exists, and a corresponding

cut-off wavenumber $q_1 < q_\ell$; see Figures 2.1c and 2.1d. As a consequence, surfaces with a cut-off lack smaller roughness features; compare Figures 2.1a where $q_1 = q_\ell$ and 2.1c where $q_1 < q_\ell$. In this case, only larger roughness features are represented, *i.e.*, the surface appears smoother for the lack of small-scale roughness. This is equivalent to a low-pass filter, roughness frequency-wise speaking. While real surfaces don't feature such a cut-off, it has been shown that ignoring theses small roughness features has negligible effects when numerically computing normal stiffness [Campañá et al., 2011] or fluid flow [Neuville et al., 2011, Vallet et al., 2009, Zimmerman and Bodvarsson, 1996b]. In other words, many phenomena in fractures depend only on the largest roughness wavelengths of the contacting surfaces, a very much intuitive finding. Introducing a cut-off wavelength is (1) unavoidable when representing a surface discretely, because at the most the discretisation bound represents the artificial limit $q_1 = q_\ell$, and (2) a convenient means of obtaining first-order solutions with limited computational efforts.

If the largest roughness wavelength present on a surface is less than the physical limit λ_L, a so-called roll-off wavelength $\lambda_0 < \lambda_L$ exists, and a corresponding roll-off wavenumber $q_0 > q_L$. This is equivalent to a high-pass filter in terms of roughness spatial frequencies. An example of such a surface is shown in Figure 2.1e, and its spectrum in Figure 2.1f. Compared to Figure 2.1a, no roughness wavelength that spans the entire surface can be identified. Surfaces of this kind may represent manufactured, flat surfaces, which are only rough below certain length-scale. A classic example is sandpaper, where the roll-off is proportional to the grind number. For this work particularly, such surfaces are indicative of the aperture field that two correlated surfaces form, which will be discussed below. A surface with both a cut-off and a roll-off in roughness is illustrated in Figure 2.1g, and its spectrum is shown in Figure 2.1h.

A commonly used parameter to characterise surfaces is the root-mean-square roughness, h_{rms}, which controls the normalisation of the power spectrum [Persson et al., 2005]:

$$h_{\mathrm{rms}} = \langle h^2 \rangle^{1/2} = \left(2\pi \int C(q) \mathrm{d}q \right)^{1/2} \tag{2.3}$$

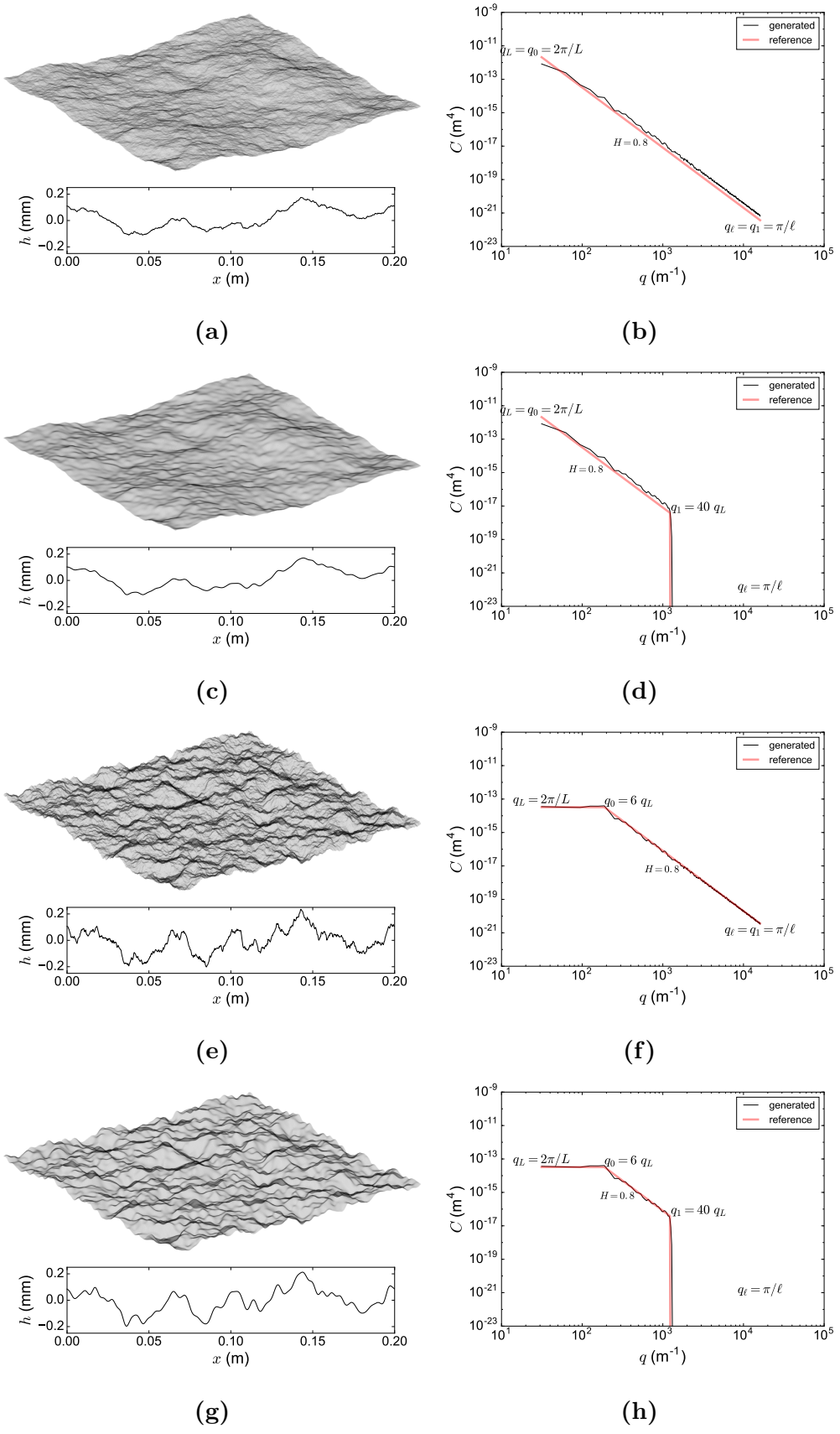


Figure 2.1: Illustration of cut-off q_1, roll-off q_0 and Hurst exponent H for isotropic rough surfaces, their traces and the corresponding PSDs. (a-b) A surface with fractal roughness across all wavenumbers. (c-d) A surface with a roughness cut-off. (e-f) A surface with a roll-off. (g-h) A surface with both roll-off and cut-off.

Given a roughness spectrum $C(q)$, self-affine surfaces can be generated numerically through a Fourier series [Persson et al., 2005]:

$$h(\boldsymbol{x}) = \sum B(\boldsymbol{q}) \mathrm{e}^{\mathrm{i}(\boldsymbol{q} \cdot \boldsymbol{x} + 2\pi\phi(\boldsymbol{q}))} \tag{2.4}$$

where $\phi(\boldsymbol{q})$ are independent uniform random variables. The factor $B(\boldsymbol{q})$ derives, for isotropic surfaces, from the frequency magnitude corresponding power. It follows that

$$B(\boldsymbol{q}) = \frac{2\pi}{L} C(\boldsymbol{q})^{1/2} \tag{2.5}$$

Since $h(\boldsymbol{x})$ is real, $B(-\boldsymbol{q}) = B(\boldsymbol{q})$ and $\phi(-\boldsymbol{q}) = \phi(\boldsymbol{q})$ [Peitgen et al., 1988]. And since the surface is isotropic, only the wavenumber matters, and $B(\boldsymbol{q}) = B(q)$, and $C(\boldsymbol{q}) = C(q)$, a function of only the magnitude $q = |\boldsymbol{q}|$ [e.g. Persson et al., 2005]. The numerical accuracy of the independent algorithms for surface characterisation and generation is illustrated in Figures 2.1f and 2.1h.

The Hurst exponent H reflects the surface height correlation length (Figures 2.2a and 2.2b), and corresponds to the slope of the power spectrum on a log-log plot; see Figure 2.2c. It is related to the fractal dimension D_f of the surface through $H = 3 - D_\mathrm{f}$. It follows that H controls what may intuitively be described as the jaggedness of a surface.

It has already been established that, for natural surfaces formed by fracture processes, no roughness roll-off exists [Brown and Scholz, 1986, Candela et al., 2012, Power et al., 1987], *i.e.*, $q_0 = q_L$ or $\lambda_0 = \lambda_L$. Further, $H \approx 0.8$ [Poon et al., 1992, Schmittbuhl et al., 1995] and $h_\mathrm{rms} \approx 0.01 L^{0.8}$ (Figure 1.2d) have been found to be good estimates. This value for the Hurst exponent has been explained by surface stability considerations [Persson, 2014], where lower values result in larger surface slopes that are likely to be unstable. With these constraints, an ideal power spectrum can be devised using Equations 2.2 and the normalisation factor [Pastewka et al., 2013]:

$$C_0 = \frac{Hs}{\pi q_0^2} h_\mathrm{rms}^2 \tag{2.6}$$

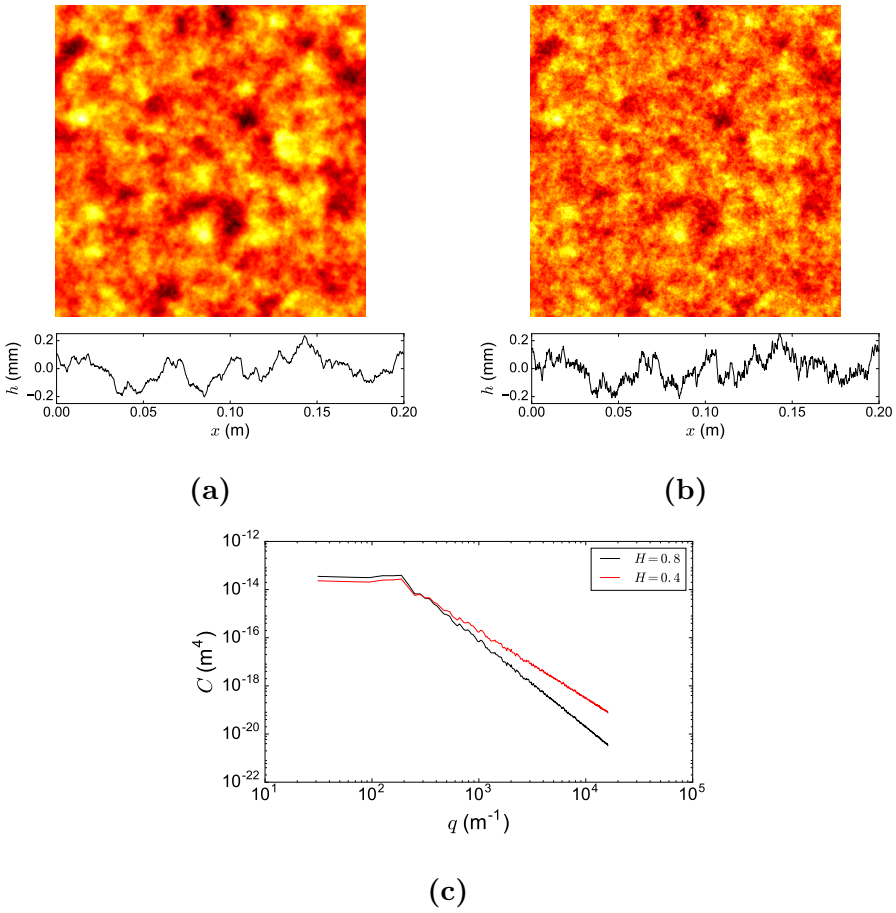


Figure 2.2: Planar representation of two surfaces with Hurst exponents of (a) $H = 0.8$ and (b) $H = 0.4$, with an identical roll-off $q_0 = 6q_L$ and $h_{\mathrm{rms}} = 9.0 \times 10^{-5}$ m. The slopes of the corresponding power spectra (c) illustrate this difference in height correlation quantitatively.

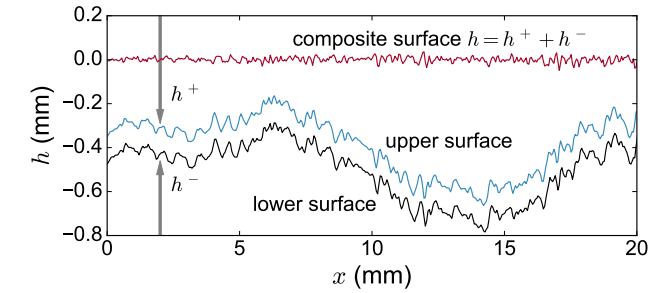
where $1/s = 1 + H(1 - (q_L/q_0)^2)$ in the limit of $q_1/q_0 \gg 1$. With the resulting spectrum, the numerical algorithm implementing Equation 2.4 can resolve the term in Equation 2.5. The power spectra of generated surfaces using this method should match the input reference spectra well in the limit of large cell numbers, as illustrated for surfaces of $\mathcal{L} = 1024$ in Figure 2.1.

Figure 2.1a illustrates rock surfaces generated here to represent the opposing sides of a fracture. When brought into contact, without lateral displacement, the two opposing surfaces should produce a perfect match and thus seal tightly. However, experiments in which tensile fractures are artificially induced, and the produced halves are reassembled to achieve maximum matedness, have always found significantly enhanced permeability [e.g. Gale, 1982, Moore et al., 1994, Morrow et al.,

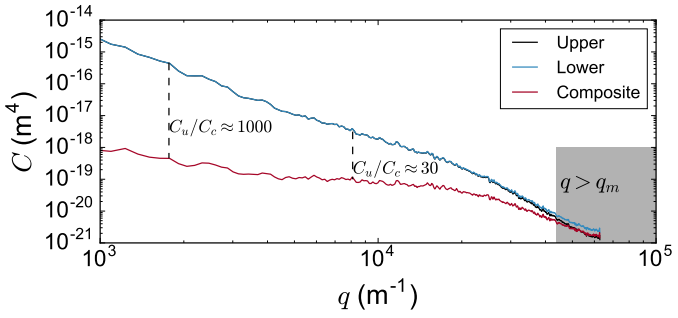
2001]. This results from a mismatch between the two surfaces at small roughness wavelengths [Brown et al., 1986], mainly due to surface damage that seems to always occur during a fracturing process. It follows that, while the opposing surfaces are correlated at the larger wavelengths, below some mismatch length-scale, λ_{m}, they are increasingly uncorrelated [Glover et al., 1998]. This mismatch, in turn, results in an aperture field which is responsible for the observed transmissivity of a tensile fracture.

The mismatch between surfaces of a tensile fracture can be illustrated using raw data from Yasuhara et al. [2006]; see Figure 2.3. After fracturing, these surfaces were cleaned, measured and reassembled to maximum matedness. The aperture field of the fracture under negligible pressure, *i.e.*, when the surfaces touch at a single point, can be obtained by addition of the two profiles with opposite reference directions; see Figure 2.3a. The thusly constructed surface is usually referred to as composite surface [Brown and Scholz, 1985b], and is related to the aperture field under negligible elastic deformation, *i.e.*, for rigid surfaces through $a = h_{\max} - h$, where $h_{\max}$ is the highest point of the composite surface and thus the point of singular contact. The main characteristic of a composite surface of tensile fractures is the lack of large wavelengths; see Figure 2.3b. This is a result of the strong correlation between the opposing surfaces. The aperture field shows a variable Hurst exponent: below a mismatch wavenumber q_{m}, its scaling exponent is $H = 0.8$ and the spectrum of the composite surface coincides with those of the original surfaces (Figure 2.3b). This reflects the fact that above this frequency, the two surfaces are uncorrelated [Glover et al., 1998, Matsuki et al., 2006]. Below this mismatch frequency, the surfaces are increasingly correlated, so that roughness at these wavelengths is not present in the aperture profile. In general, two random surfaces in contact, entirely uncorrelated, form a composite surface with identical Hurst exponent, *e.g.*, $H = 0.8$, and a lower h_{rms} [Hyun et al., 2004].

The lack of large roughness features in the aperture profile of fractures without shear displacement has led to speculations that above some length scale, hydraulic and transport properties should remain invariant [Matsuki et al., 2006]. In other words, looking at Figure 2.3a, there should exist a REV of aperture dependent



(a)



(b)

Figure 2.3: The concept of composite surfaces, or inverse rigid aperture fields, illustrated (a) for a trace of measured surface data of a Novaculite rock, and (b) using radially averaged power spectra. The mismatch roughness wavenumber, q_m, and the decreasing ratio between the spectra of the upper surface, C_u, and composite surface, C_c, illustrate the decreasing correlation between the upper and lower surface with decreasing roughness wavelength.

properties like stiffness and transmissivity. However, no conclusive studies have been conducted on this matter as of yet; this reflects perhaps that pure natural tensile fractures are not of high interest in subsurface flow, since they tend to be smaller in size and less permeable than shear fractures [for a discussion see, for example, Zoback, 2007]. Due to the isotropic nature of the mismatch, the aperture field is also isotropic. Matsuki et al. [2006] devised a numerical approach complimentary to the surface generation in Equation 2.4 to generate opposite surfaces which reflect the wavelength dependent correlation between two tensile surfaces:

$$h(\boldsymbol{x}) = \sum B(\boldsymbol{q}) \mathrm{e}^{\mathrm{i}(\boldsymbol{q}\cdot\boldsymbol{x} + 2\pi\phi(\boldsymbol{q}) + \gamma(\boldsymbol{q})2\pi\phi_\mathrm{m}(\boldsymbol{q}))} \tag{2.7}$$

where $\phi_\mathrm{m}(\boldsymbol{q})$ are uniform random variables independent of $\phi(\boldsymbol{q})$. The function

$\gamma(\boldsymbol{q})$ maps frequency magnitude to values between 0 and 1, and is 1 for $|\boldsymbol{q}| \geq q_{\mathrm{m}}$, and transitions to 0 for lower wavelengths in a manner such that the ratio of PSDs for opposing surfaces is honoured. The mismatch in the imaginary part, $\gamma(q)2\pi\phi_{\mathrm{m}}(\boldsymbol{q})$, represents a phase shift while maintaining the power (real part) of the signal. Again, the mismatch only depends on the roughness wavelength, and not its orientation, such that $\gamma(\boldsymbol{q}) = \gamma(q)$, a function of the magnitude $q = |\boldsymbol{q}|$. This requires a non-linear solution, and is here approximated as $\gamma(q) = \mathrm{erf}(2q/q_{\mathrm{m}})$. It vanishes for low frequencies, reflecting the strong correlation of the surfaces at larger roughness wavelengths. Aperture fields for tensile fractures can then be generated by constructing the lower surface, h^-, using Equation 2.4 and the upper surface, h^+, using Equation 2.7. The magnitude of q_{m} has been found to lie in the ranges of 0.529 to 7.52 mm [Brown, 1995], 0.25 to 0.83 mm [Glover et al., 1998], and 0.568 mm [Matsuki et al., 2006]. For the Novaculite fracture (Figure 2.3b), the mismatch length-scale is around 0.15 mm.

2.1.2 Shear displacement - anisotropic aperture fields

The mechanism responsible for mismatch between opposing surfaces in fractures without shear displacement is isotropic in nature. This is not the case in fractures with significant shear displacement, where a much larger mismatch results from relative displacement between the surfaces. The directional nature (Figure 2.4a) of this displacement results in an anisotropic void space (Figure 2.4b), where flow channels tend to show more pronounced percolation perpendicular ($\perp$) to the direction of relative displacement than parallel ($\parallel$) to it. The ensuing anisotropy of fracture transmissivity has been found to lie in between 1-1000 [Gentier and Hopkins, 1997, Matsuki et al., 2006, Nemoto et al., 2009, Yeo et al., 1998] for laboratory scale fractures. These experiments were set-up to preserve the original surface roughness, and to not allow for abrasion related damage during the shear displacement. The assumption of surfaces remaining undamaged during the shearing process is also made throughout this study. In natural rock, however, surface damage due to significant shearing may change both the pre-factor in the h_{rms}

length scaling, and the scaling exponent H, in an anisotropic manner [Candela et al., 2012].

A statistical description of the shear-induced composite surface is difficult [e.g. Matsuki et al., 2006]. Its anisotropic nature renders radially averaged power spectra ill-suited for characterisation. The established alternatives are linear power spectra of traces along the fracture surface, and subsequent averaging of all trace PSDs of the same direction. This procedure results in separate $C_{\perp}(q)$ and $C_{\parallel}(q)$ spectra. The difficulty in stochastic generation of the aperture field results from a discontinuous spectrum in the shear-parallel direction; see Figure 2.4c. In general, the composite surface shows a roll-off similar to those in fractures without shear displacement, which reflects that the opposing rock surfaces are correlated at wavelengths greater than the displacement magnitude.

An approximative method to generate composite surfaces similar to those seen in natural fractures was outlined by Brown [1995], using a single value for H and an anisotropy ratio between the x and y axis. Candela et al. [2009] devised a similar algorithm which directly incorporates H_x and H_y as input values, but is restricted to $q_0 = q_L$. Both approaches have been implemented here (Figures 2.4d and 2.7a), along with obtaining the composite surface directly from two mismatched surfaces and a given value for the shear displacement δ_{T}; see Figure 2.4a. This approach of generating two mismatched surfaces, displacing them with respect to each other, and bringing them into contact as a response to compression, marries methods presented by Matsuki et al. [2006] and Borri-Brunetto et al. [1999], and will be used herein to represent shear fractures and their contact.

2.1.3 Contact

The frictionless contact between elastic bodies with rough surfaces is known to depend only on the aperture field before loading [e.g. Greenwood and Williamson, 1966]. It follows that this contact problem can be reduced to the equivalent contact between a rigid realisation of the composite surface (Figure 2.3a), and an

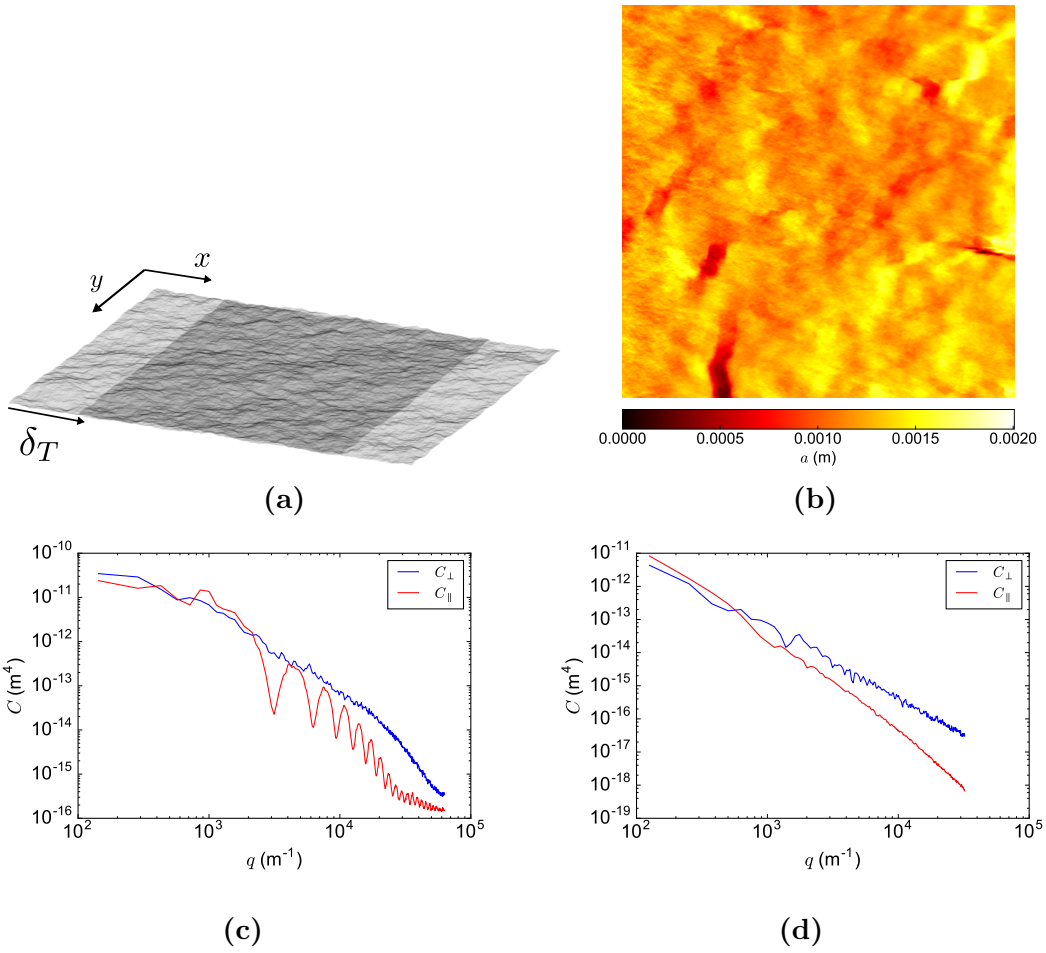


Figure 2.4: (a) Displacement δ_T between two correlated surfaces produces (b) an anisotropic aperture field where percolation of flow channels occurs preferably perpendicular to the direction of shear. The discontinuous axis-averaged power spectra of the resulting aperture field (c) are approximated by smooth spectra (d) for stochastic surface generation.

elastic, flat body; see Figure 2.5a. As discussed, the rigid composite surface (Figure 2.3a) has a surface height profile that reproduces the original aperture field upon contact with the planar surface. The deformable body, correspondingly, has an elastic composite modulus E^*, also referred to as reduced elastic modulus [Brown and Scholz, 1985b]. For a homogeneous system, $E^* = E/2(1-\nu^2)$, or half the plane-stress modulus, where E and ν are the rocks native Young's modulus and Poisson's ratio, respectively. The numerical solution to the non-linear contact problem implemented for this study is based on a Fast Fourier Transform of the stress-displacement integrals [Stanley and Kato, 1997]. Therein, the contact pressure is transformed to the frequency domain by a Fast Fourier Transform

(FFT) algorithm, multiplied by stiffness coefficients from the Westergaard [1939] solution for contact pressure due to a sinusoidal height profile, and the resulting displacement solution is brought back to the space domain by an inverse FFT. The inherent non-linearity of the elastic contact problem that arises from the mutual dependence of contact area, contact pressure and deformation is addressed within a conjugate gradient solver. This form of algorithm [e.g. Sainsot and Lubrecht, 2011] has been used in numerous studies to solve the frictionless contact between rough surfaces [e.g. Almqvist et al., 2007, Jackson and Green, 2011, Sainsot and Lubrecht, 2011, Yastrebov et al., 2015].

The underlying grid is of square shape with $\mathcal{L} \times \mathcal{L}$ rectangular cells of uniform size. In response to an external effective confining pressure, p, the obtained solution yields the contact stress, $\sigma(\boldsymbol{x})$, and the normal displacement, over the fracture plane, $\boldsymbol{x} = (x, y)$. A mechanical aperture field, $a_{\mathrm{m}}(\boldsymbol{x})$, is defined as the cell-wise separation between the rigid and the elastic surface, with zero-apertures at points of contact; see Figures 2.5b and 2.6. Regarding the implementation of the contact algorithm, it should be noted that the solution is retained in memory as an initial guess for subsequent computations on slightly altered surfaces when transient chemical processes are being incorporated. This helps to increase the efficiency of the transient computation, as discussed below.

The normal stiffness is a key parameter that relates relevant fracture properties to the magnitude of the normal stress. As such, it represents the stiffness contribution attributable to the closure of the void space between the rock walls, and the excess compression of contacting asperities therein with respect to the intact rock [Cook, 1992]. The fracture normal stiffness is the main factor that controls the P-wave transmission and reflection coefficients [Pyrak-Nolte et al., 1990], and is closely correlated to the hydraulic transmissivity [Pyrak-Nolte and Morris, 2000]. The numerical value of the normal stiffness will strongly depend on the morphological properties of the fracture, such as roughness and the correlation between the surfaces in contact, and the elastic moduli of the rock [Hopkins et al., 1990, Pyrak-Nolte and Morris, 2000, Zimmerman et al., 1990].

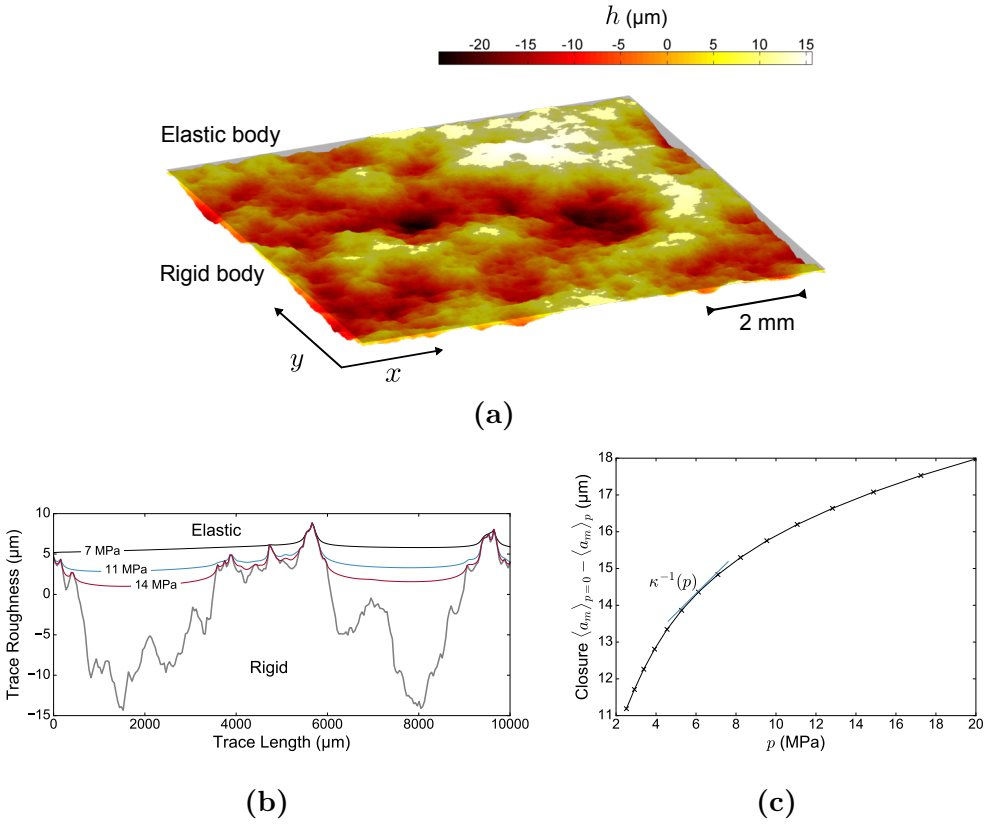


Figure 2.5: Contact of a rigid, rough composite surface with an elastic, planar body. (a) Three-dimensional model, (b) cross-section for three different values of confining pressure p, (c) closure curve with tangential normal stiffness κ.

The tangent normal stiffness of a fracture using the composite surface-frictionless contact approach implemented here can be evaluated for increasing compression as

$$\kappa\left(p\right) = \frac{\mathrm{d}p}{\mathrm{d}\langle a_{\mathrm{m}}\rangle} \tag{2.8}$$

where the brackets denote a spatial average. The incremental reduction in the average separation, $\mathrm{d}\langle a_{\mathrm{m}}\rangle$, is a direct measure of the additional deformation due to the presence of the fracture [Cook, 1992]. The difference between the average aperture of the unstressed fracture, $\langle a_{\mathrm{m}}\rangle_{p=0}$, and the average aperture under compression,$\langle a_{\mathrm{m}}\rangle_{p}$, increases with p and is commonly represented by means of closure curves and the total reduction in aperture, $\Delta\langle a_{\mathrm{m}}\rangle_{p}$; see Figure 2.5c. Numerically, Equation 2.8 is evaluated for discrete increments of p using a first-order finite difference approximation for the lowest and highest pressures and second-order finite difference approximation for all values of pressure in between.

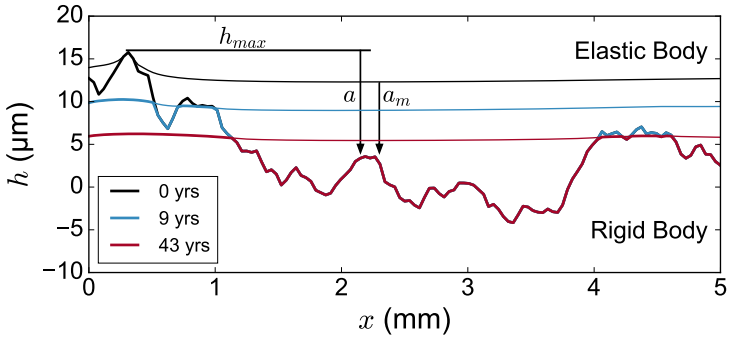


Figure 2.6: The rigid composite surface and elastic body for progressing time under pressure solution. The difference between rigid aperture a and mechanical aperture a_{m} is highlighted, where the latter accounts for elastic deformation and the former is independent thereof.

Finally it should be highlighted that numerical solutions for the elastic contact between rough surfaces produce power law contact size distributions (Figure 2.7c) similar to those of direct observations (Figure 1.3b). Furthermore, aperture distributions under elastic compression (Figure 2.7b) agree qualitatively well with those reported in experiments [Sharifzadeh et al., 2006].

Numerical-analytical comparison

The contact algorithm has been verified independently in several studies, and the verification of the implementation here is presented in Figure 2.8 using the Hertz solution for the contact between a sphere and a infinite plane. The dimensionless pressure is denoted as $p' = p/E^*$, where p is the pressure applied nominal $p = F/L^2$, and F is the acting normal force. The sphere is of radius r, and the model edge length is chosen to sufficiently cover the contact area as $L = 2.4r$, and a discretisation of $\mathcal{L} \times \mathcal{L} = 1024 \times 1024$. The Hertz solution to this contact problem is then given by [Jackson and Green, 2005] as $r_{\mathrm{c}} = (3FR/(4E^*))^{1/3}$, $\delta = r_{\mathrm{c}}^2/R$ and $\sigma_{\max} = 3F/(2\pi r_{\mathrm{c}}^2)$, where $R = r/2$ is the equivalent radius, r_{c} is the contact radius, δ is the rigid body approach and $\sigma_{\max}$ is the maximum contact stress at the center of the circular contact region. The solution variables can be normalised as $r'_{\mathrm{c}} = r_{\mathrm{c}}/r$, $\delta' = \delta/r$, and $\sigma'_{\max} = \sigma_{\max}/p$, and the numerical solution is within 1% accurate over the entire range of physically meaningful values of F;

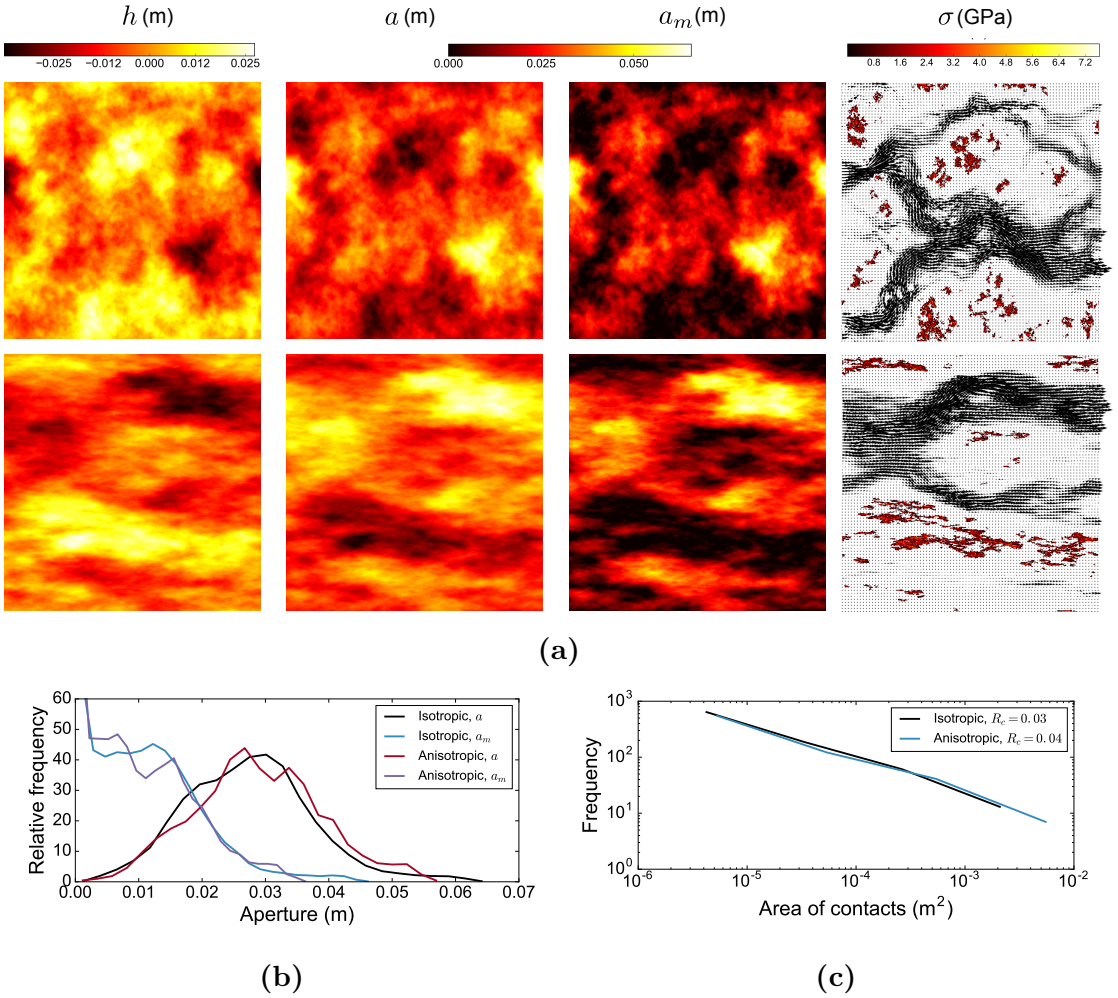


Figure 2.7: Surfaces, apertures and flow field for iso- and anisotropic fractures. (a) Top: Isotropic fracture. Bottom: Anisotropic fracture. From left to right: The composite surface, h, the rigid aperture field, a, the mechanical aperture field under elastic compression, a_{m}, and the contact stress, σ, and flow velocity field. (b) The aperture distribution of a and a_{m} for both cases, and (c) the power law distributed contact cluster size.

see Figure 2.8. A qualitative comparison of the three-dimensional contact stress as from Hertzian theory and the numerical solution is presented in Figure 2.9b for a similar verification problem.

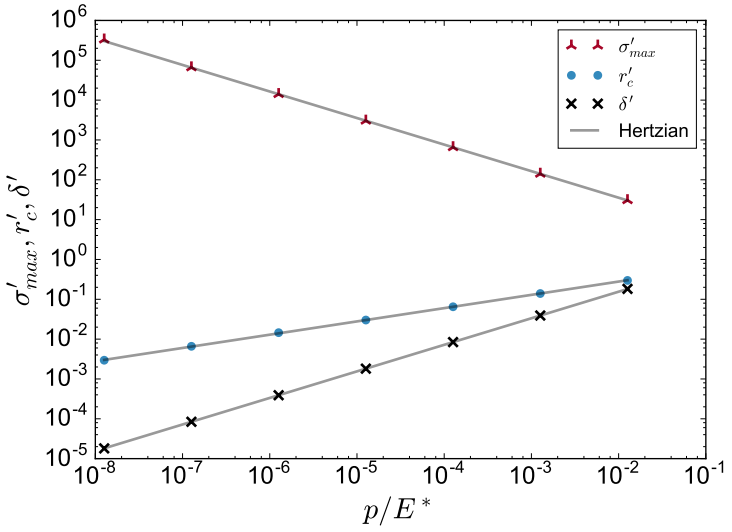


Figure 2.8: Comparison between analytical and numerical results for the frictionless elastic contact between a sphere and a flat plate.

2.1.4 Pressure solution

To model pore-scale pressure solution of three-dimensional fracture surfaces, two methods have been implemented: a numerical solution to the non-linear diffusion-reaction equation, and a closed-form approximation derived from spherical contact. Both algorithms are based on the previously introduced methods on surface generation and frictionless elastic contact between rough surfaces.

Bernabé and Evans (BE) numerical model

Based on theoretical derivations by Lehner and Leroy [2004], the instantaneous pressure dissolution mass flux, $J(\boldsymbol{x})$, in the contact zone is given as [Bernabé and Evans, 2007]

$$J(\boldsymbol{x}) = \rho_{\mathrm{s}} k_{\mathrm{d}} \left(\frac{\Omega_{\mathrm{s}}}{k_{\mathrm{B}} T} \sigma(\boldsymbol{x}) - \ln \left(\frac{c(\boldsymbol{x})}{c_{\mathrm{eq}}} \right) \right) \tag{2.9}$$

where ρ_{s} is the solid density, k_{d} is a temperature-dependent dissolution rate constant, Ω_{s} is the molecular volume, k_{B} is the Boltzmann constant, T is the temperature, σ is the local contact stress, c and c_{eq} are, respectively, the local intergranular concentration and the temperature-dependent equilibrium concentration in the

free pore space, expressed as mass fraction. Note that the dissolution rate constant k_d in its convergence rate form (m s^{-1}) is obtained by multiplying dissolution rate constants (mol m^{-2} s^{-1}) as reported in Rimstidt and Barnes [1980] by the molar volume (m^3 mol^{-1}) of quartz. Equation 2.9 reflects the combined dependency of pressure dissolution on the contact stress, σ, and super-concentration c/c_eq in the intergranular zone.

If diffusion is slow, transport of dissolved mass towards the free pore space is limited, and its accumulation in the contact zone results in high interfacial concentration, limiting the dissolution flux J. Omitting the logarithmic term in Equation 2.9 yields dissolution limited flux, a linear function of the contact stress. Under the assumption of a steady-state, thickness-averaged concentration distribution within the intergranular contact zone, J can be used as a source term to obtain the diffusion-reaction Poisson problem [Bernabé and Evans, 2014]

$$D(\boldsymbol{x})\nabla^2 c(\boldsymbol{x}) + \frac{\rho_\mathrm{s} k_\mathrm{d}}{\rho_\mathrm{f} w}\left(\frac{\Omega_\mathrm{s}}{k_\mathrm{B}T}\sigma'(\boldsymbol{x}) - \ln\left(\frac{c(\boldsymbol{x})}{c_\mathrm{eq}}\right)\right) = 0 \tag{2.10}$$

where w is the interface layer thickness of the grain-to-grain contact, and ρ_f is the fluid density. The physical bounds for values of $c(\boldsymbol{x})$ are as minimum and maximum, respectively, the temperature-dependent equilibrium concentration of the free fluid, c_eq, and the stress-enhanced equilibrium concentration in the grain-contact zone, $c_\mathrm{eq,s}$. The latter scales exponentially with the contact stress, and it follows that, after replacing the molecular volume by the molar volume, and the gas constant by the Boltzmann constant in Equation 26 of Neretnieks [2014],

$$c_\mathrm{eq,s}(\sigma) = c_\mathrm{eq}\exp\left(\frac{\sigma\Omega_\mathrm{s}}{k_\mathrm{B}T}\right) \tag{2.11}$$

The temperature-dependent diffusion constant, D, varies over the fracture surface field as follows:

$$D(\boldsymbol{x}) = \begin{cases} D & \text{free pore volume} \\ D^* = D \times f & \text{contact zones} \\ \frac{2}{1/D+1/D^*} & \text{contact-free interface} \end{cases} \tag{2.12}$$

where $0 < f < 1$ is a scaling constant that expresses the reduced diffusivity of the compressed contact zone with respect to the free pore space [He, 2003, Revil, 2001]. A harmonic average is used for the diffusion coefficient at the interface between the contact zone and the free fluid. Given the contact stress field $\sigma(\boldsymbol{x})$, which is considered constant over Δt, Equation 2.10 can be solved using a non-linear solution strategy to address the recursive dependence of c. The chosen initial guess for the concentration profile is $c(\boldsymbol{x}) = c_{\text{eq}}$. Since the effects of free-face precipitation/dissolution are not being accounted for, the solution of c is constrained to c_{eq} in the free pore space, i.e., for all $\sigma(\boldsymbol{x}) = 0$. To discretise Equation 2.10, a finite-volume scheme [Guyer et al., 2009] is employed on a cell-centred grid that is congruent with the mesh used to solve the elastic contact problem. This allows the local stress values to be used directly, without the need for interpolation. The boundary conditions are chosen as:

$$c_\Gamma = \begin{cases} c_{\text{eq}} & \text{Dirichlet-type, for free boundary faces} \\ \frac{\partial c}{\partial n} = 0 & \text{Neumann-type, for contact adjacent faces} \end{cases} \tag{2.13}$$

The Neumann-type boundary condition reflects the periodicity of the fracture surface model, assuming continued contact at the model boundary. A Picard iterative approach was found to be the more robust solution strategy, as the convergence of a Newton scheme required pressure/temperature-dependent fine-tuning in some cases. After the solution for $c(\boldsymbol{x})$ is found, and retained in memory as initial guess for subsequent solutions, the dissolution rate can be obtained by back-calculating the mass flux functional:

$$\frac{\mathrm{d}h}{\mathrm{d}t}(\boldsymbol{x}) = \frac{J(\boldsymbol{x})}{\rho_{\text{s}}} \tag{2.14}$$

The above procedure can then be repeated to form a time-stepping loop: (1) the solution of the elastic contact problem yields $\sigma(\boldsymbol{x})$ based on the surface $h(\boldsymbol{x}, t)$ and effective confining pressure p; (2) ensuing solution of the concentration distribution $c(\boldsymbol{x})$; (3) calculation of dissolution flux, change of surface geometry $h(\boldsymbol{x}, t + \Delta t) = h(\boldsymbol{x}, t) - \Delta t \ \mathrm{d}h(\boldsymbol{x})/\mathrm{d}t$, where Δt is the time increment of the explicitly coupled contact-dissolution algorithm; see Figure 2.10. Any rotation of the elastic body during dissolution can be ruled out due to the periodic nature of fracture surfaces generated by Equations 2.4 and 2.7. This periodicity follows from the Fourier transform on which the algorithm is based, and this transform works on periodic signals.

Lehner and Leroy (LL) closed-form model

Under the assumption of a constant equilibrium concentration at the hydrostatically stressed grain-to-grain contact perimeter, Bernabé and Evans [2007] simplified a constitutive relationship for the convergence rate between two spherical grains in contact developed by Lehner and Leroy [2004]. The total dissolution rate of asperity thickness, $\mathrm{d}h/\mathrm{d}t$, can be expressed as

$$\frac{\mathrm{d}h}{\mathrm{d}t} = \frac{2\frac{\Omega_\mathrm{s}}{k_\mathrm{B}T}\langle\sigma\rangle}{\frac{2}{k_\mathrm{d}} + \frac{\rho_\mathrm{s}}{\rho_\mathrm{f}}\frac{r_\mathrm{c}^2}{4c_\mathrm{eq}wD^*}} \tag{2.15}$$

where $\langle..\rangle$ denotes a spatial average, and r_c is the contact radius between the two spheres to account in a linearised manner for the diffusion distance. Equation 2.15 is extended to a more general form in this study:

$$\frac{\mathrm{d}h}{\mathrm{d}t}(\boldsymbol{x}) = \frac{2\frac{\Omega_\mathrm{s}}{k_\mathrm{B}T}\sigma'(\boldsymbol{x})}{\frac{2}{k_\mathrm{d}} + \frac{\rho_\mathrm{s}}{\rho_\mathrm{f}}\frac{r_\mathrm{d}(\boldsymbol{x})^2}{4c_\mathrm{eq}wD^*}} \tag{2.16}$$

where $r_\mathrm{d}(\boldsymbol{x})$ is the diffusion distance for each point at the interface, i.e., the distance to the nearest free pore space part of the fracture, and $\sigma(\boldsymbol{x})$ is the effective normal contact stress field; see Figure 2.10. The transient algorithm can be simplified given the linear dependence of dissolution on the contact stress and diffusion distance. Instead of a solution to the diffusion-reaction problem, the

computation of the field $r_{\mathrm{d}}(\boldsymbol{x})$ is required for each time step. The algorithm now follows as: (1) the solution of the elastic contact problem yields $\sigma(\boldsymbol{x})$ based on the surface $h(\boldsymbol{x}, t)$ and effective confining pressure p; (2) the diffusion distance field $r_{\mathrm{d}}(\boldsymbol{x})$ is computed; (3) the change of surface geometry is obtained as $h(\boldsymbol{x}, t + \Delta t) = h(\boldsymbol{x}, t) - \Delta t \ \mathrm{d}h(\boldsymbol{x})/\mathrm{d}t$; see Figure 2.10.

Time Stepping

The explicit coupling of dissolution and elastic contact gives rise to a critical value for the time increment Δt, above which the algorithm becomes unstable. The maximum value for the time increment is determined using sensitivity analysis. If the chosen increment is too large, oscillations in the rigid surface and contact stress profile ensue, leading to convergence failure of the diffusion-reaction problem [Lang et al., 2015]. Below this critical time step, stress profiles remain smooth and any further decrease in Δt has no effect on the transient solution, reflecting the convergence of the coupled contact-dissolution problem. Quantitatively, the critical value for Δt depends on the ratio of maximum dissolution rate and the slope of the surface around these maxima. In the present simulations it ranges from 10^6 to 10^7 s, for temperatures of 473 and 423 K, respectively.

Numerical-analytical comparison

Figure 2.9 illustrates cut-planes through a single spherical asperity of radius $r = 600$ μm undergoing pressure solution upon contact with the planar surface of the elastic, semi-infinite body proposed in Bernabé and Evans [2007]. An imposed normal force of $F = 0.56$ N results in a nominal normal stress $p = F/A_0 = 6.22$ MPa, where the nominal area, A_0, is chosen to sufficiently cover the contact region as $A_0 = (r/2)^2$ (m^2), and $\mathcal{L} = 256$. Upon initial contact, the analytic Hertz solution for the contact radius $r_{\mathrm{c}}(t = 0) = 17.37$ μm is recovered within one percent and yields a mean contact stress $\langle \sigma(0) \rangle$ of 590 MPa; see Figures 2.9a and 2.9b. The resulting dissolution process is studied over 6.5 years for temperatures between

373 and 473 K for $f = 0.001$ and compared to a semi-analytical approximation. To this end, the change in contact radius r_c for a discrete time interval, Δt, can be expressed by the rate of height change of the asperity, $\mathrm{d}h/\mathrm{d}t$, as expressed in Equation 2.15 of the LL model. For the case of a spherical grain, it follows that

$$r_c(t+\Delta t) = \sqrt{r_c(t)^2 - \Delta t \left(\frac{\mathrm{d}h}{\mathrm{d}t}\right)^2 + \Delta t \frac{\mathrm{d}h}{\mathrm{d}t}\sqrt{r^2 - r_c(t)^2}} \tag{2.17}$$

The concurrent change in average contact stress used for the evaluation of $\mathrm{d}h/\mathrm{d}t$ can be expressed as a function of the change in contact radius and its initial value:

$$\langle\sigma(t)\rangle = \langle\sigma(0)\rangle \frac{r_c(t)^2}{r_c(0)^2} \tag{2.18}$$

The coupled system of equations 2.15, 2.17, and 2.18 form an explicit form that can be solved numerically in a straightforward manner. Two key characteristics of the process of pressure solution are illustrated here. First, the equilibrating effect on the contact stress distribution (Figure 2.9b), by preferential solution that eventually yields flat contact surfaces; see Figure 2.9a. Second, the parabolic shape of the concentration field as a consequence of the steady-state flux assumption and circular contact area; see Figure 2.9c. The discrepancy between the semi-analytic LL model and the numerical BE model at higher temperatures (Figure 2.9d) is likely to be explained by the transition towards diffusion-dominated dissolution at high temperatures and large contact radii [Revil, 2001]. Under these conditions, an early deviation of the stress profile from parabolic Hertzian type to a more uniform distribution [Bernabé and Evans, 2007], and the ensuing non-linear decrease in the concentration of the inter-granular fluid film, takes place. These effects can only be accounted for to a limited extent by the closed-form LL model.

2.1.5 Precipitation

To model precipitation of dissolved mass, the assumed scenario is that pressure solution constitutes the rate-limiting process [Rutter, 1983, Weyl, 1959] and that the

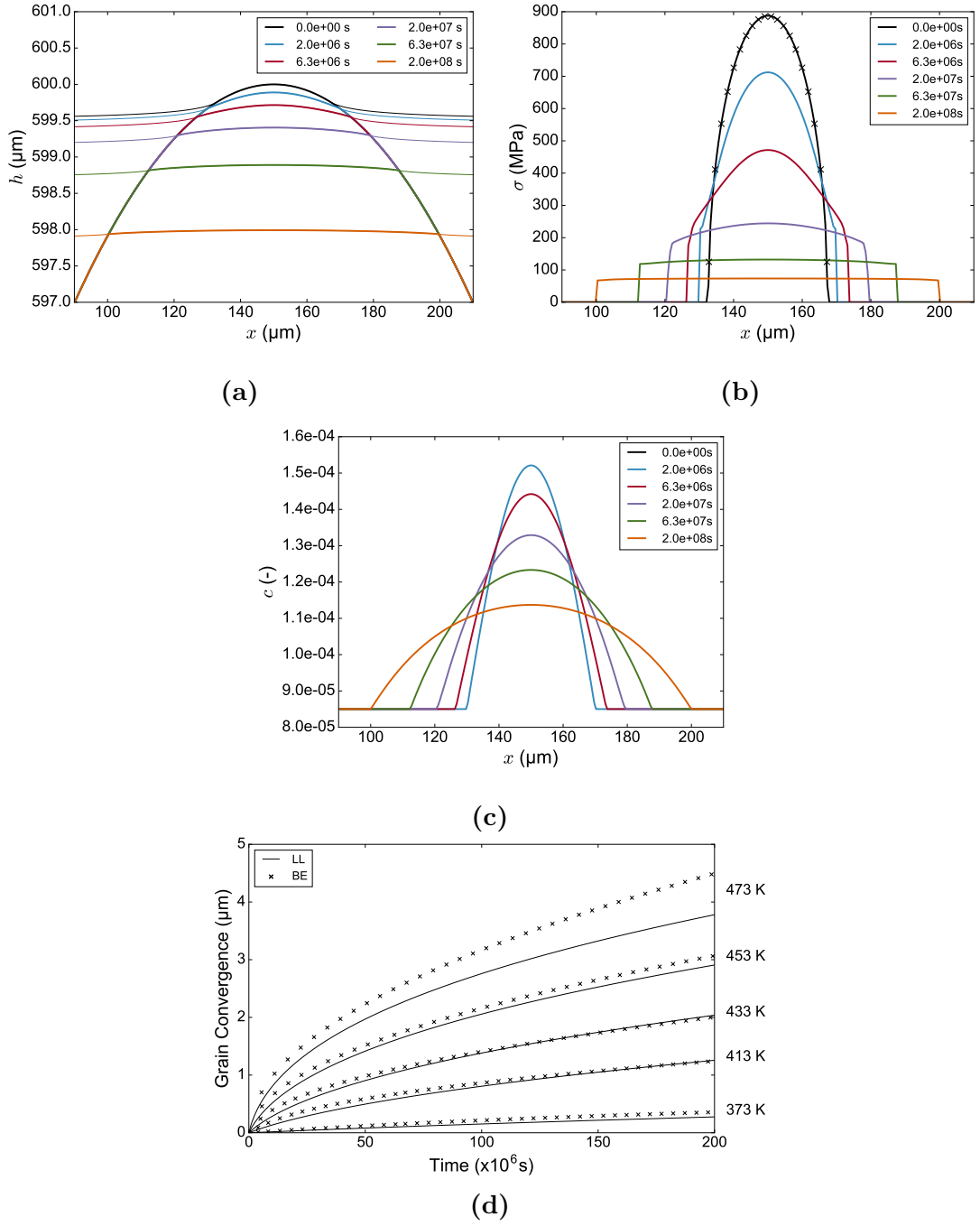


Figure 2.9: Pressure-solution of a single grain over time in three dimensions. Center-traces through (a) the rigid-elastic bodies, (b) the contact-stress field, and (c) the concentration field. (d) A comparison between the numerical model and a semi-analytical approximation.

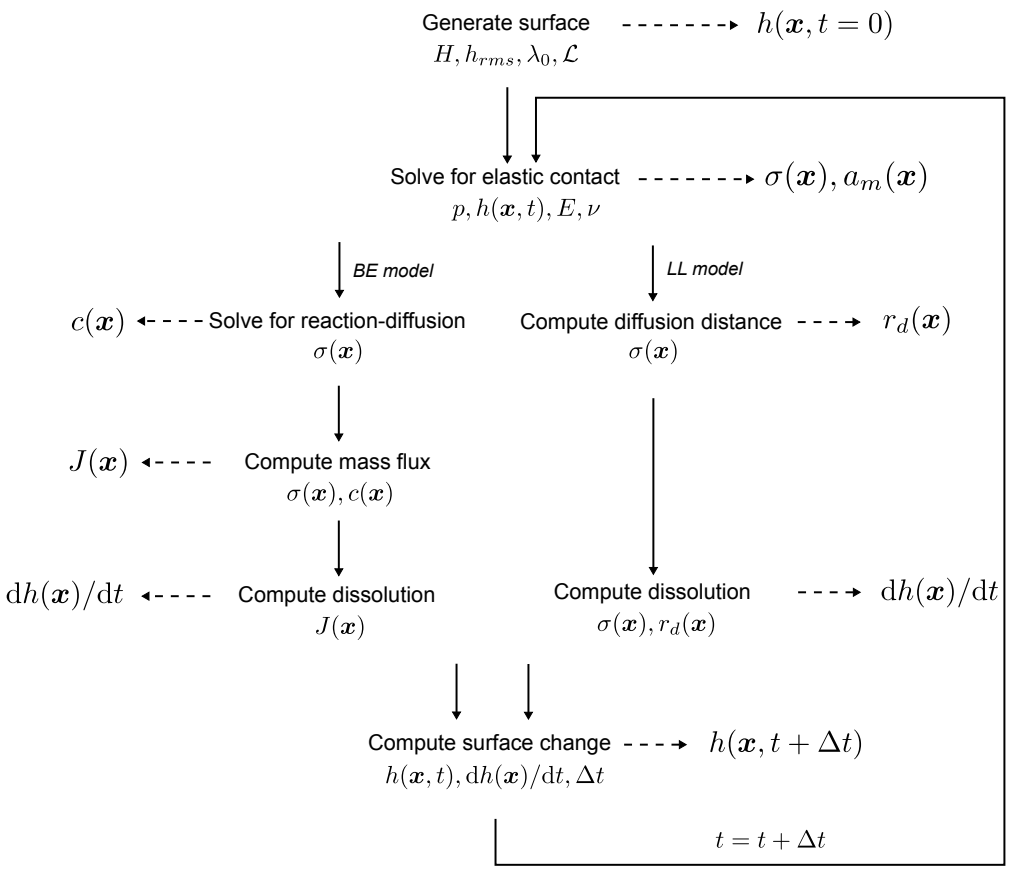


Figure 2.10: Flow chart of the THMC model.

pore fluid remains at its equilibrium concentration. The redistribution of dissolved silica follows a volume-conservative approximation to the diffusion-reaction problem, strictly proportional to the inverse of the distance from the surface contacts. Two end-members with respect to dissolution-precipitation have been studied. (1) 'Open' systems model pressure-solution only, and any dissolved mass is assumed to be subject to advective transport that prevents re-precipitation. (2) 'Closed' systems assume that any dissolved mass is locally conserved and precipitates near the fracture contacts in a solid volume conservative manner. For 'closed' systems, precipitation is evaluated concurrently with dissolution (Figure 2.10) to find $\mathrm{d}h/\mathrm{d}t$.

2.1.6 Flow

Similar to the stiffness of a fracture model (Equation 2.8), its hydraulic properties can be evaluated at any point in time during the transient process of chemical dissolution based on the current composite surface $h(\boldsymbol{x}, t)$; see also Figure 2.10. Given the two-dimensional mechanical aperture field $a_{\mathrm{m}}(\boldsymbol{x})$ as local separation between the rigid and the elastic surface (Figure 2.6), a depth-averaged fluid pressure field, $p_{\mathrm{f}}(\boldsymbol{x})$, is obtained by solving the Reynolds lubrication equation [e.g. Zimmerman et al., 1991]:

$$\nabla \cdot \left(\frac{a_{\mathrm{m}}^3(\boldsymbol{x})}{12\mu_{\mathrm{f}}} \nabla p_{\mathrm{f}} \right) = 0 \tag{2.19}$$

where μ_{f} is fluid viscosity. As the numerical value of μ_{f} is constant over the fracture, it has no influence on the steady-state solution of the pressure field and is set to unity. Any zero mechanical aperture of contacting elements is replaced by the interfacial diffusion thickness w for flow simulations. Two solutions are obtained to Equation 2.19, which re-purpose the aperture field congruent, cell-centred finite-volume discretisation used for the diffusion-reaction problem. For each of these solutions, indicated by I and II, boundary conditions impose macroscopic flow along the x- and y-axis, respectively. Specifically, fluid pressure is prescribed as a constant on opposing boundaries perpendicular to the main flow direction, and no-flow constraints are assigned to the flow-parallel boundaries.

The effective transmissivity of the fracture model is then obtained in conventional manner [*e.g.* Tsang, 1984]: (1) calculation of the flow rate vector field $\boldsymbol{u}(\boldsymbol{x})$ using Darcy's law as $\boldsymbol{u} = a_{\mathrm{m}}^2/(12\mu_{\mathrm{f}})\nabla p_{\mathrm{f}}$ (Figure 2.7); (2) integration of the flow rate component along the macroscopic flow direction over the inlet cells to find the total inflow Q, e.g., over the left edge for flow parallel to the x-axis (Figure 2.7); and (3) calculation of the fracture transmissivity, K, as

$$K = -\frac{Q\mu_{\mathrm{f}}}{W\overline{\overline{\nabla p_{\mathrm{f}}}}} \tag{2.20}$$

where W is the width of the fracture inlet, or edge length of the quadratic composite surface model, and $\overline{\overline{\nabla p_{\mathrm{f}}}}$ is the macroscopic fluid pressure gradient. For fractures

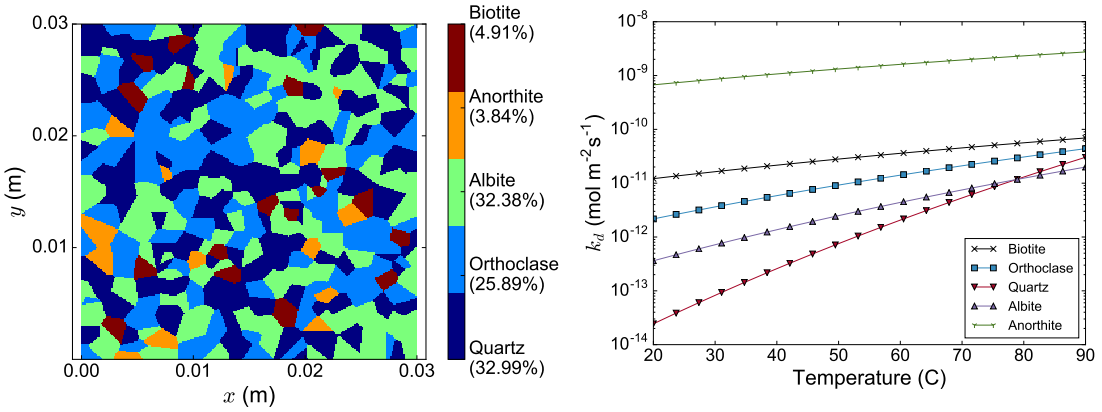
without shear displacement, K is a scalar property obtained as the harmonic average of K_{I} and K_{II}. For fractures with shear displacement, transmissivity is a diagonal tensor $\boldsymbol{K}$ with components $K_{\perp}$ and $K_{\parallel}$. The corresponding parallel-plate hydraulic aperture, a_{h} of the fracture in both directions are obtained through the relationship

$$K = \frac{a_{\mathrm{h}}^3}{12} \tag{2.21}$$

2.1.7 Coupled dissolution and reactive transport

To model fractured core flood experiments [Yasuhara et al., 2011, 2006] a two-scale approach couples the above approach for flow and contact between rough surfaces with a one-dimensional transport model. Elastic contact, transmissivity and transient chemical reactions are modelled over a hypothesised representative volume element (REV) of a discrete fracture surface. The discretised version of a surface covers about half the total fracture, and has an edge length equal to the inlet width W of the physical fracture studied in the lab experiments. The ensuing transport of dissolved mass along the axis of the core is solved for a true length, one-dimensional model. The physical processes accounted for in this coupled model, and the assumptions made in the derivation of the governing equations, are: mechanical contact is elastic and frictionless; pressure solution is reaction limited; free-face dissolution is uniform over the free surface, with the pore-fluid far below equilibrium concentration; and transport is advection dominated along the axis of the core.

The complete algorithm then proceeds as follows (Figure 2.12). Based on the initial composite surface and contact stress solution, the transmissivity of the fracture is computed to yield an equivalent hydraulic aperture from the resulting field of local separations between the surfaces, using a steady-state solution of the lubrication equation. Then, based on the contact stress field and the contacting/free surface partitioning, the dissolution rate field is calculated. The ensuing source terms for pressure and free-face solution are used to solve for the concentration distribution along the core axis, together with the experimentally imposed pressure gradient, or



(a) **(b)**

Figure 2.11: Mineral composition and dissolution rate models. (a) Discrete composition (DC) model granite. (b) Temperature dependence of dissolution rate constants k_{d}.

injection rate and the computed hydraulic aperture. Finally, dissolution-induced changes are applied to the surface, and the global time is incremented by an adaptive time increment.

For the experiment on granite [Yasuhara et al., 2011], two approaches have been implemented to model dissolution of the fracture. An averaged composition model (AC) [Yasuhara et al., 2011], which assumes contact zones to consist of all minerals according to their volume fraction observed in the bulk of the rock, and a discrete composition model (DC), which assigns to every cell a single mineral based on a stochastically generated Voronoi distribution of grains; see Figure 2.11a. The composition model of the Mizunami granite follows an alternative description [Quintessa, 2014].

Dissolution rates for each mineral are computed using an Arrhenius relationship and pre-exponential factors and activation energies as in Yasuhara et al. [2011], which are based on data suggested by the U.S. Geological Survey [Palandri and Kharaka, 2004]; see Figure 2.11b. Under the assumption of reaction-limited conditions [Revil, 2001], the pressure solution mass term in cell i, j for mineral min as a function of the local contact pressure $\sigma_{i,j}$ is expressed as

$$\frac{\mathrm{d}M_{\mathrm{ps},min,i,j}}{\mathrm{d}t} = \eta_{\mathrm{ps}}\chi_{min}\frac{3\psi_{\mathrm{d},min}\ell^2\sigma_{i,j}\rho_{\mathrm{s},min}V_{\mathrm{m},min}^2}{RT} \tag{2.22}$$

where $\psi_{\mathrm{d},min}$ is the solution rate from an Arrhenius type function of the ambient temperature, a is the cell length, $\rho_{\mathrm{s},min}$ and $V_{\mathrm{m},min}$ are, respectively, the mineral's density and molar volume. The factor η_{ps} is the pressure solution calibration factor, and χ_{min} depends on the composition model. For the AC case it represents the volume fraction of mineral min, and for the DC case it is 1 if cell i, j is assigned to mineral min, and 0 otherwise.

The advective transport of dissolved ions is modelled for Si, Ca, Mg, Al, K, Fe, and Na. The fracture-volume normalised mass source due to pressure solution for each ion is calculated by evaluating the pressure solution term of all minerals (Equation 2.22) and accumulating the stoichiometric contribution of each mineral to the ion. It follows that

$$\mathcal{S}_{\mathrm{ps},el,min} = \frac{1}{W^2 \langle a_{\mathrm{m}} \rangle} \frac{v_{min,el} m_{el}}{\rho_{\mathrm{s},min} V_{\mathrm{m},min}} \sum \frac{\mathrm{d}M_{\mathrm{ps},min,i,j}}{\mathrm{d}t} \tag{2.23}$$

where $v_{min,el}$ is the stoichiometric coefficient of element el in mineral min, m_{el} is the element mass, W is the edge length of the composite surface, and $\langle a_{\mathrm{m}} \rangle$ is the average mechanical aperture of the elastic contact model, so that the product $W^2 \langle a_{\mathrm{m}} \rangle$ is the pore-volume of the REV model under compression. The summation of dissolved mineral mass is performed over all cells of the elastic contact model. The cumulative source to element el from all minerals is finally obtained as the sum over all minerals:

$$\mathcal{S}_{\mathrm{ps},el} = \sum \mathcal{S}_{\mathrm{ps},el,min} \tag{2.24}$$

The free-face dissolution source term is expressed in a similar manner as

$$\frac{\mathrm{d}M_{\mathrm{ff},min,i,j}}{\mathrm{d}t} = 2\eta_{\mathrm{ff}} \chi_{min} \psi_{\mathrm{d},min} \ell^2 \rho_{\mathrm{s},min} V_{\mathrm{m},min} \tag{2.25}$$

assuming the pore-fluid concentration far from equilibrium. The factor 2 accounts for the dissolution process occurring on both sides of the fracture surface, and η_{ff} is the free-face dissolution calibration factor. The corresponding normalised source

term is obtained in a similar manner as

$$\mathcal{S}_{\mathrm{ff},el,min} = \frac{1}{W^2 \langle a_\mathrm{m} \rangle} \frac{v_{min,el} m_{el}}{\rho_{\mathrm{s},min} V_{\mathrm{m},min}} \sum \frac{\mathrm{d}M_{\mathrm{ff},i,j}}{\mathrm{d}t} \tag{2.26}$$

and the combined source from all dissolving minerals as

$$\mathcal{S}_{\mathrm{ff},el} = \sum \mathcal{S}_{\mathrm{ff},el,min} \tag{2.27}$$

After accumulating all free-face and pressure solution sources, a separate advective transport equation per ion is solved in one dimension. Assuming incompressible flow, which implies a divergence free velocity field $\nabla \cdot \boldsymbol{u} = 0$, the concentration c_{el}, here in dimensional form of (kg m^{-3}), along the core is governed by

$$\frac{\partial c_{el}}{\partial t} + \boldsymbol{u} \cdot \nabla c_{el} = \mathcal{S}_{\mathrm{ff},el} + \mathcal{S}_{\mathrm{ps},el} \tag{2.28}$$

where $\boldsymbol{u}$ is the interstitial velocity, computed using the volumetric inflow rate, the fracture inlet width, and the current average mechanical aperture. A numerical solution to the advection Equation 2.28 is obtained using a cell-centred finite-volume scheme [Guyer et al., 2009], where the fracture length is discretised into $\mathcal{L} = 100$ cells. As the transport velocity vector is one-dimensional in the direction of the core's axis, its only component is given by

$$u = \frac{Q}{W \langle a_\mathrm{m} \rangle} \tag{2.29}$$

where $\langle a_\mathrm{m} \rangle$ is the average aperture under compression from the elastic contact model, and the inflow rate Q is given by the experimentally imposed macroscopic pressure difference $\overline{\overline{\Delta p_\mathrm{f}}}$ over the core length L

$$Q = \frac{{a_\mathrm{h}}^3 W \overline{\overline{\Delta p_\mathrm{f}}}}{12 \mu_\mathrm{f} L} \tag{2.30}$$

and a_h is the hydraulic aperture determined from steady-state flow experiments on the REV contact model as described above, and μ_f is the temperature-dependent viscosity of water.

For comparison with reported values [Yasuhara et al., 2011], the concentration at the outlet of the model in terms of (mol L^{-1}) is obtained through the conversion

$$c\left(\frac{\mathrm{mol}}{\mathrm{L}}\right) = \frac{\frac{c\left(\frac{\mathrm{kg}}{\mathrm{m}^3}\right)}{\text{molar density}\left(\frac{\mathrm{kg}}{\mathrm{mol}}\right)}}{\text{liter per cubic meter}\left(\frac{\mathrm{L}}{\mathrm{m}^3}\right)} \tag{2.31}$$

A further conversion to arrive at a concentration in form of (ppm) [Yasuhara et al., 2006] is by multiplication with the molar density of Si,

$$c\,(\mathrm{ppm}) = c\left(\frac{\mathrm{mol}}{\mathrm{L}}\right) \text{molar density}\left(\frac{\mathrm{mg}}{\mathrm{mol}}\right) \tag{2.32}$$

Finally, the discrete surface height change for cell i, j is evaluated as

$$\frac{\mathrm{d}h_{i,j}}{\mathrm{d}t} = \frac{\sum\left(\frac{\mathrm{d}M_{\mathrm{ff},i,j}}{\mathrm{d}t} + \frac{\mathrm{d}M_{\mathrm{ps},i,j}}{\mathrm{d}t}\right)\frac{1}{\rho_{\mathrm{s},min}}}{\ell^2} \tag{2.33}$$

where the summation is taken over all minerals. A global time increment Δt is used to integrate the transient terms. The explicit coupling between the mechanical-chemical and transport model is necessary due to the disparate time scale of contact and transport processes, and gives rise to a maximum value for Δt above which the simulation becomes unstable. The time increment is limited by the three-dimensional contact-dissolution model, and determined by sensitivity analysis in a similar manner as for the pressure-solution-only work-flow established above.

2.2 Fracture network

Discrete fracture models (DFMs) most commonly represent fractures as planar surfaces [Bogdanov et al., 2003, Koudina et al., 1998]. The effects of small-scale features, such as roughness, are then incorporated by means of parameters to the governing equations, such as transmissivity and friction coefficient. In the presented framework, a novel down-scale up-scale approach is developed. Shear

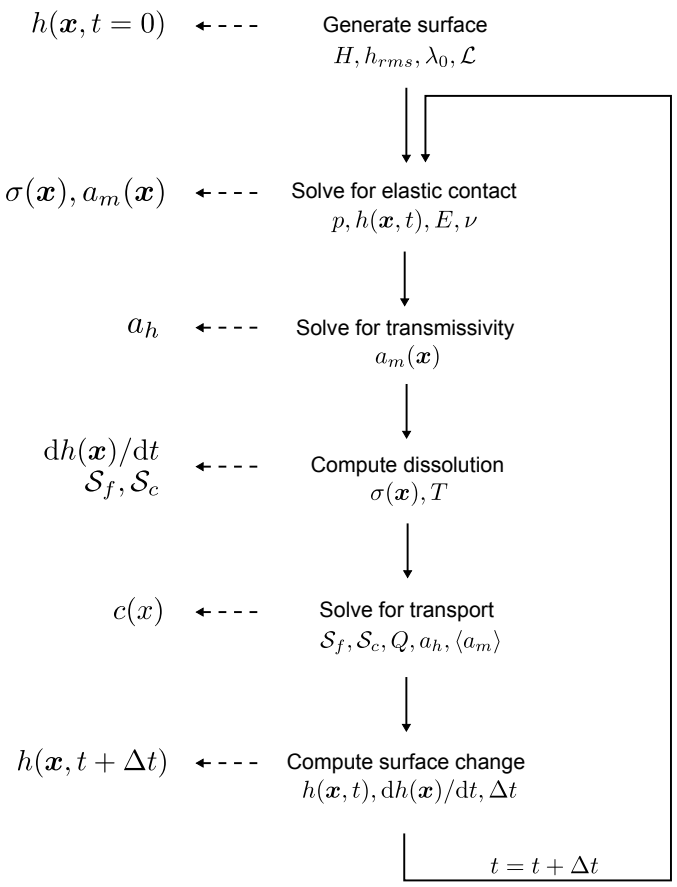


Figure 2.12: Flow chart of the single fracture THMC coupled reactive transport model.

displacement and normal stress on fractures is solved for at the DFM scale, in response to far-field stresses and the hypothesised opening-closure processes. Based on these values, individual fracture-scale models are created to compute the transmissivity that results from bespoke displacement and compression. The fracture transmissivities are fed back to the DFM where global flow problems can then be solved. The full macro-scale permeability tensor of a rock mass can be computed for arbitrary fracture networks with the friction coefficient as the only free parameter. The incorporation of chemical reaction models at the fracture scale allows to predict changes in global permeability as a result of fracture-scale changes.

2.2.1 Contact

The normal displacement, and, by extension, the normal stiffness between rough surfaces, is known to depend predominantly on the largest roughness wavelengths [Campañá et al., 2011]. This allows for direct, first principle modelling of this problem by explicit representation of rough surfaces. As larger and larger wavenumbers are included in the surface representation, *i.e.*, q_1 is being increased, normal contact results converge, similar to results of transmissivity between rough surfaces [Neuville et al., 2011, Schmittbuhl et al., 2008]. This is not the case for shear displacement, *i.e.*, frictional contact. Many attempts have been made to extend the normal contact approach to also account for direct simulation of small-scale shear displacement [Bucher et al., 2002, Karpenko and Akay, 2001], but it's generally believed that there is no first-principle model for friction because it is thought to depend on roughness across all wavelengths [Persson, 2001, Persson et al., 2005]. It follows that friction is a phenomenological concept at the scale where the surfaces in contact are approximatively planar. Even at this scale, it is not entirely clear what the dominating characteristics of the fracture are with respect to friction, as it has been shown that at high level of normal stress the surface characteristics of rock don't seem to play an important role, and the friction coefficient converges to $\mu \approx 0.6$ [Byerlee, 1978].

To model the effects that far-field stress has on the transmissivity of individual fractures, and in turn on the permeability of a fractured rock mass, the frictional contact at the DFM scale is solved first. Fractures at this scale are modelled as split surfaces, which in numerical terms means that a duplicate set of nodes exist at fracture elements, one for each side of the fracture. Within a finite element (FE) framework there exists therefore no explicit connectivity across the fracture, and contact between the two sides is accommodated by a supplementary problem based on an isoparametric contact discretisation and a gap-based augmented Lagrangian algorithm. The formulation is given in detail in [Nejati et al., 2016]. The material behaviour is assumed to be linear elastic, homogeneous and isotropic.

The FE model uses an unstructured mesh based on quadratic tetrahedral elements to discretise the domain. The surfaces of the model, including the internal fracture surfaces and external ones, are also discretised using quadratic triangular elements. Conformal meshes are employed over the two surfaces of fracture, leading to an element-to-element contact discretisation based on triangular elements. The elements of the two fracture surfaces, which are often called master and slave surfaces, are paired, which allows to enforce contact constraints between each pair of elements. For quadratic models, the singular stress field near the crack front is modelled using quarter-point tetrahedra [Nejati et al., 2015a,b].

The frictional contact constraints are implemented in terms of an augmented Lagrangian-Uzawa method [Nejati et al., 2016]. This approach contains inner and outer loops, where the contact constraints are enforced using a penalty treatment in the inner loop, while the contact forces are updated through augmentation in the outer loop. This allows enforcing the contact constraints very accurately using small penalty parameters. It is noteworthy that when using a penalty method, large penalty parameters induce ill-conditioning into the system, while small values cannot enforce contact tractions accurately. As a remedy, contact forces are augmented using the augmented Lagrangian method to facilitate accurate constraints using small penalty parameters. The classical augmented Lagrangian method is based on Lagrange multipliers which are defined as nodal values of contact tractions [Simo and Laursen, 1992, Wriggers, 2006]. However, this approach is not suitable for enforcing contact constraints over fracture surfaces since the nodal tractions are not available for the nodes located on the crack front. Nejati et al. [2016] recently developed a gap-based augmented Lagrangian method which circumvents this difficulty, and uses a singular variation of penalty parameter near the crack front, which compensates for zero gaps at the crack front nodes. This allows computing accurate contact tractions even very close to the crack front.

2.2.2 Hypothesised opening-closure process

Contact between fracture surfaces on the DFM scale is solved for by a set of subsequent boundary conditions, resulting in a form of opening-closure history; see Figure 2.13. First, an initial opening of fractures is modelled by applying an initial fluid (normal) pressure p_f over the fracture surfaces, and solving for the ensuing deformation. An initial normal gap, $\hat{g}_\mathrm{N}$, between opposing surfaces results (Figure 2.13a). Secondly, the fluid pressure is set to zero, the solid deformation due to fluid pressure is discarded, and deformation and frictional contact is solved for under an external triaxial compressive stress applied to the cube's boundaries. The far-field stress tensor

$$\boldsymbol{S} = \begin{bmatrix} S_x & 0 & 0 \\ 0 & S_y & 0 \\ 0 & 0 & S_z \end{bmatrix} = \begin{bmatrix} S_3 & 0 & 0 \\ 0 & S_2 & 0 \\ 0 & 0 & S_1 \end{bmatrix} = \begin{bmatrix} S_\mathrm{h} & 0 & 0 \\ 0 & S_\mathrm{H} & 0 \\ 0 & 0 & S_\mathrm{V} \end{bmatrix} \tag{2.34}$$

is used for this purpose (Figure 2.13b), where throughout the examples presented here $S_\mathrm{V} > S_\mathrm{H} > S_\mathrm{h}$ is assumed. As a result of this compression the individual crack surfaces may or may not go into contact. Moreover, during the closure phase, crack surfaces experience a relative tangential displacement before and after going into contact. The value of tangential displacement before contact is called the initial tangential gap, $\hat{\boldsymbol{g}}_\mathrm{T}$, and any subsequent slip under compression is denoted $\boldsymbol{g}_\mathrm{T}$. The magnitude of the total local shear displacement between the surfaces is determined as $\delta_\mathrm{T} = |\boldsymbol{\delta}_\mathrm{T}| = |\hat{\boldsymbol{g}}_\mathrm{T} + \boldsymbol{g}_\mathrm{T}|$. If in contact, local values for contact pressure, p, and shear stress, τ are further obtained (Figure 2.13b). Conceptually, this process is thought to mimic fracture initiation due to short-time, localised tensile stresses, and subsequent closure due to the dominantly compressive state of stress that exists underground.

A complete treatment of fracturing in rock would require the incorporation of numerous other processes, such as fracture propagation and fracturing due to shear; modelling of these mechanisms is under way in independent studies and outside

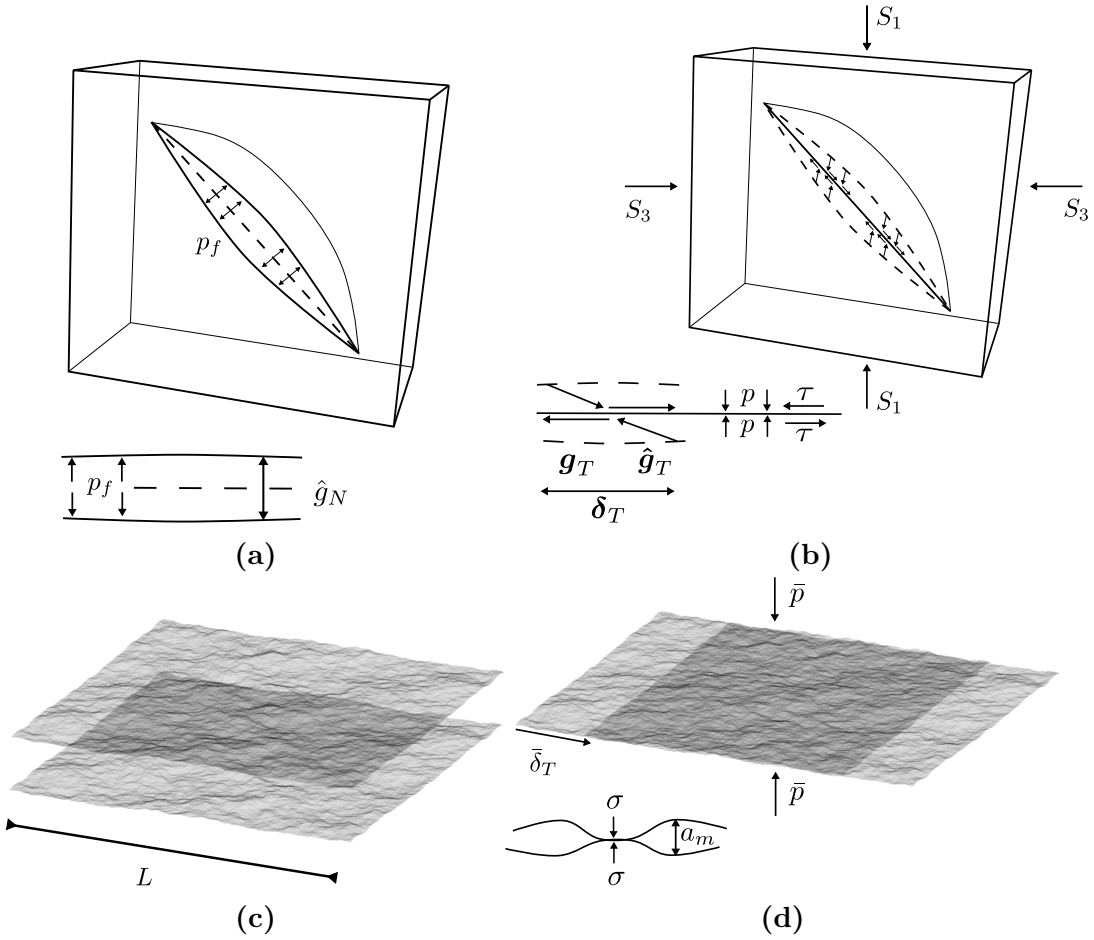


Figure 2.13: Hypothesised mechanical opening-closure model: (a) An initial fluid pressure p_f acts to open fractures to an initial normal gap $\hat{g}_\mathrm{N}$. (b) Subsequent triaxial compression leads to fracture closure under contact pressure p, shear stress τ, tangential displacement before contact $\hat{g}_\mathrm{T}$, and tangential displacement in contact g_T. Concurrently, individual models at the rough fracture scale (c) are constructed, and subsequently (d) displaced and compressed based on network scale average parameters per fracture.

the scope of this work. Rather, the intention here is to have some geomechanically relevant mechanism that allows the prediction of normal stresses and shear displacement in fractures as a result of network geometry and boundary conditions. Thus, in principle, the presented approach is capable of a complete analysis of the combined hydro-mechanical problem upon integration of extended fracture mechanics. More details about the fracture contact model can be found in Nejati et al. [2016].

2.2.3 Flow

Fluid flow through fractured rock as a response to a hydraulic head gradient will vary heterogeneously throughout the domain. Within the fractures, flux will vary locally depending on orientation, conductivity, and connectivity of individual joints. Flux in the rock matrix depends on the matrix permeability and whether or not the fracture network allows for pressure gradients to exist across individual blocks [Matthäi and Belayneh, 2004]. Overall, a certain volumetric flow will result as an ensemble fracture-matrix response. The proportionality factor between the block's pressure gradient and this total flow is referred to as block, or equivalent, permeability [e.g. Amaziane et al., 2001, Renard and de Marsily, 1997]. The distinction to effective permeability is based on observations that a representative elementary volume cannot always be defined in fractured rock due to the fractal nature of joint geometry and the resulting lack of homogenisation scale [e.g. Bonnet et al., 2001]. Thus, the permeability of fractured rock is not an intrinsic property but varies strongly with scale and sample. In the context of this study permeability, $\tilde{\boldsymbol{k}}$, is a symmetric second-rank tensor [e.g. Durlofsky, 1991] that refers to the equivalent permeability of a fractured rock mass at a specific scale of investigation. It follows that

$$\tilde{\boldsymbol{k}} = \begin{bmatrix} \tilde{k}_{xx} & \tilde{k}_{xy} & \tilde{k}_{xz} \\ \tilde{k}_{yx} & \tilde{k}_{yy} & \tilde{k}_{yz} \\ \tilde{k}_{zx} & \tilde{k}_{zy} & \tilde{k}_{zz} \end{bmatrix} \tag{2.35}$$

where $\tilde{k}_{ij}$ are the components relating the flux and pressure gradients along the x, y, z axes in a three-dimensional Cartesian system. Principal permeabilities are defined in direction by the eigenvectors, and in magnitude by the corresponding eigenvalues, of $\tilde{\boldsymbol{k}}$. These eigenvalues are referred to here as the minimum, medium and maximum equivalent permeability, i.e. $\tilde{k}_{\min}$, $\tilde{k}_{\text{med}}$ and $\tilde{k}_{\max}$, respectively. Anisotropy, $\mathcal{N}$, is defined as the ratio of the maximum to minimum principal equivalent permeability:

$$\mathcal{N} = \frac{\tilde{k}_{\max}}{\tilde{k}_{\min}} \tag{2.36}$$

It is important to highlight that the distinction between effective permeability, $\boldsymbol{k}$ and equivalent permeability $\tilde{\boldsymbol{k}}$ is based on conceptual grounds only, *i.e.*, whether one models domains with fracture lengths L well below the domain length L_Ω over which permeability is evaluated. A ratio L_Ω/L of around 4-5 is commonly assumed sufficient [Bogdanov et al., 2007, Mourzenko et al., 2011] for the resulting value to be classified as effective, such that no significant change with increasing L_Ω occurs. Numerically, there is no difference in the way these two permeabilities are obtained, and any method suitable for one should work for the other. On occasion, the notations $\tilde{\boldsymbol{k}}$ and $\boldsymbol{k}$, and the corresponding magnitudes of components and eigenvalues, $\tilde{k}$ and k, are used interchangeably and their meaning arises from the context of the model geometry.

2.2.4 Permeability

To arrive at a full equivalent permeability tensor, a series of incompressible, single-phase filtration problems are solved over a porous medium domain using the finite-element method. For each simulation, the resulting scalar pressure field is post-processed to yield a pressure gradient vector field. Element-wise constant fluxes are computed using local element pressure gradients, and permeability is computed by applying Darcy's law. Contributions to the equivalent permeability tensor components are a function of element-volume weighted averaging of pressure gradients and fluxes. The resulting over-constrained problem is solved using a least squares approximation. The asymmetric effect of permeameter-type flow constraints is relaxed by excluding a boundary adjacent peripheral region from the tensor approximation. In other words, permeability is evaluated over a subdomain of the flow model only.

Governing equations and numerical solution

The Laplace problem is solved to model incompressible, single-phase flow in porous media, in which conservation of mass reduces to conservation of volume, and

volume flux can in turn be expressed using Darcy's law. It follows that for such a divergence free velocity field with said constitutive relationship for velocity

$$\nabla \cdot (\frac{\boldsymbol{k}}{\mu_{\mathrm{f}}} \nabla p_{\mathrm{f}}) = 0 \tag{2.37}$$

where the solution of pressure, p, is approximated at nodes of unstructured finite element grids in three dimensions, employing standard Galerkin method. The viscosity, μ_{f}, is assumed to be constant, for local variation of the intrinsic and isotropic permeability, k, is permitted. After solution of the pressure field, element-wise constant barycentric velocity is arrived at by applying Darcy's law, to find

$$\boldsymbol{u} = -\frac{\boldsymbol{k}}{\mu_{\mathrm{f}}} \nabla p_{\mathrm{f}} \tag{2.38}$$

which results in a vector field of element piece-wise constant velocities, $\boldsymbol{u}$, that reflect local element pressure gradients ∇p_{f} and permeabilities, $\boldsymbol{k}$. The representation of fractures in the mesh is a discrete lower-dimensional one. In three dimensions, fractures are modelled using surface elements defined between volumetric elements. Two-dimensional models, correspondingly, use line elements in between surface elements. Flux in fracture elements relates to the local pressure gradient through the aperture squared divided by twelve, a relationship that results from the assumption of laminar flow between parallel plates obeying a parabolic velocity profile, commonly referred to as the cubic law [e.g. Witherspoon et al., 1980, Zimmerman et al., 1991].

It is important to note that, in the Finite Element solution of Equation 2.37, the lower-dimensional representation of fractures requires special treatment of the local permeability coefficient $\boldsymbol{k}$

$$\boldsymbol{k} = \begin{cases} \boldsymbol{k}\ (m^2) & \text{permeability for volumetric matrix elements} \\ \boldsymbol{K}\ (m^3) & \text{transmissivity for planar fracture elements} \end{cases} \tag{2.39}$$

This is necessary because the contribution of two-dimensional elements in three-dimensional space to the global stiffness matrix results from integration over their

surface. Implicitly, this contribution is interpreted as though the area of the element constituted a volume, *i.e.*, the surface element having a unit thickness. The use of $\boldsymbol{K}$ instead of $\boldsymbol{k}$ normalises this implicit integration. This is similar to analytic models in hydrology, where permeability is used when the volume of the domain is know, and transmissivity when the domain is approximated as a layer of undefined thickness [Zimmerman and Bodvarsson, 1996b]. When post-processing the local velocity (Equation 2.38) after the FE solution of the pressure field, the permeability $\boldsymbol{k}$ (m^2) is used for both volumetric and surface elements, as required for dimensional consistency and due to the fact that the result is a velocity ($\mathrm{m\ s}^{-1}$) and not a volume integrated flow ($\mathrm{m}^3\ \mathrm{s}^{-1}$).

Equivalent Permeability Tensor: 2D

The volume averaged form of Equation 2.38, with a viscosity of $\mu_\mathrm{f} = 1$ from here on, can be expressed as [Durlofsky, 1991]

$$\tilde{\boldsymbol{k}}\langle\nabla p_\mathrm{f}\rangle = -\langle\boldsymbol{u}\rangle \tag{2.40}$$

where $\langle ...\rangle$ stands for volume averages over a domain Ω where a solution p_f to Equation 2.37 and a subsequently computed velocity field $\boldsymbol{u}$ exists. The component-wise averages are denoted as $\langle\partial p_\mathrm{f}/\partial x_i\rangle$ and $\langle u_i\rangle$, such that [Durlofsky, 1991]

$$\langle u_i\rangle = \frac{1}{V_\Omega}\sum_e \int_{V_e} u_i^e \mathrm{d}V_e \tag{2.41}$$

$$\langle\frac{\partial p_f}{\partial x_i}\rangle = \frac{1}{V_\Omega}\sum_e \int_{V_e} \frac{\partial p_f^e}{\partial x_i}\mathrm{d}V_e \tag{2.42}$$

for all elements e within a domain Ω of the volume V_Ω. Note that fractures in the form of lower dimensional elements require a local thickness attribute for volume integration, and a parameter for the average mechanical aperture is used for this purpose herein. This is an extension to Lang et al. [2014] in that it allows for tensorial hydraulic aperture and a separate scalar variable quantifying the void space of the fracture.

With two linearly independent pressure solutions, *e.g.*, permeameter conditions along the x- (I) and y-axis (II), the matrix form in two-dimensional analysis [Azizmohammadi and Paul, 2012, Wen et al., 2003], is

$$\begin{bmatrix} \langle \frac{\partial p_\mathrm{f}}{\partial x} \rangle^{\mathrm{I}} & \langle \frac{\partial p_\mathrm{f}}{\partial y} \rangle^{\mathrm{I}} & 0 & 0 \\ 0 & 0 & \langle \frac{\partial p_\mathrm{f}}{\partial x} \rangle^{\mathrm{I}} & \langle \frac{\partial p_\mathrm{f}}{\partial y} \rangle^{\mathrm{I}} \\ \langle \frac{\partial p_\mathrm{f}}{\partial x} \rangle^{\mathrm{II}} & \langle \frac{\partial p_\mathrm{f}}{\partial y} \rangle^{\mathrm{II}} & 0 & 0 \\ 0 & 0 & \langle \frac{\partial p_\mathrm{f}}{\partial x} \rangle^{\mathrm{II}} & \langle \frac{\partial p_\mathrm{f}}{\partial y} \rangle^{\mathrm{II}} \\ 0 & 1 & -1 & 0 \end{bmatrix} \begin{bmatrix} \tilde{k}_{xx} \\ \tilde{k}_{xy} \\ \tilde{k}_{yx} \\ \tilde{k}_{yy} \end{bmatrix} = - \begin{bmatrix} \langle u_x \rangle^{\mathrm{I}} \\ \langle u_y \rangle^{\mathrm{I}} \\ \langle u_x \rangle^{\mathrm{II}} \\ \langle u_y \rangle^{\mathrm{II}} \\ 0 \end{bmatrix}. \tag{2.43}$$

Equivalent Permeability Tensor: 3D

Equation 2.43 is extended to three dimensions, which requires now three separate solutions to Equation 2.37. Correspondingly, permeameter boundary conditions align with the three global coordinate axes, indicated by superscripts I, II and III for flow along the x-, y- and z-axis, respectively. Using symmetry conditions as constraints it follows that the linear problem to be solved of form $\boldsymbol{Ax} = \boldsymbol{b}$ is given

by

$$\begin{bmatrix}
\langle\frac{\partial p_f}{\partial x}\rangle^{I} & \langle\frac{\partial p_f}{\partial y}\rangle^{I} & \langle\frac{\partial p_f}{\partial z}\rangle^{I} & 0 & 0 & 0 & 0 & 0 & 0 \\
0 & 0 & 0 & \langle\frac{\partial p_f}{\partial x}\rangle^{I} & \langle\frac{\partial p_f}{\partial y}\rangle^{I} & \langle\frac{\partial p_f}{\partial z}\rangle^{I} & 0 & 0 & 0 \\
0 & 0 & 0 & 0 & 0 & 0 & \langle\frac{\partial p_f}{\partial x}\rangle^{I} & \langle\frac{\partial p_f}{\partial y}\rangle^{I} & \langle\frac{\partial p_f}{\partial z}\rangle^{I} \\
\langle\frac{\partial p_f}{\partial x}\rangle^{II} & \langle\frac{\partial p_f}{\partial y}\rangle^{II} & \langle\frac{\partial p_f}{\partial z}\rangle^{II} & 0 & 0 & 0 & 0 & 0 & 0 \\
0 & 0 & 0 & \langle\frac{\partial p_f}{\partial x}\rangle^{II} & \langle\frac{\partial p_f}{\partial y}\rangle^{II} & \langle\frac{\partial p_f}{\partial z}\rangle^{II} & 0 & 0 & 0 \\
0 & 0 & 0 & 0 & 0 & 0 & \langle\frac{\partial p_f}{\partial x}\rangle^{II} & \langle\frac{\partial p_f}{\partial y}\rangle^{II} & \langle\frac{\partial p_f}{\partial z}\rangle^{II} \\
\langle\frac{\partial p_f}{\partial x}\rangle^{III} & \langle\frac{\partial p_f}{\partial y}\rangle^{III} & \langle\frac{\partial p_f}{\partial z}\rangle^{III} & 0 & 0 & 0 & 0 & 0 & 0 \\
0 & 0 & 0 & \langle\frac{\partial p_f}{\partial x}\rangle^{III} & \langle\frac{\partial p_f}{\partial y}\rangle^{III} & \langle\frac{\partial p_f}{\partial z}\rangle^{III} & 0 & 0 & 0 \\
0 & 0 & 0 & 0 & 0 & 0 & \langle\frac{\partial p_f}{\partial x}\rangle^{III} & \langle\frac{\partial p_f}{\partial y}\rangle^{III} & \langle\frac{\partial p_f}{\partial z}\rangle^{III} \\
0 & 1 & 0 & -1 & 0 & 0 & 0 & 0 & 0 \\
0 & 0 & 1 & 0 & 0 & 0 & -1 & 0 & 0 \\
0 & 0 & 0 & 0 & 0 & 1 & 0 & -1 & 0
\end{bmatrix}$$

$$\begin{bmatrix} \tilde{k}_{xx} \\ \tilde{k}_{xy} \\ \tilde{k}_{xz} \\ \tilde{k}_{yx} \\ \tilde{k}_{yy} \\ \tilde{k}_{yz} \\ \tilde{k}_{zx} \\ \tilde{k}_{zy} \\ \tilde{k}_{zz} \end{bmatrix} = - \begin{bmatrix} \langle u_x \rangle^{I} \\ \langle u_y \rangle^{I} \\ \langle u_z \rangle^{I} \\ \langle u_x \rangle^{II} \\ \langle u_y \rangle^{II} \\ \langle u_z \rangle^{II} \\ \langle u_x \rangle^{III} \\ \langle u_y \rangle^{III} \\ \langle u_z \rangle^{III} \\ 0 \\ 0 \\ 0 \end{bmatrix} \tag{2.44}$$

where $\tilde{k}_{ij}$, are the equivalent permeability components, with $i, j = x, y, z$, and $\langle u_{x,y,z} \rangle^{I,II,III}$ are the averaged flux components for each experiment. This matrix problem (Equation 2.44) constitutes an overdetermined system of twelve equations in nine unknowns, which also must satisfy the constraint $\tilde{k}_{xy} = \tilde{k}_{yx}$, $\tilde{k}_{xz} = \tilde{k}_{zx}$ and

$\tilde{k}_{yz} = \tilde{k}_{zy}$. Using a pseudo-inverse approach, it follows that

$$\boldsymbol{A}^{\mathrm{T}}\boldsymbol{A}\boldsymbol{x} = \boldsymbol{A}^{\mathrm{T}}\boldsymbol{b} \tag{2.45}$$

to arrive at a solution for the tensor components, which permits a least squares minimisation [Sanford and Dally, 1979]. The presented matrix problems are based on Darcy's law in tensor form, which in physical terms implies that the diagonal permeability terms relate flux to pressure gradient along the same direction, and the off-diagonal terms relate flux to the perpendicularly oriented pressure gradient. This applies to both the local (element) and the global (fracture-matrix) scale, where fluxes and pressure gradients are discrete and averaged, respectively.

Boundary Conditions

The tensor approximation for the three-dimensional case presented in Equation 2.44 requires that three numerical flow experiments are to be run. The original approach by Durlofsky [1991] works on structured meshes and constrains opposite boundaries to honour periodicity of fluxes. For unstructured grids of discrete fracture networks, however, such conditions are not practicable. Instead, asymmetric permeameter boundary conditions are used in the presented approach. In each of the flow simulations, the pressures on a pair of opposing boundary surfaces are set to yield a prescribed macroscopic pressure difference $\overline{\overline{\Delta p_{\mathrm{f}}}}$. Bounding box-surfaces oriented parallel to this macroscopic flow direction are assigned to no-flow conditions, or a zero pressure-gradient normal to their plane. As a consequence, calculated equivalent permeability will be a function of the applied boundary conditions [e.g. Farmer, 2002, Renard and de Marsily, 1997] and their asymmetry to some extent. Close to the boundary, element pressure gradients will reflect the prescribed physical flow constraints rather than the effects of local permeability and geometry. The resulting flow response is illustrated in Figure 2.14, where boundary-adjacent flux vectors honour no-flow boundary conditions - their contribution to the averaging problems in Equation 2.44 distorts the average orientation of fluid flow.

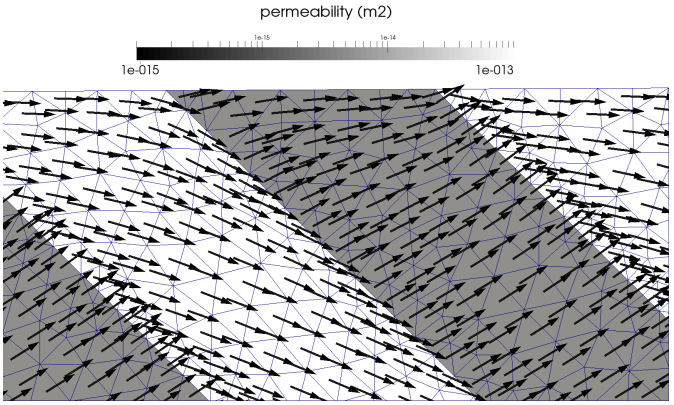


Figure 2.14: Boundary effects in the flow solution, where flow directions reflect constraints rather than geometry.

Sampling Domain

To retrieve a representative symmetric tensor from flux and pressure fields that, at least near the periphery, are physically influenced by asymmetric constraints, averages in Equation 2.44 are computed only over a restricted sub-volume Ω of the flow region, away from the borders. This approach is referred to here as sub-sampling, since the pressure diffusion problem is solved over the entire model, but equivalent permeability is calculated by sampling the fluxes and pressure gradients in a sub-domain only. Other authors refer to similar approaches as 'flow jacket' or 'oversampling', and find that this procedure reduces boundary effects, and better reflects the connectivity of the sampling domain [e.g. Holden and Lia, 1992, Wu et al., 2002]. The sampling sub-domain will be chosen such that only those elements are included that keep a minimum distance to all model boundaries, see Figure 2.15.

The concept of a sampling region is not a drawback, but a major advantage of the developed method. Once the fluid flow problem is solved, which represents the computationally more expensive part, any number of arbitrarily chosen regions within the model can be evaluated by means of cheap mesh traversals. This allows for investigations as to the existence of homogenisation scales, walking averages of permeability and optimisation of the way an upscaled coarse grid may be superimposed on the DFM. For each coarse-grid cell, the permeability tensor can be obtained, and the orientation and size of the upscaled cell can be adjusted to

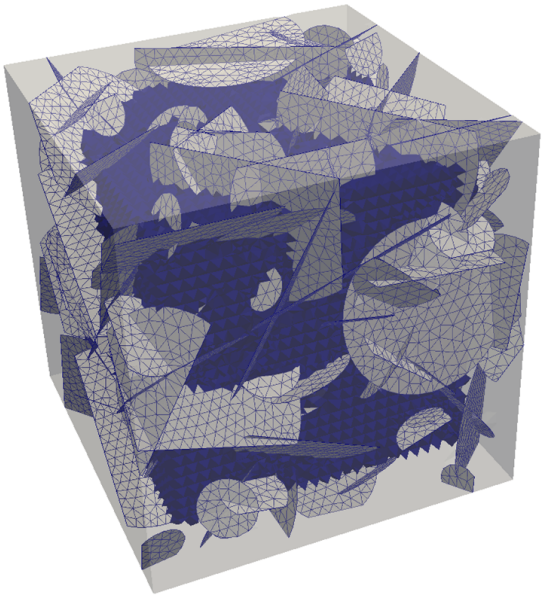


Figure 2.15: A discrete fracture model (DFM). Permeability of the fractured rock mass is evaluated over a subdomain Ω, here of cubic form and highlighted in blue.

minimise the error that arises from misalignments with the directions of principal permeabilities.

Numerical-analytical comparison

A reference problem (Figure 2.16a) is proposed which challenges the key novelties of the developed upscaling method, which cannot be solved by any other method to date. First, the fracture network is not periodic. Secondly, both fracture and matrix have locally anisotropic permeability coefficients in full tensor form, *i.e.*, the local permeability eigenvectors are not aligned with the global coordinate system (Figures 2.16c and 2.16d). Thirdly, the resulting effective permeability eigenvectors of the DFM are not aligned with the global coordinate system or, more importantly, aligned with the axes of the bounding box; see Figure 2.16b.

The fracture hydraulic aperture is anisotropic with, in local coordinates, $a_{\mathrm{h},x} = 1.4 \times 10^{-4}$ and $a_{\mathrm{h},y} = 2.0 \times 10^{-4}$ m, and an average mechanical aperture, which quantifies the physical thickness of the fracture, of $\langle a_{\mathrm{m}} \rangle = 0.0001$ m. The local transmissivity tensor thus has diagonal components of $K_x = (1.4 \times 10^{-4})^3/12$ and

$K_y = (2.0 \times 10^{-4})^3/12$ m^3. The local matrix permeability tensor has diagonal components of $k_x = 12 \times 10^{-15}$, $k_y = 7.5 \times 10^{-15}$, and $k_z = 5 \times 10^{-15}$ m^2. The geometry is formed by xy-plane parallel fractures with a spacing in z-direction of $b = 14.14$ m, which is equivalent to the matrix bed thickness. The edge length of the cubic bounding box is 100 m. The fracture geometry is then rotated by $\pi/4$ counter-clock-wise about the z-axis and $\pi/4$ clock-wise about the x-axis (Figure 2.16a), using the common right-hand convention. The sampling region reflects the separation between fractures, i.e., Ω is a cubic subdomain of edge length $L_\Omega = 100 - b\cos(\pi/4) = 90$ m.

The element-wise constant local permeability and transmissivity tensors, initially and after rotation, follow as

$$\boldsymbol{k}(\mathrm{m}^2) = \begin{bmatrix} k_x & 0 & 0 \\ 0 & k_y & 0 \\ 0 & 0 & k_z \end{bmatrix} \longrightarrow \begin{bmatrix} 9.1250 & 2.8750 & 0.8839 \\ 2.8750 & 9.1250 & -0.8839 \\ 0.8839 & -0.8839 & 6.2500 \end{bmatrix} 10^{-15} \tag{2.46}$$

and

$$\boldsymbol{K}(\mathrm{m}^3) = \begin{bmatrix} K_x & 0 & 0 \\ 0 & K_y & 0 \\ 0 & 0 & 0 \end{bmatrix} \longrightarrow \begin{bmatrix} 2.8100 & -0.5233 & 2.3570 \\ -0.5233 & 2.8100 & -2.3570 \\ 2.3570 & -2.3570 & 3.3333 \end{bmatrix} 10^{-13} \tag{2.47}$$

respectively, and are illustrated in Figures 2.16c and 2.16d.

The analytical solution to the effective permeability tensor of the fractured rock mass consists of the weighted averages parallel to the fracture planes and to the matrix permeability perpendicular to it. The latter implies that fractures do not

contribute to flow perpendicular to their plane. It follows that

$$\boldsymbol{k}_{\mathbf{ref}}(\mathrm{m}^2) = \begin{bmatrix} \frac{bk_x+\langle a_\mathrm{m}\rangle K_x/a_{\mathrm{h},x}}{b+\langle a_\mathrm{m}\rangle} & 0 & 0 \\ 0 & \frac{bk_y+\langle a_\mathrm{m}\rangle K_y/a_{\mathrm{h},y}}{b+\langle a_\mathrm{m}\rangle} & 0 \\ 0 & 0 & k_z \end{bmatrix} \tag{2.48}$$

$$= \begin{bmatrix} 2.3551 & 0 & 0 \\ 0 & 3.1074 & 0 \\ 0 & 0 & 0.5000 \end{bmatrix} 10^{-14} \tag{2.49}$$

and after rotation

$$\boldsymbol{k}_{\mathbf{ref}}(\mathrm{m}^2) = \begin{bmatrix} 2.0794 & 0.2757 & 0.9218 \\ 0.2757 & 2.0794 & -0.9218 \\ 0.9218 & -0.9218 & 1.8037 \end{bmatrix} 10^{-14} \tag{2.50}$$

The numerical solution is obtained as

$$\boldsymbol{k}_{\mathbf{num}}(\mathrm{m}^2) = \begin{bmatrix} 2.0796 & 0.2757 & 0.9219 \\ 0.2757 & 2.0796 & -0.9219 \\ 0.9219 & -0.9219 & 1.8039 \end{bmatrix} 10^{-14} \tag{2.51}$$

and the resulting eigenvalues are

$$\begin{bmatrix} 2.3553 & 0 & 0 \\ 0 & 3.1078 & 0 \\ 0 & 0 & 0.5000 \end{bmatrix} 10^{-14} \tag{2.52}$$

Both the full tensor of the network (Equations 2.50 and 2.51) and the eigenvalues (Equations 2.49 and 2.52) are accurate within 1% using elements with internal diameters of roughly $L/20$.

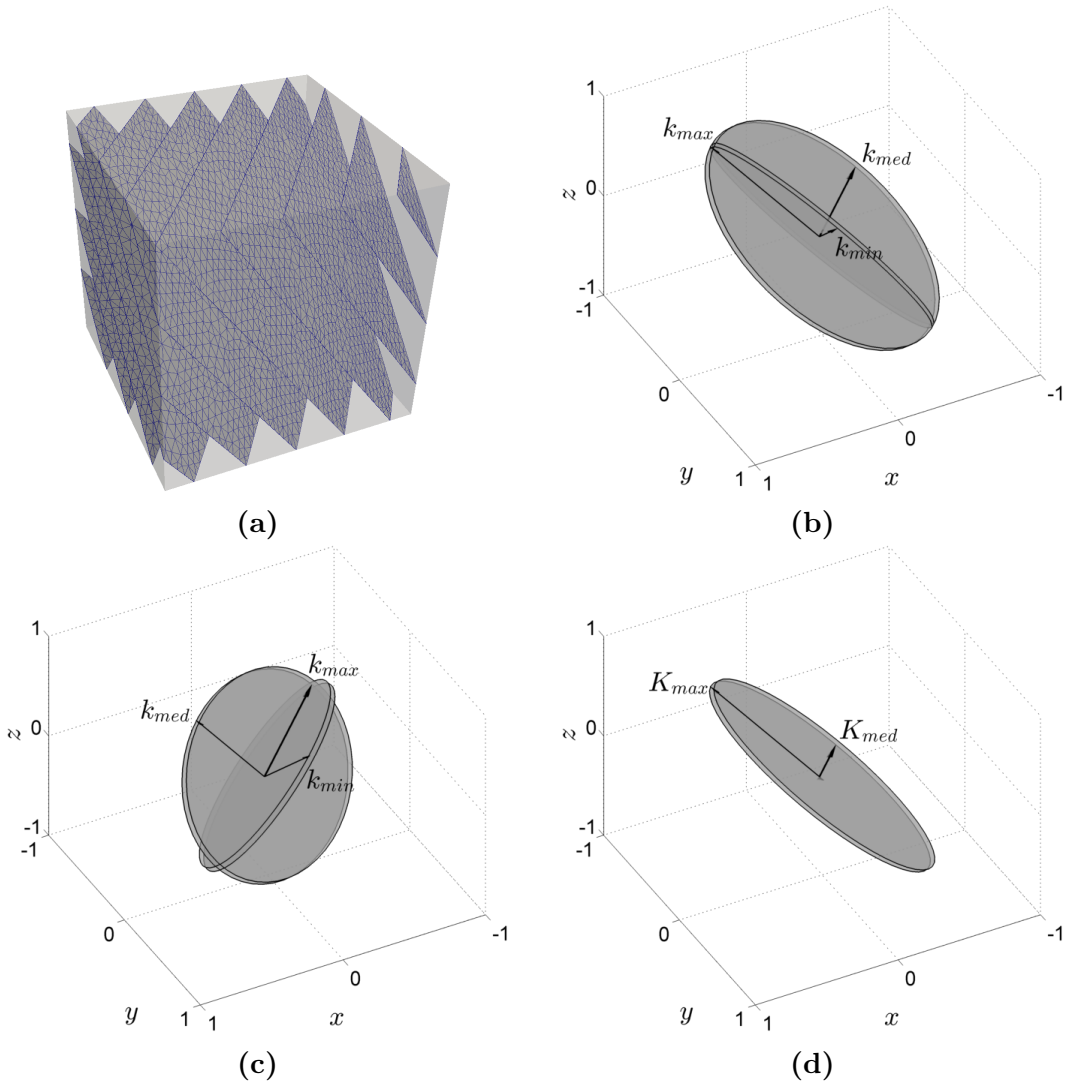


Figure 2.16: Effective permeability benchmark model. (a) The DFM finite element mesh. (b) Ellipsoid form of the upscaled effective permeability tensor. (c) Local permeability tensor of the rock matrix. (d) Local transmissivity tensor of the fractures.

2.2.5 Two-scale coupling

Concurrently with the DFM solution to the frictional contact problem, a rough surface model is constructed for each fracture in the network. This model consists of two fracture surfaces (Figure 2.13c), one of which contains a mismatch factor as described in Section 2.1.1. The rough surface depends only on the size of the fracture, which determines its roughness. Based on the harmonic average of shear displacement over the DFM fracture, $\bar{\delta}_{\mathrm{T}}$, the two surfaces are offset with respect to each other along the x-axis, and the elastic, frictionless contact between them

is solved for under a confining pressure, $\bar{p}$, which is also obtained as the harmonic average of the local pressure p over the surface; see Figure 2.13d. With the obtained mechanical aperture and contact stress field, the transmissivity of the fracture can either be directly computed, or fracture alterations due to dissolution and precipitation may be modelled first. In both cases, with or without incorporation of chemical processes, a fracture-averaged transmissivity is fed back to the network-scale model as a parameter $\boldsymbol{K}$, which is a diagonal tensor of the form

$$\boldsymbol{K} = \begin{bmatrix} K_{\parallel} & 0 & 0 \\ 0 & K_{\perp} & 0 \\ 0 & 0 & 0 \end{bmatrix} \tag{2.53}$$

which is aligned with a local coordinate system of the fracture, where the x-axis is in the direction of the shear displacement vector $\boldsymbol{\delta}_{\mathrm{T}}$, the y-axis is perpendicular to this vector on the fracture plane, and the local z-axis is perpendicular to the fracture plane, *i.e.*, the fracture plane normal vector. Any change to fracture transmissivity due to chemical reactions is computed at the fracture scale and incorporated as updated transmissivity to the DFM. The finite element meshes for the mechanical and pressure solution are identical, except for the fracture representation which is split in the former and continuous in the latter, which is accomplished internally by merging split fracture walls.

The resulting hydro-mechanical-chemical modelling approach across the two scales of single fractures and fracture networks is one-way coupled; see Figure 2.17. Two main assumptions are implicit to this sequential procedure. Firstly, pore pressure within a fracture is assumed constant, and does not change during opening and closure or compaction. Secondly, the friction coefficient is time-invariant, *i.e.* not influenced by chemically mediated reactions that alter rock surface topology. As discussed, the fracture network geometry is an input to the model, and does not change over time. This assumes that fractures do not propagate during the simulated time.

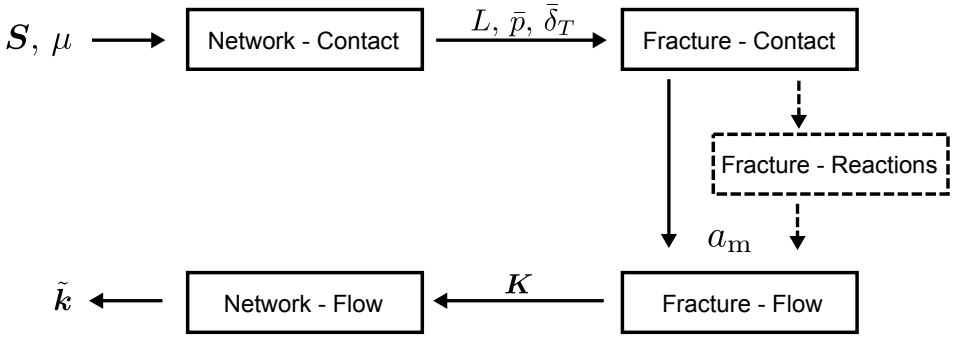


Figure 2.17: Basic workflow and key variables of the two-scale hydro-mechanical model. Optionally, dissolution/precipitation is incorporated after the fracture-scale contact solution. The only other input, in addition to the far-field stress $\boldsymbol{S}$ and the friction coefficient μ, are the fracture network geometry and material properties for matrix permeability, the Young's modulus and Poisson's ratio, E and ν, respectively, and the pre-factor and mismatch length for fracture surfaces, see Equation 2.7.

2.3 Implementation

The presented algorithms are implemented in an modularised application using a high-level/low-level, or front-end/back-end encapsulation using Python/C++, respectively, coupled through a Simplified Wrapper and Interface Generator (Swig) based interface. The surface generation, characterisation and elastic contact solution is based on Numpy data type interfaces to C arrays (`http://www.numpy.org/`) and a C implementation of the Fast Fourier Transform (`https://github.com/FFTW/fftw3`). A cell-centred finite-volume method solves the pressure solution, fracture-scale fluid flow and one-dimensional reactive transport problem and is based on the data structures used for surface generation [Guyer et al., 2009]. The Finite Element solutions to the network-scale flow and contact problem are written in C++ and based on a data structure- and algorithm-framework CSMP++ (`http://thmc-project.unileoben.ac.at:8010/waterfall`), which is used in numerous studies on fluid flow [Matthäi et al., 2007], geomechanics [Paluszny and Zimmerman, 2011] and reactive transport [Nick et al., 2011]. The contact-side part of the algorithm is the original implementation by Nejati et al. [2016], all other components have been written solely by the author (`https://github.com/plang85`). Fracture network geometries have been generated using the Python front-end of Rhino3D (`https://www.rhino3d.com/`). Finite element meshes have

been generated using ANSYS Icem in non-interactive manner (`http://www.ansys.com/`).

2.4 Computational effort

Table 2.1 lists representative wall clock-run times of examples presented in this work, for models of varying size. The runs were performed on a Intel Xeon server with 30 MB cache, 2 processors, 12 cores per processor, 2 threads per core, which yields $2 \times 24 = 48$ threads in total. This layout makes the machine optimised for single instruction multiple data (SIMD), or multi-threading parallelism. For the elastic contact algorithm, a relative residual reduction of 10 orders of magnitude was chosen, equal to that used for the verification example (Figure 2.8). This limit is very strict - it can be relaxed to reduce run times by a half while still obtaining accurate solutions. Solver settings for the network flow problem also are identical to those used for the respective reference problem (Figure 2.16). For fracture network models with fewer fractures than the number of available threads, the computation of fracture properties is quasi-constant in time, since each fracture problem is solved as a separate process.

Single fracture

Step \ $\mathcal{L}$	256	512	1024	2048	parallelisation	processes	threads per process
Geometry	1 s	1 s	1 s	1 s	SIMD	1	4
Contact	7 s	38 s	4 min	18 min	none	1	1
Flow	4 s	27 s	3 min	10 min	MISD†	2	1
Dissolution BE	57 s	5 min	42 min	6 h	SIMD	1	4
Dissolution LL	7 min	46 min	9 h	NA	none†	1	1

Fracture network

Step \ N	1	2	8	200	parallelisation	processes	threads per process
Geometry	11 s	11 s	13 s	21 s	none	1	1
Meshing	47 s	56 s	3 min	manual	SIMD♣	4	1
Contact	5 min	8 min	16 min	4 h	none‡	1	1
Fracture properties	see single fracture				SIMD	N - 2N	1-4
Flow	11 s	11 s	15 s	42 s	MISD‡	3	1

† Plus parallelisation of PySparse solver (1 process, 2 threads).
‡ Plus parallelisation of SAMG solver (1 process, 1-32 threads).
♣ ANSYS Icem parallelisation (4 processes, 1 thread each).

Table 2.1: Representative wall clock-run times for simulations presented in this work. For single fracture models, run times for elastic contact and steady-state flow may change significantly with varying surface characteristics. Contact was solve for at $p = 10$ MPa, and dissolution with $T = 423$ K. For fracture networks, N denotes the number of fractures as a proxy for the total number of nodes in a model and the number of contact nodes. Implemented parallelisation strategies are single instruction multiple data (SIMD) and multiple instruction single data (MISD), on top of which the external linear solvers may add implementation dependent strategies.

Chapter 3

Hydro-mechanical characteristics of a single fracture

The fractures that have the strongest effect on large-scale fluid flow are those with significant shear displacement [e.g. Zoback, 2007], and thus will be the focus of the presented single fracture-scale investigations. A key characteristic of fractures with shear displacement is a pronounced anisotropy of transmissivity. The underlying anisotropic nature of the fracture pore-space and its effects on fracture closure, or stiffness/compliance, has received little attention so far, up to a point where suggested universal relationships between flow and stiffness [Petrovitch et al., 2014, Pyrak-Nolte and Nolte, 2016] treat fractures as isotropic void spaces, with little explanation of what physical process leads to different simulated correlation lengths and roll-off length-scales. The approach to fracture aperture used herein differs in that the aperture space *is* a result of physical processes: fracturing, shear displacement and chemical processes. The contrast between the scalar nature of fracture specific stiffness κ and the tensorial nature of fracture transmissivity $\boldsymbol{K}$ will be the focus of this section. Two characteristic traits of shear-fractures will further be discussed. The non-uniqueness of flow-stiffness relationship and the existence of a representative elementary volume for either transmissivity or stiffness.

Rock type	E (GPa)	ν (-)
Iidate granite	29.4	0.15
Slate	66	0.15

Table 3.1: Mechanical properties used for the single fracture simulations.

3.1 Tensorial transmissivity and scalar stiffness

To study anisotropic hydro-mechanical properties, three experiments ([Bandis, 1980, Nemoto et al., 2009, Watanabe et al., 2008]) have been modelled with the presented hydro-mechanical framework for single fractures. All have been conducted on freshly induced fractures and with shear displacement under unstressed conditions to not damage the initial rock surface roughness. The length L of the numerical fracture models is chosen as the shorter edge length in case of non-square experimental fractures. The Young's modulus E equals the reported values, *i.e.*, 66 GPa for Slate [Bandis, 1980] and 29.4 GPa for Iidate granite [Hashida et al., 1993]. The value for Poisson's ratio has little effect on the frictionless contact between rough surfaces and has been chosen as $\nu = 0.15$ for all models; see Table 3.1. It follows that two model geometries are created, one of $L = 100$ mm [Watanabe et al., 2008] and $L = 50$ mm [Bandis, 1980, Nemoto et al., 2009].

The first comparison of numerical with experimental results was made for the Watanabe et al. [2008] flow experiment. Performed on an induced tensile fracture in Iinada granite, three assemblies with increasing lateral offset between the surfaces were set-up. Resulting fracture permeabilities were evaluated perpendicular to the shear direction by means of permeameter experiments. For each offset δ_{T}, a series of permeability values were further obtained for increasing levels of confining pressure; see Figure 3.1a. A follow-up experiment using the same rock type and set-ups was conducted later [Nemoto et al., 2009] to visually characterise areas of discrete contact that form due to increasing compression. This experiment solely focused on the mechanical properties of the fracture.

The numerical model to reproduce observed permeabilities in Watanabe et al. [2008] is generated as follows. Two 100×100 mm surfaces with $\mathcal{L} \times \mathcal{L} = 512 \times 512$

cells are created and displaced with respect to each other (Figure 2.4a) by distances equal to the shear offset used in the experiments, *i.e.*, $\delta_{\mathrm{T}} = 0$, 1 and 3 mm, respectively. The composite surface, or aperture space, for each set-up is then obtained by direct addition of the offset profiles. As the numerical contact algorithm works on a square model, any excess surface in the shear parallel direction is discarded. From the shear displacements of 0, 1 and 3 mm, it thus follows that the resulting surfaces are 100×100, 99×99 and 97×97 mm in size. Successively increasing confining pressures are then applied to obtain subsequent elastic contact solutions, and the hydraulic apertures of the resulting compressed aperture space are evaluated parallel, $a_{\mathrm{h},\parallel}$, and perpendicular, $a_{\mathrm{h},\perp}$, to the shear direction, along with the harmonic mean aperture between the two, $a_{\mathrm{h},\times}$. Finally, the resulting values for $a_{\mathrm{h},\perp}$ are compared to the experimentally obtained values. This procedure is repeated with varying values for the roughness pre-factor α in $h_{\mathrm{rms}} = \alpha L^{0.8}$ and mismatch wavelength λ_{m} for upper surface. A reasonable match (Figure 3.1a) is obtained with $\alpha = 0.0023$ and $\lambda_{\mathrm{m}} = 55$ μm. Note that the transmissivity of the fracture without displacement, *i.e.*, $\delta_{\mathrm{T}} = 0$, depends mostly on λ_{m}, and the transmissivity of the shear fractures depends mostly on the roughness pre-factor α. The permeability of a fracture, as reported in Watanabe et al. [2008], is related to its transmissivity by $k = K/a_{\mathrm{h}}$.

The resulting mechanical aperture space for the $\delta_{\mathrm{T}} = 3$ mm, 10 MPa case is illustrated in Figure 3.1b; a qualitative comparison of the contact area distribution measured experimentally [Nemoto et al., 2009] under identical conditions using pressure sensitive film is shown in Figure 3.1c, for fifteen statistically identical fracture realisations. There is fair agreement between the two distributions, and this mechanical characteristic arises independent from the hydraulic matching procedure. Note that the nature of the distribution, a power law, and its approximate slope, is more significant than its magnitude, or integrated value, since the latter depends on the absolute value of contact area. This absolute value, as discussed above, is in turn a scale-dependent property. It is expected to differ between numerical results and whatever visualisation means have been used in the experiment.

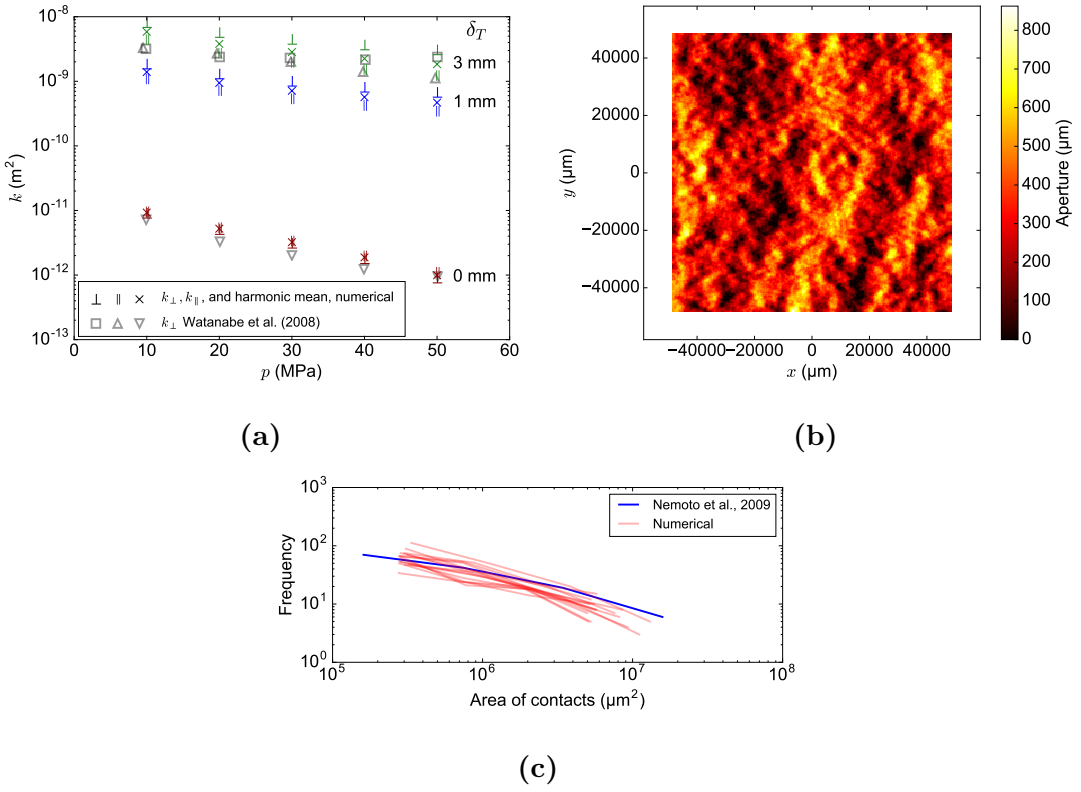
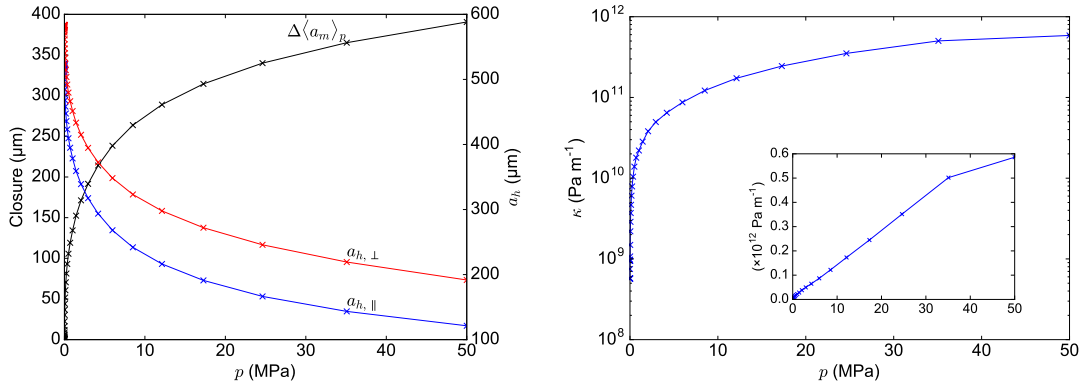


Figure 3.1: Experimental-numerical comparison of permeability for a single fracture with different amounts of shear displacement. (a) Fracture permeability compared to Watanabe et al. [2008], (b) mechanical fracture aperture of the numerical model with $\delta_\mathrm{T} = 3$ mm and 10 MPa, and (c) contact ratio of fifteen statistically identical numerical models and Nemoto et al. [2009] at the same conditions.

The hydraulic properties of the $\delta_T = 3$ mm case have been further evaluated for pressures up to 50 MPa; see Figure 3.2a. Discrete pressure values have been chosen as log-spaced intervals, since this has been shown to be a useful functional relation between closure and pressure [Goodman, 1976], and thus facilitates higher resolution in regions of high curvature, *i.e.*, regions of strongly varying stiffness. The hydraulic anisotropy, $a_{\mathrm{h},\perp}/a_{\mathrm{h},\parallel}$, is pronounced already at low pressures and increases with increasing compression p, up to a value of $\approx 195/120 = 1.625$. This implies a permeability ratio of $(1.625)^2$ and a ratio between the two transmissivity components of $(1.625)^3$. The fracture specific normal stiffness κ of the $\delta_\mathrm{T} = 3$ mm model shows conventional linear behaviour (Figure 3.2b), which is the expected functional form of stiffness between randomly rough surfaces [Akarapu et al., 2011, Bandis et al., 1983, Berthoud and Baumberger, 1998, Hopkins et al., 1990, Swan,



(a) **(b)**

Figure 3.2: Hydro-mechanical characteristics of the $\delta_T = 3$ mm Watanabe et al. [2008] numerical. (a) Closure and shear-parallel and shear-perpendicular hydraulic apertures. (b) Plot of fracture specific stiffness with linear inset.

1983]. Note that the deviation of the last stiffness value from the linear trend is due to the first-order finite difference approximation used for the end-points of the closure curves. As discussed previously, the linear scaling reflects the fact that, with increasing p, existing contact areas grow and new contact areas form in a way that the distributions of stress and contact spot size remain constant if normalised to the area of discrete contact [Persson, 2006, Sun et al., 1985]. It follows that the contact ratio R_c varies linearly with p [Dieterich and Kilgore, 1996, Goodman, 1976], and that the distributions of contact stress and contact patch size scale linearly with p when normalised to the nominal area [Campañá et al., 2011]. It should be noted that this linear scaling of contact ratio with pressure applies in the regime of low loads and elastic deformation [Carbone and Bottiglione, 2008, Greenwood and Williamson, 1966, Yastrebov et al., 2015].

The same surface parameters obtained for the permeability match of the Watanabe model have been used to independently reproduce the closure behaviour of a fresh slate fracture with shear displacement of $\delta_T \approx 1$ mm; see Figure 3.3a. This experiment has again been chosen based on the prerequisites that fractures have been freshly induced and the shear offset has been conducted under no load to preserve the original surface roughness. The agreement between numerical and experimental closure results is excellent (Figure 3.3a), in particular considering

that both the Young's modulus and surface size between the experiments differ by a factor of two, specifically by 29 vs. 66 GPa and 100 vs. 50 mm, respectively.

The pressure-dependence of the hydraulic properties (Figure 3.3b) is qualitatively similar to that observed for the Watanabe et al. [2008] model. The absolute value of the perpendicular-parallel hydraulic aperture ratio, however, is smaller in magnitude, specifically $a_{\mathrm{h},\perp}/a_{\mathrm{h},\parallel} \approx 120/80 = 1.5$. This reduced anisotropy reflects the smaller relative shear displacement, $\delta'_{\mathrm{T}} = 1/50$ [Bandis, 1980] as opposed to 3/100 [Watanabe et al., 2008]. This highlights that the ratio of absolute displacement to fracture size is an important indicator for hydraulic anisotropy. In other words, the ratio between shear offset and largest present roughness wavelengths is a key parameter in the prediction of mechanical and hydraulic properties of a fracture. The agreement between numerically and experimentally obtained specific stiffness is similarly good (Figure 3.3c), a non-trivial conclusion given that the direct differentiation of experimental closure data is difficult due to the inherent aggravation of noise. In fact, it has become common practice to evaluate stiffness based on smooth curve-fits to closure data [e.g. Zangerl et al., 2008], and it should be expected that for this approach the numerical and experimentally obtained stiffness may be identical. As to the discussion of mechanical versus hydraulic aperture [*e.g.* Renshaw, 1995], it follows that the hydraulic aperture in shear parallel direction may very well lie below the isotropic aperture. The same cannot be said for the shear perpendicular hydraulic aperture.

It is concluded that the transmissivity anisotropy of a single fracture increases both with relative shear displacement and increasing compression. The former controls the extent of flow channels that form due to the relative offset between the surfaces, and the latter reflects the fact that, as contact zones grow with increasing compression, they tend to percolate in the shear-perpendicular direction first, which follows in the sealing of shear-parallel flow at high compression. It should be obvious that the normalised shear displacement δ'_{T} is a physically more relevant parameter than the absolute value δ_{T}. The influence of the shear displacement on the fracture stiffness highlights the long established notion that characteristics of the structural process that result in the formation of fractures are directly linked

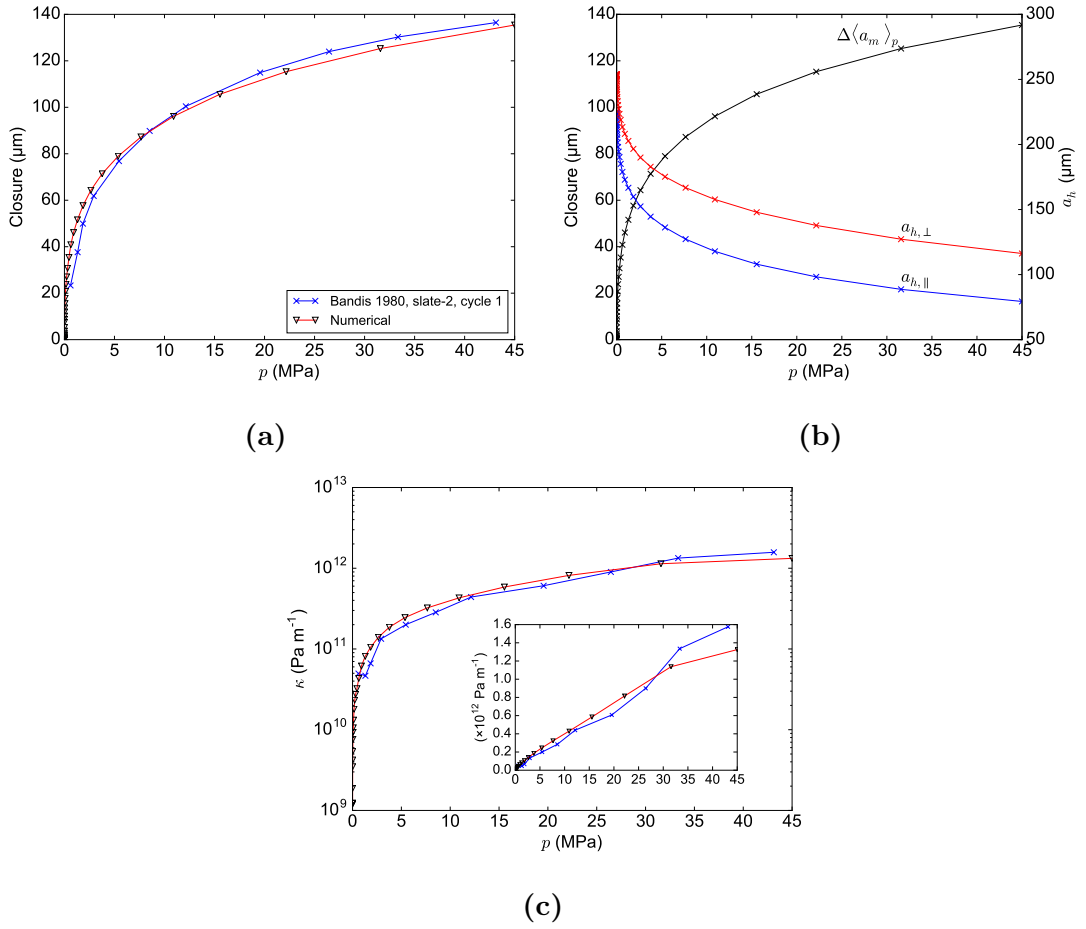


Figure 3.3: Experimental-numerical comparison of mechanical closure for a single fracture with shear displacement of $\delta_T = 1$ mm [Bandis, 1980]. (a) Mechanical closure comparison between the numerical model and the first cycle of the slate-2 experiment. (b) Closure and shear-parallel and perpendicular hydraulic aperture as a function of confinement. (c) Stiffness of numerical and experimental closure curves obtained through direct differentiation.

to their stiffness. The logical question to address next is whether, above a certain fracture size, a representative elementary volume exists with respect to specific stiffness or transmissivity, if δ'_T is assumed constant.

3.2 Stiffness as a function of size and shear displacement

Under the assumption that rock surfaces retain their initial roughness, the specific stiffness of a fracture is a function of its size and shear displacement. For elastic moduli equivalent to that of slate (Table 3.1) a series of fracture models have been generated with different lengths and shear displacements, to study the effect of both variables independently. Common to all realisations were, besides the elastic moduli, the mismatch length of $\lambda_{\mathrm{m}} = 55$ μm and the roughness amplitude scaling which followed from $h_{\mathrm{rms}} = 0.0023L^{0.8}$, as from the hydraulic fit to the Watanabe et al. [2008] data above, and the mechanical agreement these values produced with the Bandis [1980] experiment. The variables between different realisations were the length L, the discretisation resolution $\mathcal{L}$ or ℓ, and the length-normalised shear displacement $\delta'_{\mathrm{T}} = \delta_{\mathrm{T}}/L$; see Figure 3.4a. Note that the cell count $\mathcal{L}$ is a power of two for the generated surfaces; this increases the efficiency of the underlying FFT algorithms since it eliminates the need of zero-padding. After offsetting the two surfaces with respect to each other, the resulting composite surface has a reduced cell count due to the cut-off of excess surface not in contact. The resulting composite surface $\mathcal{L}$ is not a power of two, and the surface is not periodic. The former issue is addressed through zero-padding within the FFT implementation, and the latter is compensated for by padding the contact pressure field with zeros in the contact algorithm to eliminate periodicity errors [Sainsot and Lubrecht, 2011].

In naturally fractured rock, it is generally assumed that the average shear displacement of a fracture is somewhat proportional to its length. This logic also follows from considerations of the opposite end-case, in which fractures of very different lengths experience displacement of similar magnitude, for which it would be hard to imagine a responsible physical scenario. It is also the primary motivation between length-correlated fracture transmissivity models. A fracture-length normalised shear displacement thus seems a more appropriate measure than the

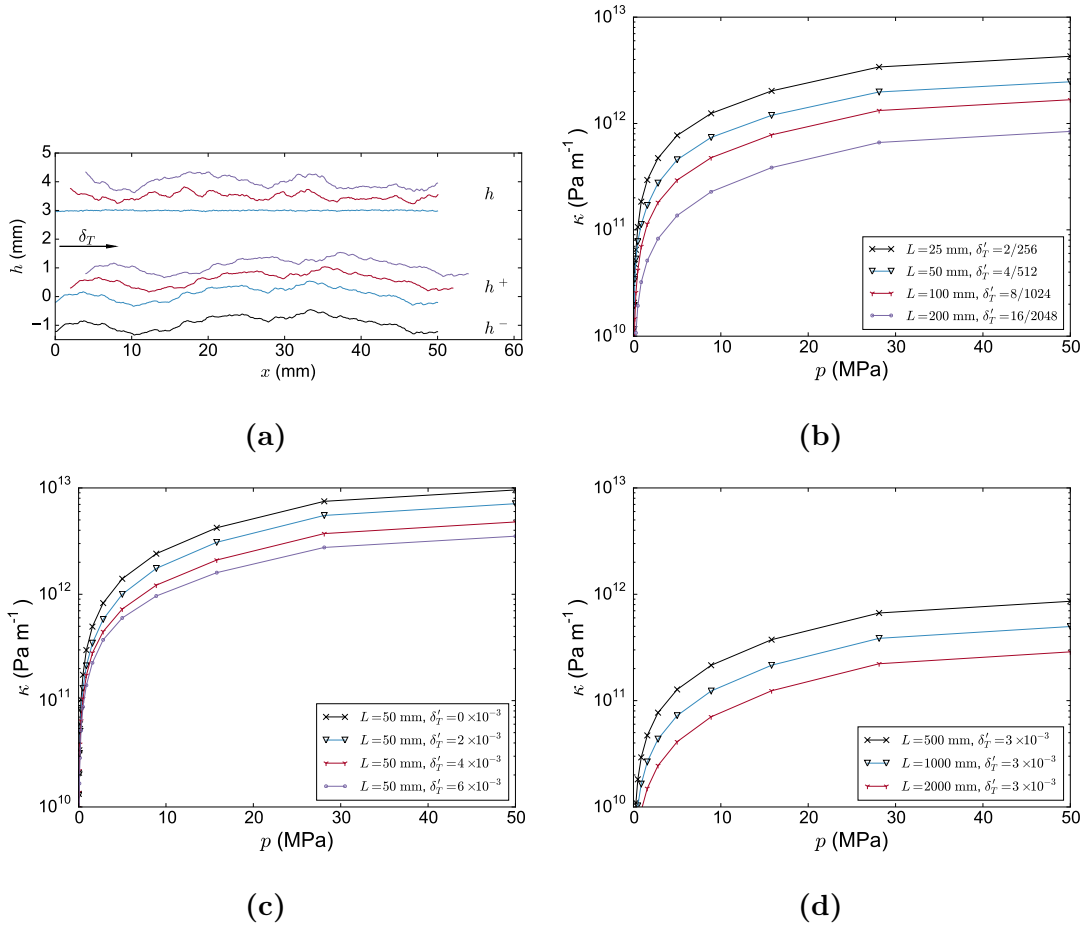


Figure 3.4: Stiffness as a function of size and shear displacement. (a) Concept of obtaining the initial aperture profile from two surfaces and shear displacement. (b) Specific stiffness for fractures of increasing size L and a constant relative offset δ'_{T}. (c) Specific stiffness for fractures of identical size and increasing relative offset. (d) Specific stiffness for meter-scale fractures and constant relative offset.

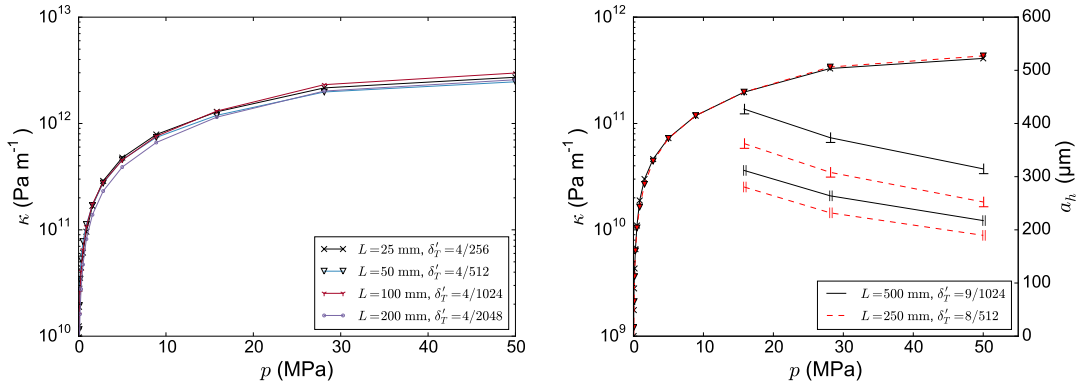
absolute value, in particular to answer questions along the lines of 'Can we distinguish large fractures with small displacements from small fractures with large displacements?'. A first set of models to study the effects of size and offset were created with a constant cell size $\ell = 25/256$ mm and increasing lengths $L = 25$, 50, 100, and 200 mm. It follows that the number of cells along one axis were $\mathcal{L} =$ 256, 512, 1024, and 2048, respectively. The relative shear displacement of the fracture remained invariant for $\delta'_{\mathrm{T}} = 2/256 = 4/512 = 8/1024 = 16/2048$, such that the absolute displacement increases linearly with fracture length as $\delta_{\mathrm{T}} = 50/256$, 100/256, 200/256, and 400/256 mm. Results clearly show a significant reduction of stiffness with fracture size for a constant normalised displacement (Figure 3.4a),

which is not necessarily an intuitive result. Interestingly, the specific stiffness in this case scales approximately linear with fracture size, *i.e.*, a doubling of fracture size and absolute shear displacement results roughly in a doubling of fracture compliance, or a reduction of stiffness by a factor of 1/2.

For fractures of constant length $L = 50$ mm, cell count $\mathcal{L} = 1024$, and increasing values of shear displacement $\delta_T = 0$, 0.1, 0.2, and 0.3 mm, κ decreases roughly proportional to $\delta'_T = 0$, 0.002, 0.004, and 0.006; see Figure 3.4c. As fractures increase in size above the metre-scale (Figure 3.4d), it is clear that stiffness doesn't converge for constant normalised displacement. It has been argued, however, that for a constant correlation length of the aperture field, an increase in fracture size above a certain length scale does not affect the obtained specific stiffness any more [Pastewka et al., 2013, Petrovitch et al., 2014]. Within the presented framework of aperture fields resulting from shear displacement, this translates to the existence of a mechanical REV for a fixed displacement.

3.3 Representative elementary volumes and non-uniqueness

For fracture models of increasing size $L = 25$, 50, 100, and 200 mm but identical absolute shear offset $\delta_T = 0.39$ mm, the size of a representative elementary volume has been obtained in a specific stiffness sense; see Figure 3.5a. A direct consequence of the existence of a mechanical REV for fractures with a fixed absolute shear displacement δ_T is that small fractures with a relatively large offset and large fractures with a relatively small offset cannot be distinguished. Specifically, two fracture models of $L = 250$ and 500 mm have been generated with constant cell size such that $\mathcal{L} = 512$ and 1024, respectively. A similar absolute offset $\delta_T \approx 4$ mm has been imposed on both models, and their specific stiffness is identical for all practical purposes; see Figure 3.5b.



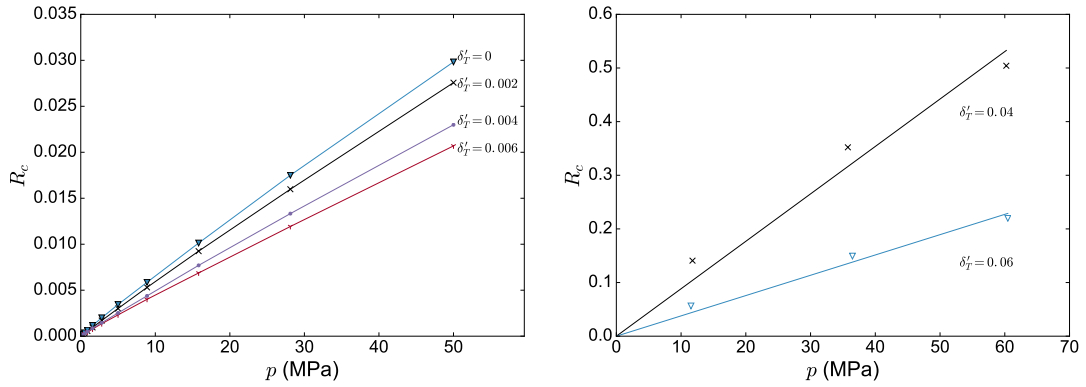
(a) **(b)**

Figure 3.5: Mechanical REV and non-uniqueness of transmissivity-stiffness. (a) Specific stiffness for fractures with increasing size L but identical absolute shear displacement δ_{T}. (b) Stiffness and hydraulic apertures, parallel $\parallel$ and perpendicular $\perp$ to shear direction, for surfaces of different size and identical absolute shear displacement.

The REV in a specific stiffness sense, however, does not translate to the transmissivity of a fracture. This primarily reflects that stiffness/compliance represents the change in fracture void space with respect to pressure, but not its absolute value. Relationships between stiffness and transmissivity, therefore, are based on scaling laws that account for the size of the fracture in some way [Petrovitch et al., 2014, Pyrak-Nolte and Nolte, 2016]. The established notion that stiffness alone cannot be used as a proxy for transmissivity is extended here by the observation that there exists no direct to the value of transmissivity anisotropy either (Figure 3.5b). This is a non-trivial finding, in that the ratio $a_{\mathrm{h},\perp}/a_{\mathrm{h},\parallel}$ also does not depend on the void area in an absolute sense, and that both stiffness and transmissivity anisotropy here depend on size and offset only.

3.4 Evolution of contact area with load

The evolution of contact area between rough surfaces under normal load is one of the more exhaustively studied problems in mechanics, and lies at the core of tribology and contact mechanics [Johnson, 1985]. Most engineering applications deal with uncorrelated surfaces in contact which are not the result of a common



(a) **(b)**

Figure 3.6: The dependence of contact ratio, R_c, on pressure, p, and shear displacement. (a) Numerical results for surfaces with $\mathcal{L} = 1024$ and $L = 50$ mm. (b) Experimental results up to 60 MPa derived from pressure sensitive film images for a 50×50 mm granite fracture [Nemoto et al., 2009].

fracturing process. As a consequence, the contact between partially correlated surfaces received relatively little attention [Borri-Brunetto et al., 1999], at least in the form of numerical studies and direct simulations. The most significant finding of the general rough surface contact problem is that the area of discrete contact depends only on the applied load, and is independent of the surface size [Greenwood and Williamson, 1966]. Furthermore, it has long been established that, in the elastic regime under low loads, the area of discrete contact increases linearly with load [Bush et al., 1975, Greenwood and Williamson, 1966, Persson, 2001]. It follows that the contact ratio increases linearly with the applied pressure; see also Figure 3.6a.

The slope of the contact ratio-pressure relationship has been found to depend on the Hurst exponent of the composite surface [e.g. Yastrebov et al., 2015]. Specifically, larger Hurst exponents lead to a smaller proportionality factor [Hyun et al., 2004]. As discussed above, the Hurst exponent of the composite surface between uncorrelated surfaces equals to those of the surfaces in contact, *i.e.*, $H \approx 0.8$ for most applications. For partially correlated surfaces, however, the scaling exponent is smaller for the largest fraction of the wave spectrum (Figures 2.3b and 2.4c). With increasing shear offset, the PSD frequency fraction of $H \approx 0.8$ increases

[Matsuki et al., 2006]. From the dependence of the contact ratio-pressure proportionality factor on Hurst exponent and the low-high exponent split that depends on shear offset, it follows that the slope of $R_c(p)$ decreases with increasing δ'_T; see Figure 3.6a. This reduction in contact area with increasing offset is in qualitative agreement with experimental observations (Figure 3.6b), and also with previous numerical simulations [Borri-Brunetto et al., 1999]. The absolute value of contact ratio depends on the lower cut-off of the scale of investigation, as discussed.

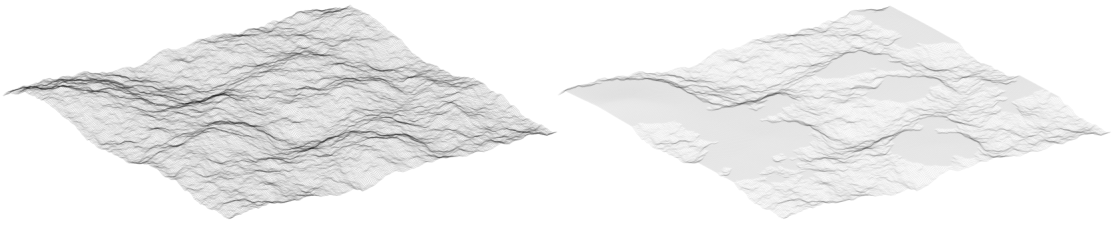
Chapter 4

Chemically-mediated compaction of a single fracture

The effects of pressure solution and precipitation are studied on generic fracture models of isotropic void space first. This allows for comparisons to analytic models and previous numerical approaches, which use surfaces based on isotropic parameters [Petrovitch et al., 2014, Pyrak-Nolte and Morris, 2000, Zimmerman et al., 1990]. Furthermore, the effects of numerical discretisation and the ensuing roughness wavelength cut-off are studied on such generic models. A reactive transport solution is coupled with the single-fracture THMC approach to model transmissivity changes observed in core flood experiments. Qualitative comparisons are made to the post-experiment contact area between the surfaces, and quantitative comparisons are made for the observed time dependent hydraulic aperture and effluent concentration. General effects of pressure solution on stiffness and transmissivity evolution are discussed for these isotropic, generic fracture models. The time-dependent relative magnitude of acting compaction processes are discussed, illustrating that elastic compression dominates in the short term, and pressure-solution driven convergence between the rock surfaces dominates in the long time. Finally, effects of dissolution and precipitation are studied specifically with respect to fractures with shear offset, focusing on the change in transmissivity anisotropy over time. For property values used for a siliciclastic sandstone the

Constant	Value	Unit
D	9.0 $\times 10^{-7}$ exp(-15000/RT)	m^2 s^{-1}
Ω_s	3.7 $\times 10^{-29}$	m^3
ρ_s	2650	kg m^{-3}
ρ_f	1000	kg m^{-3}
w	1.0 $\times 10^{-8}$	m
c_{eq}	0.055 E(0.254+1107.12/T)	-
k_d	2.27 E-(3.826+0.002028T+4158/T)	m s^{-1}
E	95.6 $\times 10^9$	Pa
ν	0.08	-

Table 4.1: Chemical properties used for THMC Water-Quartz system simulations. Note the use of the universal gas constant, R, and the ambient temperature, T.



(a) **(b)**

Figure 4.1: Illustration of dissolution-precipitation effects on a fracture surface; $L = 1$ cm, $\mathcal{L} = 256$, $H = 0.8$, $h_{rms} = 8$ μm, and $\lambda_L/\lambda_0 = 1$. (a) Initial surface. (b) After 100 years under 10 MPa and 423 K under 'closed' conditions.

reader is referred to Table 4.1. These properties will be used for all but the granite simulations, for which mineral specific dissolution rates will be presented below.

4.1 Evolution of pore-space due to dissolution and precipitation

Changes in rock surface morphology due to pressure solution and precipitation are illustrated in Figure 4.1. After the fracturing process and subsequent shear displacement, opposing surfaces are mismatched, and touch at a minuscule fraction of their nominal area, resulting in large stress concentrations at the contacts (Figure 4.2a). Early-time effects of chemical alteration are studied on a 1×1 cm fracture

model (Figure 4.2) under an effective confining pressure of $p = 10$ MPa and a temperature of $T = 423$ K under 'open' conditions, *i.e.*, without re-precipitation of dissolved mass. In an attempt to reach a more equilibrated state, pressure solution acts to smooth the elevated, contacting fractions of the surface (Figure 4.1b). As a consequence, the initial distribution of surface height is truncated, and small-scale roughness features in contact zones are dissolved to yield more rounded structures. Most notably, this results in (1) a more uniform distribution of contact pressure, (2) less pronounced stress concentrations, (3) an increase in contact area, and (4) newly formed contact regions as a result of the convergence, or approach, of the two surfaces; see Figures 4.3c and 4.3d.

The generic composite surface to illustrate early-time effects (Figure 4.2) has been generated using a composite surface with a Hurst exponent of $H = 0.8$, a root-mean-square roughness of $h_{\mathrm{rms}} = 8.0$ μm, and a uniform square grid of $\mathcal{L} = 256$. Upon initial contact, an average mechanical aperture of $\langle a_{\mathrm{m}} \rangle = 11.3$ μm is obtained. In contrast, the initial aperture of the rigid model is a significantly larger 21.1 μm. The aperture-averaged flow solution yields an hydraulic aperture of $a_{\mathrm{h}} = 8.6$ μm. Using the non-linear LL model (Equation 2.10), pressure solution is modelled assuming that the diffusivity in the confined intergranular layer is reduced by one order of magnitude [Revil, 2001] with respect to the free fluid, i.e., $f = 0.1$. After a simulated time of ten years, elevated regions have been dissolved (Figure 4.2b), and the contact area increased by a factor of more than four. This leads to increased flow channelling by closure of narrow, low aperture junctions in the vicinity of contact regions; see Figures 4.2a and 4.2b for the initial and late flow fields, respectively. The contact zone growth is accompanied by a truncation of the surface height distribution and reduced contact stress concentration. The combined effect of contact stress and contact zone geometry on the dissolved silica concentration is illustrated in Figures 4.2c and 4.2d. Small contact zones, albeit subjected to large contact stress, show lower concentration build-ups than their larger peers. This is a direct result of the smaller diffusion distance and faster dissipation of dissolved mass towards the free pore-space.

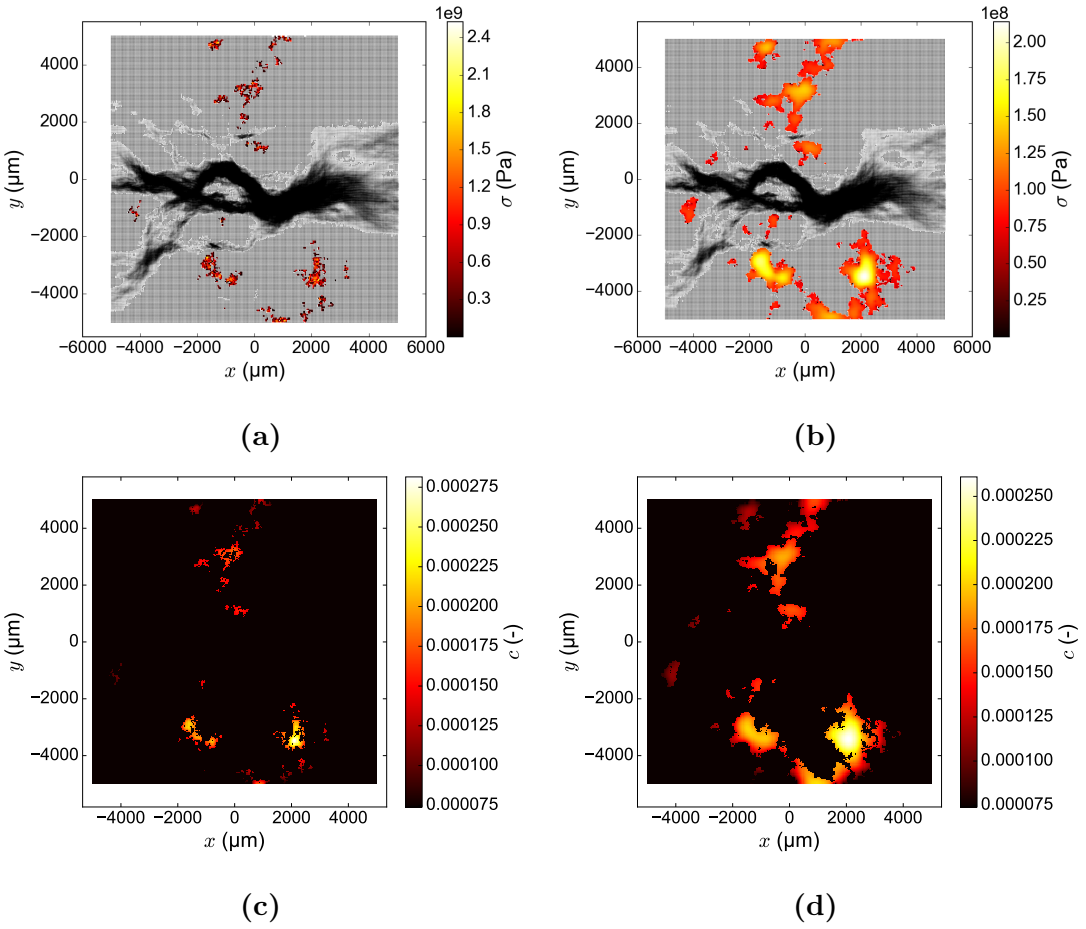


Figure 4.2: Early time effects of pressure solution in an 'open' fracture; $L = 1$ cm, $\mathcal{L} = 256$, $H = 0.8$, $h_{\text{rms}} = 8.0$ μm and $\lambda_L/\lambda_0 = 1$. (a) Initial hydro-mechanical state. (b) Hydro-mechanical state after ten years. (c) Initial intergranular concentration. (d) Intergranular concentration after ten years.

A qualitative comparison of 'open' and 'closed' systems is presented in Figure 4.3d for an isotropic fracture of $L = 0.5 \times 0.5$ m, generated using a strictly periodic structure [Peitgen et al., 1988], as opposed to periodic boundary conditions (*e.g.* Figure 4.2). In 'closed' systems, precipitation facilitates the growth of existing contact regions without significant convergence of the surfaces (Figure 4.3d). Large aperture channels are thus preserved, while they tend to close for 'open' systems where no precipitation takes place (Figures 4.3c and 4.3d). It follows that the loss of pore-volume occurs faster in 'open' systems than in 'closed' systems (Figure 4.4a). At the same time, the contacting fraction of the surface is made up of a larger number of contact spots for the 'open' no-precipitation system, and of

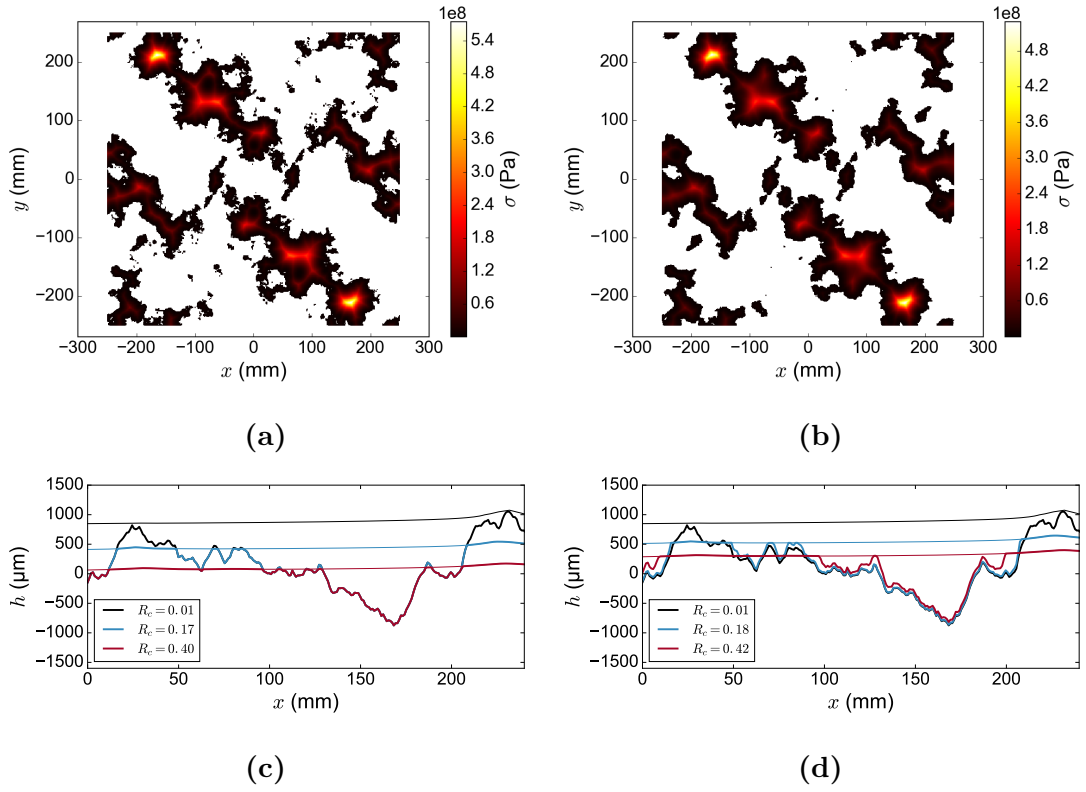
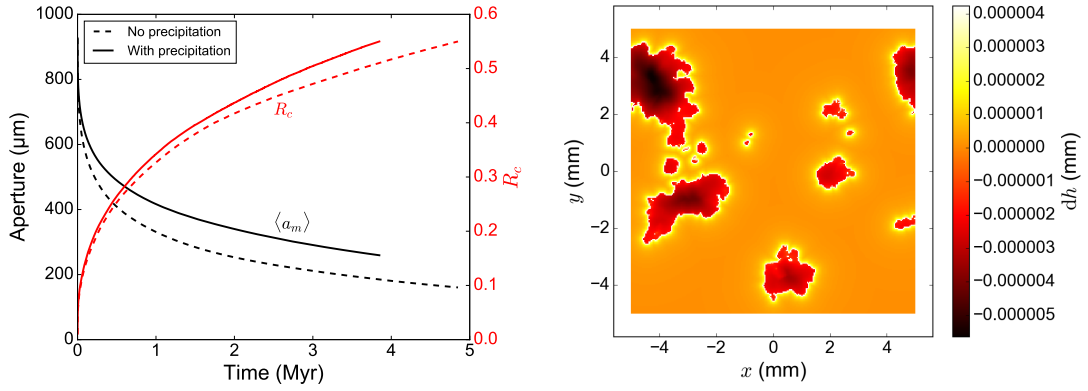


Figure 4.3: Qualitative evolution of hydro-mechanical state for closed and open fractures; $L = 0.5$ m, $\mathcal{L} = 512$, $h_{\text{rms}} = 500$ μm, and $\lambda_L/\lambda_0 = 4$ under 10 MPa and 423 K. (a) Contact stress σ in 'open' fracture system at $R_c = 0.4$. (b) Contact stress σ in 'closed' fracture system at $R_c = 0.42$. (c) Partial traces over time and increasing contact ratio, R_c, for the 'open' system. (d) Partial traces over time and increasing contact ratio, R_c, for the 'closed' system.

larger individual, but fewer in number contact spots for 'closed' systems with precipitation (Figures 4.3a and 4.3b). The driving force of pressure solution-driven compaction is the contact stress, which, to first order, is a function of the contact ratio, and to second order is a function of the size and roughness or curvature over the discrete contacts. It follows that the increase in contact ratio evolves in a similar manner for both systems, with precipitation acting to accelerate its increase (Figures 4.4a).

The distribution of elevation change, $\mathrm{d}h/\mathrm{d}t$, over the fracture surface (Figure 4.4b) emerges from the combined effects of diffusion distance and contact stress. Precipitation occurs preferably at the perimeter of contacts, which reflects the diffusion equation approximation. Dissolution within the contact interface is non-uniform,



(a) **(b)**

Figure 4.4: Qualitative and quantitative illustration of 'closed' and 'open' systems under 10 MPa and 423 K. (a) Decrease of pore space, $\langle a_{\mathrm{m}} \rangle$ and increase of contact ration, R_{c} over time; $L = 0.5$ m, $\mathcal{L} = 512$, $h_{\mathrm{rms}} = 500$ µm, $\lambda_L/\lambda_0 = 4$. (b) Surface height change, dh, due to dissolution and precipitation over one month; $L = 1$ cm, $\mathcal{L} = 256$, $H = 0.8$, $h_{\mathrm{rms}} = 8$ µm, and $\lambda_L/\lambda_0 = 1$.

as it depends on both the local stress and the diffusion of mass towards the free pore-space. This in turn depends on the current surface morphology, *i.e.*, the local roughness of contacts, and the confining pressure.

4.2 Pressure solution formulations

The explicitly coupled transient solution of two non-linear problems, the elastic contact and the diffusion-reaction process, poses a computational challenge that in the current state of implementation restricts predictions to the short term, *i.e.*, simulated times of less than ten years for models of $O(10^5)$ grid cells. For the purpose of long-term predictions exceeding simulated times of one thousand years, the linearised LL model is used; see Equation 2.16 see Figure 2.10. A comparison over an initial ten years to the BE model is presented in Figure 4.5, for 50 realisations of statistically identical surfaces. Average parameters such as contact ratio and mechanical aperture show good agreement over the time of comparison between the two dissolution models. The effects of relatively large differences in maximum height between statistically identical surfaces are mitigated to some extent as a

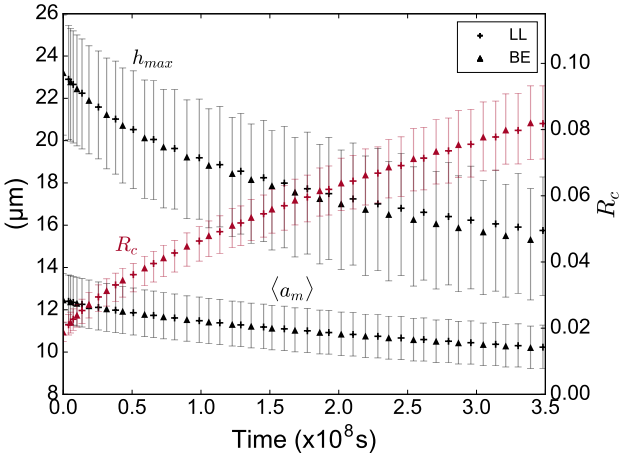
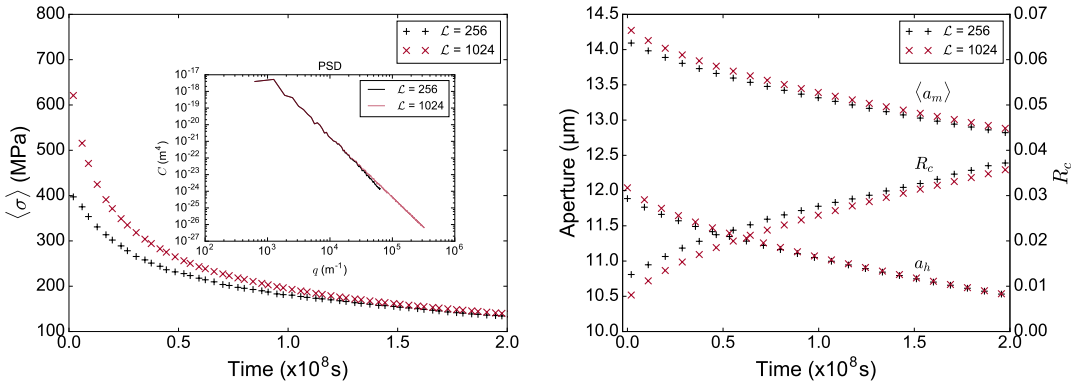


Figure 4.5: Comparison between dissolution results obtained using the Lehner-Leroy (LL) and Bernabé-Evans (BE) formulation. Indicated with error bars are the average, minimum and maximum values for 50 models with statistically identical parameters; $L = 1$ cm, $\mathcal{L} = 256$, $H = 0.8$, $h_{\text{rms}} = 8$ μm, and $\lambda_L/\lambda_0 = 1$.

result of the elastic compression. With larger stresses and temperatures, similar disagreements in the evolution of the maximum surface height as obtained for the single grain case (Figure 2.9d) are found. It follows that the LL model tends to slightly underestimate dissolution rates and, as a consequence, contact ratio and porosity reduction in the long term, with respect to the BE model.

4.3 Effects of roughness cut-off

As discussed, the contact stress field and contact area depend intrinsically on the cell size of the underlying grid. For early-time contact, surfaces of high resolution yield high contact stresses and small contact areas, a state that leads to high initial dissolution rates when compared to surfaces discretised using a lower resolution. The tendency of pressure solution to equilibrate contact stress distributions acts to mitigate this discrepancy in the long term. Figure 4.6a illustrates that the decline of the mean contact stress and the hydraulic aperture converge early for a surface discretised to different cut-off wavelengths, so that $\mathcal{L} = 1024$ and 256. The roughness power spectra for both surfaces are shown in Figure 4.6a, and



(a) **(b)**

Figure 4.6: Effects of roughness cut-off on dissolution results; $L = 1$ cm, $H = 0.8$, $h_{\mathrm{rms}} = 8$ μm, and $\lambda_L/\lambda_0 = 1$ under 10 MPa and 423 K. (a) Mean contact stress with inset showing the PSDs of the two surfaces. (b) Evolution of average mechanical aperture, $\langle a_{\mathrm{m}} \rangle$, hydraulic aperture, a_{h} and contact ratio, R_{c}.

illustrate the larger range of represented roughness frequencies in the $\mathcal{L} = 1024$ surface. The smaller roughness features lead to a reduced contact area (Figure 4.6b), higher contact stresses (Figure 4.6a) and slightly larger apertures (Figure 4.6b) at the beginning of the simulation. The higher contact stress leads to faster dissolution rates initially. However, the relationship between contact stress and dissolution rates results in the fast equilibration of averaged parameters between the two surfaces. It can be concluded that, while there is no grid-convergence of the elastic contact solution, compaction rates and the hydraulic response to the combined process of contact and pressure solution is less sensitive to cell size and converges in the early- to medium-time for the chosen spatial discretisation. The convergence rate of a fracture therefore depends initially on small roughness wavelengths, but in the long term is a function primarily of large wavelengths. As a consequence, the largest wavelengths that form the aperture profile must be represented in order to correctly model long-term behaviour. This leads to a convergence of long term predictions with decreasing cut-off. Combined with the established notion that that results of normal contact and laminar flow converge with decreasing cut-off, this permits prediction of long-term evolution using the direct approach presented here.

4.4 Changes in transmissivity

The hydraulic response to dissolution-precipitation driven compaction and contact zone growth shows that the flow field retreats to channels of large initial apertures (Figure 4.7). Considering a constant macroscopic flow rate, the effect on transport is one of increased flow velocity and tortuosity, along with the creation of stagnant dead-end zones that reduce the fraction of effective void space. The effect on the fracture surface resembles that of a polishing mechanism, or plastic damage acting preferentially on the uppermost asperities; see Figure 4.1b and Brown and Scholz [1986] (Figure 9 therein) and Persson [2014] (Figure 7 therein). For a Hurst exponent of $H = 0.8$, two composite surface configurations of $h_{\mathrm{rms}} = 8$ and 16 μm of 1×1 cm are studied using a resolution of $\mathcal{L} = 256$. Prediction runs proceed under conditions of $p = 5$ and 10 MPa and $T = 423$ and 473 K [Yasuhara and Elsworth, 2004, Zhao et al., 2014] until the fracture model acts hydraulically sealing. Specifically, the termination criterion chosen here is $a_{\mathrm{h}} < 0.1$ μm.

A characteristic evolution of average parameters of a single fracture from the onset of pressure solution to the loss in hydraulic conductivity is shown in Figure 4.8a. It can be seen that the inequality $\langle a \rangle > \langle a_{\mathrm{m}} \rangle > a_{\mathrm{h}}$ holds over the entire duration of the experiment. More importantly, the ratio between the different apertures is not constant, but reflects the effects of contact zone growth and surface convergence on both the hydraulic and mechanical state of the fracture. Upon initial contact, the contact ratio is small, and the elastic energy acting on the fracture is mainly accommodated by deflection of the free rock walls (Figure 4.3c) and high contact stresses at small contact zones. With dissolution and the accompanying increase of contact area, the compression of the pore space by this deflection is reduced, mainly as the result of shortened free pore walls; see Figure 4.3c.

A step-wise illustration of the degradation of hydraulic conductivity up to a state of hydraulic sealing is presented in Figure 4.7, in form of the evolving flow vector and contact stress fields. Aforementioned short-term characteristics of contact zone growth continue to further cut off some flow channels, forcing the fluid flow to retreat increasingly. High velocity junctions form where the remaining

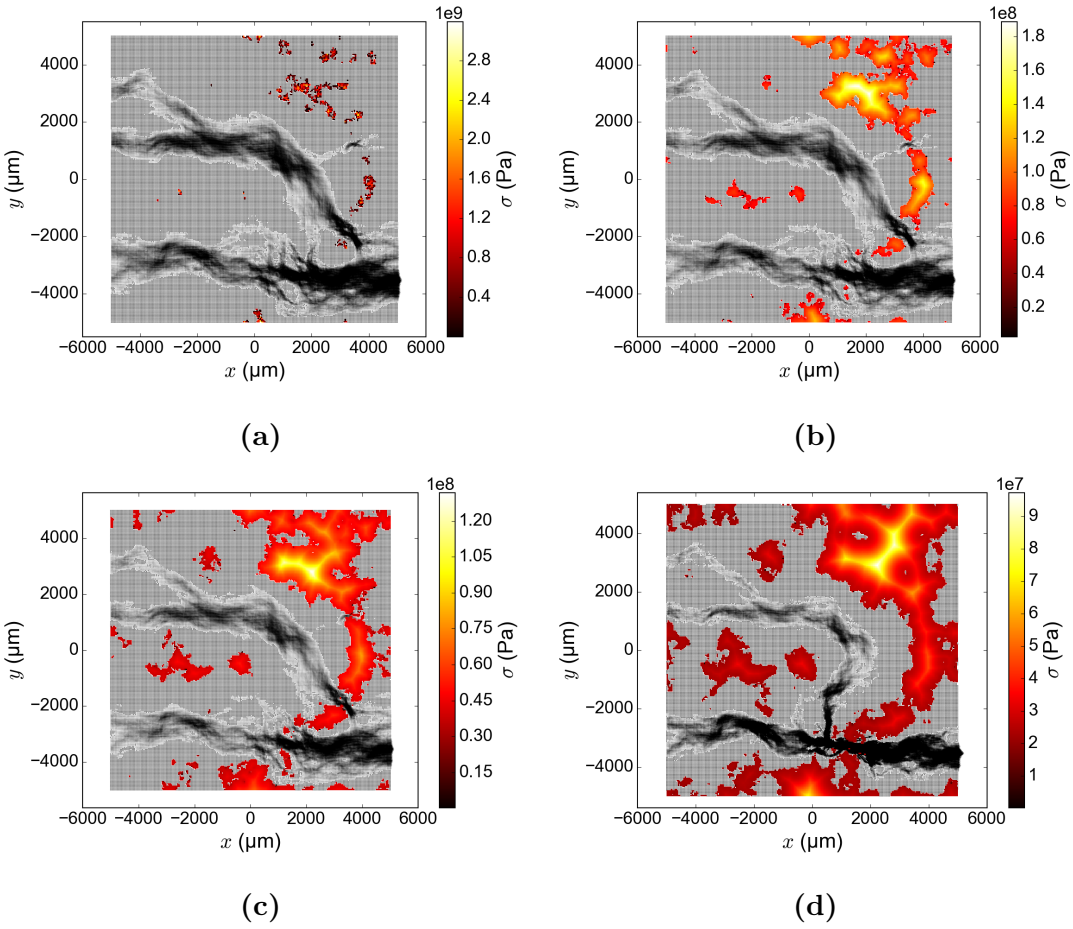


Figure 4.7: Long-time evolution of hydro-mechanical state of a fracture due to pressure solution in an 'open' system; $L = 1$ cm, $H = 0.8$, $h_{\mathrm{rms}} = 8$ µm, $\mathcal{L} = 256$, and $\lambda_L/\lambda_0 = 1$ under 10 MPa and 423 K. (a) Initial. (b) After 19 years. (c) After 48 years. (d) After 100 years.

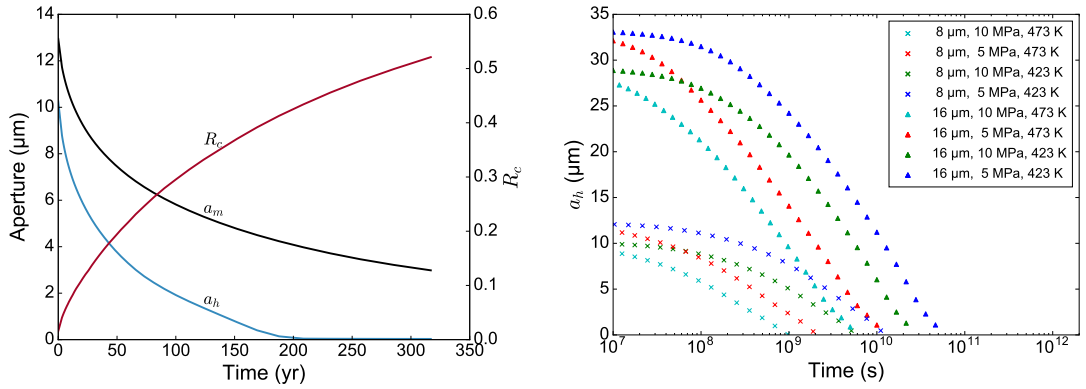
channels penetrate merging contact zones, and stagnant dead-end zones form in flow-direction perpendicular obstacles. A rising discrepancy between average mechanical and hydraulic aperture follows as a consequence. In the long-term limit, contact zones start to percolate and act to seal the pore space from flow. This onset of percolation is marked by a characteristic contact ratio approaching one half; see Figure 4.8a.

For quantitative predictions, and to reduce finite-size effects, two statistically equivalent surface realisations have been generated for each roughness amplitude, $h_{\mathrm{rms}} = 16$ and 8 µm. Quantitative results for the contact ratio and apertures (Figure 4.8b) are averaged values between simulation results for these realisations. The hydraulic aperture decays exponentially with time, and temperature is the

primary control of compaction rates; see Figure 4.8b. An increase from 423 to 472 K under constant confining pressure accelerates compaction rates significantly more than does a doubling of the confining pressure under constant temperature. The loss of hydraulic conductivity occurs as early as twenty-nine years after the onset of dissolution for $h_{\mathrm{rms}} = 8$ µm, $p = 10$ MPa and $T = 473$ K. The longest time required for a model to seal was 1455 years for a large aperture fracture at low temperature and low confining pressure, e.g., $h_{\mathrm{rms}} = 16$ µm, $p = 5$ MPa and $T = 423$ K. Contact ratios at the onset of contact zone percolation vary between 0.42 and 0.52 [Lang et al., 2015].

One of the characteristic features of rock fractures is the existence of a residual transmissivity, even at very large confining pressures [Brown and Scholz, 1985a]. This reflects an exponentially increasing repulsive force exerted by elastically deformed surface summits with continued penetration. Pressure solution acts to deteriorate such a residual transmissivity by irreversible surface alteration, dissolving uppermost asperities. This allows for a transient approach of opposing rock walls, an increase in contact ratio while the fluid pressure and compressive normal stress remain invariable. Eventually, this polishing-like mechanism will lead to hydraulic sealing if the rate of pressure solution compaction outweighs any possible dissolution processes acting on the free rock walls. Such sealing behaviour has been observed for granite fractures, where precipitation of dissolved minerals away from contacting asperities accelerated the process [Moore et al., 1994]. The effect of precipitation on the sealing rate will strongly depend on the advection-diffusion balance in the open pore space. For stagnant fluids, precipitation will occur in the contact zone periphery, leading to accelerated growth of the contact zones, and in turn the reduced contact stresses. A critical stress at which pressure solution ceases could prevent a sealing state [Taron and Elsworth, 2010, Yasuhara and Elsworth, 2004]; its existence, however, is a subject of debate [e.g. Neretnieks, 2014].

Similar to studies on the leakage behaviour of rough elastic bodies [Dapp et al., 2012, Persson and Yang, 2008], the onset of contact zone percolation was found as



(a) **(b)**

Figure 4.8: Evolution of hydraulic parameters over time due to pressure dissolution under 'open' conditions. (a) For a single model; $L = 1$ cm, $H = 0.8$, $h_{\mathrm{rms}} = 8$ μm, $\mathcal{L} = 256$, and $\lambda_L/\lambda_0 = 1$. (b) For multiple models of varying roughness and ambient conditions. Presented is the hydraulic aperture averaged over two statistically identical realisations each; the constants are $L = 1$ cm, $H = 0.8$, $\mathcal{L} = 256$, and $\lambda_L/\lambda_0 = 1$.

early as $R_{\mathrm{c}} \geq 0.42$, below the 0.5 theoretical prediction from percolation and effective medium theory [Bruggeman, 1935, Kirkpatrick, 1973]. An important question with regard to the applicability of continuum models is whether changes in the average mechanical aperture cause proportional changes in the equivalent hydraulic aperture. The effect of localised growth of contact zones is of particular interest, as their shape has been shown to be a controlling factor of fracture permeability [Zimmerman et al., 1992] and the effective fracture void space [Zimmerman and Yeo, 2000]. It has been shown that, as a consequence, long-term changes in transmissivity of a fracture cannot be conveniently expressed by averages of the rigid or elastic aperture. This indicates that the assumption in continuum models [Yasuhara and Elsworth, 2004] of a constant proportionality between mean and hydraulic aperture is not generally applicable, but may only be valid in certain cases of well correlated fractures or low confining pressures.

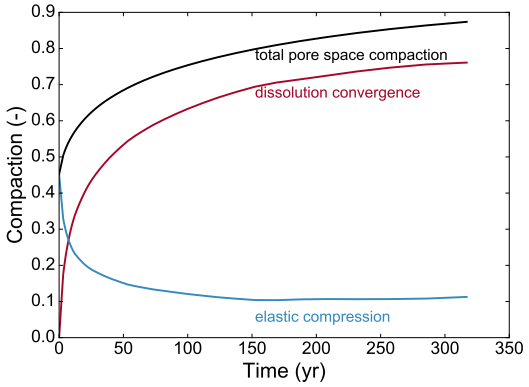


Figure 4.9: Relative dominance of compaction mechanisms over time; L = 1 cm, H = 0.8, h_{rms} = 8 μm, $\mathcal{L}$ = 256, and λ_L/λ_0 = 1 under 10 MPa and 423 K.

4.5 Compaction mechanisms over time

Results demonstrate that the overall compaction of the pore space is a result of two coupled processes: (1) the confining pressure results in contact stress at uppermost asperities and deflection of the free rock walls; and (2) pressure solution acts to create additional surface area and to equilibrate the contact stress distribution through a polishing-like effect, thus reducing elastic deformation. The relative dominance of these two compaction mechanisms varies over time as a function of the emerging pore space geometry; see Figure 4.9. The difference in total pore space compaction between the onset of the experiment and the final state of about 35% reflects the decrease in average mechanical aperture from 12.9 to 4.2 μm. The total irreversible compaction caused by dissolution convergence at the end of the experiment is 70%, and accounts for the decrease in average aperture of the unstressed pore space from 23.6 to 6.8 μm. Elastic compression is computed as the difference in pore volume between the current unstressed and stressed model, expressed in terms of fraction of the initial unstressed pore space. The compaction resulting from the convergence of opposing fracture walls caused by dissolution is computed as the relative difference in the unstressed initial pore volume and the unstressed pore volume at any given time after the dissolution process has started. The dominant compaction mechanism thus transitions from reversible elastic to irreversible structural at early times; see Figure 4.9.

4.6 Core flood experiments

The isotropic composite surface representing the experimental fracture is generated with a Hurst exponent of 0.3, reflecting the strong matedness of the fracture created in the reassembly of the cores after fracturing. This choice of the Hurst exponent is supported by qualitative agreement in contact area distribution between the simulation and a Wood's metal cast obtained from the Novaculite experiment, which is discussed below. The REV hydro-mechanical-chemical fracture surface model is created with an edge length equal to the inlet width of the fracture. It follows that the mechanical-chemical mechanism of pressure solution and the chemical mechanism of free-face dissolution are modelled using a 5×5 cm [Yasuhara et al., 2006] or 3×3 cm [Yasuhara et al., 2011] rough composite surface. Both surfaces have been discretised to $\mathcal{L} = 256$ cells and thus have slightly different cell sizes ℓ. This discrepancy should only affect early-time results, as discussed above. In terms of contact and mineral composition, this model is considered to be a representative elementary volume. The mechanical properties for Mizunami granite were assumed to be a Young's modulus of 60 GPa and a Poisson's ratio of 0.15; for the Novaculite these values were 95 GPa and 0.1. The contact pressure solution for the native fracture model is the starting point of the transient algorithm, and the mean-square surface roughness of the surfaces has been chosen to reproduce the initial hydraulic aperture to within 1 μm. The boundary and ambient conditions used for the numerical simulations of the physical experiments are summarised in Table 4.2.

4.6.1 Novaculite results

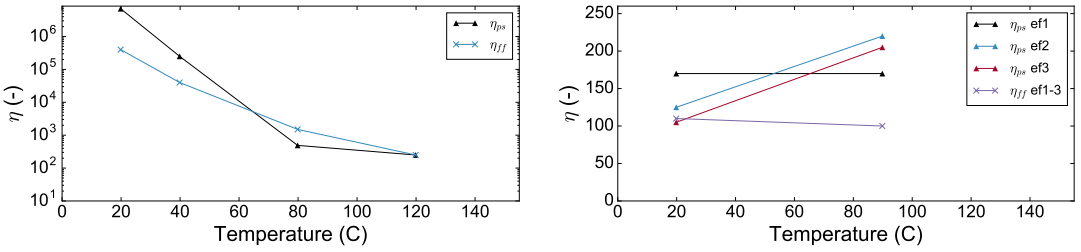
The fractured core flood experiment, here referred to as `nf2`, of an Arkansas Novaculite [Yasuhara et al., 2006] sample was conducted at a relatively low effective confining pressure of around 1.4 MPa, and at temperatures ranging from 20 to 120°C; see Figure 1.4b. The formulation of the average composition (AC) model has been used, with Quartz as the sole mineral of a volume fraction equal to unity,

Experiment	Time (s)	T (K)	Time (s)	Δp_f (Pa)	Time (s)	Q ($\mathrm{m^3\ s^{-1}}$)	Time (s)	p (MPa)
`nf2`	0	293.15	NA	NA	0	1.67E-8	0	1.38
	6728400	313.15			435600	8.33E-9		
	8118000	353.15			1368000	4.17E-9		
	10350000	393.15			3088800	0		
					3348000	4.17-9		
					4557600	2.08E-9		
					5378400	1.04E-9		
					10350000	2.08E-9		
`ef1`	0	293.15	0	500000	NA	NA	0	10
	756000	363.15						
`ef2`	0	298.15	0	100000	NA	NA	0	4.9
	1368000	363.15	666000	40000			666000	5
			1652400	100000			1652400	4.9
`ef3`	0	298.15	0	40000	NA	NA	0	5
	1368000	363.15	1919000	100000			1919000	4.9

Table 4.2: Input conditions for numerical core flood experiments. The Yasuhara et al. [2006] Novaculite experiment is denoted `nf2`, and `ef1-ef3` denote the Yasuhara et al. [2011] granite experiments. Experiments are either pressure controlled, in which case a prescribed pressure differential, Δp_f, is used for pressure-pressure boundary conditions, or flow rate, Q, controlled, in which case the boundary conditions are flow rate-pressure.

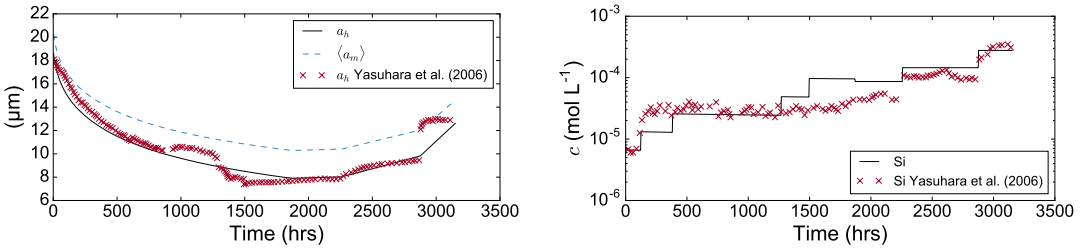
i.e., $\chi_{min} = 1$ for all cells. The chosen calibration factors are a monotonically decreasing function of temperature between $O(10^6)$ and $O(10^2)$, and a crossover point around 65°C marks a transition from pressure solution enhancement to free-face dissolution enhancement that is necessary to reproduce experimental observations, see Figure 4.10a. Under the assumption that the dominant processes are captured by the model, the obtained match of transmissivity (Figure 4.11a) and effluent concentration (Figure 4.11b) over time can be expected to be unique for the two variables of pressure and free-face calibration factors (Figure 4.10a). This uniqueness is only possible because of the direct coupling between surface alteration and reactive transport in the model.

It should be pointed out that there is no artificially induced cessation [McDermott et al., 2015] in the process of pressure solution around 1900 h, when the loss in transmissivity transitions to a gain in transmissivity (Figure 4.11a). Rather, the increased contact area leads to a reduced driving force for dissolution at contacting asperities. Combined with the temperature increase and the chosen calibration, free-face dissolution begins to overshadow compaction at the contacts. Use of the average mechanical aperture as a proxy for the equivalent hydraulic aperture



(a) **(b)**

Figure 4.10: Core flood modelling calibration factors for free-face, η_{ff}, and pressure solution, η_{ps}. (a) Novaculite experiment `nf2` [Yasuhara et al., 2006]. (b) Granite experiments `ef1-3` [Yasuhara et al., 2011].



(a) **(b)**

Figure 4.11: Comparison between numerical and experimental results for the `nf2` experiment [Yasuhara et al., 2006]. (a) Hydraulic aperture, a_{h}, along with the average mechanical aperture, $\langle a_{\text{m}} \rangle$. (b) Effluent Si concentration, c.

[Yasuhara et al., 2006] would overestimate the aperture over the entire range of the experiment, and up to 10% when a high contact ratio is reached (Figure 4.11a).

The simulated effluent concentration underestimates the experimental observations during the early stages of the experiment, and overestimates towards the late times, but reproduces the overall trend qualitatively; see Figure 4.11b. It should be noted that during the experiment, no sensitivity to flow rates is apparent (Figure 4.11b, 1200 to 1900 h). Considering the fact that concentrations remain below equilibrium concentration, this contradicts simple batch reactor principles, and should be investigated further. The evolution of contact ratio and contact stress arises directly from the presented model, and need not be constrained by constitutive relationships. This allows for the modelling of arbitrary fracture configurations, and increases the predictive capability of the approach. For the Novaculite model, the temperature increase from 20 to 40 °C that occurs at around 1900 h

marks a transition from pressure solution dominated compaction to free-face dissolution dominated, mostly resulting from the cross-over in the calibration factors (Figure 4.10a) required to model the observed increase in transmissivity.

The resulting shift from compaction to opening aperture change mechanism is further illustrated by the average change in surface height; see Figure 4.12. The aperture change over the free surface is a function of temperature. Over the contacting fraction of the surface, a strong dependency on the contact ratio is apparent, so that with an increase of contact ratio the magnitude of dissolution decreases up to $\approx$ 1900 h. With the contact ratio remaining relatively constant after $\approx$ 1900 h, the dissolution over the contacting fraction becomes a function solely of the temperature, because the driving contact stress remains constant. The competing processes of pressure solution and free-face dissolution for the Novaculite model are illustrated by means of a cross-section over time in Figure 4.12. In particular, it can be seen that small channels within early-time contact zones eventually close, while other channels expand. Whether or not channels close depends on their location and initial size. Small channels near the peaks of the surface close due to the fast initial compaction. Large channels, and small channels near the valleys of the surface, grow because they remain open until free-face dissolution becomes the dominant process. This leads to a complex evolution of the fracture transmissivity.

A qualitative comparison between the contact area distributions (Figure 4.13) shows good agreement for the size of individual clusters and their isotropic nature. The former justifies the choice of the composite surface Hurst exponent of 0.3, and the latter follows from the mated nature of the fracture with minimal shear displacement. Quantitatively, excellent agreement is achieved between the numerical value of 13.9% and the Wood's metal cast interpretation of 14.1% [Yasuhara et al., 2006]. It should be emphasised that the obtained contact area is a result of the chosen Hurst exponent and the calibration factors used to reproduce the hydraulic aperture and effluent concentration. Thus, it is an independent result that lends support to the validity of the approach. Since the discretisation-induced roughness cut-off affects primarily the early-time magnitude of the contact area,

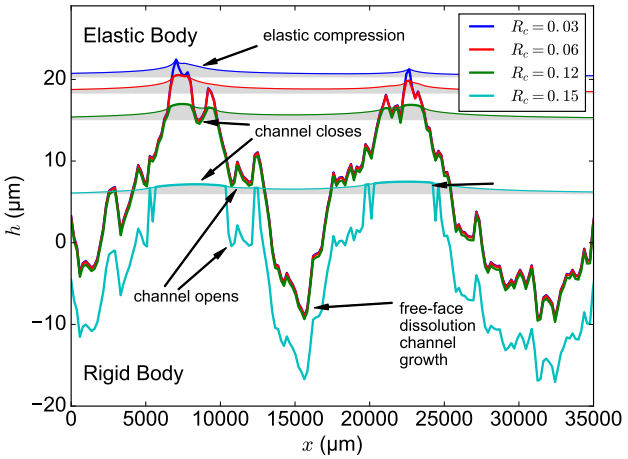
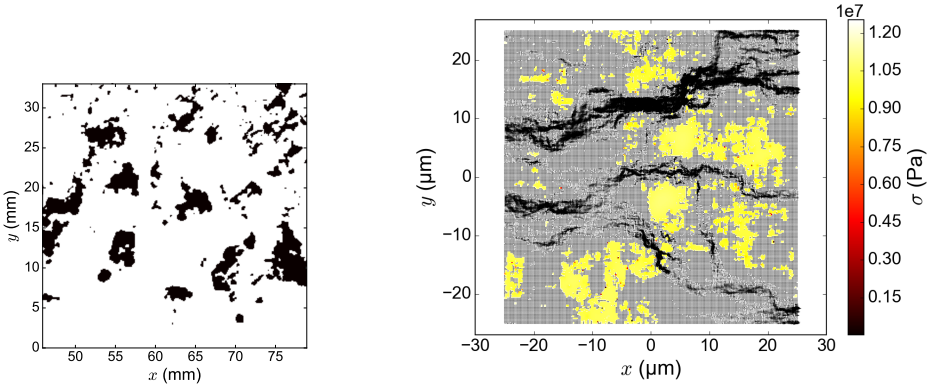


Figure 4.12: Tracemap illustrating opening-closing history of the numerical model for the `nf2` [Yasuhara et al., 2006] experiment. Note the difference in ordinate and abscissa scale.



(a) **(b)**

Figure 4.13: Comparison of numerical and experimental discrete contact areas at the end of the `nf2` experiment. (a) Woods-metal cast scan of half the fracture [Yasuhara et al., 2006]. (b) Final hydro-mechanical state of the numerical model.

the final contact area distribution at late-time is not sensitive to this property of the generated surfaces. Thus, a late time comparison between absolute values of contact area between experimental observations and numerical results is feasible.

4.6.2 Granite results

Three granite experiments have been conducted at higher confining pressures of 5 MPa (`ef1`) and 10 MPa (`ef2, ef3`); see Figure 1.4b. For the average composition (AC) model, matching factors in terms of dissolution rate multipliers, η_{ps} (-), are found in magnitude around $O(10^2)$; see Figure 4.10b. As a comparison, the matching factors used in the Novaculite modelling were up to $O(10^6)$. Identical multipliers for free-face dissolution, η_{ff} (-), are used for all three experiments, while the obtained pressure-solution multipliers differ between the 10 MPa (`ef1`) and 5 MPa (`ef2, ef3`) confining pressure experiments. This may hint towards a non-linear overall dependence of compaction on pressure, and highlights the importance of modelling all three experiments.

A comparison between experimental and numerical results for the AC model is presented in Figure 4.14. For experiment `ef3`, an early time rapid decrease in aperture is observed. For this case, a surface was created to reproduce the hydraulic aperture after this drop. Early time differences in the match are considered to be less significant, because these depend on small wavelength contact components that may differ considerably between samples. Dissolution of contacting asperities that provide critical structural support could lead to micron range rearrangements of the alignment of the two surfaces, which may explain these jumps. If experiments behave significantly differently, it can be expected to happen in the early stages and to reflect different small scale surface/contact characteristics.

The other notable difference is the aperture increase at the point of increased differential pressure. This increase is not reproducible by the elastic contact model, and is probably due to effects that are not purely hydro-mechanical. The elastic compression at this point in time is much reduced and less sensitive to small changes in confining pressure. It is suggested that other effects such as removal of clogging precipitated minerals [Yasuhara et al., 2011] are responsible for this aperture jump, and not the relatively small decrease in effective pressure of 0.1 MPa. The present model also illustrates that the average dissolution over contact zones approaches the average dissolution at the free-face with increasing contact

ratio and decreasing contact stress. A critical stress at which pressure solution ceases is not assumed here [Neretnieks, 2014], and in contrast to the Novaculite experiment, the obtained set of calibration factors suggests that pressure solution, or a similar stress-dependent compaction mechanism, remains equally active over the duration of the experiment.

The effluent concentration over time is reproduced quantitatively to within an order-of-magnitude, and jump discontinuities in the temperature and flow rate changes are matched qualitatively. As for the Novaculite experiment, the decrease in hydraulic aperture and the amount of dissolved mass in the effluent concentration match the experimental values well, which suggests that matrix diffusion has a negligible influence. Thus, both effluent concentration and loss in hydraulic transmissivity can be explained by surface dissolution processes. The exact nature of these processes and governing equations is less clear, as evident by different parameterisations across all experiments (sandstone `nf2`, and granite `ef1-3`). An important point with respect to the initial contact ratio has to be made here, in particular when empirical relationships are used to determine the evolution of contact area [McDermott et al., 2015, Yasuhara et al., 2006]. In the low load regime, i.e., loads that result in an initial contact ratio of up to about 15%, contact theory and numerical results show a linear relationship between applied load and contact area [Carbone and Bottiglione, 2008, Yastrebov et al., 2015]. It follows that, for consistent modelling of both the Novaculite and granite experiments, the initial contact ratio has to increase from the former to the latter due to the increase in confining pressures (1.4 MPa vs. 5 and 10 MPa). Specifically, the presented numerical simulations yield initial contact ratios of 0.004 for the Novaculite and 0.09-0.16 for the granite experiments. These initial values reflect the scale of discretisation, but the general principle still applies. Strict linear scaling between the two experiments does not apply, due to the difference in Young's moduli between the two rock types and the difference in composite profile roughness.

A critical issue arising in the average composition (AC) approach after Yasuhara et al. [2011], which has been received little attention so far, is the averaging method used to calculate the overall dissolution rate. In this approach, it is assumed that

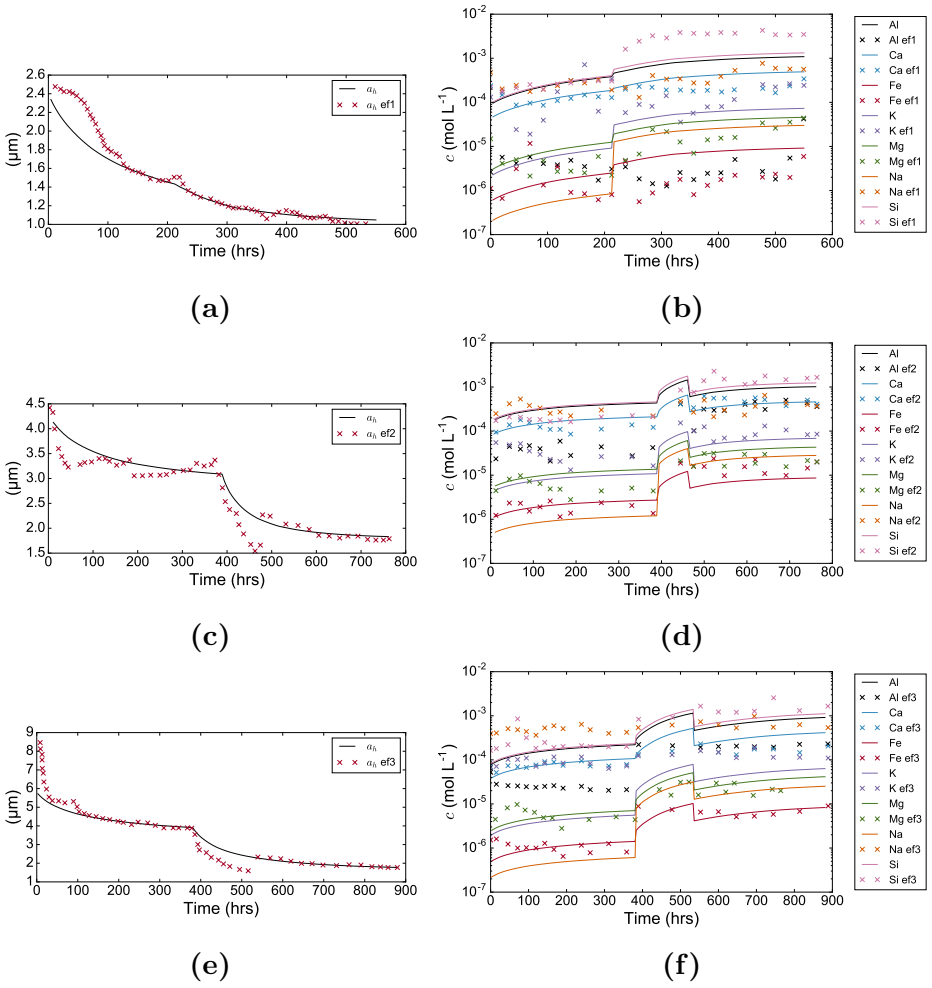


Figure 4.14: Comparison of numerical and experimental values for the `ef1-3` granite experiments [Yasuhara et al., 2011] for hydraulic aperture, a_h and effluent concentrations, c. The average composition (AC) model was used. (a) Hydraulic aperture `ef1`. (b) Effluent concentration `ef1`. (c) Hydraulic aperture `ef2`. (d) Effluent concentration `ef2`. (e) Hydraulic aperture `ef3`. (f) Effluent concentration `ef3`.

every contact zone dissolves at a rate that is given by the weighted average of all minerals, where the weighting reflects the volume fraction, χ_{min}, of each mineral in the bulk. This suggests a dominant dissolution contribution of Anorthite. This mineral is the least abundant component, but the dissolution rate constant k_{d} is two orders of magnitude higher than the remaining components; see Figure 2.11b. Thus, even at about 4% volume fraction (Figure 2.11a), the averaged dissolution rate is almost exclusively controlled by this mineral.

A more realistic representation is modelled using the discrete composition (DC) approach; see Figure 2.11a. It can be expected that contact and free zones of

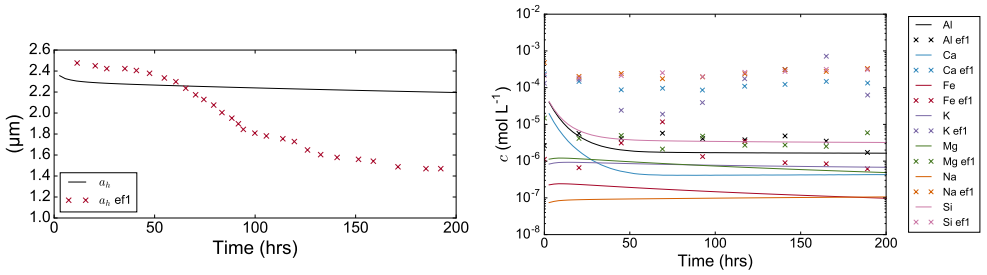
different minerals dissolve at different rates, leading to a more complex system of pressure solution driven compaction and channel developments in the free void space. Also, the precipitation of dissolved species occurs preferentially over certain minerals [Moore et al., 1994, Morrow et al., 2001, Yasuhara et al., 2011], but precipitation is not active in the core-flood models. Figure 4.15 illustrates the early time behaviour of the DC model for the `ef1` experiment. The same calibration for the pressure solution rate constants is used as in the AC fit. It can be seen that the highly soluble minerals Anorthite and Biotite dissolve rapidly, as evident by the decline in the unique Ca and Fe tracers (Figure 4.15b). The initial compaction ceases quickly (Figure 4.15a) as the local contact stress on these minerals reduces.

The overall contribution to the transmissivity loss is negligible, as the combined volume fraction of both minerals is less than 10%. The remaining minerals have dissolution rates that are orders of magnitude lower, and the overall surface structure remains very much unchanged. It can therefore be concluded that much higher rate multipliers are needed to match the hydraulic aperture loss. The rather complex parameterisation of the DC model is the subject of work in the future. It is expected, however, that using the discrete composition model, rate multipliers much closer to the Novaculite model are needed. A calibration of the DC model to fit experimental observations, however, is far from trivial, as factors may vary between the different minerals. Furthermore, any match should be expected to be non-unique due the large number of variables. It can be concluded that the lower values for matching factors of the AC model likely reflect the averaging of rate constants and the disproportional contribution of less abundant but highly soluble minerals.

4.6.3 The relationship between aperture and contact ratio

The following approximation has been proposed [Yasuhara and Elsworth, 2004] to relate the mean aperture, $\langle a \rangle$, to the contact ratio, R_c:

$$\langle a \rangle = \gamma_1 + \gamma_2 \exp(-R_c/\gamma_3) \tag{4.1}$$



(a) **(b)**

Figure 4.15: Comparison of early-time numerical and experimental values for the `ef1` granite experiments [Yasuhara et al., 2011] for hydraulic aperture, a_h and effluent concentrations, c. The discrete composition (DC) model was used. (a) Hydraulic aperture `ef1`. (b) Effluent concentration `ef1`.

where $\gamma_{1..3}$ are fitting parameters. This exponential relation has been developed based on two premises. First, no elastic deformation is accounted for, i.e., rock is treated as rigid. Second, a residual aperture exists, as pressure solution is assumed to cease below some critical contact stress [for a discussion, see Neretnieks, 2014]. Equation 4.1 has been used in conjunction with the first-order approximation $\langle a \rangle \approx \langle a_\mathrm{m} \rangle \approx a_\mathrm{h}$, independent of temperature and pressure conditions [Yasuhara and Elsworth, 2004, 2008, Yasuhara et al., 2011, 2006, Zhao et al., 2014].

While results presented here suggest that there exists no unique relationship between hydraulic aperture and contact ratio, the mean mechanical aperture of the elastically deformed pore space was shown to fit Equation 4.1 independently of pressure or temperature; see Figure 4.16. The pressure-dissolution model developed herein, analogous to Neretnieks [2014], does not assume the existence of a critical stress, i.e., pressure solution acts to dissolve any surface roughness in the long time limit. It follows that $\gamma_1 = 0$, as no residual aperture is being accounted for. A good fit is obtained for γ_2 representing the initial aperture and the exponential parameter γ_3 relating inversely to the initial aperture of the fracture, i.e., the roughness amplitude of the composite surface. Specifically, for the presented models of Hurst exponent $H = 0.8$, the exponential curve-fit yields γ_3 of 0.34 and 0.32, for h_rms of 8 and 16 μm, respectively.

Hydraulic aperture and contact ratio have also been accounted for by means of

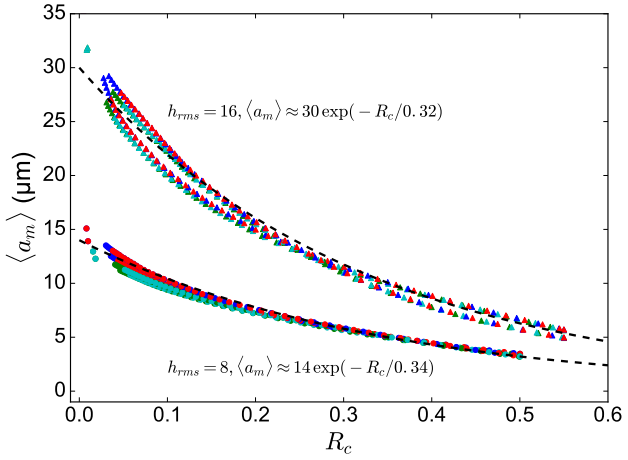


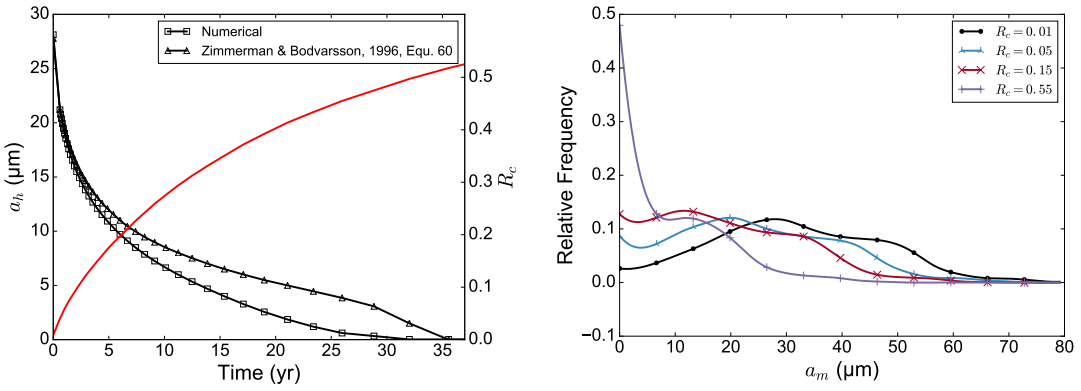
Figure 4.16: Relationship between average mechanical aperture, $\langle a_{\mathrm{m}} \rangle$ and contact ratio, R_{c}; $L = 1$ cm, $H = 0.8$, $h_{\mathrm{rms}} = 8$ μm, $\mathcal{L} = 256$, and $\lambda_L/\lambda_0 = 1$ under 10 MPa and 423 K.

effective medium and percolation theory, based on aperture distribution data [Zimmerman and Bodvarsson, 1996b]:

$$a_{\mathrm{h}}^3 \approx \langle a_{\mathrm{m}} \rangle^3 \left(1 - 1.5 \frac{\sigma_{a_{\mathrm{m}}}^2}{\langle a_{\mathrm{m}} \rangle^2}\right) (1 - 2R_{\mathrm{c}}) \tag{4.2}$$

where $\langle a_{\mathrm{m}} \rangle$ and $\sigma_{a_{\mathrm{m}}}$ are, respectively, the spatial average and standard deviation of the mechanical aperture taken only over the non-contacting fraction. A comparison to the numerically computed hydraulic aperture shows excellent agreement in the early time, *i.e.*, the low contact ratio regime; see Figure 4.17a. With prolonged pressure solution and increasing contact area, however, the closed-form expression overestimates a_{h}. The percolation term, $(1-2R_{\mathrm{c}})$, imposes the loss in transmissivity at $R_{\mathrm{c,perc}} = 0.5$ strictly, a higher value than predicted by averaged simulation results.

The discrepancy between transmissivity predictions obtained through Equation 4.2 and the discrete solution of the Reynolds equation may reflect that the aperture distribution is decreasingly representable by the Gaussian parameters $\langle a_{\mathrm{m}} \rangle$ and $\sigma_{a_{\mathrm{m}}}$. Figure 4.17b illustrates the dissolution driven shift from normal to log-normal distribution under constant confining pressure. In addition, the percolation limit of 0.5 assumes contact regions in the form of circles. The agreement between the



(a) **(b)**

Figure 4.17: Decline of hydraulic aperture, a_{h}, over time with increasing contact ratio, R_{c}; $L = 1$ cm, $H = 0.8$, $h_{\mathrm{rms}} = 16$ µm, $\mathcal{L} = 256$, and $\lambda_L/\lambda_0 = 1$ under 10 MPa and 423 K. (a) Comparison of the numerical results with an analytic model [Zimmerman et al., 1990]. (b) Evolution of aperture distribution with time.

analytical predictions and the simulated values at late times can be improved by accounting for non-circular contact areas [Zimmerman et al., 1992].

4.6.4 Discussion

The experimentally reported evolution of hydraulic aperture and effluent concentration [Yasuhara et al., 2011, 2006] has been successfully reproduced through the use of a temperature dependent calibration. This calibration takes the form of reaction rate multipliers in Equations 2.22 and 2.25. The pressure solution rate multiplier, η_{ps}, is, at the most, one order of magnitude below the local contact stress. The evolution of transmissivity, the effluent concentration and the fracture contacts are reproduced both qualitatively and quantitatively by the numerical model. Despite the magnitude of the calibration, this should indicate that the acting mechanisms are well captured. Thus, it can be assumed that the overall compaction process is a linear function of contact stress and an exponential function of temperature; see Equation 2.22. It should also be expected that the effluent concentration follows from removal of contacting asperities, and that the transmissivity loss results from convergence between the surfaces. Whether the

physical process is actually that of pressure solution is questionable, mostly due to the relatively low temperatures compared to experiments where pressure solution has been directly observed [Niemeijer et al., 2002]. The functional description used here is similar to the model for stress corrosion derived by Yasuhara and Elsworth [2008]; therein, however, the assumption is made that convergence occurs at the same rate as intra-granular crack propagation, which may be considered a physically questionable scenario. It is likely that a multitude of processes act together to result in the observed behaviour. The most likely candidates seem to be viscous creep, pressure solution and stress corrosion. Their combined effect, however, seems to be well captured by the used functional description.

4.7 Changes in stiffness

The stiffness of a generic fracture model ($L = 0.5$ m, $\mathcal{L} = 512$, $h_{\text{rms}} = 500$ µm, and $\lambda_L/\lambda_0 = 4$ under 10 MPa and 423 K, Figure 4.3) in its initial state is a linear function of the applied load, see Figure 4.18a, in agreement with empirical, numerical and theoretical models of elastic contact between randomly rough surfaces [Akarapu et al., 2011, Bandis et al., 1983, Berthoud and Baumberger, 1998, Hopkins et al., 1990, Swan, 1983]. The diagenetic processes studied here act to partition the nature of surface roughness over the fracture. While elevated regions are flattened, lower parts that are not in contact at *in situ* conditions retain their initial roughness (Figure 4.18c). The instantaneous closure of such a fracture in its chemically altered state gives rise to two contact regimes as a function of normal load. At loads roughly equal or below *in situ* conditions, stiffening of the fracture is controlled by smooth, low curvature features that result from dissolution-precipitation at and near contacts. Over these parts of the surface, a minimal increase in compression yields a disproportionately large increase in contact area. At higher loads, incremental contact occurs over the unaltered, self-affine rough fraction of the surfaces. Any incremental increase in contact area thus requires a much larger load increment over this part of the surface. The closure of the fracture, and the resulting stiffness curve, reflects these two regimes (Figure

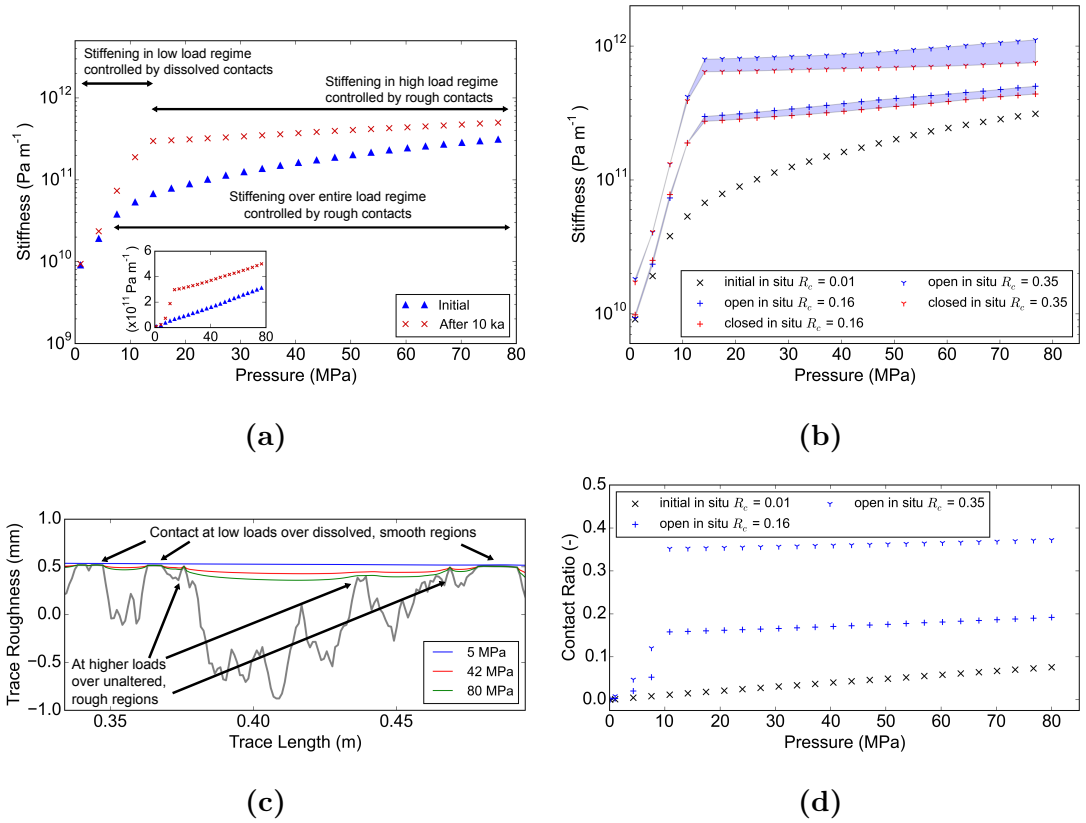


Figure 4.18: Qualitative evolution of closure-stiffness behaviour; $L = 0.5$ m, $\mathcal{L} = 512$, $h_{\text{rms}} = 500$ µm, and $\lambda_L/\lambda_0 = 4$ under 10 MPa. (a) Stiffness curves for a fracture in initial and dissolved state after 10 kyr. (b) Evolution of specific normal stiffness for a fracture in initial and dissolved state, for 'open' and 'closed' systems, with and without precipitation, respectively. (c) Illustration of elastic contact under increasing confining pressure at the dissolved state of a fracture. (d) Evolution of contact ratio, R_{c}, with pressure for a fracture in initial and dissolved state, for 'open' and 'closed' systems, with and without precipitation, respectively. The indicated *in situ* R_{c} is the contact ratio of the fracture under 10 MPa, which are the dissolution simulation ambient conditions.

4.19a). Stiffening transitions from approximately exponential to approximately linear at a load slightly larger than the 10 MPa effective confining pressure under which compaction is modelled. It follows that this *in situ* pressure roughly marks the transition in contact from 'diagenetically rounded' to 'initially rough' surface fractions.

The normal stiffness magnitude increases over the entire load spectrum as a result of these mechanical-chemical processes. Primarily, this reflects the reduced amount of normal load required to generate additional contact area in the low

load stage, and the observed increase in contact ratio at all loads. Furthermore, reduced stress concentrations over smoothened contacts result in reduced elastic compression of the contacts. Shortened free wall intervals that result from growing and newly formed contact spots reduce the deflection of surfaces into the fracture void space. Combined with the increased strain energy accommodated in larger contact structures, the elastic compression of the pore space is much reduced as compared to the fresh fracture, thus increasing its stiffness. At large loads, contact is made over fractions of the surface least affected from diagenetic processes, thus the difference in magnitude between initial and altered fracture stiffness is lessened.

For both, the 'open' system that models pressure solution only and the 'closed' system that models re-precipitation of any dissolved mass, the obtained instantaneous stiffness curves for points in time of equal *in situ* contact ratios have been found to evolve in a similar manner (Figure 4.18d). A higher stiffness throughout the load spectrum is obtained for the 'open' system. This reflects the increased convergence of the opposing surfaces. It also shows that that the contacting fraction of the surface is made up of a larger number of individual contact patches, as opposed to fewer in number but individually larger patches for the 'closed' system with precipitation (Figure 4.3). Precipitation in 'closed' systems also acts to retain deep channels, which, along with the larger separation between contact points, allow for larger elastic deformation into the void space to accommodate strain energy. These observations are in line with experimental [Kendall and Tabor, 1971] and numerical results [Hopkins et al., 1987, 1990] that relate reduced distance between contacts to higher interfacial stiffness. It can be concluded that the stiffness of the presented models is mainly a function of the magnitude of the *in situ* contact ratio [e.g. Petrovitch et al., 2013, 2014], and to a slightly lesser degree a response to the size and number of contact patches which result from whether or not dissolved mass precipitates locally. From this perspective, the non-linearity of stiffness follows the change in contact area-load relationship from classic linear to an exponential-linear function (Figure 4.18d).

4.7.1 Fracture closure and stiffness-compliance relationships

Noise in experimentally measured closure data makes direct differentiation with respect to pressure difficult, see Figure 3.3c. Stiffness, therefore, is often evaluated on smooth curve-fits [e.g. Zangerl et al., 2008]. Least-squares fits of the numerically-obtained closure data (Figure 4.19a) of the generic 0.5×0.5 m fracture have been generated for two functional models of fracture normal deformation; a hyperbolic and a logarithmic relationship. The closure models proposed by Bandis [1980] and Goodman [1976] can be generalised to a hyperbolic relationship of the form [Muralha, 1999]

$$\delta_{\mathrm{n}} = \frac{p^m}{a + bp^m} \tag{4.3}$$

where δ_{n} (m) is the fracture closure, *i.e.*, $\delta_{\mathrm{n}} = \langle a_{\mathrm{m}} \rangle_{p=0} - \langle a_{\mathrm{m}} \rangle_p$. As usual, p (Pa) is the nominal normal stress acting on the fracture, *i.e.*, the confining pressure; also, a, b and m are fitting variables. The Bandis model is a special case of Equation 4.3 for $m = 1$, and the Goodman model can be expressed by Equation 4.3 beyond a shift due to the initial seating stress [Muralha, 1999]. Besides a hyperbolic relationship, closure models for mismatched joints have also been expressed as logarithmic or exponential relationships [Bandis et al., 1983, Detournay, 1979, Goodman, 1976]. A two-parameter form was proposed by Detournay [1979]

$$\delta_{\mathrm{n}} = a \ln\left(\frac{p}{b} + 1\right) \tag{4.4}$$

Both the hyperbolic and logarithmic model provide good fits to the closure curve of the initial fracture model (Figure 4.19a), with correlation coefficients of $R = 0.996$ and $R = 0.998$, respectively. The fit of both models to the instantaneous closure of the fracture in its state after 10 kyr of pressure solution is nearly identical, with $R = 0.989$. This poorer fit is most pronounced over the low-load regime between 5 and 10 MPa, where closure transitions from being governed by the dissolved surface regions to being governed by the rough surface regions.

The misfit of smooth curves to the closure of the dissolved fracture in the low load regime has a profound effect on the nature of the obtained stiffness curves (Figure 4.19b). A smooth increase in stiffness entirely masks the transition from rapid stiffening over dissolved contacts to a much reduced stiffening over the rough surface fraction; for a comparison see Figure 4.19b for the stiffness derived from the curve fit, and Figure 4.18b for stiffness derived directly from numerical closure data. For the logarithmic closure model, Equation 4.4, normal stiffness is a linear function of pressure. The hyperbolic model, Equation 4.3, results in sub-linear stiffness for the initial fracture, and super-linear for the fracture after dissolution, thus bounding the stiffness values obtained from the logarithmic fit at larger loads. Stiffness values obtained from direct differentiation of the numerical closure data (Figure 4.18b) are closer to the logarithmic fit in each case.

Analytic models of closure often rely on the idealisation of the fracture as a simplified shape, and the stiffness results from elastic compression of the void space. With the exception of Zimmerman [2008], these models do not account for incremental increase in contact ratio with pressure, which constitutes an intrinsic link to fracture normal stiffness [e.g. Petrovitch et al., 2014]. For isolated open penny-shaped cracks of radius r, normal stiffness can be expressed as [Sayers and Kachanov, 1995]

$$\kappa = \frac{3\pi E}{16r(1-\nu^2)} \tag{4.5}$$

When the fracture is conceptualised as a collection of collinear elliptical cracks [Myer, 2000], its normal stiffness can be approximated for large contact ratios as [Jaeger et al., 2007, p. 371]

$$\kappa \approx \frac{2G}{\pi r(1-\nu)(1-c)} = \frac{E}{\pi r(1-\nu^2)(1-c)} \tag{4.6}$$

where r (m) is the half-length of the elliptical cracks, ν (-) and E (Pa) are, respectively, the Poisson's ratio and Young's modulus of the intact rock, and c (-) is the contact ratio, *i.e.*, $c = R_c$. The accuracy of the approximation in Equation 4.5 should be expected to increase with progressing pressure solution and precipitation, due to the increase in fractional contact area. This is accompanied by

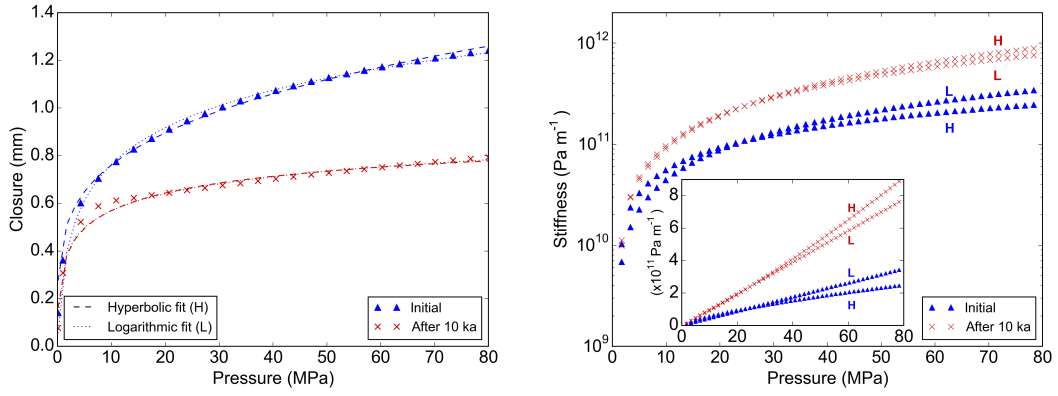


Figure 4.19: Changing mechanical closure due to dissolution; $L = 0.5$ m, $\mathcal{L} = 512$, $h_{\text{rms}} = 500$ μm, and $\lambda_L/\lambda_0 = 4$ under 10 MPa. (a) Closure curves of the initial fracture and after 100 kyr of dissolution, along with curve fits. (b) Corresponding stiffness from direct differentiation and curve fits.

an increased separation between void space segments, which reduces their mutual influence on deformation and thus renders them more and more mechanically independent. For the generic fracture model under 'closed' conditions after 1.2 Myr, an *in situ* contact ratio of 0.35 (Figure 4.4a), an estimated radius of void space segments of $r = 0.05$ m (Figure 4.3b), with $E = 60$ GPa, Equation 4.6 yields $\kappa = 6.01 \times 10^{11}$ Pa m^{-1}, comparable to the range of 6-7 $\times 10^{11}$ Pa m^{-1} obtained numerically for $p > 10$ MPa (Figure 4.18b). The good agreement affirms that larger patches of void space deform increasingly independent of each other as the fracture compacts due to pressure solution. The use of Equation 4.5 alone leads to a similar agreement, although on the low compliance side, if $r = 0.05$ m of a single void segment is used, in which case $\kappa = 7.2 \times 10^{11}$ Pa m^{-1}.

4.8 Fractures with shear displacement

It has already been illustrated (Figure 3.3b) that transmissivity anisotropy increases with increasing compression for fractures with shear displacement (Figure 3.3b). This is due to the preferential percolation direction of contacts perpendicular to the shear direction. A similar increase in anisotropy results from pressure solution driven growth of contact zones, which occurs under constant confinement;

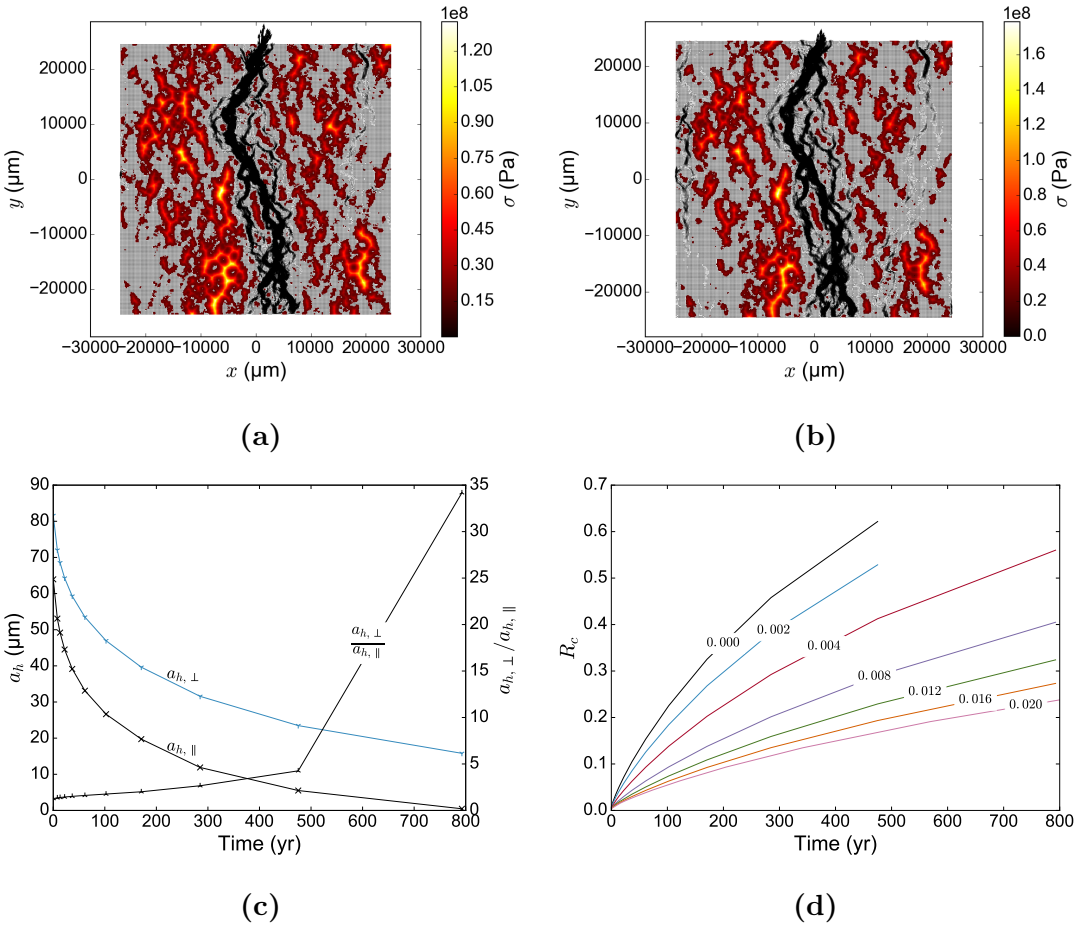


Figure 4.20: Changes in contact and flow over time due to dissolution in fractures with shear offset for a $L = 50$ mm and $\mathcal{L} = 512$ under 10 MPa and 423 K. (a) Hydro-mechanical state after 700 years under 'open' conditions for $\delta_T = 1$ mm. (b) Hydro-mechanical state after 700 years under 'closed' conditions for $\delta_T = 1$ mm. (c) Evolution of hydraulic apertures and ratio over time for $\delta_T = 400$ μm. (d) Evolution of contact ratio for different values of relative shear offset, δ'_T.

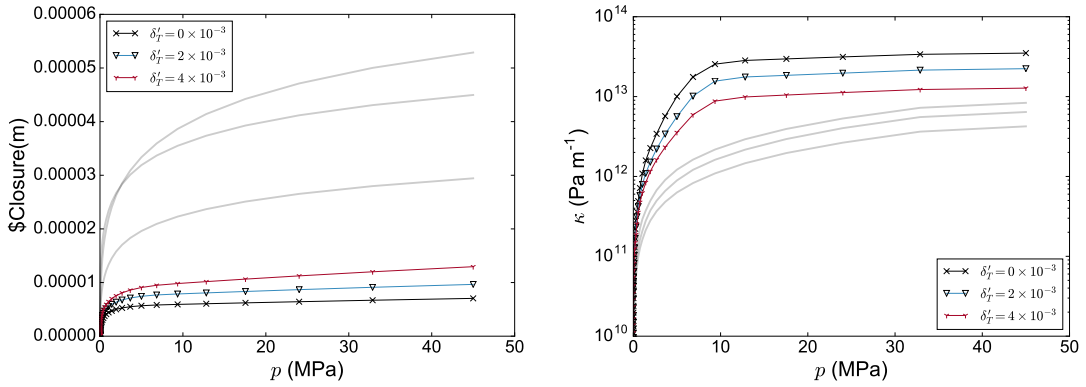
see Figure 4.20c. The increase of $a_{h,\perp}/a_{h,\parallel}$ is a common of all fractures with shear offset studied here. Transmissivity in the shear parallel direction ceases long before complete sealing of the fracture. Beyond the point of shear parallel sealing, the anisotropy $a_{h,\perp}/a_{h,\parallel}$ is not longer defined, and the fracture acts as a conduit solely in one direction. Analogous to the isotropic fracture case, precipitation in 'closed' systems acts to preserve flow channels and delays compaction of the pore-space; see Figures 4.20b and 4.20a.

The most significant characteristics of increased shear offset between the surfaces

are the presence of larger flow channels in the fracture, decreased stiffness, increased transmissivity and transmissivity anisotropy, and a reduced slope in the contact ratio-pressure relationship. Similarly, large offset fractures delay pressure solution driven compaction (Figure 4.20d). This follows from the nature of the void space, its larger channels and reduced stress concentration at the contacts that form in large offset fractures. The mechanical compression of partially dissolved fractures shows fast convergence towards the residual aperture, as illustrated by rapid asymptotic approach of closure curves (Figure 4.21a). Similar flattening follows in the semi-log representation of stiffness above the *in situ* pressure of 10 MPa. As in the isotropic fracture case, this reflects that compression is accommodated increasingly by bulk deformation as opposed to fracture void space closure. With increasing dissolution, the compression of the discontinuity formed by the fracture will contribute less and less to the overall compression of the rock mass, due to the lack of roughness. This results in a constant stiffness, proportional to the Young's modulus of the fracture, which reflects the linear elastic material model. In the limiting case of a completely dissolved fracture, *i.e.* a perfectly flat interface, a constant stiffness over the entire load regime should be expected, which describes the deformation of the bulk by definition.

4.9 Summary

A first-principle model for hydraulic-mechanical-chemical processes occurring in a rock fracture has been developed. It is based on the discrete representation of surfaces and the elastic contact between them. Chemically-mediated processes are modelled directly in the resulting space of free and contacting asperities. Free-face and pressure solution act to alter the surface as a function of temperature and local contact stress. Changes in void space, transmissivity, contact areas and local contact stresses arise directly from the evolving surface. Complex, emergent behaviour is captured that sees some channels close, and other channels open as a result of their location and size. Reactive transport is modelled through a coupled true length transport model in one dimension. Using calibration factors for



(a) **(b)**

Figure 4.21: Closure and stiffness evolution due to dissolution in fractures with shear offset of $L = 50$ mm and $\mathcal{L} = 512$ under 10 MPa and 423 K after 60 years in an 'open' system. (a) Closure for shear displacements of 0, 100, and 200 µm. Closure curves of initial, undissolved surfaces in translucent gray. (b) Corresponding stiffness from direct differentiation of closure curves for shear displacements of 0, 100, and 200 µm. Stiffness of initial, undissolved surfaces in translucent gray; see Figure 3.4c.

free-face and pressure solution, a qualitative and quantitative (to within an order of magnitude) match to experimentally observed transmissivity and effluent concentration was obtained. The main discrepancies between numerical results and experimental observations lie in jump discontinuities, and insensitivity of effluent concentration to flow rate variations. The former may be explained by dissolution of contacting asperities that provide critical support and ensuing macroscopic shifts between the opposing surfaces in the micron range. The latter discrepancy poses a fundamental contradiction with respect to general batch reactor behaviour under kinematic conditions, and has not yet been adequately explained. Independent of the precise formulation of the kinematics of the acting processes, it has been shown that surface dissolution mechanisms can explain both the changes in fracture transmissivity and effluent concentration. This is supported by good agreement, both qualitatively and quantitatively, of the contact area distribution at the end of the experiment. It has further been demonstrated that the average mechanical aperture, obtained from the average of local separation between the rock surfaces, can overestimate the actual equivalent hydraulic aperture by over 10%, when used as a proxy.

For the monomineralic Novaculite experiment, a unique match of the calibration factors for free-face and contact dissolution can be obtained, given the two experimental constraints of the transmissivity and pore-fluid concentration evolution. Suitable calibration factors are a function of temperature only. Comparisons between the average composition and the discrete composition model suggest that the discrepancy in calibration for the Novaculite and granite experiment results mainly from the contribution of sparsely present, highly soluble minerals to the average dissolution rate.

The presented findings further suggest that matrix diffusion constitutes a second-order process. To explain the strong compaction at the early stages of the experiments, matrix diffusion must act as a sink, thus failing to explain a mechanism responsible for the observed effluent concentration. To explain the high effluent concentration at late times, matrix diffusion must act as a source, failing to explain the increase in aperture. The required switch from sink to source is not trivial to be conceptualised. Finally it should be noted that, while the granite experiments [Yasuhara et al., 2011] behave similarly to comparable independent experiments [Moore et al., 1994, Morrow et al., 2001], the increase in transmissivity of the Novaculite [Yasuhara et al., 2006] towards the end of the experiment is different to the continuous sealing observed by [Polak et al., 2003]. The main difference between the two experiments is the higher confining pressure, so that 3.5 MPa resulted in continuous sealing, whereas 1.4 MPa resulted in a transmissivity increase.

Results show that there exists a limit, far from complete contact and zero mean aperture, that marks a cessation of hydraulic connectivity of the fracture void space. Preceding this sealing effect is a disproportional decline of mean and hydraulic aperture, indicative of the progressing isolation of fracture void space, and a transition period from effective to ineffective porosity. Elastic compression, initially the dominant compaction process, over time gives way to the irreversible convergence of rock walls, due to mass dissolution at contact zones. It has been shown that the difference in average aperture between the rigid and elastically compressed pore space of the fracture is significant, but decreases over time due

to the added support in the form of larger contact zones and concurrent reduction in elastic compression of the remaining free rock wall.

At all times, the inequality $\langle a \rangle > \langle a_{\mathrm{m}} \rangle > a_{\mathrm{h}}$ holds, and individual differences exceed ten percent. Specifically, a fracture model with an initial hydraulic aperture of 13 µm has been shown to close hydraulically after thirty years under a temperature and effective confining pressure of 473 K and 10 MPa, respectively. In contrast, larger aperture fractures of 33 µm subject to 5 MPa and 423 K have been shown not to reach a sealing state before 1400 years. In either case, the primary control over compaction rate is the temperature, and the second order control is the confining pressure. A relationship between mean mechanical aperture and contact ratio has been found to fit an exponential relationship, dependent only on the initial aperture and not on conditions such as confining pressure or temperature.

With respect to continuum models, it can be concluded that the assumption of proportionality between the transient decrease in average and hydraulic aperture is not generally applicable. In addition, it has been shown that convergence rates depend in the early-time on small wavelength roughness, and in the late-time on long wavelength roughness. The existence of roughness across all length scales in fracture surfaces suggests that the assumption of a characteristic length scale, e.g., by means of a roughness factor, a uniform grain diameter or distributions thereof, results in a model with an associated characteristic time scale. It follows that dissolution or convergence rates will be underestimated before this time scale and overestimated thereafter. For accurate long term predictions, models have to represent the largest roughness features of a fracture.

In fractures with shear offset, compaction due to the presented processes acts to increase the structurally motivated transmissivity anisotropy over time. Contact zones percolate along the shear-perpendicular direction first, thus sealing shear-parallel flow, but still allowing for flow in the parallel-directions. The impact of chemical processes on the preferential flow directions in fractured rock should therefore be expected to be profound.

It has long been established that characteristics of the structural process that result in the formation of fractures is directly linked to their stiffness. Primarily, it is the size of the initial fracture and subsequent shear displacement that govern the magnitude and evolution of fracture closure as a function of pressure. The presented findings make a strong case that the history of *in situ* conditions has similarly profound implications, through diagenetic processes that change the morphology of the surfaces in contact. For the modelled processes of pressure solution and precipitation, the key mechanism causing the general increase in stiffness is the growth and levelling of contact zones due to pressure solution, which decreases free wall deflection and the extent to which contacting asperities are compressed. Apart from an increase in magnitude, a distinct change in the nature of the normal stiffness curve is observed.

The *in situ* confining pressure of the fracture marks a transition from rapid, exponential-like increase towards approximately linear stiffening with increasing load. This reflects the diagenetically induced surface roughness partitioning of the fracture surface. Elevated regions in contact are smooth, well rounded to flat, as a result of dissolution and precipitation. These regions control fracture closure at low loads. Regions of the surfaces that are not in contact under *in situ* conditions retain their self-affine rough nature, and control the incremental increase in stiffness at high loads. Similar to plastic yield at contacting asperities, a decrease in initial aperture occurs, and the residual aperture is reached at much lower levels of compression. In the long-time limit, fracture stiffness approaches a constant over the entire load regime, proportional to the bulk Young's modulus. This follows from the lack of contribution to bulk deformation for perfectly flat interfaces, where any compression is accommodated by the solid volume only, since no void space remains. While the presented model accounts only for pressure solution and free-face precipitation, other diagenetic processes, such as stress corrosion [Atkinson, 1980] or contact overgrowth [Beeler and Hickman, 2015] should be expected to affect stiffness in a similar manner.

Chapter 5

Hydro-mechanical characteristics of fractured rock masses

The fundamental behaviour of the developed hydro-mechanical modelling approach in DFMs is first examined for a single fracture and a pair of conjugate fractures embedded in an otherwise homogeneous rock matrix. These models clearly show how fracture transmissivity varies as a function of orientation relative to the applied far-field stress. Next, networks of fractures with isotropic, random orientation and power law size distributions are studied. In these models, effects of fracture size can be studied, and mechanical interaction between fractures plays a bigger role. Among the main findings are the preferential directions of the equivalent permeability eigenvectors with respect to a far-field stress state, the transmissivity distribution of the fractures in the network, and the distribution of permeability eigenvalues of the network as a continuum. These characteristics are obtained over a large number of statistically identical realisations. A discussed on the lack of REVs in fractured rocks follows this analysis.

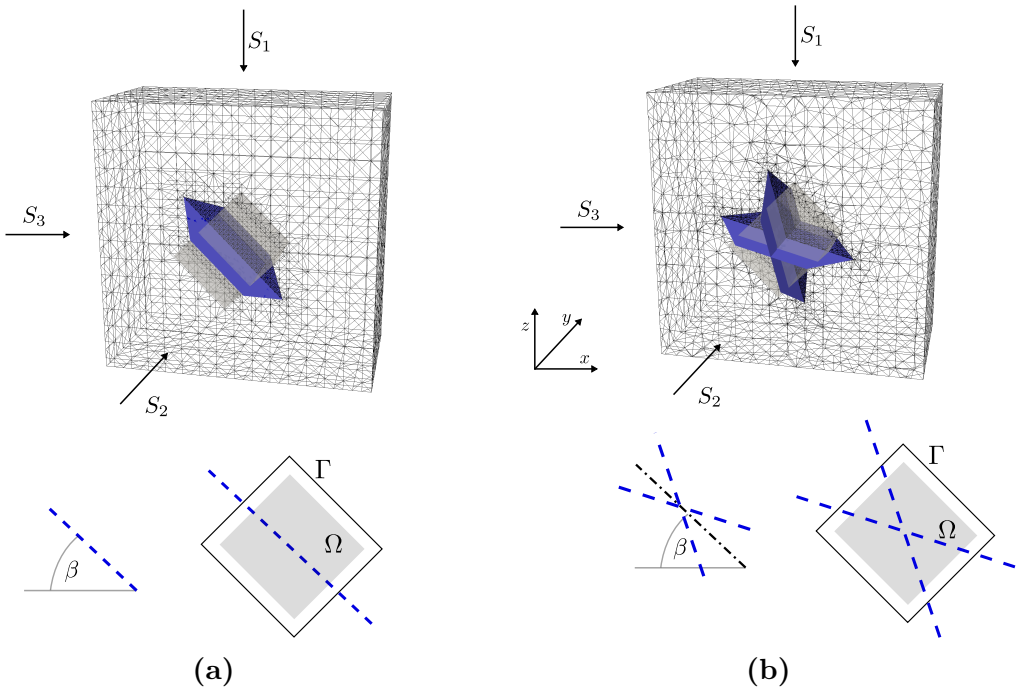


Figure 5.1: Rotating fracture geometry DFMs with a hexagon fracture representation, highlighted in blue. The matrix block is cut in half normal to the y-axis. The internal pressure boundaries, Γ, are shown in translucent grey, and the sampling region is denoted Ω. Models have been generated for different values of β, the angle between the symmetry axis and the horizontal in the x-z plane. (a) Single fracture and (b) conjugate fracture pair with an angle of 60 degrees between the fractures.

5.1 Single and conjugate fractures embedded in a rock matrix

Two models with rotating fracture geometries have been generated to illustrate the fundamental behaviour of the coupled HM, multi-scale modelling approach for DFMs; see Figure 5.1. A hexagonal fracture representation has been chosen for these models; this allows for a precise discretisation of the fractures as a finite element surface. Disc-shaped representations necessarily bring about a cell-size dependent discretisation error, albeit small, since the straight edges of finite elements cannot accurately represent the round perimeter of a circle. This error might be of second- or third-order to the resulting displacement and flow solutions, but for the sake of an illustrative reference example a precise discretisation is chosen. This might be prove useful for independent reproduction of the presented results.

Of the models depicted in Figures 5.1a and 5.1b, thirteen realisations have been generated with different angles β of the symmetry axis with respect to the horizontal. The opening-closure process of the models has been simulated with an initial opening pressure $p_\mathrm{f} = 0.9\,S_3$, and a subsequent triaxial far-field compression applied over the external model boundaries of

$$\boldsymbol{S} = \begin{bmatrix} S_3 & 0 & 0 \\ 0 & S_2 & 0 \\ 0 & 0 & S_1 \end{bmatrix} = \begin{bmatrix} 1.0 & 0 & 0 \\ 0 & 2.0 & 0 \\ 0 & 0 & 3.1 \end{bmatrix} 30 \times 10^6 \text{ Pa} \tag{5.1}$$

The stress ratio is $S_1/S_3 = 3.1$, which is theoretically the highest value that does not induce sliding in a critically oriented fracture for friction coefficient of $\mu = 0.6$; see Jaeger et al. [2007], p. 47.

A surface mesh box has been placed at the centre of the model, aligned with the centre of the symmetry axis in the x-z plane (denoted Γ in Figures 5.1a and 5.1b). The purpose of this internal box is to force nodes to exist over its surfaces; it acts as a set of internal boundaries, on which the pressure boundary conditions of the flow problem are prescribed. This is done for the following two reasons. First, to have the fracture(s) percolate the flow region, so that the obtained permeability reflects the fractured subsection of the model. Secondly, to have the sampling domain (denoted Ω in Figures 5.1a and 5.1b) to rotate with the fracture geometry for all values of β, so that the shape of the sampled fracture-matrix domain remains the same. This allows for direct comparison of the obtained equivalent values, with a constant fracture length and fracture-rock volume ratio over all configurations β.

The edge length of the cubic finite element models (Figures 5.1a and 5.1b) is chosen to be $10 \times 10 \times 10$ m, and the fracture length is $L = 5$ m. The domain is discretised by isoparametric tetrahedra. The underlying shape functions are quadratic for the elastic deformation-contact part, and linear for the flow problem. The maximum element size was set to 10/15, and adaptively decreased to 10/40 within the flow region Γ; this flow domain has an edge length of $3 \times 3 \times 3$ m. The mechanical moduli of the rock matrix are $E = 60$ GPa and $\nu = 0.15$. Upon

solution of the mechanical opening-closure process, the hydraulic properties of the fracture(s) are evaluated, based on the FEM fracture average shear displacement, $\bar{\boldsymbol{\delta}}_{\mathrm{T}}$ and average normal pressure, $\bar{p}$. The opposing fracture surfaces are generated with $H = 0.8$, $\lambda_L/\lambda_0 = 1$, $h_{\mathrm{rms}} = L\,0.01^H$, $\mathcal{L} = 8192$ and a mismatch length scale of $\lambda_{\mathrm{m}} = 500$ μm. After application of the absolute shear displacement, the composite surface is generated and down-sampled to $\mathcal{L} = 512$ using a bivariate spline approximation for the fracture-scale contact and flow analysis. The obtained transmissivity tensor is then assigned to the fracture in the finite-element model by tensor rotation to align with the shear direction $\bar{\boldsymbol{\delta}}_{\mathrm{T}}$, so that the parallel and perpendicular transmissivies align correctly with the shear direction. The matrix permeability is set to 1 mD. The subsequent pressure solution of the flow problem is obtained within Γ, and the permeability of the rock matrix ensemble is sampled over the subdomain Ω; see Figure 5.1.

5.1.1 Embedded single fracture

The complimentary hydro-mechanical results across the two scales are best illustrated for the single fracture DFM. At the fracture scale, where frictionless contact and laminar flow are modelled, results for hydraulic aperture, contact ratio and elastic compression of the void space are obtained; see Figure 5.2b. The hydraulic apertures over the range of fracture orientations can be normalised with respect to their maximum value to obtain a'_h, which here represents the shear perpendicular hydraulic aperture. The elastic compression of the fracture void space is the fractional reduction of the rigid void space due to elastic compression, *i.e.*, $\Delta a'_{\mathrm{E}} = \langle a_{\mathrm{m}} \rangle / \langle a \rangle$. These follow from the network scale solution to the frictional contact problem, *i.e.*, the normal pressure and shear displacement; see Figure 5.2a. The contact parameters on the network scale for a fracture can be normalised using the fracture length for the amount of shear displacement, $\bar{\delta_{\mathrm{T}}}' = \bar{\delta_{\mathrm{T}}}/L$, and the normal pressure can be normalised using the magnitude of S_1, such that $\bar{p}' = \bar{p}/S_1$.

There is no shear displacement between the fracture surfaces for the two orientations of $\beta = 0$ and $\pi/2$, since negligible shear stresses act on the surfaces. It follows

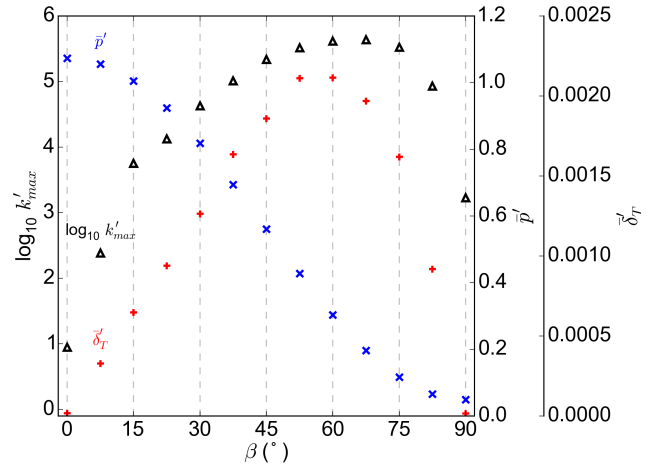
that the composite surface, or fracture pore space, is identical for both configurations. The higher transmissivity at $\beta = \pi/2$ results from the lessened compression, as this configuration has the fracture normal aligned with the direction of the least principal stress, S_3; see Figure 5.1. At $\beta = 0$, the fracture is exposed to the largest possible compression as it is oriented perpendicular to the direction of S_1; it follows that transmissivity reaches its low. In both configurations, fracture transmissivity is a consequence of the λ_{m}-induced surface mismatch and is thus isotropic. Between the two end-members of β, shear displacement between the fracture surfaces reaches a maximum between 52 and 60 degrees; see Figure 5.2a. This is interesting in that this range also represents the critical orientation of the fracture, *i.e.*, the fracture orientation most prone to friction-induced failure. However, no sliding between the surfaces is observed, as they stick once in contact. This stick condition, $\boldsymbol{g}_{\mathrm{T}} = \mathbf{0}$, is consistent with the stress ratio $S_1/S_3 = 3.1$ and the friction coefficient $\mu = 0.6$. It can be concluded that not only frictional failure, but also the closing process before contact, forms the largest offset between the surfaces in the range of $\beta \approx 60$ degrees. The opening-closing induced aperture reaches a maximum thereabouts due to an optimal combination of shear and normal stress, which allows for maximum displacement during the fracture closure and relatively little compression in contact.

The uncompressed, rigid aperture of a fracture is proportional to its shear displacement. The hydraulic aperture of the fracture, however, reaches its maximum (Figure 5.2b) at a larger angle, $\beta \approx 60 - 67\,^{\circ}$. This results from the relatively large compression that the fracture experiences at its maximum shear displacement. The optimal ratio of the combined displacement and normal pressure occurs at a slightly steeper angle, which reflects the non-linear drop in $\bar{p}'$; see Figure 5.2a and the reduced elastic compression of the void space, $\Delta\bar{a}'_{\mathrm{E}}$ in Figure 5.2b. The contact ratio between the surfaces, R_{c}, has its maximum at the no-offset configuration at $\beta = 0$, and decreases with increasing inclination of the fracture. This reflects the different combinations of offset and normal compression through all fracture orientations. A slight increase in R_{c} at the $\beta = \pi/2$, 'no-shear' configuration is observed (Figure 5.2b), because of the large effect that shear displacement

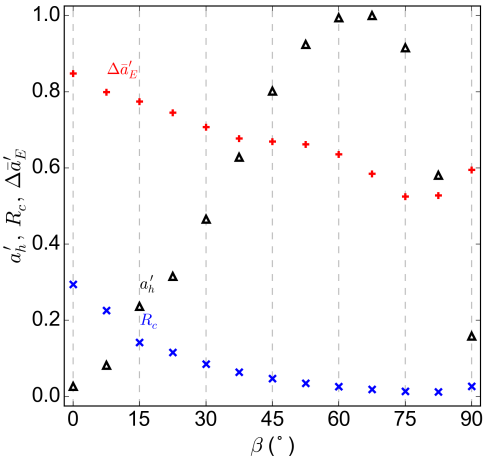
has on the contact area-load relationship (Figure 3.6). The permeability of the fractured rock region Ω (Figure 5.1), is proportional to the hydraulic aperture of the single fracture in a non-linear manner (Figure 5.2a). The contribution of the rock matrix acts to mitigate large gradients, to some extent. From the fact that $a_{\mathrm{h},\perp} > a_{\mathrm{h},\parallel}$ it follows that k'_{max} (Figure 5.2a) is aligned with the y-axis, except for the two no-offset configurations, where the orientation either lies in the y-direction or in the x/z-direction, depending on whichever of the latter is numerically larger. To conclude, it should be highlighted that the opening-closure process developed here, albeit a very much simplified model in the framework of linear elasticity and without fracture propagation, qualitatively reproduces the established notion that critically oriented fractures are the most likely to be hydraulically conductive [Barton et al., 1995].

5.1.2 Embedded pair of conjugate fractures

For the pair of conjugate fractures (Figure 5.1b), the direction of maximum permeability, k_{max}, of the fractured rock region Ω is always along the y-axis, since shear, and thus the displacement $\boldsymbol{\delta}_{\mathrm{T}}$, occurs only in the x-z plane. The more interesting question relates to the direction of the medium permeability eigenvector, k_{med}, which has to be located in the x-z plane. A prime example of such networks are bedding-plane-perpendicular fractures that form conjugate sets in limestone beds along the British Channel coast [*e.g.*, Figure 7 in Belayneh et al., 2006]. In such bedded sedimentary rocks, flow occurs primarily along the bedding plane, and the direction of largest permeability is of great interest. For thirteen realisations of different inclinations β of the symmetry axis with respect to the x-y plane, the hydro-mechanical results for the orientation of the intermediate permeability eigenvector in the bedding plane are shown in Figure 5.3. The two end-member configurations, $\beta = 0\ ^\circ$ and $90\ ^\circ$, have the expected orientation of k_{med} along the symmetry line, since both fractures experience identical amounts of shear displacement and compression. In terms of magnitude, the bed-parallel permeability k_{med} is higher at $\beta = \pi/2$ than at $\beta = 0$. This is due to larger shear



(a)



(b)

Figure 5.2: Coupled multi-scale hydro-mechanical results a the single fracture DFM on (a) the network scale and (b) the single fracture scale as a function of the inclination β. At the network scale (a), the mechanical results of fracture confining pressure, $\bar{p}'$, and shear displacement, $\bar{\delta}_T$, are obtained from the contact solution, and the maximum rock-fracture permeability, k'_{max}, results. At the single fracture scale, the elastic compression of the pore-space, $\Delta\bar{a}'_{\mathrm{E}}$, the contact ratio, R_{c}, and the hydraulic aperture, a'_{h}, result.

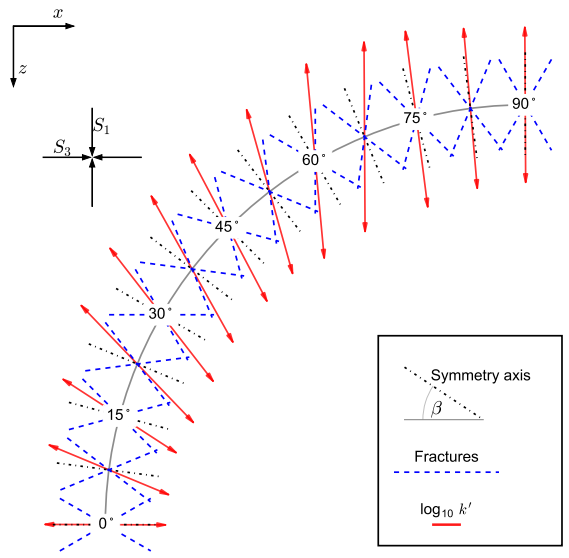


Figure 5.3: Coupled multi-scale hydro-mechanical results for the conjugate fracture pair DFM as a function of the inclination β. The permeability eigenvector that lies in the $x - z$ plane has been normalised with respect to the matrix permeability, $k' = k/k_{\text{matrix}}$.

and lessened compression when the symmetry axis is aligned with the maximum principal stress.

As β increases from 0 to $\pi/2$, *i.e.*, the orientation of the principal stresses with respect to the fractures rotates, the direction of k_{med} strongly favours the fracture with larger offset and lower compression. This is most pronounced around $\beta \approx 30$ degrees, where one fracture is oriented perpendicular to the maximum principal stress, S_1. In this configuration, the horizontally-aligned fracture is offset-free and exposed to the largest possible compression, while the other fracture is near-critically oriented, with large offset and lessened confinement as a result. Beyond this inclination, the average flow direction moves gradually back towards the fracture pair symmetry axis. The largest permeability of the fracture-rock ensemble region Ω is obtained for a symmetry axis that is inclined 60 degrees with respect to the S_1-S_2 plane, very similar to the single fracture case. At this configuration, k_{med} is almost three orders of magnitude larger than at the two no-offset orientations, as indicative by the length of the corresponding eigenvectors; see Figure 5.3.

5.2 Fracture networks

A series of 265 statistically identical fractured rock DFMs (Figure 5.4a) have been generated to study hydro-mechanical results on networks of fractures. The outer boundaries of the finite-element model form a cubic domain with edge length of $40 \times 40 \times 40$ m. The fracture region is restricted to the interior, such that all fracture centres are located at a distance equal or greater than $1.5 \times R_{\max}$ from all outer boundaries, where $R_{\max}$ is the upper limit of truncation in the fracture radii distribution. This distance to the outer model boundaries serves the purpose to isolate the effect of the fractures to the interior deformation of the model, and to avoid interference with the applied stress boundary conditions. Eight fractures were generated in each model, following a power law size distribution with exponent -2.0 and upper and lower fracture length truncation of 20 and 6.66 m, respectively. Analogous to the single and conjugate fracture models, internal fluid pressure boundaries, Γ, were created in form of a centred cubic domain of $10 \times 10 \times 10$ m to assess the fractured rock permeability in a percolating domain. Figure 5.4 illustrates the multi-scale hydro-mechanical concept developed here, as a visual counterpart to the flow chart presented in Figure 2.17. After the solution of the deformation-contact problem at the network scale as a response to outer stress-boundary conditions (Figure 5.4a), the averaged values of confining pressure and shear displacement are obtained for each fracture (Figure 5.4b). Based on these results, each fracture's composite surface is created, and used to solve for rough surface elastic contact and ensuing transmissivity (Figures 5.4c and 5.4d). Equipped with the resulting transmissivity tensor and mechanical aperture, the network scale flow is determined (Figure 5.4e). The permeability tensor, $\tilde{\boldsymbol{k}}$, finally results (Figure 5.4f), here for the $8 \times 8 \times 8$ m domain, Ω (Figure 5.4e) embedded in the flow domain, Γ (Figure 5.4b).

As illustrated using the single and conjugate fracture models, shear displacement and compression are functions of fracture orientation, which certainly holds true for monodisperse fracture populations. However, the amount of shear displacement is also a strong function of fracture size (Figure 5.4e), a fact that contributes to the

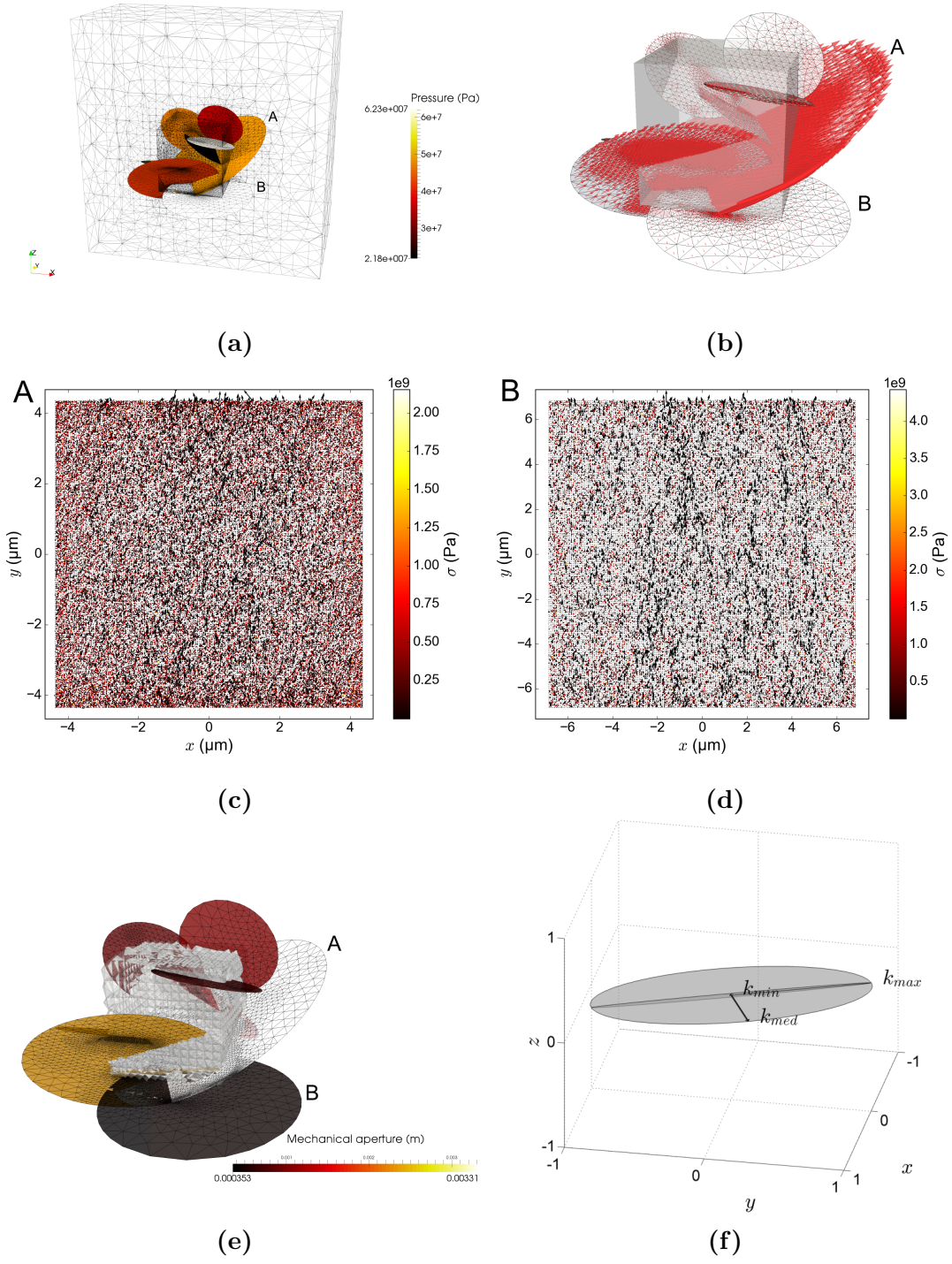


Figure 5.4: Quantitative DFM results. (a) Cut through computational domain, with outer stress-boundaries, interior fluid pressure-boundaries, Γ, and fractures showing average normal pressure, $\bar{p}$. (b) Zoomed-in fraction showing fractures and interior fluid pressure-boundaries, Γ, along with average shear displacement, $\overline{\boldsymbol{\delta}}_{\mathrm{T}}$, as vectors. (c) Hydro-mechanical state of fracture far from Coulomb-failure with little shear displacement and large compression (denoted 'A' in throughout this Figure). (d) Hydro-mechanical state of fracture close to Coulomb-failure with large shear displacement and low compression (denoted 'B' in throughout this Figure). (e) Zoomed-in fraction showing fractures and permeability sampling region, Ω, and the average fracture mechanical aperture, $\langle a_{\mathrm{m}} \rangle$. (f) Resulting equivalent permeability tensor in ellipsoid form.

motivation behind length-dependent fracture transmissivity relationships, which are commonly used for flow modelling in DFMs [Olson, 2003]. The developed model qualitatively reproduces the observations that larger fractures, and those that are near-critically oriented, are stronger hydraulic conduits. The physical explanation for these differences are the larger pore space that results from large displacements (Figure 5.4b), low contact ratios, and low levels of compression for fractures close to the Coulomb failure regime (Figure 5.4d). In contrast, fractures far away from this characteristic shear-normal are charaterised by a small pore space and large contact ratios (Figure 5.4c). A good illustration of the dependence of aperture on fracture size and shear displacement is provided by comparing Figures 5.4b and 5.4e.

To isolate the effect of orientation with respect to the far-field stress from the effect of fracture size on transmissivity, length-normalised hydraulic apertures of all fractures in the generated networks are plotted as a function of the fracture poles; see Figure 5.5a. This normalised hydraulic aperture is defined as $a'_{\mathrm{h}} = a_{\mathrm{h}}/L$, where a_{h} is the mean hydraulic aperture of the parallel and perpendicular component, and L is the fracture length. The isolated effect of fracture orientation on transmissivity that results from the developed model (Figure 5.5a) clearly shows a preference for fractures oriented critically in the x-y plane, which is the plane of least and maximum principal stresses, S_3 and S_1, respectively. This can be further illustrated by plotting a'_{h} based on their projected stress state on a Mohr circle; see Figure 5.5c. The population of normalised hydraulic apertures span one order of magnitude, which has even more pronounced consequences for the flow through these fractures because of the cubic scaling of transmissivity.

Since fracture transmissivity is largest in the direction perpendicular to the shear displacement, the preferred orientation of the overall $k_{\max}$ (Figure 5.5b) of the fractured rock mass tends to be aligned with the y-axis, *i.e.*, the direction of the intermediate principal stress, S_2. This trend is clearly visible despite the fact that single fractures often dominate the flow direction within a model regardless of their orientation because of their relatively large size. In the cases where single fractures dominate the orientation of $k_{\max}$, its magnitude is generally reduced by a factor of

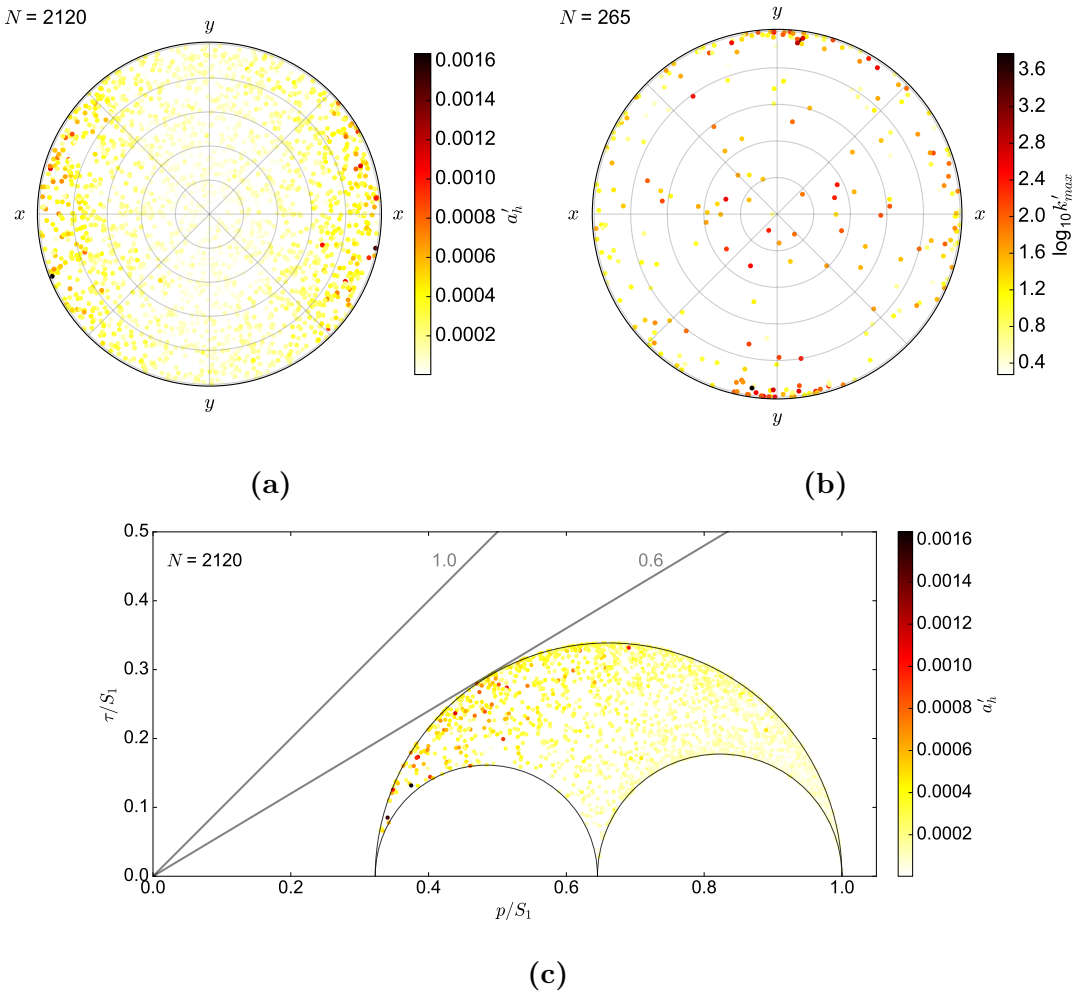
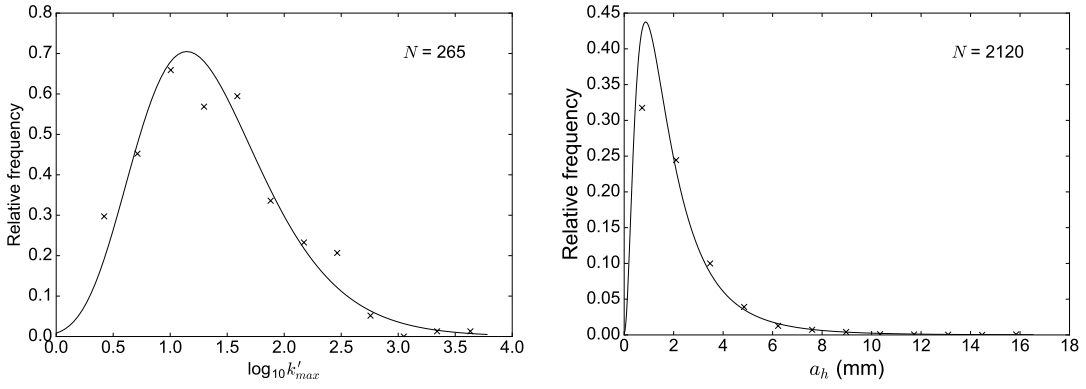


Figure 5.5: Quantitative results from 265 network DFM realisations. (a) Length-normalised hydraulic aperture, a'_{h}, on a stereonet where point locations mark poles of all fractures. (b) Normalised maximum permeability, k'_{max}, of the fracture rock mass subdomain Ω, on a stereonet projection where point locations mark orientation of corresponding eigenvectors. (c) Mohr circle plot, showing relation between a'_{h} and τ/p for all fractures.

around 1/3, and this reduction is most pronounced if the direction of maximum permeability approaches the direction of S_3; see Figure 5.5b. An illustration of how single fractures control the permeability of the rock mass is shown in Figure 5.4f. In this case, two connected fractures percolate in the horizontal direction (Figures 5.4b and 5.4e), resulting in k_{max} being aligned with the x-y plane. A subset of fractures controlling the overall flow of a rock mass is a characteristic of the equivalent permeability paradigm. Despite the isotropic random orientation of the fractures, and the equivalent permeability nature that results from fractures

being at the same scale as our rock mass, the preferential direction of $k_{\max}$ aligned with S_2 over all realisations is still pronounced; see Figure 5.5b. The S_2-aligned orientation of $k_{\max}$ is not only more frequent, but results in this area are also larger in magnitude. This trend should be expected to be even stronger for a more representative number of fractures, and for fracture sizes well below the size of Ω, which would move the model towards effective medium assumptions.

The finding that $k_{\max}$ is preferentially oriented along the intermediate stress S_2 is significant in that it can only be obtained by accounting for the locally anisotropic transmissivity of individual fractures. Simulations in two-dimensions, where fracture transmissivity is *de facto* isotropic, have also found the direction of $k_{\min}$ aligned with S_3 [Baghbanan and Jing, 2008, Min et al., 2004b]. However, due to the two-dimensional limitation in incorporating anisotropic fracture transmissivity and both S_2 and S_3, the direction of maximum permeability was found to be aligned with S_1 [Baghbanan and Jing, 2008, Jing et al., 2013], instead of S_2. This is solely due to the direct incorporation of the anisotropy effect $a_{\mathrm{h},\perp} > a_{\mathrm{h},\parallel}$ developed here. If an average, isotropic hydraulic aperture were used in the flow simulations, the finding of $k_{\max} \parallel S_1$ [Baghbanan and Jing, 2008, Jing et al., 2013, Min et al., 2004b] would be supported. These effects should be expected to be even more pronounced for large offset fractures, beyond the framework of linear elastic and small deformations upon which the opening-closure concept developed herein is based. The population of obtained maximum permeability values, $k_{\max}$, follows a normal distribution; see Figure 5.6a. The opposing permeability outliers span three orders of magnitude. This is typical of equivalent permeability results, as opposed to effective permeability results. The latter is typically characterised by a much narrower standard deviation for large, statistically identical populations [Mourzenko et al., 2011]. The population of obtained hydraulic apertures over all realisations can be fit by a log-normal distribution; see Figure 5.6b.



(a) **(b)**

Figure 5.6: Distributions of (a) maximum permeability magnitude over 265 DFM realisations, where $k'_{\mathrm{max}} = k_{\mathrm{max}}/k_{\mathrm{matrix}}$, and (b) of the hydraulic aperture, a_{h}, of all fractures therein. Note the implicit log-scaling of the abscissa in (a).

Chapter 6

Chemically mediated compaction of fractured rock masses

The models presented in the previous chapter are here studied with respect to pressure solution induced changes to their hydraulic behaviour. The only modification to the developed framework (Figure 2.17) is that pressure solution compaction is modelled on a fracture-by-fracture basis. After a simulated time of 4.75 Myr, the individual fracture transmissivities are evaluated on the chemically altered fractures, and fed back to the DFM flow solution to solve for the new permeability tensor. It is thus assumed that the stress state to which the fractured rock mass is subjected does not change during the compaction process. Since precipitation has been shown to have second-order effects on the qualitative evolution of the fracture pore-space, 'open' systems have been modelled here. The *in situ* temperature that the studied fractured rock mass is subjected to have been chosen as 423 K, and the far-field stress state is identical to that used in the previous section (Equation 5.1). It will be shown that this chemically-mechanically mediated compaction tends to further increase the mechanically induced preferential flow direction, which tends to be controlled by critically stressed fractures.

6.1 Single and conjugate fractures embedded in a rock matrix

For the single fracture embedded in a rock matrix (Figure 5.1a), the first two fracture orientations of $\beta = 0$ and 7.5 degrees show complete sealing, *i.e.*, the permeability of the fractured rock region is equal to that of the rock matrix (Figure 6.1c). This state is the expected state for all fractures in the long time limit. Indicative for a sealing fracture is a contact ratio of above 0.5 (Figure 6.1b) and a zero hydraulic aperture (Figure 6.1a). The absolute increase in contact ratio due to pressure solution rises with decreasing offset between the fracture surfaces, *i.e.*, away from the $\beta \approx 60$ to 75 degree configuration; see Figure 6.1b. This is primarily a function of the offset and resulting composite surface, and to second order is a function of the increased confining pressure acting on the other configurations; see Figure 4.20d for corresponding single fracture experiments under constant confinement, but different values for shear displacement between the surfaces. The absolute decrease in hydraulic aperture, on the other hand, is relatively uniform over all orientations (Figure 6.1a). It follows that the relative reduction in a_h is stronger over the low transmissivity orientations closer to $\beta = 0$, and smallest around critically oriented fractures. Interestingly, fracture aperture did not change quantitatively, but also the qualitative trend as a function of fracture orientation changed; see Figure 6.1a. While for the initial fractures the orientation of largest transmissivity was around $\beta = 60$ degrees, in the chemically dissolved state this angle changed to 75 degrees, as a result of the shear offset to normal stress combination.

It can be concluded that compaction acts relatively stronger on fractures that are less transmissive to begin with, due to the mechanical state they are in: large confinement and small shear displacement. For the pair of conjugate fractures (Figure 6.2), it follows that the initially preferred flow direction, which results from a preferential mechanical activation during the opening-closing stage of one fracture, is further enhanced over time. In particular, for orientations between $\beta = 7.5$ to 60 °, the permeability after pressure solution favours the mechanically

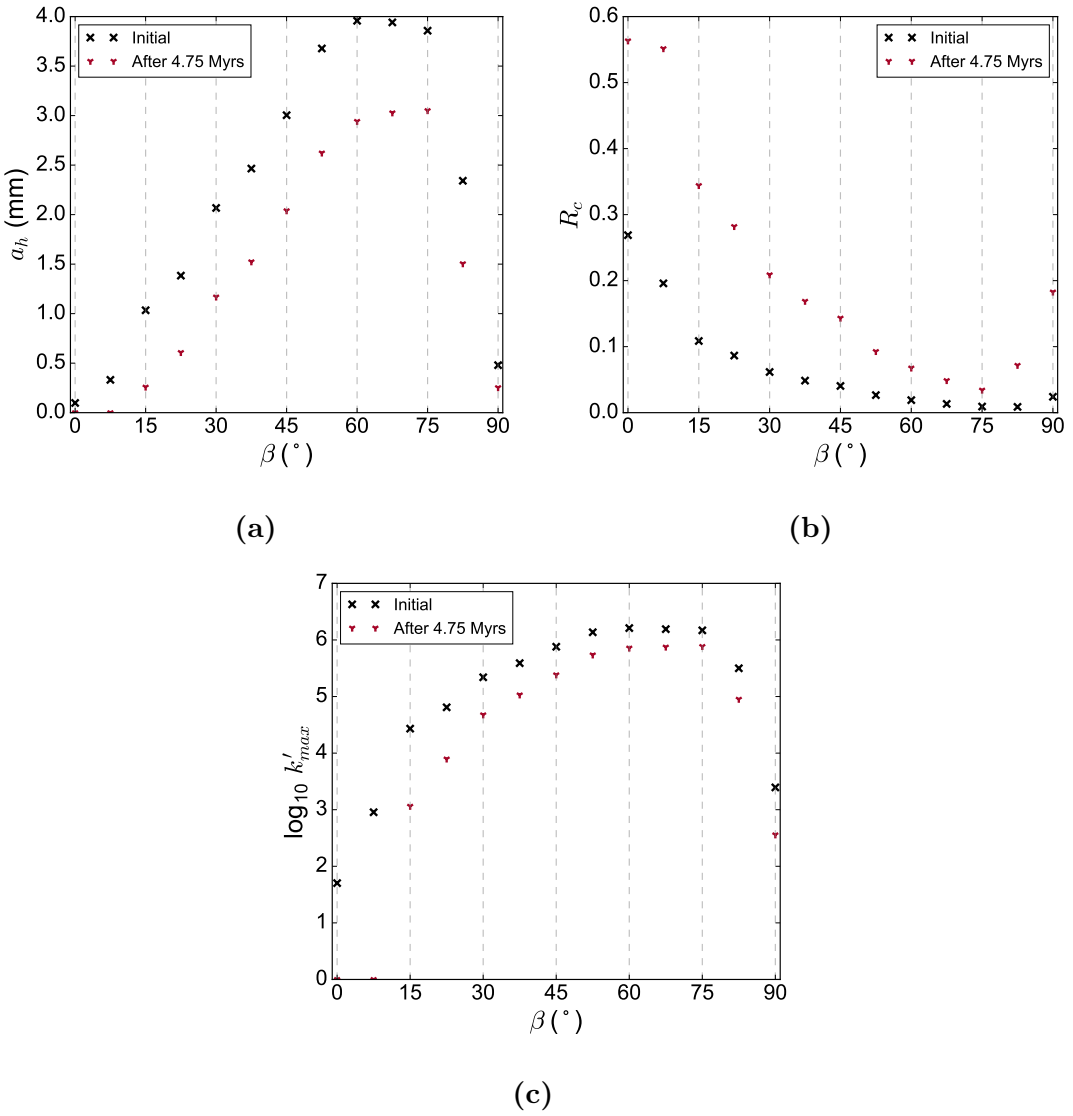


Figure 6.1: Coupled multi-scale thermo-hydro-mechanical-chemical results for the single fracture DFM in its initial state and after 4.75 Myr of pressure solution at 423 K. (a) Hydraulic aperture, a_{h}, (b) contact ratio, R_{c}, and (c) normalised maximum permeability, k'_{max}, of fractured rock region Ω.

activated fracture even more than is the case for the initial, chemically unaltered model. The configuration in which both fractures are subject to the largest compression, and experience the smallest shear displacement, $\beta = 0$, has experienced a reduction in permeability down to almost equal to that of the rock matrix. On the other hand, at $\beta = 90$ °, the compression is less and offsets are larger for both fractures. It follows that the compaction is not nearly as pronounced; see Figure 6.2.

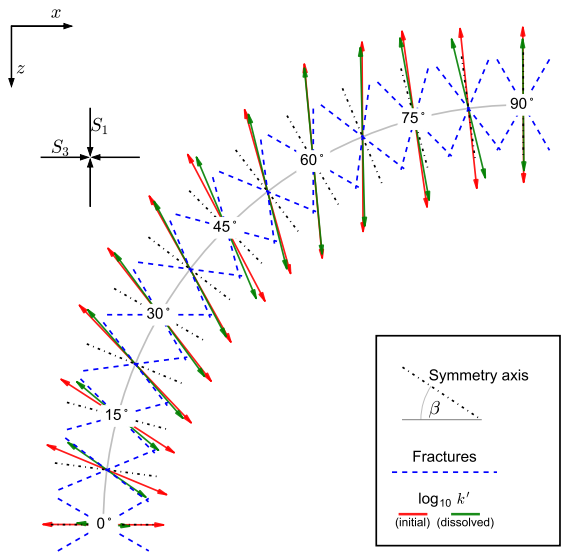


Figure 6.2: Coupled multi-scale hydro-mechanical results for the conjugate fracture pair DFM as a function of the inclination β, in its initial state and after 4.75 Myr of pressure solution at 423 K. The permeability eigenvector that lies in the x-z plane has been normalised with respect to the matrix permeability, $k' = k/k_{\text{matrix}}$.

6.2 Fracture networks

The observations that the studied compaction process further strengthens mechanically induced preferences as to the average flow directions translates to the fractured rock mass models. Figures 6.3 and 5.5 can be directly compared as snapshots of the networks' hydraulic state, before and after dissolution, respectively. Hydraulic apertures of fractures oriented perpendicular to S_1, characterised by poles around the centre of the hemispherical projection (Figure 6.3a), are much reduced compared to their initial state (Figure 5.5a); fractures oriented near-critically, on the other hand, show a much retained transmissivity. Models with an orientation of k_{max} (Figure 6.3b) not aligned with S_2 are also much reduced as a result, when compared to their initial state (Figure 5.5b). The preferential overall compaction of fractures with certain orientations is not the only explanation for the strengthening of S_2 aligned maximum permeability. It is also the disproportional decline of shear perpendicular and parallel transmissivity; see Figure 4.20c. Since slip preferably occurs in the S_1-S_3 plane, transmissivities of large offset fractures will

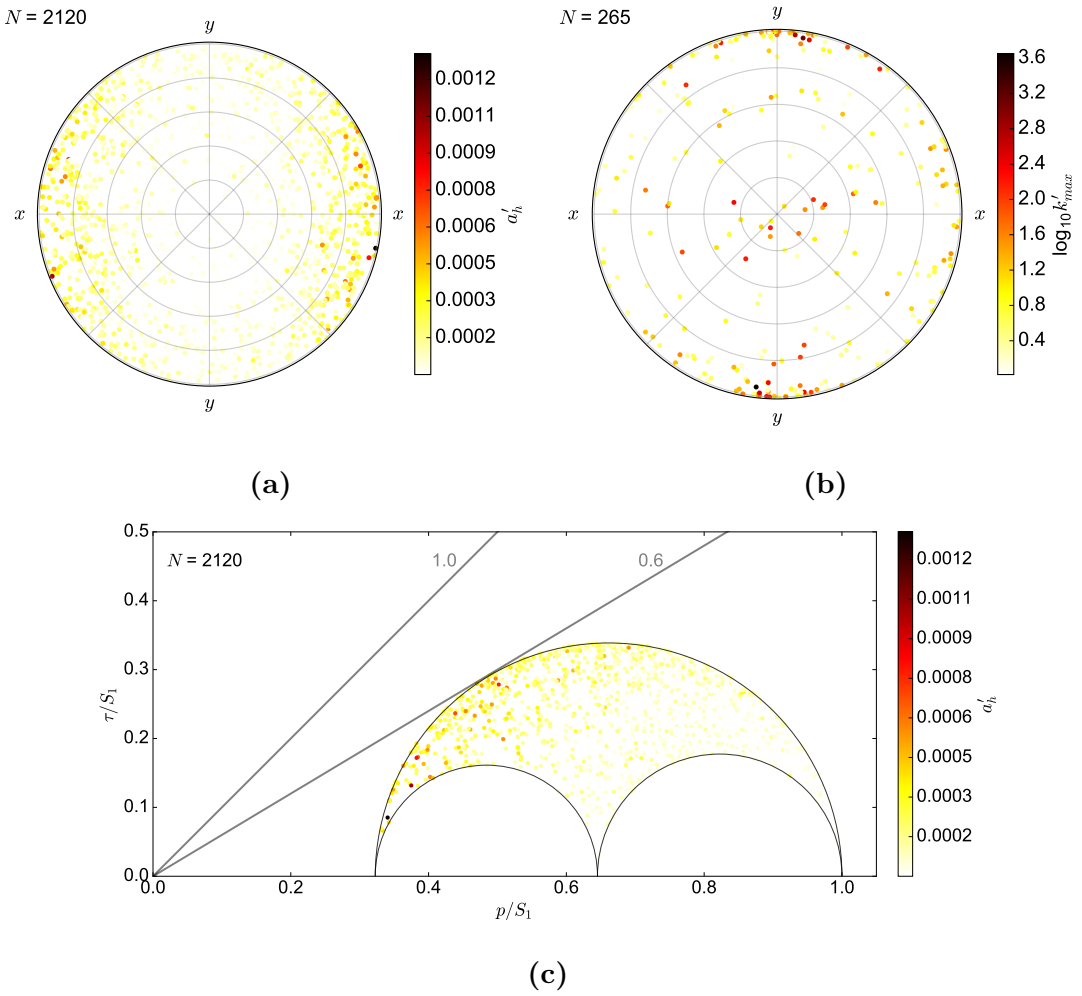
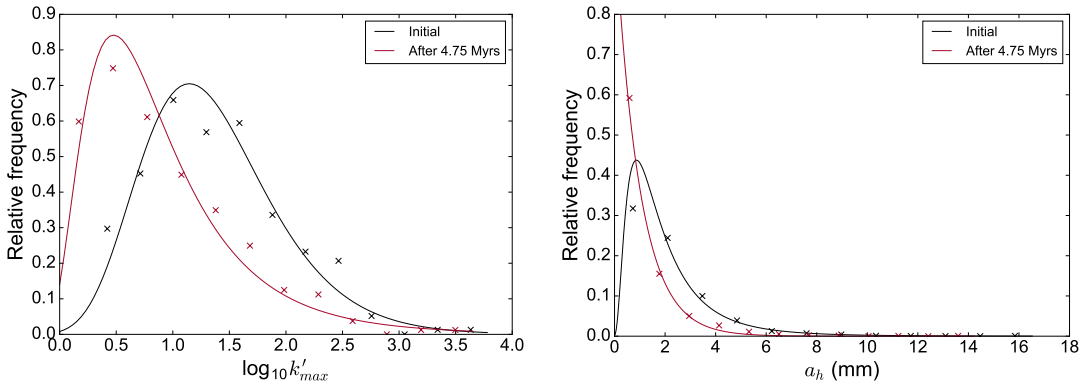


Figure 6.3: Quantitative results from 265 network DFM realisations after 4.75 Myr of pressure solution at 423 K. (a) Length-normalised hydraulic aperture, a'_{h}, on a stereonet where point locations mark poles of all fractures. (b) Normalised maximum permeability, k'_{max}, of the fracture rock mass subdomain Ω, on a stereonet projection where point locations mark orientation of corresponding eigenvectors. (c) Mohr circle plot, showing relation between a'_{h} and τ/p for all fractures.

increasingly favour the direction of the intermediate stress, S_2. In the long time limit, $a_{\mathrm{h},\parallel}$ will drop to zero long before $a_{\mathrm{h},\perp}$, which further supports this trend. Thus, the disproportional decline of the two transmissivity components in a single fracture contributes to the observed preferential flow direction over time. The post-dissolution hydraulic aperture of all fractures as a function of the projected stress-state paints the same picture, that fractures with large normal stress and little shear stress experience relatively larger compaction; see Figures 6.3c and 5.5c.



(a) **(b)**

Figure 6.4: Distributions before and after 4.75 Myr of pressure solution at 423 K of (a) maximum permeability magnitude over 265 DFM realisations, where $k'_{\mathrm{max}} = k_{\mathrm{max}}/k_{\mathrm{matrix}}$, and (b) of the hydraulic aperture, a_{h}, of all fractures therein. Note the implicit log-scaling of the abscissa in (a).

The distribution of maximum permeability (Figure 6.4a) and the underlying hydraulic apertures of all fractures (Figure 6.4b) both reflect the bespoke compaction of individual fractures. In combination with the preferential orientation of the k_{max} corresponding eigenvectors (Figure 6.3b), it can be concluded that the largest values at the right side of the spectrum (Figure 6.4a) are those aligned with the S_2 direction. While the initial distribution of fracture apertures can be fit by a log-normal, this shifts to an exponential distribution in the late time of the dissolution process (Figure 6.4b). This is due to the majority of fractures being in a sealed or near-sealing state close to a zero-aperture value.

It can be concluded that mechanically-chemically coupled compaction processes have at least the potential to be a contributing factor to field observations that critically oriented fractures are the most likely hydraulic conduits. The underlying explanations for this is that compaction is much reduced with increasing shear displacement (Figure 4.20d), which often characterises fractures that are close to Coulomb-failure due to their orientation with respect to the far-field stress [Barton et al., 1995]. Following the rationale that stress shear-activated fractures are the dominating conductors, it should also be expected that the preferential flow direction is aligned with the intermediate principal stress, an immediate consequence of the shear perpendicular transmissivity being larger than the shear parallel one. In

case of pressure dissolution, this inequality can extend to complete sealing in the parallel direction, thus leading to a further pronounced preference of flow along the orientation of the intermediate principal stress.

Chapter 7

Discussion and Conclusions

This work set out to predict properties of fractured rock by direct representation of geometrical features and first-principle simulations of physical processes. Specifically, the geometric features accounted for are power law size distributed fractures and self-affine rock surfaces - these characteristics are the most challenging from a modelling point of view, in particular with respect to scaling issues. The processes accounted for are elastic deformation, fracture contact, and pressure solution and precipitation. The central idea is that processes are responsible for the geometrical making of subsurface structures. Properties, such as transmissivity, stiffness and permeability, then result from this geometrical structure. The modelling of how processes control structure and how properties follow from the structural model are independent. A direct approach of this sort replaces scale-dependent empirical relationship and assumptions on property distributions. The resulting model should be able to capture emergent behaviour which transcends intuitive predictions.

The emerging key results from the presented approach are the anisotropic transmissivity of individual fractures, the transmissivity distribution of the fracture population, and the full permeability tensor of the fractured rock mass; all may be functions of time owing to the transient nature of processes with a chemical component. It has been shown that the developed model qualitatively reproduces two common field observations: critically oriented fractures should be expected

to be highly transmissive [Barton et al., 1995], and, given conjugate fracture sets, the direction of maximum permeability occurs when one set is aligned with the in-plane maximum principal stress [Heffer, 2002]. The integration of pore-scale chemical effects has shown that certain compaction processes have the potential to contribute to the notion that critically oriented fractures [Barton et al., 1995] are likely hydraulic conduits. Moreover, the studied compaction processes of pressure solution and precipitation tend to enhance the mechanically-induced preferential flow directions in two ways. First, fractures with large shear displacement are less prone to pressure solution compaction. Secondly, the decline of shear-parallel and -perpendicular transmissivity evolves disproportionally, with the shear-parallel direction sealing first. Both effects, combined with the mechanically-mediated preference, favour the direction of maximum permeability aligned with the intermediate stress. This orientation is, on average, aligned with the shear perpendicular direction.

This finding as to the most likely orientation of the maximum permeability is a significant contribution of this work. Previous hydro-mechanical simulations in two dimensions on the permeability of fractured rock masses have indicated that the most likely direction of the maximum principal permeability is aligned with the direction of the maximum principal stress [Baghbanan and Jing, 2008, Jing et al., 2013, Min et al., 2004b]. The extension to three dimensions developed herein, and the coupled direct simulation of individual fracture transmissivities as a result of network-scale shearing, showed that the shear-displacement induced anisotropic transmissivity of fractures leads to $k_{\max}$ favouring the direction of S_2, *i.e.*, the direction of maximum permeability is most likely to be aligned with the direction of the intermediate principal stress. If fracture transmissivities were assumed isotropic, the presented findings support conclusions of $k_{\max} \parallel S_1$ [Baghbanan and Jing, 2008, Jing et al., 2013, Min et al., 2004b], due to a preferential mechanical activation of S_1 aligned fractures. These conclusions should represent expectations given no particular information on the underlying fracture network geometry. These have been assumed isotropic herein, so any geometry induced

bias, which should be assumed to be severe, if not the dominating control, has not been accounted for.

Furthermore, the studied fracture networks have all been generated with the concept of equivalent permeability in mind. This is based on the observation of power law distributed fracture size, which, as a consequence, means that a fractured rock mass should be expected to be controlled by a few, large fractures present in the domain. The application of equivalent permeability lies in the quantification of total through flow between two open boundaries. As an example, the total flow between an excavated tunnel and an overlying lake can be quantified in that manner.

A further main contribution of the presented work is the accurate computation of equivalent and effective permeability independent of the reference system and fracture network geometry in full tensor form. This eliminates the need for periodic fracture network models as means to quantify the full permeability tensor [Malinouskaya et al., 2014], and is perfectly suitable for realistic fracture geometries, which result from outcrop mapping [Bisdom et al., 2016, Geiger et al., 2010, Hardebol et al., 2015, Matthäi and Belayneh, 2004], fracture growth algorithms [Paluszny and Matthäi, 2009, Paluszny and Matthai, 2010, Paluszny et al., 2016, Paluszny and Zimmerman, 2011, 2013], or are obtained from direct characterisation of natural fracture networks using micro-seismic surveys [Jones et al., 2014]. None of the resulting geometries can be expected to be periodic.

A critical point in the presented approach is the assignment of the average fracture hydraulic properties to the entire fracture for the permeability calculation at the rock mass scale. This assumes that individual fractures themselves have a representative scale, hydraulically speaking. This contradicts observations that single shear induced channels exist that are larger than others, and that no representative scale for rock fracture transmissivity has been found as of yet [Ishibashi et al., 2015, Raven and Gale, 1985, Witherspoon et al., 1980]. However, the option on the opposing side of the spectrum, to impose a spatially distributed transmissivity across each fracture [De Dreuzy et al., 2012, Hamzehpour et al., 2009], will not

converge with decreasing cell size until a very small discretisation is reached. This would, in turn, defeat the purpose and ability to model large-scale domains. The presented approach is a compromise, and a rigorous solution may not be possible due to the lack of a representative elementary volume. It follows that rigorous upscaling at this scale boundary may not be possible; this considered, the chosen path represents a compromise consistent with the majority of work in this area [Bogdanov et al., 2007, Davy et al., 2006, De Dreuzy et al., 2001, Ebigbo et al., 2016, Lang et al., 2014, Mourzenko et al., 2011, Sævik et al., 2014], while additionally preserving the anisotropy of fracture transmissivity.

From the use of an average transmissivity over individual fractures follows a more subtle question regarding proper representation of connectivity between intersecting fractures. The channelised nature of the fracture pore-space more often than not results in a single, dominating channel. When two fractures intersect, chances are that their dominant channels do not - another consequence of the lack of a representative elementary volume of the fracture pore-space. The non-communication between dominant flow channels of intersecting fractures may have significant impact on the connectivity of the network [for a discussion, see De Dreuzy et al., 2012]. This connectivity effect may very well be mitigated to a significant extent by highly permeable fracture intersections. Even though intersection permeability is not explicitly represented in the flow model, numerical simulations show relatively larger displacements at the intersections. The resulting high permeability zones would allow for pressure to equilibrate between flow channels and permit better connectivity, even if the channels themselves do not intersect.

The developed one-way hydro-mechanical-chemical coupling of processes implies a time-invariant friction coefficient. At appreciable depth, this assumption reflects the observation that the coefficient of friction has a well-defined mean of ≈ 0.6 at high pressures [Byerlee, 1978]. However, at low pressures, or low depths, surface topology should be expected to constitute a first-order control of the friction coefficient. The effects of pressure solution and precipitation on this coefficient are difficult to anticipate. This is mostly due to the difficulties associated with direct modelling of friction between rough surfaces [Persson et al., 2005]. On one hand,

the increased contact area that results from chemical processes could increase the friction coefficient, due to the increased area over which attractive van der Waals interaction forces can take place. In fact, smoother rock surfaces have been found to have higher friction coefficients than their rougher counterparts at low levels of confining pressures [Biegel et al., 1992]. On the other hand, friction is considered a function of the average surface slope [Li et al., 2013], which decreases during the dissolution process.

In conclusion it can be stated that some of the most important characteristics of fractured rock, namely those of stiffness, transmissivity, and permeability emerge from a direct representation of geometry, physical states and ensuing processes across different scales. The inputs to the developed framework are limited to the fracture geometry and material properties. The friction coefficient is the only free parameter employed, and represents the link between the scales where fractures are treated as planar continuities, and as rough surfaces. The need for empirical relationships is therefore widely eliminated, and a path forward is presented that clears the way for simulations that capture emergent behaviour.

References

Ahmed, R., Edwards, M. G., Lamine, S., Huisman, B. A., and Pal, M. (2015). Three-dimensional control-volume distributed multi-point flux approximation coupled with a lower-dimensional surface fracture model. *Journal of Computational Physics*, 303:470–497.

Akarapu, S., Sharp, T., and Robbins, M. O. (2011). Stiffness of contacts between rough surfaces. *Physical Review Letters*, 106(20):204301.

Almqvist, A., Sahlin, F., Larsson, R., and Glavatskih, S. (2007). On the dry elasto-plastic contact of nominally flat surfaces. *Tribology International*, 40(4):574–579.

Amaziane, B., Hontans, T., and Koebbe, J. (2001). Equivalent permeability and simulation of two-phase flow in heterogeneous porous media. *Computational Geosciences*, 5(4):279–300.

Archard, J. F. (1957). Elastic deformation and the laws of friction. *Proceedings of the Royal Society A: Mathematical, Physical and Engineering Sciences*, 243(1233):190–205.

Atkinson, B. K. (1980). Stress corrosion and the rate-dependent tensile failure of a fine-grained quartz rock. *Tectonophysics*, 65(3-4):281–290.

Auradou, H., Drazer, G., Hulin, J. P., and Koplik, J. (2005). Permeability anisotropy induced by the shear displacement of rough fracture walls. *Water Resources Research*, 41(9):1–10.

Azizmohammadi, S. and Paul, J. D. (2012). Scale dependence of equivalent permeability tensor in naturally fractured reservoirs. In *European Geosciences Union - General Assembly*.

Baghbanan, A. and Jing, L. (2008). Stress effects on permeability in a fractured rock mass with correlated fracture length and aperture. *International Journal of Rock Mechanics and Mining Sciences*, 45(8):1320–1334.

Bandis, S. C. (1980). *Experimental studies of scale effects on shear strength, and deformation of rock joints*. Phd thesis, University of Leeds.

Bandis, S. C., Lumsden, A. C., and Barton, N. R. (1983). Fundamentals of rock joint deformation. *International Journal of Rock Mechanics and Mining Sciences & Geomechanics Abstracts*, 20(6):249–268.

Barton, C. A., Zoback, M. D., and Moos, D. (1995). Fluid flow along potentially active faults in crystalline rock. *Geology*, 23(8):683–686.

Barton, C. C. (1995). Fractal analysis of scaling and spatial clustering of fractures. In Barton, C. C. and La Pointe, P. R., editors, *Fractals in the Earth Sciences*, pages 141–178. Springer, Boston.

Barton, N. (2007). Thermal over-closure of joints and rock masses and implications for HLW repositories. In *11th ISRM congress*, pages 109–116.

Barton, N. and Quadros, E. (2015). Anisotropy is everywhere, to see, to measure, and to model. *Rock Mechanics and Rock Engineering*, 48(4):1323–1339.

Barton, N. R., Bandis, S. C., and Bakhtar, K. (1985). Strength, deformation and conductivity coupling of rock joints. *International Journal of Rock Mechanics and Mining Sciences & Geomechanics Abstracts*, 22(3):121–140.

Bear, J. (1972). *Dynamics of fluids in porous media*. American Elsevier, New York.

Beeler, N. M. and Hickman, S. H. (2004). Stress-induced, time-dependent fracture closure at hydrothermal conditions. *Journal of Geophysical Research*, 109(B2):B02211.

Beeler, N. M. and Hickman, S. H. (2015). Direct measurement of asperity contact growth in quartz at hydrothermal conditions. *Journal of Geophysical Research: Solid Earth*, 120(5):3599–3616.

Belayneh, M., Geiger, S., and Matthäi, S. K. (2006). Numerical simulation of water injection into layered fractured carbonate reservoir analogs. *AAPG Bulletin*, 90(10):1473–1493.

Bernabé, Y. and Evans, B. (2007). Numerical modelling of pressure solution deformation at axisymmetric asperities under normal load. *Geological Society, London, Special Publications*, 284(1):185–205.

Bernabé, Y. and Evans, B. (2014). Pressure solution creep of random packs of spheres. *Journal of Geophysical Research: Solid Earth*, 119(5):4202–4218.

Berthoud, P. and Baumberger, T. (1998). Shear stiffness of a solid-solid multicontact interface. *Proceedings of the Royal Society A: Mathematical, Physical and Engineering Sciences*, 454(1974):1615–1634.

Biegel, R. L., Wang, W., Scholz, C. H., Boitnott, G. N., and Yoshioka, N. (1992). Micromechanics of rock friction 1. Effects of surface roughness on initial friction and slip hardening in westerly granite. *Journal of Geophysical Research*, 97(B6):8951.

Bisdom, K., Bertotti, G., and Nick, H. M. (2016). The impact of in-situ stress and outcrop-based fracture geometry on hydraulic aperture and upscaled permeability in fractured reservoirs. *Tectonophysics*, in print.

Blaisonneau, A., Peter-Borie, M., and Gentier, S. (2016). Evolution of fracture permeability with respect to fluid/rock interactions under thermohydromechanical conditions: development of experimental reactive percolation tests. *Geothermal Energy*, 4(1):3.

Bogdanov, I., Mourzenko, V., Thovert, J.-F., and Adler, P. (2007). Effective permeability of fractured porous media with power-law distribution of fracture sizes. *Physical Review E*, 76(3):036309.

Bogdanov, I. I., Mourzenko, V. V., Thovert, J.-F., and Adler, P. M. (2003). Effective permeability of fractured porous media in steady state flow. *Water Resources Research*, 39(1):1023.

Boggs, S. (2006). *Principles of sedimentology and stratigraphy*. Pearson Prentice Hall, 4th edition.

Bonnet, E., Bour, O., Odling, N. E., Davy, P., Main, I., Cowie, P., and Berkowitz, B. (2001). Scaling of fracture systems in geological media. *Reviews of Geophysics*, 39(3):347–383.

Borri-Brunetto, M., Carpinteri, A., and Chiaia, B. (1999). Scaling phenomena due to fractal contact in concrete and rock fractures. *International Journal of Fracture*, 12:221–238.

Borri-Brunetto, M., Chiaia, B., and Ciavarella, M. (2001). Incipient sliding of rough surfaces in contact: a multiscale numerical analysis. *Computer Methods in Applied Mechanics and Engineering*, 190(46-47):6053–6073.

Brown, S. (1987). Fluid flow through rock joints: the effect of surface roughness. *Journal of Geophysical Research*, 92:1337–1347.

Brown, S. (1995). Simple mathematical model of a rough fracture. *Journal of Geophysical Research-Solid Earth*, 100(B4):5941–5952.

Brown, S. R., Kranz, R. L., and Bonner, B. P. (1986). Correlation between the surfaces of natural rock joints. *Geophysical Research Letters*, 13(13):1430–1433.

Brown, S. R. and Scholz, C. H. (1985a). Broad bandwidth study of the topography of natural rock surfaces. *Journal of Geophysical Research*, 90(B14):12575.

Brown, S. R. and Scholz, C. H. (1985b). Closure of random elastic surfaces in contact. *Journal of Geophysical Research*, 90(B7):5531.

Brown, S. R. and Scholz, C. H. (1986). Closure of rock joints. *Journal of Geophysical Research*, 91(B5):4939.

Bruggeman, D. A. G. (1935). Berechnung verschiedener physikalischer Konstanten von heterogenen Substanzen. I. Dielektrizitätskonstanten und Leitfähigkeiten der Mischkörper aus isotropen Substanzen. *Annalen der Physik*, 416(7):636–664.

Bucher, F., Knothe, K., and Theiler, A. (2002). Normal and tangential contact problem of surfaces with measured roughness. *Wear*, 253(1-2):204–218.

Bush, A. W., Gibson, R. D., and Thomas, T. R. (1975). The elastic contact of a rough surface. *Wear*, 35:87–111.

Byerlee, J. (1978). Friction of rocks. *Pure and Applied Geophysics*, 116(4-5):615–626.

Campañá, C., Persson, B. N. J., and Müser, M. H. (2011). Transverse and normal interfacial stiffness of solids with randomly rough surfaces. *Journal of Physics: Condensed Matter*, 23(8):085001.

Candela, T., Renard, F., Bouchon, M., Brouste, A., Marsan, D., Schmittbuhl, J., and Voisin, C. (2009). Characterization of fault roughness at various scales: Implications of three-dimensional high resolution topography measurements. *Pure and Applied Geophysics*, 166(10-11):1817–1851.

Candela, T., Renard, F., Klinger, Y., Mair, K., Schmittbuhl, J., and Brodsky, E. E. (2012). Roughness of fault surfaces over nine decades of length scales. *Journal of Geophysical Research*, 117(B8):B08409.

Carbone, G. and Bottiglione, F. (2008). Asperity contact theories: Do they predict linearity between contact area and load? *Journal of the Mechanics and Physics of Solids*, 56(8):2555–2572.

Caulk, R. A., Ghazanfari, E., Perdrial, J. N., and Perdrial, N. (2016). Experimental investigation of fracture aperture and permeability change within Enhanced Geothermal Systems. *Geothermics*, 62:12–21.

Cook, N. G. W. (1992). Natural joints in rock: Mechanical, hydraulic and seismic behaviour and properties under normal stress. *International Journal of Rock Mechanics and Mining Sciences & Geomechanics Abstracts*, 29(3):198–223.

Cundall, P. A. (1980). UDEC - A generalised distinct element program for modelling jointed rock. Technical report, Cundall Associates.

Dapp, W. B., Lücke, A., Persson, B. N. J., and Müser, M. H. (2012). Self-affine elastic contacts: Percolation and leakage. *Physical Review Letters*, 108(24):244301.

Davy, P., Bour, O., De Dreuzy, J.-R., and Darcel, C. (2006). Flow in multi-scale fractal fracture networks. *Geological Society, London, Special Publications*, 261(1):31–45.

De Dreuzy, J. R., Davy, P., and Bour, O. (2001). Hydraulic properties of two-dimensional random fracture networks following a power law length distribution 2. Permeability of networks based on lognormal distribution of apertures. *Water Resources Research*, 37(8):2079–2095.

De Dreuzy, J. R., Méheust, Y., and Pichot, G. (2012). Influence of fracture scale heterogeneity on the flow properties of three-dimensional discrete fracture networks (DFN). *Journal of Geophysical Research B: Solid Earth*, 117(11):1–21.

Deng, H., Fitts, J., Peters, C., Li, L., Crandall, D., and Bromhal, G. (2013). Experimental study of reactive flow in an Eau Claire fracture exposed to CO2-rich brine. In *47th US Rock Mechanics / Geomechanics Symposium*.

Deng, H., Fitts, J. P., Crandall, D., McIntyre, D., and Peters, C. A. (2015). Alterations of fractures in carbonate rocks by CO2-acidified brines. *Environmental Science & Technology*, 49(16):10226–10234.

Detournay, E. (1979). *The interaction of deformation and hydraulic conductivity in rock fracture: An experimental and analytical study*. Msc thesis, University of Minnesota.

Detwiler, R. L. (2008). Experimental observations of deformation caused by mineral dissolution in variable-aperture fractures. *Journal of Geophysical Research*, 113(B8):B08202.

Dieterich, J. H. and Kilgore, B. D. (1996). Imaging surface contacts: power law contact distributions and contact stresses in quartz, calcite, glass and acrylic plastic. *Tectonophysics*, 256(1-4):219–239.

Dove, P. M. (1995). Geochemical controls on the kinetics of quartz fracture at subcritical tensile stresses. *Journal of Geophysical Research*, 100(B11):22349.

Durlofsky, L. J. (1991). Numerical calculation of equivalent grid block permeability tensors for heterogeneous porous media. *Water Resources Research*, 27(5):699–708.

Ebigbo, A., Lang, P. S., Paluszny, A., and Zimmerman, R. W. (2016). Inclusion-based effective medium models for the permeability of a 3D fractured rock mass. *Transport in Porous Media*, 113(1):137–158.

Elkhoury, J. E., Ameli, P., and Detwiler, R. L. (2013). Dissolution and deformation in fractured carbonates caused by flow of CO2-rich brine under reservoir conditions. *International Journal of Greenhouse Gas Control*, 16:S203–S215.

Faoro, I., Elsworth, D., and Candela, T. (2015). Evolution of the transport properties of fractures subject to thermally and mechanically activated mineral alteration and redistribution. *Geofluids*.

Fardin, N., Feng, Q., and Stephansson, O. (2004). Application of a new in situ 3D laser scanner to study the scale effect on the rock joint surface roughness. *International Journal of Rock Mechanics and Mining Sciences*, 41(2):329–335.

Fardin, N., Stephansson, O., and Jing, L. (2001). The scale dependence of rock joint surface roughness. *International Journal of Rock Mechanics and Mining Sciences*, 38(5):659–669.

Farin, D. and Avnir, D. (1987). Reactive fractal surfaces. *The Journal of Physical Chemistry*, 91(22):5517–5521.

Farmer, C. L. (2002). Upscaling: a review. *International Journal for Numerical Methods in Fluids*, 40(1-2):63–78.

Farough, A., Moore, D. E., Lockner, D. A., and Lowell, R. P. (2016). Evolution of fracture permeability of ultramafic rocks undergoing serpentinization at hydrothermal conditions: An experimental study. *Geochemistry, Geophysics, Geosystems*, 17(1):44–55.

Figueiredo, B., Tsang, C.-F., Rutqvist, J., and Niemi, A. (2015). A study of changes in deep fractured rock permeability due to coupled hydro-mechanical effects. *International Journal of Rock Mechanics and Mining Sciences*, 79:70–85.

Fox, A., Pointe, P. L., Hermanson, J., and Öhman, J. (2007). Statistical geological discrete fracture network model. Technical Report November, Swedish Nuclear Fuel and Waste Management Co.

Gale, J. E. (1982). The effects of fracture type (induced versus natural) on the stress-fracture closure-fracture permeability relationships. *The 23rd US Symposium on Rock Mechanics*, pages 290–298.

Garipov, T. T. and Tchelepi, H. A. (2016). A discrete fracture model for coupled flow and geomechanics. *Computational Geosciences*, in press.

Geiger, S., Cortis, A., and Birkholzer, J. T. (2010). Upscaling solute transport in naturally fractured porous media with the continuous time random walk method. *Water Resources Research*, 46(12).

Geiger, S., Roberts, S., Matthäi, S. K., Zoppou, C., and Burri, A. (2004). Combining finite element and finite volume methods for efficient multiphase flow simulations in highly heterogeneous and structurally complex geologic media. *Geofluids*, 4(4):284–299.

Gentier, S. S. and Hopkins, D. L. (1997). Mapping fracture aperture as a function of normal stress using a combination of casting, image analysis and modeling techniques. *International Journal of Rock Mechanics and Mining Sciences*, 34(3-4):132.e1–132.e14.

Glover, P. W. J., Matsuki, K., Hikima, R., and Hayashi, K. (1998). Synthetic rough fractures in rocks. *Journal of Geophysical Research*, 103:9609.

Goodman, R. E. (1976). *Methods of Geological Engineering in Discontinuous Rocks*. West Publishing, New York, NY.

Greenwood, J. A. and Williamson, J. B. P. (1966). Contact of nominally flat surfaces. *Proceedings of the Royal Society A: Mathematical, Physical and Engineering Sciences*, 295(1442):300–319.

Guyer, J. E., Wheeler, D., and Warren, J. A. (2009). FiPy: Partial differential equations with python. *Computing in Science & Engineering*, 11(3):6–15.

Hamzehpour, H., Mourzenko, V. V., Thovert, J. F., and Adler, P. M. (2009). Percolation and permeability of networks of heterogeneous fractures. *Physical Review E - Statistical, Nonlinear, and Soft Matter Physics*, 79(3):1–12.

Hardebol, N. J., Maier, C., Nick, H., Geiger, S., Bertotti, G., and Boro, H. (2015). Multiscale fracture network characterization and impact on flow: A case study on the Latemar carbonate platform. *Journal of Geophysical Research: Solid Earth*, 120(12):8197–8222.

Hashida, T., Oghikubo, H., Takahashi, H., and Shoji, T. (1993). Numerical simulation with experimental verification of the fracture behavior in granite under confining pressures based on the tension-softening model. *International Journal of Fracture*, 59(3):227–244.

He, W. (2003). Creep compaction of quartz aggregates: Effects of pore-fluid flow–A combined experimental and theoretical study. *American Journal of Science*, 303(2):73–93.

Heffer, K. (2002). Geomechanical Influences in Water Injection Projects: an Overview. *Oil & Gas Science and Technology*, 57(5):415–422.

Hermanson, J., Hansen, L., Olofsson, J., Sävås, J., and Vestgård, J. (2003). Detailed fracture mapping at the KFM02 and KFM03 drill sites. Technical report, Swedish Nuclear Fuel and Waste Management Co.

Holden, L. and Lia, O. (1992). A tensor estimator for the homogenization of absolute permeability. *Transport in Porous Media*, 8(1):37–46.

Hopkins, D. L., Cook, N. G. W., and Myer, L. R. (1987). Fracture stiffness and aperture as a function of applied stress and contact geometry. In *28th US Symposium on Rock Mechanics*, pages 673–680, Tucson.

Hopkins, D. L., Cook, N. G. W., and Myer, L. R. (1990). Normal joint stiffness as a function of spatial geometry and surface roughness. In Barton and Stephansson, editors, *Rock Joints*, pages 203–210. Balkema, Rotterdam.

Huseby, O., Thovert, J.-F., and Adler, P. M. (1997). Geometry and topology of fracture systems. *Journal of Physics A: Mathematical and General*, 30(5):1415–1444.

Hyun, S., Pei, L., Molinari, J.-F., and Robbins, M. (2004). Finite-element analysis of contact between elastic self-affine surfaces. *Physical Review E*, 70(2):026117.

Ishibashi, T., Watanabe, N., Hirano, N., Okamoto, A., and Tsuchiya, N. (2015). Beyond-laboratory-scale prediction for channeling flows through subsurface rock fractures with heterogeneous aperture distributions revealed by laboratory evaluation. *Journal of Geophysical Research: Solid Earth*, 120(1):106–124.

Jackson, R. L. and Green, I. (2005). A finite element study of elasto-plastic hemispherical contact against a rigid flat. *Journal of Tribology*, 127(2):343.

Jackson, R. L. and Green, I. (2011). On the modeling of elastic contact between rough surfaces. *Tribology Transactions*, 54(2):300–314.

Jaeger, J. C., Cook, N. G. W., and Zimmerman, R. W. (2007). *Fundamentals of Rock Mechanics*. Blackwell, 4th edition.

Jing, L., Min, K.-B., Baghbanan, a., and Zhao, Z. (2013). Understanding coupled stress, flow and transport processes in fractured rocks. *Geosystem Engineering*, 16(1):2–25.

Johnson, K. (1985). *Contact Mechanics*. Cambridge University Press, Cambridge.

Jones, G. A., Kendall, J. M., Bastow, I., Raymer, D. G., and Wuestefeld, A. (2014). Characterization of fractures and faults: A multi-component passive microseismic study from the Ekofisk reservoir. *Geophysical Prospecting*, 62(4):779–796.

Karcz, Z., Aharonov, E., Ertas, D., Polizzotti, R., and Scholz, C. H. (2008). Deformation by dissolution and plastic flow of a single crystal sodium chloride indenter: An experimental study under the confocal microscope. *Journal of Geophysical Research*, 113(B4):B04205.

Karpenko, Y. a. and Akay, A. (2001). A numerical model of friction between rough surfaces. *Tribology International*, 34:531–545.

Katz, O. (2004). Microfracturing, damage, and failure of brittle granites. *Journal of Geophysical Research*, 109(B1):B01206.

Kendall, K. and Tabor, D. (1971). An ultrasonic study of the area of contact between stationary and sliding surfaces. *Proceedings of the Royal Society A: Mathematical, Physical and Engineering Sciences*, 323(1554):321–340.

Kirkpatrick, S. (1973). Percolation and Conduction. *Reviews of Modern Physics*, 45(4):574–588.

Koudina, N., Gonzalez Garcia, R., Thovert, J.-F., and Adler, P. (1998). Permeability of three-dimensional fracture networks. *Physical Review E*, 57(4):4466–4479.

Lang, P. S., Paluszny, A., and Zimmerman, R. W. (2014). Permeability tensor of three-dimensional fractured porous rock and a comparison to trace map predictions. *Journal of Geophysical Research: Solid Earth*, 119(8):6288–6307.

Lang, P. S., Paluszny, A., and Zimmerman, R. W. (2015). Hydraulic sealing due to pressure solution contact zone growth in siliciclastic rock fractures. *Journal of Geophysical Research: Solid Earth*, 120(6):4080–4101.

Lehner, F. (1995). A model for intergranular pressure solution in open systems. *Tectonophysics*, 245(3-4):153–170.

Lehner, F. and Leroy, Y. (2004). Sandstone compaction by intergranular pressure solution. In Guéguen, Y. and Boutéca, M., editors, *Mechanics of Fluid-Saturated Rocks*, volume 89, pages 115–168. International Geophysics Series.

Lei, Q., Latham, J.-p., Tsang, C.-f., Xiang, J., and Lang, P. (2015a). A new approach to upscaling fracture network models while preserving geostatistical and geomechanical characteristics. *Journal of Geophysical Research: Solid Earth*, 120(7):4784–4807.

Lei, Q., Latham, J.-P., Xiang, J., and Tsang, C.-F. (2015b). Polyaxial stress-induced variable aperture model for persistent 3D fracture networks. *Geomechanics for Energy and the Environment*, 1:34–47.

Lei, Q. and Wang, X. (2016). Tectonic interpretation of the connectivity of a multiscale fracture system in limestone. *Geophysical Research Letters*, 43(4):1551–1558.

Leung, C. T. O. and Zimmerman, R. W. (2012). Estimating the hydraulic conductivity of two-dimensional fracture networks using network geometric properties. *Transport in Porous Media*, 93(3):777–797.

Li, B., Zhao, Z., Jiang, Y., and Jing, L. (2015). Contact mechanism of a rock fracture subjected to normal loading and its impact on fast closure behavior during initial stage of fluid flow experiment. *International Journal for Numerical and Analytical Methods in Geomechanics*, 39(13):1431–1449.

Li, Q., Popov, M., Dimaki, A., Filippov, A. E., Kürschner, S., and Popov, V. L. (2013). Friction Between a Viscoelastic Body and a Rigid Surface with Random Self-Affine Roughness. *Physical Review Letters*, 111(3):034301.

Liu, R., Li, B., and Jiang, Y. (2016). A fractal model based on a new governing equation of fluid flow in fractures for characterizing hydraulic properties of rock fracture networks. *Computers and Geotechnics*, 75:57–68.

Long, J. C. S., Remer, J. S., Wilson, C. R., and Witherspoon, P. A. (1982). Porous media equivalents for networks of discontinuous fractures. *Water Resources Research*, 18(3):645–658.

Luan, B. and Robbins, M. O. (2005). The breakdown of continuum models for mechanical contacts. *Nature*, 435(7044):929–932.

Malinouskaya, I., Thovert, J.-F., Mourzenko, V. V., Adler, P. M., Shekhar, R., Agar, S., Rosero, E., and Tsenn, M. (2014). Fracture analysis in the Amellago outcrop and permeability predictions. *Petroleum Geoscience*, 20(1):93–107.

Matsuki, K., Chida, Y., Sakaguchi, K., and Glover, P. (2006). Size effect on aperture and permeability of a fracture as estimated in large synthetic fractures. *International Journal of Rock Mechanics and Mining Sciences*, 43(5):726–755.

Matsuki, K., Wang, E., Sakaguchi, K., and Okumura, K. (2001). Time-dependent closure of a fracture with rough surfaces under constant normal stress. *International Journal of Rock Mechanics and Mining Sciences*, 38(5):607–619.

Matthäi, S. K. and Belayneh, M. (2004). Fluid flow partitioning between fractures and a permeable rock matrix. *Geophysical Research Letters*, 31(7):L07602.

Matthäi, S. K., Geiger, S., Roberts, S. G., Paluszny, A., Belayneh, M., Burri, A., Mezentsev, A., Lu, H., Coumou, D., Driesner, T., and Heinrich, C. A. (2007). Numerical simulation of multi-phase fluid flow in structurally complex reservoirs. *Geological Society, London, Special Publications*, 292(1):405–429.

McDermott, C., Bond, A., Harris, A. F., Chittenden, N., and Thatcher, K. (2015). Application of hybrid numerical and analytical solutions for the simulation of coupled thermal, hydraulic, mechanical and chemical processes during fluid flow through a fractured rock. *Environmental Earth Sciences*.

McGuire, T. P., Elsworth, D., and Karcz, Z. (2013). Experimental measurements of stress and chemical controls on the evolution of fracture permeability. *Transport in Porous Media*, 98(1):15–34.

Menke, H., Andrew, M., Blunt, M., and Bijeljic, B. (2016). Reservoir condition imaging of reactive transport in heterogeneous carbonates using fast synchrotron tomography — Effect of initial pore structure and flow conditions. *Chemical Geology*, 428:15–26.

Min, K.-B., Jing, L., and Stephansson, O. (2004a). Determining the equivalent permeability tensor for fractured rock masses using a stochastic REV approach: Method and application to the field data from Sellafield, UK. *Hydrogeology Journal*, 12(5):497–510.

Min, K.-B., Rutqvist, J., Tsang, C.-F., and Jing, L. (2004b). Stress-dependent permeability of fractured rock masses: a numerical study. *International Journal of Rock Mechanics and Mining Sciences*, 41(7):1191–1210.

Moore, D. E., Lockner, D. A., and Byerlee, J. D. (1994). Reduction of permeability in granite at elevated temperatures. *Science*, 265(5178):1558–61.

Morrow, C. A., Moore, D. E., and Lockner, D. A. (2001). Permeability reduction in granite under hydrothermal conditions. *Journal of Geophysical Research*, 106(B12):30551.

Mourzenko, V., Thovert, J.-F., and Adler, P. (2005). Percolation of three-dimensional fracture networks with power-law size distribution. *Physical Review E*, 72(3):036103.

Mourzenko, V. V., Thovert, J.-F., and Adler, P. M. (2011). Permeability of isotropic and anisotropic fracture networks, from the percolation threshold to very large densities. *Physical Review E*, 84(3):036307.

Munier, R. (2004). Statistical analysis of fracture data, adapted for modelling Discrete Fracture Networks-Version 2. Technical report, Swedish Nuclear Fuel and Waste Management Co.

Muralha, J. (1999). A probabilistic model for the normal compliance of rock joints. In *9th ISRM Congress, 25-28 August, Paris, France*. International Society for Rock Mechanics.

Myer, L. R. (2000). Fractures as collections of cracks. *International Journal of Rock Mechanics and Mining Sciences*, 37:231–243.

Nayak, P. R. (1971). Random process model of rough surfaces. *Journal of Lubrication Technology*, 93(3):398.

Nejati, M., Paluszny, A., and Zimmerman, R. W. (2015a). A disk-shaped domain integral method for the computation of stress intensity factors using tetrahedral meshes. *International Journal of Solids and Structures*, 69-70:230–251.

Nejati, M., Paluszny, A., and Zimmerman, R. W. (2015b). On the use of quarter-point tetrahedral finite elements in linear elastic fracture mechanics. *Engineering Fracture Mechanics*, 144:194–221.

Nejati, M., Paluszny, A., and Zimmerman, R. W. (2016). A finite element framework for modeling internal frictional contact in three-dimensional fractured media using unstructured tetrahedral meshes. *Computer Methods in Applied Mechanics and Engineering*, in press.

Nemoto, K., Watanabe, N., Hirano, N., and Tsuchiya, N. (2009). Direct measurement of contact area and stress dependence of anisotropic flow through rock fracture with heterogeneous aperture distribution. *Earth and Planetary Science Letters*, 281(1-2):81–87.

Neretnieks, I. (2014). Stress-mediated closing of fractures: Impact of matrix diffusion. *Journal of Geophysical Research: Solid Earth*, 119(5):4149–4163.

Neuville, A., Toussaint, R., and Schmittbuhl, J. (2011). Hydraulic transmissivity and heat exchange efficiency of open fractures: a model based on lowpass filtered apertures. *Geophysical Journal International*, 186(3):1064–1072.

Nick, H. M. and Matthäi, S. K. (2011). Comparison of three FE-FV numerical schemes for single- and two-phase flow simulation of fractured porous media. *Transport in Porous Media*, 90(2):421–444.

Nick, H. M., Paluszny, A., Blunt, M. J., and Matthai, S. K. (2011). Role of geomechanically grown fractures on dispersive transport in heterogeneous geological formations. *Physical Review E*, 84(5):056301.

Niemeijer, A., Spiers, C., and Bos, B. (2002). Compaction creep of quartz sand at 400-600 C: experimental evidence for dissolution-controlled pressure solution. *Earth and Planetary Science Letters*, 195(3-4):261–275.

Ochi, J. and Vernoux, J.-F. (1998). Permeability decrease in sandstone reservoirs by fluid injection. *Journal of Hydrology*, 208(3-4):237–248.

Oda, M. (1985). Permeability tensor for discontinuous rock masses. *Geotechnique*, 35(4):483–495.

Olson, J. E. (2003). Sublinear scaling of fracture aperture versus length: An exception or the rule? *Journal of Geophysical Research*, 108(B9):2413.

Palandri, J. L. and Kharaka, Y. K. (2004). A compilation of rate parameters of water-mineral interaction kinetics for application to geochemical modeling. *U.S. Geological Survey Open file Report*.

Paluszny, A. and Matthäi, S. K. (2009). Numerical modeling of discrete multi-crack growth applied to pattern formation in geological brittle media. *International Journal of Solids and Structures*, 46(18-19):3383–3397.

Paluszny, A. and Matthai, S. K. (2010). Impact of fracture development on the effective permeability of porous rocks as determined by 2-D discrete fracture growth modeling. *Journal of Geophysical Research*, 115(B2):B02203.

Paluszny, A., Matthäi, S. K., and Hohmeyer, M. (2007). Hybrid finite element-finite volume discretization of complex geologic structures and a new simulation workflow demonstrated on fractured rocks. *Geofluids*, 7(2):186–208.

Paluszny, A., Tang, X., Nejati, M., and Zimmerman, R. W. (2016). A direct fragmentation method with Weibull function distribution of sizes based on finite- and discrete element simulations. *International Journal of Solids and Structures*, 80:38–51.

Paluszny, A. and Zimmerman, R. W. (2011). Numerical simulation of multiple 3D fracture propagation using arbitrary meshes. *Computer Methods in Applied Mechanics and Engineering*, 200(9-12):953–966.

Paluszny, A. and Zimmerman, R. W. (2013). Numerical fracture growth modeling using smooth surface geometric deformation. *Engineering Fracture Mechanics*, 108:19–36.

Pastewka, L., Prodanov, N., Lorenz, B., Müser, M. H., Robbins, M. O., and Persson, B. N. J. (2013). Finite-size scaling in the interfacial stiffness of rough elastic contacts. *Physical Review E - Statistical, Nonlinear, and Soft Matter Physics*, 87(6):1–9.

Peitgen, H.-O., Saupe, D., Barnsley, M. F., Fisher, Y., and McGuire, M. (1988). *The science of fractal images*. Springer New York.

Persson, B. N. J. (2001). Theory of rubber friction and contact mechanics. *Journal of Chemical Physics*, 115(8):3840.

Persson, B. N. J. (2006). Contact mechanics for randomly rough surfaces. *Surface Science Reports*, 61(4):201–227.

Persson, B. N. J. (2014). On the fractal dimension of rough surfaces. *Tribology Letters*, 54(1):99–106.

Persson, B. N. J., Albohr, O., Tartaglino, U., Volokitin, A. I., and Tosatti, E. (2005). On the nature of surface roughness with application to contact mechanics, sealing, rubber friction and adhesion. *Journal of Physics: Condensed Matter*, 17(1):R1–R62.

Persson, B. N. J. and Yang, C. (2008). Theory of the leak-rate of seals. *Journal of Physics: Condensed Matter*, 20(31):315011.

Petrovitch, C. L., Nolte, D. D., and Pyrak-Nolte, L. J. (2013). Scaling of fluid flow versus fracture stiffness. *Geophysical Research Letters*, 40(April):2076–2080.

Petrovitch, C. L., Pyrak-Nolte, L. J., and Nolte, D. D. (2014). Combined scaling of fluid flow and seismic stiffness in single fractures. *Rock Mechanics and Rock Engineering*, 47(5):1613–1623.

Polak, A., Elsworth, D., Liu, J., and Grader, A. S. (2004). Spontaneous switching of permeability changes in a limestone fracture with net dissolution. *Water Resources Research*, 40(3).

Polak, A., Elsworth, D., Yasuhara, H., Grader, A. S., and Halleck, P. M. (2003). Permeability reduction of a natural fracture under net dissolution by hydrothermal fluids. *Geophysical Research Letters*, 30(20):2020.

Pollard, D. and Aydin, A. (1988). Progress in understanding jointing over the past century. *Geological Society of America Bulletin*, 100(8):1181.

Poon, C. Y., Sayles, R. A., and Jones, T. A. (1992). Surface measurement and fractal characterization of naturally fractured rocks. *Journal of Physics D: Applied Physics*, 25(8):1269–1275.

Power, W. L., Tullis, T. E., Brown, S. R., Boitnott, G. N., and Scholz, C. H. (1987). Roughness of natural fault surfaces. *Geophysical Research Letters*, 14(1):29.

Putignano, C., Afferrante, L., Carbone, G., and Demelio, G. (2012). A new efficient numerical method for contact mechanics of rough surfaces. *International Journal of Solids and Structures*, 49(2):338–343.

Pyrak-Nolte, L. J. and Morris, J. P. (2000). Single fractures under normal stress: The relation between fracture specific stiffness and fluid flow. *International Journal of Rock Mechanics and Mining Sciences*, 37(1-2):245–262.

Pyrak-Nolte, L. J., Myer, L. M., Cook, N. G. W., and Witherspoon, P. A. (1987). Hydraulic And Mechanical Properties of Natural Fractures In Low Permeability Rock. In *6th ISRM Congress, Montreal, Canada*.

Pyrak-Nolte, L. J., Myer, L. R., and Cook, N. G. W. (1990). Transmission of seismic waves across single natural fractures. *Journal of Geophysical Research*, 95:8617.

Pyrak-Nolte, L. J. and Nolte, D. D. (2016). Approaching a universal scaling relationship between fracture stiffness and fluid flow. *Nature Communications*, 7:10663.

Quintessa (2014). DECOVALEX 2015 C1. Technical report, Quintessa Ltd.

Raven, K. G. and Gale, J. E. (1985). Water flow in a natural rock fracture as a function of stress and sample size. *International Journal of Rock Mechanics and Mining Sciences & Geomechanics Abstracts*, 22(4):251–261.

Renard, P. and de Marsily, G. (1997). Calculating equivalent permeability: a review. *Advances in Water Resources*, 20(5-6):253–278.

Renshaw, C. (1995). On the relationship between mechanical and hydraulic apertures in rough-walled fractures. *Journal of Geophysical Research*, pages 629–636.

Revil, A. (2001). Pervasive pressure solution transfer in a quartz sand. *Journal of Geophysical Research*, 106(B5):8665.

Rimstidt, J. and Barnes, H. (1980). The kinetics of silica-water reactions. *Geochimica et Cosmochimica Acta*, 44(11):1683–1699.

Robin, P.-Y. F. (1978). Pressure solution at grain-to-grain contacts. *Geochimica et Cosmochimica Acta*, 42(9):1383–1389.

Rutqvist, J., Leung, C., Hoch, A., Wang, Y., and Wang, Z. (2013). Linked multicontinuum and crack tensor approach for modeling of coupled geomechanics, fluid flow and transport in fractured rock. *Journal of Rock Mechanics and Geotechnical Engineering*, 5(1):18–31.

Rutter, E. H. (1976). The kinetics of rock deformation by pressure solution [and discussion]. *Philosophical Transactions of the Royal Society A: Mathematical, Physical and Engineering Sciences*, 283(1312):203–219.

Rutter, E. H. (1983). Pressure solution in nature, theory and experiment. *Journal of the Geological Society*, 140(5):725–740.

Sævik, P. N., Berre, I., Jakobsen, M., and Lien, M. (2013). A 3D computational study of effective medium methods applied to fractured media. *Transport in Porous Media*, 100(1):115–142.

Sævik, P. N., Jakobsen, M., Lien, M., and Berre, I. (2014). Anisotropic effective conductivity in fractured rocks by explicit effective medium methods. *Geophysical Prospecting*, 62(6):1297–1314.

Sainsot, P. and Lubrecht, A. A. (2011). Efficient solution of the dry contact of rough surfaces: a comparison of fast Fourier transform and multigrid methods. *Proceedings of the Institution of Mechanical Engineers, Part J: Journal of Engineering Tribology*, 225(6):441–448.

Sandve, T., Berre, I., and Nordbotten, J. (2012). An efficient multi-point flux approximation method for Discrete Fracture–Matrix simulations. *Journal of Computational Physics*, 231(9):3784–3800.

Sanford, R. J. and Dally, J. W. (1979). A general method for determining mixed-mode stress intensity factors from isochromatic fringe patterns. *Engineering Fracture Mechanics*, 11(4):621–633.

Sayers, C. M. and Kachanov, M. (1995). Microcrack-induced elastic wave anisotropy of brittle rocks. *Journal of Geophysical Research*, 100(B3):4149.

Schmittbuhl, J., Schmitt, F., and Scholz, C. H. (1995). Scaling invariance of crack surfaces. *Journal of Geophysical Research*, 100:5953–5973.

Schmittbuhl, J., Steyer, A., Jouniaux, L., and Toussaint, R. (2008). Fracture morphology and viscous transport. *International Journal of Rock Mechanics and Mining Sciences*, 45(3):422–430.

Sharifzadeh, M., Mitani, Y., and Esaki, T. (2006). Rock joint surfaces measurement and analysis of aperture distribution under different normal and shear loading using GIS. *Rock Mechanics and Rock Engineering*, 41(2):299–323.

Simo, J. and Laursen, T. (1992). An augmented lagrangian treatment of contact problems involving friction. *Computers & Structures*, 42(1):97–116.

Snow, D. T. (1969). Anisotropie permeability of fractured media. *Water Resources Research*, 5(6):1273–1289.

Spiers, C. J., Schutjens, P. M. T. M., Brzesowsky, R. H., Peach, C. J., Liezenberg, J. L., and Zwart, H. J. (1990). Experimental determination of constitutive parameters governing creep of rocksalt by pressure solution. *Geological Society, London, Special Publications*, 54(1):215–227.

Stanley, H. M. and Kato, T. (1997). An FFT-Based method for rough surface contact. *Journal of Tribology*, 119(3):481.

Sun, Z., Gerrard, C., and Stephansson, O. (1985). Rock joint compliance tests for compression and shear loads. *International Journal of Rock Mechanics and Mining Sciences & Geomechanics Abstracts*, 22(4):197–213.

Swan, G. (1983). Determination of stiffness and other joint properties from roughness measurements. *Rock Mechanics and Rock Engineering*, 16:19–38.

Taron, J. and Elsworth, D. (2010). Constraints on compaction rate and equilibrium in the pressure solution creep of quartz aggregates and fractures: Controls of aqueous concentration. *Journal of Geophysical Research*, 115(B7):B07211.

Tatone, B. S. A. and Grasselli, G. (2013). An investigation of discontinuity roughness scale dependency using high-Resolution surface measurements. *Rock Mechanics and Rock Engineering*, 46(4):657–681.

Taylor, W. L., Pollard, D. D., and Aydin, A. (1999). Fluid flow in discrete joint sets: Field observations and numerical simulations. *Journal of Geophysical Research*, 104(B12):28983.

Tsang, Y. (1984). The effect of tortuosity on fluid flow through a single fracture. *Water Resources Research*, 20(9):1209–1215.

Ucar, E., Berre, I., and Keilegavlen, E. (2015). Simulation of slip-induced permeability enhancement accounting for multiscale fractures. In *Proceedings of 40th Stanford Geothermal Workshop*.

Vallet, C., Lasseux, D., Zahouani, H., and Sainsot, P. (2009). Sampling effect on contact and transport properties between fractal surfaces. *Tribology International*, 42(8):1132–1145.

Voegele, M., Hardin, E., Lingle, D., Board, M., and Barton, N. (1981). Site characterization of joint permeability using the heated Block test. In *The 22nd US Symposium on Rock Mechanics (USRMS)*. American Rock Mechanics Association.

Watanabe, N., Hirano, N., and Tsuchiya, N. (2008). Determination of aperture structure and fluid flow in a rock fracture by high-resolution numerical modeling on the basis of a flow-through experiment under confining pressure. *Water Resources Research*, 44(6):1–11.

Wei, Z. Q. and Hudson, J. A. (1988). Permeability of jointed rock masses. In *ISRM International Symposium*, Madrid. International Society for Rock Mechanics.

Wen, X., Durlofsky, L., and Edwards, M. (2003). Use of border regions for improved permeability upscaling. *Mathematical Geology*, 35(5):521–547.

Westergaard, H. M. (1939). Bearing pressures and cracks. *Journal of Applied Mechanics*, 61:A49–A53.

Weyl, P. K. (1959). Pressure solution and the force of crystallization: a phenomenological theory. *Journal of Geophysical Research*, 64(11):2001–2025.

Witherspoon, P. A., Wang, J. S. Y., Iwai, K., and Gale, J. E. (1980). Validity of Cubic Law for fluid flow in a deformable rock fracture. *Water Resources Research*, 16(6):1016–1024.

Wriggers, P. (2006). *Computational Contact Mechanics*. Springer, Berlin.

Wu, X., Hou, T., and Efendiev, Y. (2002). Analysis of upscaling absolute permeability. *Discrete and Continuous Dynamical Systems - Series B*, 2(2):185–204.

Yang, C., Tartaglino, U., and Persson, B. N. J. (2006). A multiscale molecular dynamics approach to contact mechanics. *The European Physical Journal E: Soft Matter*, 19(1):47–58.

Yastrebov, V. A., Anciaux, G., and Molinari, J.-F. (2015). From infinitesimal to full contact between rough surfaces: Evolution of the contact area. *International Journal of Solids and Structures*, 52:83–102.

Yasuhara, H. and Elsworth, D. (2004). Evolution of permeability in a natural fracture: Significant role of pressure solution. *Journal of Geophysical Research*, 109(B3):B03204.

Yasuhara, H. and Elsworth, D. (2006). A numerical model simulating reactive transport and evolution of fracture permeability. *International Journal for Numerical and Analytical Methods in Geomechanics*, 30(10):1039–1062.

Yasuhara, H. and Elsworth, D. (2008). Compaction of a Rock Fracture Moderated by Competing Roles of Stress Corrosion and Pressure Solution. *Pure and Applied Geophysics*, 165(7):1289–1306.

Yasuhara, H., Kinoshita, N., Ohfuji, H., Lee, D. S., Nakashima, S., and Kishida, K. (2011). Temporal alteration of fracture permeability in granite under hydrothermal conditions and its interpretation by coupled chemo-mechanical model. *Applied Geochemistry*, 26(12):2074–2088.

Yasuhara, H., Kinoshita, N., Ohfuji, H., Takahashi, M., Ito, K., and Kishida, K. (2015). Long-term observation of permeability in sedimentary rocks under high-temperature and stress conditions and its interpretation mediated by microstructural investigations. *Water Resources Research*, 51(7):5425–5449.

Yasuhara, H., Polak, A., Mitani, Y., Grader, A., Halleck, P., and Elsworth, D. (2006). Evolution of fracture permeability through fluid–rock reaction under hydrothermal conditions. *Earth and Planetary Science Letters*, 244(1-2):186–200.

Yeo, I. W., de Freitas, M. H., and Zimmerman, R. W. (1998). Effect of shear displacement on the aperture and permeability of a rock fracture. *International Journal of Rock Mechanics and Mining Sciences*, 35(8):1051–1070.

Zangerl, C., Evans, K. F., Eberhardt, E., and Loew, S. (2008). Normal stiffness of fractures in granitic rock: A compilation of laboratory and in-situ experiments. *International Journal of Rock Mechanics and Mining Sciences*, 45(8):1500–1507.

Zhang, N., Yao, J., Xue, S., and Huang, Z. (2016). Multiscale mixed finite element, discrete fracture–vug model for fluid flow in fractured vuggy porous media. *International Journal of Heat and Mass Transfer*, 96:396–405.

Zhang, X. and Sanderson, D. (2002). Evaluation of 2-Dimensional Permeability Tensors. In Zhang, X. and Sanderson, D., editors, *Numerical Modeling of Fluid Flow and Deformation*. Elsevier.

Zhang, X., Sanderson, D., Harkness, R., and Last, N. (1996). Evaluation of the 2-D permeability tensor for fractured rock masses. *International Journal of Rock Mechanics and Mining Sciences & Geomechanics Abstracts*, 33(1):17–37.

Zhao, Z., Liu, L., Neretnieks, I., and Jing, L. (2014). Solute transport in a single fracture with time-dependent aperture due to chemically medicated changes. *International Journal of Rock Mechanics and Mining Sciences*, 66:69–75.

Zimmerman, R. M. (1984). Ambient temperature testing of the G-tunnel heated block. In *The 25th US Symposium on Rock Mechanics (USRMS)*. American Rock Mechanics Association.

Zimmerman, R. W. (1990). *Compressibility of sandstones*, volume 29. Elsevier.

Zimmerman, R. W. (2008). A Simple Model for Coupling between the Normal Stiffness and the Hydraulic Transmissivity of a Fracture. In *42nd U.S. Rock Mechanics Symposium*, San Francisco.

Zimmerman, R. W. and Bodvarsson, G. S. (1996a). Effective transmissivity of two-dimensional fracture networks. *International Journal of Rock Mechanics and Mining Sciences & Geomechanics Abstracts*, 33(4):433–438.

Zimmerman, R. W. and Bodvarsson, G. S. (1996b). Hydraulic conductivity of rock fractures. *Transport in Porous Media*, 23(1):1–30.

Zimmerman, R. W., Chen, D.-W., and Cook, N. G. W. (1992). The effect of contact area on the permeability of fractures. *Journal of Hydrology*, 139(1-4):79–96.

Zimmerman, R. W., Chen, D.-W., Long, J. C. S., and Cook, N. G. W. (1990). Hydromechanical coupling between stress, stiffness, and hydraulic conductivity of rock joints and fractures. In Barton and Stephansson, editors, *Rock Joints*, pages 571–577. Balkema, Rotterdam.

Zimmerman, R. W., Kumar, S., and Bodvarsson, G. S. (1991). Lubrication theory analysis of the permeability of rough-walled fractures. *International Journal of Rock Mechanics and Mining Sciences & Geomechanics Abstracts*, 28(4):325–331.

Zimmerman, R. W. and Yeo, I. W. (2000). Fluid Flow in Rock Fractures: From the Navier-Stokes Equations to the Cubic Law. In Faybishenko, B., Witherspoon, P. A., and Benson, S. M., editors, *Dynamics of fluids in fractured rock*, volume 122 of *Geophysical Monograph Series*, pages 213–224. American Geophysical Union, Washington, D. C.

Zoback, M. D. (2007). *Reservior Geomechanics*. Cambridge University Press.

Zoback, M. L., Zoback, M. D., Adams, J., Assumpção, M., Bell, S., Bergman, E. A., Blümling, P., Brereton, N. R., Denham, D., Ding, J., Fuchs, K., Gay, N., Gregersen, S., Gupta, H. K., Gvishiani, A., Jacob, K., Klein, R., Knoll, P., Magee, M., Mercier, J. L., Müller, B. C., Paquin, C., Rajendran, K., Stephansson, O., Suarez, G., Suter, M., Udias, A., Xu, Z. H., and Zhizhin, M. (1989). Global patterns of tectonic stress. *Nature*, 341(6240):291–298.

Appendix A

Application IO

A.1 THMC module

Example JSON input file to the THMC module, along with the finite-element geometry files *csp*.asc, *csp*.dat, *csp*-regions.txt

```
{
  "model name": "csp",
  "contact": {
    "S1": 1.0,
    "S2 to S1": 2.0,
    "S3 to S1": 3.1,
    "it max": 8,
    "it uzawamax": 11,
    "mu": 0.6,
    "debug": true,
    "p0": 0.9,
    "penalty scale": 0.1,
    "run cont": true
  },
  "permeability": {
    "E": 60000000000.0,
    "N": 13,
    "N_c": 9,
    "dij_flow": 0,
    "lambda_m": 0.0005,
    "matrix permeability": 1.0e-15,
    "debug": true,
    "nu": 0.15,
```

```
    "omega distance": 0.75,
    "plots": false,
    "precipitation": false,
    "maximum time increment": 2.0E12,
    "restart": false,
    "run diss": true,
    "run flow": true,
    "run mech": true,
    "seed": 42,
    "stress denormalization": 30000000.0,
    "temperature": 423,
    "time": 150000000000000.0
  }
}
```


Example JSON result file of the THMC module, here for the DFM of two embedded conjugate fractures (Figure 5.1b) in the $\beta = 90$ degree configuration.


```
{
  "fractures": {
    "FRACTURE_1": {
      "ah": 0.00396034894826,
      "ah_para": 0.00374614642586,
      "ah_perp": 0.00417455147065,
      "am": 0.00392425018921,
      "ar": 0.00864457232914,
      "idx": 0,
      "normg": 1.30437474258e-05,
      "normt": 19368301.7257,
      "radius": 5.0,
      "rc": 0.0195045471191,
      "shear_x": 0.00655110519355,
      "shear_y": 2.32236762903e-05,
      "shear_z": -0.0113468454839,
      "sheard": 0.0118162506485,
      "sheart": 10799326.0744,
      "state": "closed",
      "unormal": [
        0.8660248698252083,
        1.0867198366518868e-07,
        0.5000009248433637
      ]
    },
    "FRACTURE_2": {
      "ah": 0.00392850263068,
      "ah_para": 0.0037148540073,
      "ah_perp": 0.00414215125405,
```

```
      "am": 0.00389159320245,
      "ar": 0.00864457232914,
      "idx": 1,
      "normg": 2.03214835752e-05,
      "normt": 20185669.0912,
      "radius": 5.0,
      "rc": 0.0202484130859,
      "shear_x": -0.00665766918584,
      "shear_y": -3.33688000885e-05,
      "shear_z": -0.0115314177876,
      "sheard": 0.0121326566258,
      "sheart": 11263609.2197,
      "state": "closed",
      "unormal": [
        -0.8660253028382491,
        -2.4957208727224674e-07,
        0.5000001748438261
      ]
    }
  },
  "network": {
    "k_eigen": [
      3.644e-09,
      2.1696e-09,
      2.352e-13
    ],
    "k_tensor": [
      2.9769e-13,
      -7.8621e-14,
      -1.1643e-11,
      -7.8621e-14,
      3.644e-09,
      -1.4953e-12,
      -1.1643e-11,
      -1.4953e-12,
      2.1695e-09
    ],
    "k_vectors": [
      1.8337e-05,
      -1.0,
      0.001014,
      -0.0053672,
      0.0010139,
      0.99999,
      -0.99999,
      -2.3779e-05,
      -0.0053672
    ]
```

```
  }
}
```

Appendix B

Permissions

ELSEVIER LICENSE
TERMS AND CONDITIONS

May 18, 2016

This is a License Agreement between Philipp D Lang ("You") and Elsevier ("Elsevier") provided by Copyright Clearance Center ("CCC"). The license consists of your order details, the terms and conditions provided by Elsevier, and the payment terms and conditions.

All payments must be made in full to CCC. For payment instructions, please see information listed at the bottom of this form.

Supplier	Elsevier Limited The Boulevard,Langford Lane Kidlington,Oxford,OX5 1GB,UK
Registered Company Number	1982084
Customer name	Philipp D Lang
Customer address	4 Sinclair Road London, W14 0NH
License number	3823550598394
License date	Mar 07, 2016
Licensed content publisher	Elsevier
Licensed content publication	Geothermics
Licensed content title	Experimental investigation of fracture aperture and permeability change within Enhanced Geothermal Systems
Licensed content author	Robert A. Caulk,Ehsan Ghazanfari,Julia N. Perdrial,Nico Perdrial
Licensed content date	July 2016
Licensed content volume number	62
Licensed content issue number	n/a
Number of pages	10
Start Page	12
End Page	21
Type of Use	reuse in a thesis/dissertation
Portion	figures/tables/illustrations
Number of figures/tables/illustrations	1
Format	electronic
Are you the author of this Elsevier article?	No
Will you be translating?	No
Original figure numbers	figure 8
Title of your thesis/dissertation	Multiscale modeling of thermo-hydro-mechanical-chemical processes in fractured rock
Expected completion date	May 2016
Estimated size (number of pages)	120
Elsevier VAT number	GB 494 6272 12

ELSEVIER LICENSE
TERMS AND CONDITIONS

May 18, 2016

This is a License Agreement between Philipp D Lang ("You") and Elsevier ("Elsevier") provided by Copyright Clearance Center ("CCC"). The license consists of your order details, the terms and conditions provided by Elsevier, and the payment terms and conditions.

All payments must be made in full to CCC. For payment instructions, please see information listed at the bottom of this form.

Supplier	Elsevier Limited The Boulevard,Langford Lane Kidlington,Oxford,OX5 1GB,UK
Registered Company Number	1982084
Customer name	Philipp D Lang
Customer address	4 Sinclair Road London, W14 0NH
License number	3811830018017
License date	Feb 18, 2016
Licensed content publisher	Elsevier
Licensed content publication	Tectonophysics
Licensed content title	Imaging surface contacts: power law contact distributions and contact stresses in quartz, calcite, glass and acrylic plastic
Licensed content author	James H. Dieterich,Brian D. Kilgore
Licensed content date	15 May 1996
Licensed content volume number	256
Licensed content issue number	1-4
Number of pages	21
Start Page	219
End Page	239
Type of Use	reuse in a thesis/dissertation
Portion	figures/tables/illustrations
Number of figures/tables/illustrations	1
Format	electronic
Are you the author of this Elsevier article?	No
Will you be translating?	No
Original figure numbers	9
Title of your thesis/dissertation	Multiscale modeling of thermo-hydro-mechanical-chemical processes in fractured rock
Expected completion date	May 2016
Estimated size (number of pages)	120
Elsevier VAT number	GB 494 6272 12